

---

Theses and Dissertations

---

Fall 2014

## Control of polymer biochemical, mechanical, and physical properties for the rational design of retinal regenerative tissue scaffolds

Kristan Sorenson Worthington  
*University of Iowa*

Follow this and additional works at: <https://ir.uiowa.edu/etd>

 Part of the [Chemical Engineering Commons](#)

Copyright 2014 Kristan Sorenson Worthington

This dissertation is available at Iowa Research Online: <https://ir.uiowa.edu/etd/2023>

---


### Recommended Citation

Worthington, Kristan Sorenson. "Control of polymer biochemical, mechanical, and physical properties for the rational design of retinal regenerative tissue scaffolds." PhD (Doctor of Philosophy) thesis, University of Iowa, 2014.

<https://doi.org/10.17077/etd.yl3zlvzi>

---

Follow this and additional works at: <https://ir.uiowa.edu/etd>

 Part of the [Chemical Engineering Commons](#)

CONTROL OF POLYMER BIOCHEMICAL, MECHANICAL, AND PHYSICAL  
PROPERTIES FOR THE RATIONAL DESIGN OF RETINAL REGENERATIVE  
TISSUE SCAFFOLDS

by

Kristan Sorenson Worthington

A thesis submitted in partial fulfillment  
of the requirements for the Doctor of  
Philosophy degree in Chemical and Biochemical Engineering  
in the Graduate College of  
The University of Iowa

December 2014

Thesis Supervisor: Professor C. Allan Guymon

Copyright by  
KRISTAN SORENSON WORTHINGTON  
2014  
All Rights Reserved

Graduate College  
The University of Iowa  
Iowa City, Iowa

CERTIFICATE OF APPROVAL

---

PH.D. THESIS

---

This is to certify that the Ph.D. thesis of

Kristan Sorenson Worthington

has been approved by the Examining Committee  
for the thesis requirement for the Doctor of Philosophy  
degree in Chemical and Biochemical Engineering at the December 2014  
graduation.

Thesis Committee: \_\_\_\_\_  
C. Allan Guymon, Thesis Supervisor

\_\_\_\_\_  
Aliasger K. Salem

\_\_\_\_\_  
Budd A. Tucker

\_\_\_\_\_  
Julie L.P. Jessop

\_\_\_\_\_  
Jennifer Fiegel

\_\_\_\_\_  
Eric E. Nuxoll

To my husband and parents

From the cowardice that shrinks from new truth;  
From the laziness that is content with half-truth;  
From the arrogance that thinks it has all truth;  
O God of Truth, deliver us.

Ancient Prayer

## ACKNOWLEDGMENTS

First, I would like to express thanks to my advisors, Drs. Allan Guymon, Aliasger Salem, and Budd Tucker. All three provided vital guidance and feedback these past five years and were incredibly patient while I determined my career goals and navigated the ups and downs of research. From Dr. Guymon I have learned a great deal about presenting my work in an organized and compelling way, from Dr. Salem I have come to know the art of positive thinking and applying creative problem-solving to research challenges, and Dr. Tucker has given me the creative freedom to pursue captivating and challenging projects. All three have contributed significantly to my personal development and I am grateful for the ways in which they have helped me grow.

Numerous other faculty members have also added to my success and deserve thanks. My committee members, for example, have given valuable research feedback that has enabled me to think outside the box. Furthermore, they are always willing to meet with me to give career development guidance. I am also grateful to the department support staff, past and current, for their assistance with a multitude of day-to-day operations that are vital to student success. I have also been fortunate to receive funding from various sources including the National Science Foundation, the Wynn Institute for Vision Research, and the University of Iowa Graduate College. Faculty and staff at the Graduate College have also been incredibly helpful, supportive, and friendly; their generous support has given me the freedom to find joy in my research.

Several undergraduate students have contributed to my success and provided beneficial teaching opportunities; each gave me something valuable and unique to shape me as a researcher and leader. Furthermore, my research group members and other peers have been invaluable to me throughout my graduate school experience. Although there are too many to name here, many of these close friends encouraged me through difficult

times, served as sounding boards for good and bad ideas, and made the past five years pleasant and memorable.

Lastly, I must express appreciation to my wonderful family members, who have always been more than supportive. My parents have spent many years facilitating my curiosity, teaching me the value of hard work through their examples, and demonstrating how to find humor in life. My husband consistently believes in my abilities and exercises patience with my faults during even the most stressful times. My close friends, siblings, in-laws, and extended family show interest and express encouragement at every turn. Overall much of my success can be attributed in part to the love and support of exemplary family, friends, and mentors – thank you all.



## ABSTRACT

Although millions of individuals worldwide are affected by blinding retinal degenerative diseases, most have very few options for treatment and no hope for vision restoration. Induced pluripotent stem cell (iPSC) replacement therapies represent a promising treatment option, but their effectiveness is limited by an overall lack of physical support for injected cells. Stem cell scaffolds can be used to provide this support by serving as an attachment platform for cells before, during, and after implantation. Thus, the design of polymer scaffolds with appropriate biochemistry, mechanical properties, and morphology is a critical step toward developing feasible stem cell therapies for blinding eye diseases. In this work, we aim to design a regenerative scaffold for the retina and determine the interplay among these three key design parameters. First, the feasibility of using a synthetic scaffold to grow and differentiate iPSCs to neural progenitor cells is demonstrated. The porous and degradable poly(lactic-co-glycolic acid) scaffolds employed were able to support a greater density of differentiating iPSCs than traditional tissue culture plastic. Additionally, the power of chitosan, a naturally occurring polymer, to overcome the toxic effects of copper nanoparticles is described. For two different cell types, various doses, and several time points, chitosan coated copper nanoparticles were significantly less toxic than non-coated particles. The mechanical properties of the human retina and the effects of aging and disease were also estimated using measurements of compressive modulus in animal models. In order to reach a range similar to native tissue, polymer mechanical properties were controlled using cross-linking density and surfactant templating. The influence of morphology was studied by inducing polymer structure changes via surfactant templating. Morphology significantly influenced water uptake and compressive modulus for both cross-linked poly(ethylene glycol) (PEG) and cross-linked chitosan hydrogels. Surfactant templating did not negatively affect the biocompatibility of PEG hydrogels and slightly improved the

ability of chitosan hydrogels to support the growth and differentiation of iPSCs. Overall we have demonstrated the ability to tune polymer structure, mechanical properties, and biochemistry. These results add to the growing body of research aimed to understand and control cell/material interactions for biomaterial optimization.

## TABLE OF CONTENTS

LIST OF TABLES .....	xi
LIST OF FIGURES .....	xii
CHAPTER	
I. INTRODUCTION .....	1
Retinal Degeneration .....	2
Biomaterials for Retinal Regeneration .....	3
Biochemical Properties .....	5
Naturally Occurring Polymers .....	6
Inert Synthetic Polymers .....	9
Degradable Synthetic Polymers .....	11
Bio/Synthetic Composites .....	13
Mechanical Properties .....	16
Morphology .....	19
Direct Fabrication .....	21
Direct Templating .....	22
Self-Assembled Templates .....	23
Photopolymerization .....	30
Research Summary .....	33
II. OBJECTIVES .....	35
III. DIFFERENTIATION OF INDUCED PLURIPOTENT STEM CELLS TO NEURAL PROGENITOR CELLS ON A THIN, POROUS PLGA SCAFFOLD .....	39
Introduction .....	39
Materials and Methods .....	40
Scaffold Fabrication .....	40
Cell Culture .....	41
Scanning Electron Microscopy .....	42
Porosity Quantification .....	42
Growth Quantification .....	43
Results .....	43
Scaffold Characterization .....	43
Cell Proliferation .....	44
Cell Differentiation .....	45
Discussion .....	47
IV. CHITOSAN COATING OF COPPER NANOPARTICLES REDUCES IN VITRO TOXICITY AND INCREASES INFLAMMATION IN THE LUNG .....	50
Introduction .....	51
Materials and Methods .....	54
Reagents .....	54
Cu NP Coating .....	54
Particle Size Analysis .....	55
Composition Analysis .....	55
Surface Analysis .....	56

Dissolution of the Coated and Uncoated Particles .....	57
Cytotoxicity Analysis in vitro .....	57
Animal Models .....	58
Nasal Instillation Exposure.....	59
Bronchoalveolar Lavage (BAL) Fluid.....	59
Copper Analysis in Exposure Solutions, Lung Tissue, and BAL Fluid.....	60
Statistical Analysis .....	61
Results and Discussion .....	61
Conclusions.....	70
V. MECHANICAL PROPERTIES OF MURINE AND PORCINE OCULAR TISSUES IN COMPRESSION.....	72
Introduction.....	72
Materials and Methods .....	75
Animals and Dissection.....	75
Polymers.....	76
Stress and Strain Measurement .....	77
Data Analysis.....	78
Statistics.....	78
Results.....	79
Discussion.....	84
VI. PHYSICAL AND BIOCHEMICAL PROPERTIES OF SURFACTANT TEMPLATED POLY(ETHYLENE GLYCOL) DIMETHACRYLATE.....	87
Introduction.....	87
Materials and Methods .....	90
Sample Preparation.....	90
Diffraction Studies.....	91
Morphology .....	91
Physical Properties .....	91
Surfactant Extraction .....	92
Cell Culture and Toxicity.....	93
Results and Discussion .....	94
Diffraction .....	94
Morphology and Physical Properties.....	95
Surfactant Extraction and Biocompatibility.....	99
Conclusions.....	101
VII. PROPERTY CONTROL OF CHITOSAN HYDROGELS FOR NEURONAL DIFFERENTIATION .....	103
Materials and Methods .....	108
Chitosan Functionalization.....	108
Sample Preparation.....	108
Physical Properties .....	111
Bioactivity .....	112
Results and Discussion .....	113
Surfactant Templating .....	114
Copolymerization .....	119
Bioactivity .....	121
Conclusions.....	123
VIII. CONCLUSIONS AND RECOMMENDATIONS .....	126
Biochemical Properties .....	126

Mechanical Properties .....	128
Morphology .....	129
Recommendations.....	131
Biochemical Properties.....	131
Mechanical Properties .....	133
Morphology .....	134

## APPENDIX

A. MATERIALS AND METHODS.....	137
Materials and Sample Preparation .....	137
Monomers and Polymers .....	137
Surfactants .....	140
Polymerization and Processing.....	141
Characterization.....	143
Chemical Composition .....	143
Structure .....	144
Physical Properties .....	145
Bioactivity.....	146
Cell Culture and Seeding.....	146
Proliferation and Viability .....	148
Animals.....	150
REFERENCES .....	153

## LIST OF TABLES

## Table

1. Relationships between amphiphile shape, water content, and preferred aggregate structure, based on the Isrealachvili Model (adapted from Gin et al. 2001).226 .....	27
2. Size, zeta potential, and dissolution of Cu NPs with and without coating .....	64
3. Characterization of lung tissue and fluid after nasal instillation of coated and uncoated Cu NPs. Except where noted, data was obtained from the post-necropsy BAL fluid. Data are expressed as mean $\pm$ standard error.....	68
4. Sample size, mean, standard error of the mean, and average or estimated thickness for each group of porcine tissue samples.....	80
5. Sample size before and after outlier and aberrant data rejection, mean, standard error of the mean, and estimated thickness for each group of murine retina samples .....	81
6. Sample size, mean, standard error of the mean, and average thickness for each group of polymer samples. ....	83
7. Chain length information for surfactants used to template functionalized chitosan hydrogels. ....	110
8. Formulations for samples prepared in this study with. Values are given in wt% of total sample. ....	111
9. Chain lengths of surfactants used for templating.....	142

## LIST OF FIGURES

## Figure

1. Schematic of the human retina and underlying support layers. ....1
2. Compared to normal vision (A), an example of how age-related macular degeneration (B) and retinitis pigmentosa (C) may affect visual acuity. ....3
3. Chemical structures of A) Poly(methyl methacrylate) (PMMA), B) poly(dimethylsiloxane) (PDMS), C) Poly (lactic-co-glycolic acid) (PLGA), D) Poly(caprolactone) (PCL), E) Poly(glycerol sebacate) (PGS), F) Poly(hydroxy butyrate-co-valerate) (PHBV), and G) Chitosan. ....9
4. Representations of typical lyotropic liquid crystalline phases and geometries. Shown are A) micellar, B) cubic micellar, C) hexagonal, D) biocontinuous cubic, and E) lamellar.....27
5. Schematic of the process of templating crosslinked PEG with surfactant in ordered LLC geometries. ....29
6. Schematic of porous PLGA scaffolds fabrication process .....41
7. Characterization of PLGA scaffold porosity: A) scanning electron micrograph of a scaffold and B) histogram of pore sizes based on three independent scanning electron micrographs. ....44
8. Cell proliferation on porous PLGA scaffolds was captured after 1 week (A) and 2 weeks (B) using scanning electron microscopy and quantified using an MTT assay (C). ....45
9. Cell differentiation on porous PLGA scaffolds captured at various magnifications after 1 week. ....46
10. Cell differentiation on porous PLGA scaffolds captured at various magnifications after 2 weeks. ....47
11. TEM images of Cu NPs with a) no coating (Cu NPs), b) a Tween<sup>®</sup> 80 coating (Cu NPs + Tw), and c) a Tween<sup>®</sup> 80 coating followed by chitosan coating (Cu NPs + Tw + Ch) .....62
12. Physical characterization of coated and uncoated Cu NPs. Shown are a)confocal microscopy images of Cu NPs with no coating (inset), and coated with Tween<sup>®</sup> 80 and rhodamine-conjugated chitosan; b) XPS data in the N1s binding energy region for Cu NPs, Cu NPs + Tw, and Cu NPs + Tw + Ch where only the Cu NPs + Tw + Ch show the presence of nitrogen on the surface of nanoparticles; and c) XRD characterization of Cu NPs, Cu NPs + Tw, Cu NPs + Tw + Ch, and unprocessed Cu NPs.....63
13. Toxicity of coated and uncoated Cu NPs to A549 cells. Toxicity was measured relative to untreated cells of coated and uncoated Cu NPs on A549 cells exposed for a) 24 and b) 52 hours. Statistical analysis was

- performed by a two-way analysis of variance followed by Bonferonni post tests. DHE oxidation levels (c) of A549 cells after 24 hours of exposure to coated and uncoated Cu NPs. Statistical analysis was performed by a Kruskal-Wallis test followed by Dunn's post tests. For all panels, the statistical significance shown is relative to Cu NPs. Error bars represent the standard error mean, \*\*  $p < 0.01$ , \*\*\*  $p < 0.001$  .....67
14. Inflammatory response in the post-necropsy lung BAL fluid 24 hrs after nasal instillation of coated and uncoated Cu NPs. Differential cell counts (a) show the number of macrophages, neutrophils and lymphocytes, while chemokine/cytokine analysis (b) shows the levels of selected inflammatory markers. Statistical analyses were performed by Kruskal-Wallis tests for each cell type or chemokine/cytokine followed by Dunn's post tests. Statistical comparisons shown are relative to the naive group for each cell type or inflammatory marker. The differences between all other groups are not statistically significant. Error bars represent the standard error mean,  $n = 5-7$ , \*  $p < 0.05$ , \*\*\*  $p < 0.001$ , \*\*\*  $p < 0.001$  .....70
15. Schematic of the retina (A) under tension (B) and compression (C) showing directionality of forces.....75
16. Mechanical analysis of eye tissues in compression. 5 mm circular punches of the RPE/Choroid (A) are shown in the DMA compression clamp. B: A schematic diagram depicting the compression paradigm/tissue instrument interaction. The mean compressive modulus (C) of porcine corneal and sclera tissue is greater than that of retinal tissue, while the modulus of choroid with retinal pigment epithelium (RPE) is slightly lower. Error bars represent standard error of the mean, \*\* $p < 0.01$ , \*\*\* $p < 0.001$ . .....80
17. Moduli of whole mouse retinas at different ages and disease states. A–B: Exemplary whole mouse retina that has been dissected free of the optic cup, placed photoreceptor side down and prepared for compression analysis. As liquid is removed surface tension allows the dissected retina to lay flat (A), edges of the retinal cup are gently teased out to their most extreme limit taking care not to disrupt tissue integrity (B). C: Analysis of the development and degeneration of mouse retina mechanical properties demonstrate that the compressive modulus of mouse retina stays relatively constant in the range of ages examined (wild type C57BL/6J) but rapidly deteriorates with mutation-induced degeneration (C3H/HeJ<sup>Pde6rd1</sup>). Error bars represent standard error of the mean, \*\*\* $p < 0.001$ .....83
18. Compressive modulus of various polymers. The compressive modulus of gelatin and fully-hydrated crosslinked PEG (FHC PEG) most closely approximate the transverse compressive modulus observed for healthy retinas, where semi-hydrated crosslinked PEG (SHC PEG) and fully hydrated PDMS moduli are much higher. Error bars represent standard error of the mean.....84
19. Schematic of the process of templating crosslinked PEG with surfactants .....88
20. Chemical structures of A) PEGDMA 875, B) Brij 30, C) DTAB, and D) SDS .....90



21. Small x-ray scattering (A) before (dotted lines) and after polymerization (solid lines) and polarized light microscopy (B-C) post-polymerization evaluation of nanostructure of PEG templated with no surfactant (blue), Brij 30 (red), DTAB (green), and SDS (purple). .....	96
22. SEM images showing the morphology of PEG templated with no surfactant (A), Brij 30 (B), SDS (C), and DTAB (D).....	97
23. Water uptake (A) and compressive modulus (B) of PEG hydrogels templated with no surfactant (red), non-ionic surfactant (Brij 30, blue), and cationic surfactant (DTAB, green) are inversely correlated (C). Statistical significance was determined using two-way analysis of variance (ANOVA). * $p < 0.05$ , ** $p < 0.01$ , *** $p < 0.001$ .....	98
24. Removal of nonionic surfactant (Brij 30) using acetone as solvent with time, as measured gravimetrically (A) and the relative efficiency of various extraction solvents (B) after one week, measured using cell viability. ....	100
25. MiPS cells grown on isotropic (A) and Brij 30 templated (B) crosslinked PEG after one week. White arrows mark groups of non-adherent cells.....	101
26. Chemical structures of the four surfactant families: A) Pluronic block copolymers, B) Tween, C) polyoxyethylene cetyl ether (Brij), and D) quaternary ammonium surfactants .....	109
27. Nuclear magnetic resonance profile of naïve (B) and methacrylate functionalized (C) chitosan. Each peak corresponds to a distinct proton, as labeled in panel A. ....	115
28. Water uptake of 50 wt% MFCTS hydrogels templated with A) Pluronic block copolymers, B) Brij and Tween, and C) quaternary ammonium surfactants. N = 3 and error bars represent the standard error of the mean. ....	116
29. Water uptake of 50 wt% MFCTS hydrogels as a function of A) poly(ether) segment length in three families of surfactants: Tween (green), polyoxyethylene cetyl ether (blue) and quaternary ammonium (orange) and B) block copolymer hydrophobic segment length (red). N = 3 and error bars represent the standard error of the mean.....	117
30. pH-dependent water uptake (A) and compressive modulus (B) of 50 wt% MFCTS hydrogels templated with 30 wt% Brij 56 or DTAB compared to non-templated controls. N = 3 and error bars represent the standard error of the mean. ....	118
31. Water uptake (A) and compressive modulus (B) of MFCTS hydrogels copolymerized with PEGDA (blue), acrylic acid (green), and glycerol diacrylate (purple). N = 3 and error bars represent the standard error of the mean.....	120
32. Water uptake (A) and compressive modulus (B) of 50 wt% FCTS hydrogels cross-linked with PEGDA and templated with varying concentrations of DTAB. N = 3 and error bars represent the standard error of the mean.....	120

33. Water uptake (A) and compressive modulus (B) of MFCTS hydrogels templated with 30 wt% surfactant (Brij 56 or DTAB) or cross-linked with 15% PEGDA and templated with 15% DTAB. N = 3 and error bars represent the standard error of the mean.....	121
34. Scanning electron micrographs of MFCTS templated with no surfactant (A), 30 wt% Brij 56 (B), and 30 wt% DTAB (C). Scale bars represent 200 $\mu\text{m}$ . .....	122
35. Phase contrast micrographs of neuronal cells differentiating on 50 wt% MFCTS hydrogels with no surfactant template (A, D), 30 wt% Brij 56 (B, E), and 30 wt% DTAB (C, F) after one day (A-C) and three days (D-F) in culture. Scale bar represents 200 $\mu\text{m}$ . .....	124
36. Monomers and prepolymers used to create property-controlled biomaterials, including A) PEGDMA, B) PEGDA, C) glycerol diacrylate, D) AOHPMA, E) PLGA, F) PDMS, G) chitosan, H) acrylic acid and I) gelatin.....	138
37. Chemical structures of surfactants used for templating, including A) Pluronic block copolymers, B) Tween, C) Brij, D) quaternary ammonium salts, and E) sodium dodecyl sulfate.....	141
38. Schematic of the cleavage of A) Irgacure <sup>®</sup> 651 and B) Irgacure <sup>®</sup> 2959 upon exposure to UV light to yield two free radicals. ....	143
39. Drawing of glass mold used for polymerization of surfactant templated pre-polymer (orange) constructed using whole and fragmented glass slides (blue), and small binder clips (black) .....	143

## CHAPTER 1

### INTRODUCTION

Vision is arguably the most important for human survival and personal fulfilment in the modern age. Indeed, as digitization continues to cover the globe, so does the dependence of communication and other day-to-day function on the ability to see. This intricate process of light perception begins when light passes through the cornea and is focused by the lens. Focused light is then perceived by the retina, which contains light-sensing cells (rods and cones) and other types of neurons (see Figure 1). Once photoreceptor cells are activated, they send a signal to the retinal ganglion cell layer, which connects to the retinal nerve fiber layer and ultimately, the optic nerve. The optic nerve serves to carry this visual signal to the brain, where it is interpreted by the visual cortex. All of these processes work together to produce the sense we know as vision. Preservation of the retina is crucial, as it contains critical sensory neurons that cannot readily regenerate.<sup>1,2</sup>

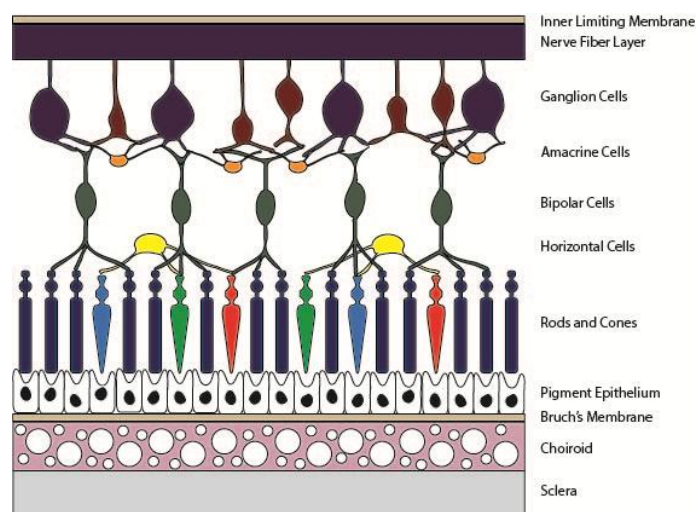


Figure 1. Schematic of the human retina and underlying support layers.

The health of the retina is normally maintained by underlying supportive layers including the retinal pigment epithelium (RPE) and the choroid. The RPE, which gets its name from its dark color, consists of a single layer of epithelial cells with tight junctions between them. Under normal conditions, the RPE also helps maintain the retina by phagocytizing, or clearing, certain parts of photoreceptor cells, making room for new growth. This RPE sheet also acts as a membrane used to actively regulate osmolarity, pH, and the transport of nutrients and oxygen to the retina. In turn, the nutrients and oxygen supplied to the retina via the RPE originate in the choroid, a dense bed of vasculature that lies between the RPE and the outer eye (sclera).<sup>1,2</sup>

### Retinal Degeneration

In some individuals, the RPE is unable to perform its intended function of phagocytizing photoreceptor outer segments. Whether due to old age or genetic misfortune, this condition ultimately leads to photoreceptor cell death and loss of vision, as represented in Figure 2.<sup>3,4</sup> The most prevalent of these diseases is age-related macular degeneration (AMD), which affects more than 2 million people over the age of 50 in the US alone.<sup>3</sup> Although rare, middle-aged and young populations can also be affected by retinal degeneration in the form of retinitis pigmentosa (RP) and other genetically inherited retinal degenerative disease.<sup>4</sup> For some early cases of disease, anti-angiogenic therapies, including photodynamic therapy and direct injection of anti-vascular endothelial growth factor agents, can help manage the symptoms and thus slow or stop visual degradation. Unfortunately, injection treatments must be repeated at least monthly, can be quite costly, and only work for a small group of those affected, while photodynamic therapy by nature destroys the retina in hundreds or thousands of regions.<sup>5-7</sup> For those with severe vision loss (later disease stage), electrostimulation of the optic nerve by implantation a “bionic eye” has recently been realized, but perceived picture quality and resolution is still relatively poor due to a lack of signal-to-nerve specificity.<sup>8,9</sup>

To date no available treatments offer hope of vision restoration to patients suffering from retinal degeneration. If underlying support tissues and functional photoreceptor cells could be regenerated in the retina, high-quality vision could be restored and greatly improve quality of life. In fact, many studies demonstrate the feasibility of using stem cells to achieve the aforementioned regeneration,<sup>10-22</sup> but the development of an effective stem cell transplantation approach is still needed for the true success of this type of therapy. Currently, devastating cell loss and minimal cellular integration occur upon transplantation of cells to the sub-retinal space. A bolus injection of photoreceptor cells, for example, has been shown in several studies to result in less than 0.01% survival of transplanted cells and an even smaller amount of integration within host retinal tissue.<sup>13,18</sup> These less than ideal results are due, in large part, to the lack of physical support that donor cells experience following the bolus injection and are particularly acute when retinal degeneration has reached late stages at the time of injection.

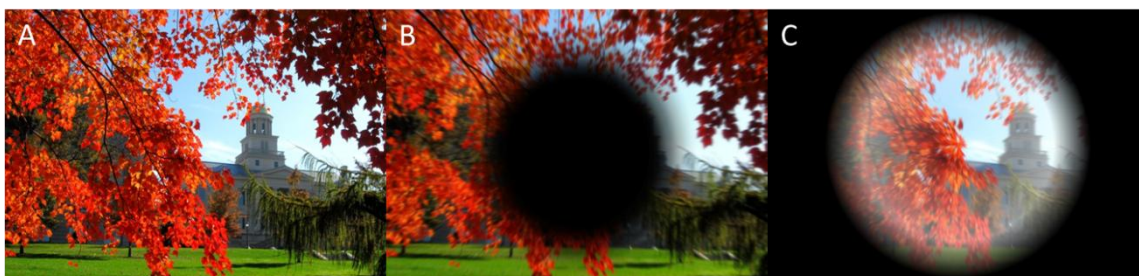


Figure 2. Compared to normal vision (A), an example of how age-related macular degeneration (B) and retinitis pigmentosa (C) may affect visual acuity.

### Biomaterials for Retinal Regeneration

In order to develop successful treatments for those with severe retinal degeneration and vision loss, it is crucial to develop effective transplantation systems for the delivery of restorative cellular therapies. Several researchers have attempted to

overcome donor cell physical support issues using natural or synthetic scaffolds on which cells attach prior to being implanted in the subretinal space. While many have seen success *ex vivo*, material successes *in vivo*, especially long term, are very limited. To design appropriate materials, the properties of such a scaffold must be controlled to improve the ability to support cell growth and differentiation.

The relationship between the eye and biomaterials has a long tradition. In fact, the first successful commercially available biomaterial, the hard contact lens, was designed for the eye. Indeed, biomaterials have been studied and used to replace or improve the function of damaged human tissues for over fifty years. Furthermore, with a global market value of over \$44 billion<sup>23</sup> and a large potential for improving human health, the study of biomaterials in general has high impact and importance. The increasing demand for biomaterials, including for the treatment of eye diseases, drives research toward the identification of key design parameters for optimizing material effectiveness and speeding the development of viable treatments for those suffering from chronic disease or injury. The first and most obvious design criterion to consider when developing a biomaterial is its biochemical properties. The implantation of a non-compatible material can lead to material failure and even more serious complications, as can a material with improper degradation products or time.

The mechanical properties of materials such as elastic modulus, and in some cases toughness, can also have a large impact on the success of biomaterials. A very stiff material embedded in very soft tissue can cause unwanted inflammation and cell death. Lastly, there is strong evidence to suggest that material morphology, or structure, also has a strong influence on the ultimate effectiveness of implanted materials. Pore size or the presence of guidance cues, for example, can both help to direct cell proliferation and differentiation. Optimizing the porosity of a material could beneficially maximize the delivery of nutrients, oxygen, and/or water to surrounding cells and tissues. In the discussion that follows, these three design considerations (biochemical properties,

mechanical properties, and morphology) are presented as separate topics. Although the three are often, if not always, inter-related, the systematic study of each is an important step toward understanding how each can be controlled to reach optimum material performance.

Understanding the influence of these three design parameters requires the ability to fabricate materials with some degree of control over each parameter. The control of biochemical properties, for example, is largely accomplished through material selection. The use of polymers (as opposed to ceramics or metals) offers expansive material variety with regard to final properties. Thus, this work focuses exclusively on polymeric biomaterials, both naturally occurring and synthetic. Unlike biochemical properties, physical properties and morphology can often be readily controlled by altering material synthesis and/or fabrication. Thus, polymerization conditions can also be used as a tool to direct final properties, offering a facile method with which to tune these three design parameters and investigate their influence.

### Biochemical Properties

Traditionally a material is deemed biocompatible if it is simply not harmful to living tissue. Within this classification though, several distinctions can be made. Naturally occurring polymers, or biopolymers, often facilitate interaction between the material and cells, and are thus considered bioactive. Meanwhile synthetic, non-degradable polymers are typically inert. These distinctions are blurred by the use of degradable synthetic polymers, for example, which can offer some control of final properties, as in non-degradable polymers, while also forming a dynamic environment for cells. Several other approaches can also be used to obtain the characteristics of both synthetic and naturally occurring polymers, as discussed below.



## Naturally Occurring Polymers

By definition, the most compatible and interactive polymers are those that occur naturally in the body. Mammalian derived whole tissues or molecules have been used for decades to build biomaterials, especially scaffolds. Transplant organs or tissues from appropriate donors are by far the most established of this type of material, yet the condition of millions of suffering patients deteriorates while they wait for available and appropriate tissues. For retinal regeneration, some have investigated the use of allogenic scaffolds from donor tissue such as the lens capsule<sup>24</sup>, Descemet's membrane,<sup>25</sup> Bruch's membrane,<sup>26</sup> amniotic membrane,<sup>27,28</sup> and the retinal inner limiting membrane<sup>29</sup> for the transplantation of cells, but these approaches have only seen real success with RPE cells. Furthermore, the availability of whole tissues or organs from healthy donors is a serious issue in almost all medical fields, including ophthalmology.

In their natural environment, cells are surrounded by extracellular matrix (ECM), a mesh of proteins and polysaccharides that serves to help regulate cell adhesion, communication, and differentiation. The most abundant fiber in this mesh and in the human body is collagen, which gives structural support to tissues. Collagen, along with its derivatives (including the hydrolyzed form, gelatin), is also the most commonly used natural polymer for biomaterials. Skin, tendon, and ligament regeneration therapies often include collagen, as do many drug delivery systems and hemostatic agents.<sup>30-32</sup> In the eye, collagen and its derivatives have been explored for decades, both as allogenic and xenogenic scaffold materials. For example, vibratomed gelatin blocks were used as early as 1989 to stabilize photoreceptor and RPE sheets during transplantation.<sup>33,34</sup> Further use of this technique, however, has revealed issues with unwanted neural rosette formation,<sup>35</sup> rapid retraction of axons<sup>36</sup> and some material folding in the subretinal space.<sup>34</sup> Thin collagen sheets have also shown some promise as ocular support materials for both donor tissue and *in vitro* RPE cells.<sup>37-39</sup> However, the use of collagen has also been shown to significantly up-regulate several angiogenic genes in RPE cells,<sup>40</sup> which could easily



exacerbate the disease. Additionally, material properties are also difficult or even impossible to control, as its complex structure must be irreversibly destroyed to isolate collagen from natural tissues.

Elastin is another abundant component of the ECM and, as its name suggests, adds flexibility and elasticity to tissues. Thus, it is most often found in blood vessels, skin, and the lung. Recently several groups have demonstrated successful fabrication of elastin materials for the regeneration of skin, vasculature, and cardiomyocytes.<sup>41-43</sup> Cell binding within the ECM can be attributed in large part to laminin, another of its main components. Although it is rarely used alone to construct biomaterials, laminin is often incorporated as an additive or material surface coating to encourage binding.<sup>44-46</sup> Other materials based on ECM molecules include those made using fibrinogen for the growth of cardiomyocytes<sup>47</sup> and hyaluronic acid for cartilage regrowth.<sup>48-50</sup> As with collagen, the properties of materials fabricated from these ECM biomolecules are often difficult to control. Though they are very biocompatible and bioactive, the availability of ECM molecules is highly dependent on donation, and their isolation or synthesis can be challenging.

Naturally occurring polymers that are not found in mammals can also be used as biomaterials. Silk fibers, for example, have been used for centuries to make sutures, and silk mats, hydrogels, and sponges have more recently been used as scaffolds to regenerate ligaments, cartilage, and bone.<sup>51-53</sup> Furthermore, plant-based polymers such as cellulose, starch, and alginate are used in materials ranging from topical wound dressings to cell delivery materials.<sup>54-56</sup>

Biomaterials based on chitosan have recently gained popularity and great interest from the research community.<sup>57,58</sup> Chitosan, whose structure is shown in Figure 3, is a naturally occurring polysaccharide that is cationic in solutions of dilute acid and directly derived from chitin. As chitin is the main component of crustacean shells and fungal cell walls, it is one of the most abundant biopolymers on earth. Many chitosan properties lend

themselves well to tissue engineering and wound healing applications, including its biocompatibility<sup>59,60</sup> and antimicrobial<sup>61,62</sup> properties. These properties have led to a diverse number of medical applications, the most widely recognized being the utilization of chitosan in haemostatic wound dressings. For example, the commercially available and FDA-approved HemCon® bandage has been lauded for decreasing clotting times and blood loss due to an ionic interaction between positively charged chitosan fibers and negatively charged blood cells. These bandages have been shown to be effective in severe hemorrhaging in swine,<sup>63</sup> were tested and found effective for bandaging trauma sites by the US military on the battlefields of Iraq and Afghanistan,<sup>64</sup> and have since gained FDA approval and made their way to civilian trauma applications.<sup>65</sup>

Some less explored utilizations of chitosan include the direct filling of a wound with a viscous chitosan solution. Some claim that this method can provide a scaffold for new cell growth (and subsequently strengthen new tissue), form a barrier against infection, absorb fluids from inflammation, and block nerve endings to reduce pain.<sup>66</sup> Chitosan has been shown to assist with the wound-healing process. For example, blood clotting can be quickened by chitosan dressings<sup>67</sup> and gels,<sup>68</sup> a property that has recently been commercialized and utilized globally. Chitosan degradation products can also enhance the inflammatory response during wound healing by activating macrophages<sup>69,70</sup> and preventing infection via its antimicrobial properties.<sup>71,72</sup> Additionally, fibroblast and keratinocyte growth can be stimulated by the presence of chitosan,<sup>73,74</sup> which contributes to the proliferation phase of wound healing. Furthermore, chitosan biomaterials have shown potential as scaffolds for retinal cell regeneration, as chitosan can also promote neuron differentiation.<sup>75,76</sup> The use of chitosan in a variety of physical forms has great potential in high-impact biomaterial applications.

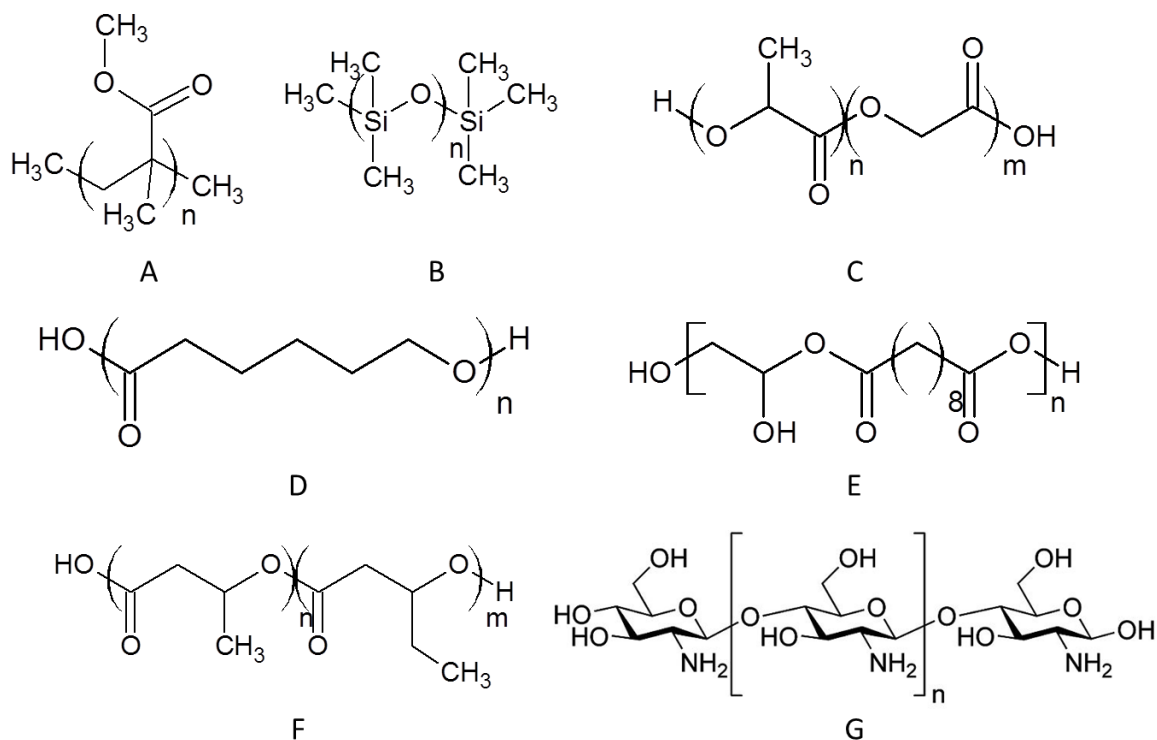


Figure 3. Chemical structures of A) Poly(methyl methacrylate) (PMMA), B) poly(dimethylsiloxane) (PDMS), C) Poly(lactic-co-glycolic acid) (PLGA), D) Poly(ε-caprolactone) (PCL), E) Poly(glycerol sebacate) (PGS), F) Poly(hydroxy butyrate-co-valerate) (PHBV), and G) Chitosan.

### Inert Synthetic Polymers

For some purposes, such as orthopedic implants meant to provide pure structural support, the use of an inert material is desirable, as infiltration by cells could lead to degradation and ultimate failure. The first discovery of this class of biomaterial (non-toxic yet bio-inert) came accidentally. World War II pilots with fragments of Perspex (aka Plexiglas) in their eyes from broken cockpit compartments suffered less adverse effects than those affected by glass fragments. Sir Harold Ridley, a British ophthalmologist, recognized the opportunity and invented the first intraocular lens. This material, poly(methyl methacrylate) (PMMA), is still used today for intraocular lenses, as well as bone cement and other orthopedic applications.<sup>77-79</sup> Later, soft contact lenses

were developed from a chemically similar but more hydrophilic polymer, poly(hydroxy ethyl methacrylate).

Depending on their properties, more chemically diverse polymers are also used for a number of other biomedical applications. Hydrogels of polyacrylamide crosslinked with bis-acrylamide, for example, are used for the separation of proteins in gel electrophoresis.<sup>80</sup> Additionally, hydrophilic poly(acrylic acid) is used in dental cements and as a mucoadhesive in drug delivery formulations, while hydrophobic polymers with good lubricity [e.g. poly(tetrafluoroethylene)] are used to make catheters and vascular grafts.<sup>81,82</sup> Another popular polymeric biomaterial is ultra-high-molecular-weight poly(ethylene), which due to its high wear resistance and toughness, is a common component of artificial hip joints.<sup>83,84</sup> Furthermore, highly rigid materials such as poly(propylene) or poly(ethylene terephthalate), are used as medical sutures and in ligament reconstruction, while materials with mechanical properties closer to those of soft tissues [e.g. poly(dimethyl siloxane) and other silicone rubbers] are used in facial reconstruction and breast implants.<sup>85,86</sup>

One very common polymer in drug delivery applications and medical coatings is poly(ethylene glycol) (PEG), which is known for its ability to “hide” particles or other drug systems from the body by discouraging protein binding, thereby increasing circulation time and decreasing the risk of unwanted encapsulation.<sup>87,88</sup> Still other polymers, such as low density poly(ethylene) and poly(vinyl chloride) are used for medical tubing, storage bags, and separation membranes.<sup>89</sup> These many examples show the versatility polymers and their properties, even for very specific applications. One important advantage of using synthetic polymers for biomaterial applications is that properties are relatively easy to control without exceeding toxicity standards.

Several non-degradable synthetic polymers have been used for retinal regeneration applications. Thin hydrogel films of cross-linked methacrylate/methacrylamide, for example, have been shown to support the formation of

a RPE monolayer with appropriate phenotype.<sup>90</sup> Thermo-responsive copolymers have also shown promise, especially for easy release of whole RPE sheets after *in vitro* growth.<sup>91</sup> Although some require oxygen plasma treatment to increase wettability, commercially available polyether urethanes can also support RPE layer formation,<sup>92</sup> as can PDMS.<sup>93</sup> Neuronal cell types, namely retinal progenitor cells (RPCs), have also been grown on synthetic polymers, including porous PMMA. Cells grown on this microfabricated scaffold integrated with the host tissue *in vivo* and expressed mature and immature photoreceptor cell markers.<sup>94</sup>

### Degradable Synthetic Polymers

Some advantages of both synthetic and bioactive polymers can be accessed through the use of degradable synthetic polymers. One of the main mechanisms involved in degradation is hydrolysis, wherein the polymer backbone, crosslinks, or side chains undergo scission due to the reaction between water and susceptible functional groups. These functional groups typically consist of carbonyls bonded to heterochain groups such as anhydrides, esters, urethanes, and amides. Polyesters and polyanhydrides degrade fairly quickly compared to polyurethanes or polyimides, which can maintain stability for several years *in vivo*.<sup>89</sup> Though the degradation rate varies a great deal with the functional group, it can be controlled slightly by blending with other polymers and changing the hydrophilicity, crystallinity, or cross-linking density. Degradation products are also a very important consideration, as the release of small fragments or toxic molecules can negatively affect the success of an implant, even long after its placement.

Degradable synthetic polymers are used in a wide variety of biomedical applications. One degradable polymer family that bridges the gap between synthetic and naturally occurring is poly(phosphazene). These polymers, which have nitrogen-phosphorous linkages in their backbone, have high thermal stability and are used in bone reconstruction and as vaccine adjuvants.<sup>95,96</sup> Additionally, poly(cyanoacrylate), a family

that includes “super glue,” is used as a tissue adhesive.<sup>97,98\*</sup> Polymer degradation rate can sometimes be tuned chemically, as in the case of polyanhydrides, which are often used in gene and drug delivery applications for their facile functionalization.<sup>89</sup> Still others degrade at a relatively constant rate, as in poly (ortho ester), whose surface erosion is often favorable for drug delivery.<sup>99</sup>

Polyesters are by far the most commonly used degradable synthetic polymers in medical applications. Poly(hydroxybutyrate) (PHB) for example, which can be isolated from intracellular storage vesicles of certain microorganisms, is a popular choice for stents, sutures, artificial skin, and vascular grafts.<sup>100,101</sup> Often PHB materials are formulated as copolymers with a similar material, poly(hydroxyvalerate) (PHV), which adds greater flexibility to the otherwise somewhat brittle polymer.<sup>102,103</sup> These copolymers (PHBV) have even been demonstrated to support the growth of an RPE monolayer for retinal tissue regeneration, but their availability is somewhat limited.<sup>104</sup> Poly(glycerol sebacate) (PGS), a polycondensate of glycerol and sebacic acid, is another flexible, rubbery, biodegradable polymer common in recent biomaterial applications. In fact, when cultured on PGS for the purpose of retinal regeneration, retinal progenitor cells express immature and mature photoreceptor markers after just seven days.<sup>105</sup> On the other hand, for very slow degradation requirements, poly(caprolactone) is a more suitable choice. This semicrystalline polymer forms blends well and is used in long-term drug delivery and orthopedic applications.<sup>106</sup> Porous PCL has also been used as an artificial Bruch’s membrane with relative success.<sup>107</sup>

The simplest linear aliphatic polyester is poly(glycolic acid) (PGA), which was used in the first completely resorbable suture (“Dexon”) in 1970 and later in bone pins (“Biofix”). PGA, however, loses mechanical strength rapidly as it degrades in 2-4 weeks.<sup>89</sup> Thus, it is most often formulated as a copolymer with poly(lactic acid) (PLA), which is more hydrophobic and thus does not hydrolyze as readily. This copolymer, widely known as PLGA, is by far the most commonly used degradable polymer, mostly

because of its early success and regulating agency approval in various biomaterial applications.<sup>108-110</sup> It is used for dental applications, bone pins, drug delivery systems, vascular and urological stents, and skin substitutes, and is also the most commonly investigated polymer for regrowing photoreceptors and RPE.<sup>111</sup> In fact, several studies have shown that PLGA supports the formation of a RPE monolayer with appropriate phenotype.<sup>112-115</sup> Furthermore, PLGA scaffolds are also able to support cell differentiation to photoreceptor morphologies, including alignment and interaction with the scaffold.<sup>116</sup> In recent work, these cell-laden scaffolds were implanted and provided 10-fold and 16-fold increases in cell survival and delivery, respectively, relative to a bolus injection.<sup>117</sup> Despite the popularity of PLGA, its degradation products are relatively strong acids, and their accumulation at an implant site can cause inflammatory responses months after their initial implantation. In addition, PLGA has a relatively high modulus, which poses a damage risk to sensitive tissues surrounding the implant.<sup>118</sup>

#### Bio/Synthetic Composites

In the case of tissue engineering, where interaction with host cells is desired, the use of synthetic polymers becomes complicated, as biodegradable varieties have a narrow range of properties, while non-degradable families are often bio-inert. Fortunately, the advantage of versatility offered by the use of synthetic polymers can be maintained by chemically rendering synthetic polymers more bioactive via functionalization. Many examples of successful incorporation of peptides, whole proteins, or other cell signaling molecules within synthetic materials have recently been reported. For example, attachment peptides such as RGD and YIGSR, which are part of the fibronectin and laminin binding domains, respectively, were first covalently bound to otherwise inert surfaces in 1990.<sup>119</sup> Since then, these and similar molecules have been incorporated into biomaterials ranging from bone scaffolds to thermo-responsive hydrogels. The resulting materials have repeatedly demonstrated improved bioactivity.<sup>120-127</sup> In fact, the inclusion

of just 0.5 mM of covalently bound RGD increased the cell viability of encapsulated cells by more than 20 times in one study.<sup>122</sup> Whole proteins or peptides containing cysteine residues can be incorporated by increasingly popular thiol-ene chemistry<sup>128-130</sup> or the more traditional N-hydroxysuccinimide chemistry,<sup>131-134</sup> among others.

Similarly, the narrow range of properties available through the use of bioactive naturally occurring polymers as the primary material component can be broadened by functionalizing with synthetic groups. For example, although chitosan biomaterials utilizing fibers or viscous gel solutions have had some success as biomaterials, the effectiveness and mechanical properties of chitosan materials can be improved by introducing physical cross-linking. These covalent bonds between chains can be induced using photopolymerization, which offers many advantages including spatial and temporal control of the reaction as well as the ability to react *in situ* at ambient conditions. Of the many techniques available for accomplishing this functionalization, the appropriate choice depends largely on each molecule's unique chemistry. Here, a few reports of the functionalization of relevant biomolecules are used to demonstrate the diverse options for achieving final property control while maintaining bioactivity.

Chitosan chains modified with photopolymerized methacrylate side groups have been used for tissue scaffolds,<sup>135</sup> injectable hydrogels,<sup>136</sup> and other biomaterials.<sup>137</sup> Methacrylate groups can be added to chitosan chains using a simple Michael-addition reaction.<sup>136,137</sup> Therein, free amine groups on the chitosan chain accept an electron from a double bond, such as that in an acrylate group, forming a covalent bond. This reaction can be performed under relatively mild reaction conditions with little solvent. If a di-functional molecule, such as a diacrylate, is used to functionalize the chitosan chain, the remaining double bonds, now pendant to the chitosan backbone, can undergo photocrosslinking in the presence of a photoinitiator.

Azide polymerization is another method of cross-linking chitosan chains. This option is attractive because it does not require the presence of a photoinitiator, and thus



has a decreased likelihood of causing adverse reactions if polymerized *in situ*. Azide-functionalized chitosan hydrogels have been shown to be effective in applications such as bioadhesion,<sup>138</sup> wound dressings,<sup>139</sup> and neural regeneration.<sup>140</sup> Upon exposure to UV light, the azide moiety degrades into N<sub>2</sub> gas and a reactive nitrene group, which can combine with another nitrene group to form a covalent bond.

Some proteins can be crosslinked using a naturally occurring photosensitizer, riboflavin 5 phosphate (R5P). In one study, mixtures of fibrinogen and fibronectin were isolated from donated human blood, crosslinked by addition of R5P and overnight exposure to UV light, and used as scaffolds for RPE cells. The matrix was shown to support the attachment and growth of RPE with appropriate phenotypes.<sup>141</sup> In a later study, small pieces of this matrix with attached RPE formed microspheres, which were injected to the subretinal space of rabbits. Although the RPE cells survived for up to one month, retinal degeneration was noted in areas adjacent to injected particles.<sup>142</sup>

The functionalization of biomolecules with synthetic groups can be a powerful tool for accessing the benefits of both synthetic and naturally occurring polymers, as can the functionalization of synthetic polymers with bioactive moieties. Some aspects of both material types are also observed in biodegradable synthetic polymers, which are bioactive and have properties that can be controlled to some degree. The properties of synthetic non-degradable polymers can be readily controlled by changing chemical groups, crosslinking density, or processing methods. While these synthetic polymers are typically inert to biological interactions, naturally occurring polymers are inherently the most bioactive of the groups discussed here. This bioactivity, however, comes at the cost of the ability to easily alter properties, which is quite difficult without the approaches described above. The appropriate control of biochemical properties can be complicated, but is crucial for effective material performance and avoidance of negative inflammatory responses.

### Mechanical Properties

Most implanted materials are tested for material or chemical biocompatibility, clearly an essential property of an implanted polymer, prior to implantation using *in vitro* culture techniques. However, the mechanical behavior of a material also plays an important role in the ultimate compatibility, efficacy and outcome of the implant *in vivo*. The importance of proper mechanical shear forces has been known for some time in vasculature development. In this case, the endothelium acts as a mechanosensor and produces biochemical signals (e.g. nitric oxide and prostacyclin) that cause the adjacent smooth muscle cells to dilate or contract.<sup>143</sup> Likewise, mechanical stress causes bone remodeling, while unstressed bone regions lose density over time.<sup>144</sup> Recently, specific changes in cell gene expression, differentiation, and signaling in many different tissue types as a result of changing mechanical forces have been described by several groups.

To overcome potential rejection issues and for stimulation of optimal cellular differentiation and transplant integration, it is generally believed that the mechanical properties of an implanted material should match those of the recipient tissue as closely as possible. Soft polyacrylamide gels that mimic the modulus of brain tissue, for example, direct stem cells towards adopting neuronal morphologies, while those that mimic muscle and bone direct towards myogenic and osteogenic cell types, respectively.<sup>145</sup> Thus, directing stem cell differentiation and cellular proliferation with mechanical cues<sup>146,147</sup> has long been utilized for generating cartilage<sup>148</sup> and bone.<sup>149</sup> More recently this concept has also been applied to materials meant to regenerate softer tissues such as tendons,<sup>150</sup> cardiac valves,<sup>151</sup> cardiac muscles,<sup>152,153</sup> and neurons.<sup>154,155</sup>

Despite encouraging biomaterials developments for retinal regeneration *in vitro*, none of polymer materials investigated are well tolerated by the host retina.<sup>19,156</sup> In the case of electrospun PLGA systems, the negative effects observed can in large part be explained by the inherent rigidity of the scaffold and its mechanical incongruity with the remaining host retinal tissue,<sup>19,117</sup> resulting in injury to the delicate retinal neurons. These

findings point to the need for other polymer systems that more closely mimic the mechanical properties of the native tissue in which they will eventually be placed. As noted above, achieving material biomimicry is not only important for permanent implantation, but also in situations where the role of the polymer is to enhance cellular differentiation and development *in vitro*.

Polymer mechanical properties are characterized by their stress-strain behavior. Typically force, or stress, is applied to a polymer in order to elongate or compress the material until it fails or breaks. The resulting deformation, normalized to the sample length, is recorded as the strain. Resistance to deformation, or modulus, can be quantified by the slope of a stress-strain plot at initial deformations (typically less than 10% of sample length). Relatively speaking, elastomers have very low moduli, while flexible plastics have higher initial moduli followed by extensive irreversible deformation. Furthermore, rigid plastics have relatively high moduli.<sup>157</sup>

In order to identify an appropriate modulus range for a specific biomaterial application, the mechanical properties of the native tissue must be characterized. Measuring the stiffness of natural tissues meant to be replaced provides insight into appropriate material stiffness ranges. For example, until recently, the majority of published studies on the stiffness of retinal tissue have focused on determining the structural properties of the retina in the horizontal dimension, i.e., perpendicular to the path of light in the living tissue. Although potentially useful for understanding retinal tearing,<sup>158</sup> these measurements have little meaning when translated to the design of biomaterials. It has been found, however, that the direction in which retinal samples are cut significantly affects the tensile modulus.<sup>158</sup> In a later study, these and similar differences were attributed to the presence and size of blood vessels in the tissue.<sup>159</sup> Thus, although mechanical properties can be uniform with respect to direction for most synthetic materials, this isotropy does not translate to complex anisotropic biological tissues, especially those that are layered, such as the retina. For the purpose of developing

cell delivery scaffolds, transverse compressive stress and strain behavior would appear to be a better representation of the actual mechanical pressures encountered during chronic implantation. Likewise, the modulus of the polymer or tissue that a developing or transplanted cell will perceive is more similar to that obtained under a compressive rather than a uniaxial tensile force.

Once an appropriate modulus range is identified, the mechanical properties of scaffold materials can be tuned to match the natural tissue. This level of control can be achieved by considering the intermolecular forces present within a material and how they contribute to its overall mechanical behavior. There are two broad classification of mechanical behavior for amorphous polymers. Some polymers such as PMMA and polystyrene (PS) are rigid and hard at room temperature; they are otherwise known as glassy plastics. On the other hand, some polymers are soft and flexible, known as rubbery, at room temperature such as polybutadiene and polyisoprene. These behaviors are highly temperature dependent; most polymer mechanical behavior shifts from glassy to rubbery at a fixed temperature or narrow range of temperatures. This temperature is known as the glass transition temperature ( $T_g$ ).<sup>157</sup>

The difference between these two mechanical behaviors begins with molecular motion. In the glassy state, available thermal energy is adequate for the motion of a few atoms along the backbone or in pendant groups. However, flexing and uncoiling of polymer chains, or motion of entire molecules do not occur in this state. Conversely, in the rubbery state, entire molecules can shift and flex, and polymer chains can move much more freely than in the glassy state, resulting in elasticity. Activation energies for these four types of movement dictate  $T_g$ , and are in turn determined by polymer free volume, attractive forces between polymer chains, internal chain mobility, backbone stiffness, and chain length. Thus, mechanical behavior can be controlled to a great extent by altering polymer molecular weight and chemistry.<sup>157</sup>

Since crosslinking of polymer chains by definition introduces more bonds between polymer chains, chains are restricted from movement they would otherwise undergo in the amorphous state. Thus, increased crosslinking translates to increased modulus. Furthermore, in hydrogels the inclusion of a greater number of cross-links translates to more cohesive forces that resist dissolution, or water infiltration. With the accompanying plasticization this effect results in a higher modulus than materials with lower cross-linking density. Mechanical properties of cross-linked hydrogels can be further tuned by adjusting the length of the cross-linking molecule. For a fixed number of cross-links, a material with high molecular weight cross-links will have a lower modulus than one with smaller cross-linkers.<sup>160</sup> This ability to tune mechanical properties provides the freedom to study the role of mechanical forces in cell/material interactions and thereby the opportunity to optimize biomaterial technologies.

### Morphology

One of the most fascinating aspects of biology is the organization and structure that occurs at all size levels. If replacement materials are meant to mimic natural tissues, they too must contain some degree of order. An integral part of human and animal connective tissue, the extracellular matrix is a supporting gel that fills the space between cells and is composed of polysaccharides and fibrous proteins. To facilitate diffusion of nutrients and cell signaling molecules through the matrix, as well as to properly regulate growth and healing, the ECM has a distinct and inherent structure.<sup>161-164</sup> Unfortunately, disease or trauma can sometimes damage important tissues, impairing the natural function of the ECM and requiring the implantation of mimicking biomaterials to achieve tissue regeneration.<sup>165,166</sup> Therefore, many implant materials require porosity for proper function, each with a specific set of requirements. The effect of morphology on biomaterial success is far from inconsequential. For example, while the optimal pore size for bone ingrowth is 75-250  $\mu\text{m}$ , fibrocartilagenous tissue infiltrates best in materials

with 200-300  $\mu\text{m}$  pores.<sup>167,168</sup> Furthermore, pore interconnectivity, interconnection throat size, and the influence of these pores on mechanical properties can also change the behavior and success of biomaterials.<sup>169</sup>

Meanwhile, the presence of nanofeatures can significantly enhance cell adhesion to a substrate and improve tissue regeneration of biomaterials.<sup>170-172</sup> Recent research suggests that nanostructured polymers exhibit significantly different properties than their isotropic counterparts. Of particular interest are the controllable diffusion properties and increased cell attachment of nanostructured polymers.<sup>173,174</sup> The generation of materials with controlled nanometer-sized structures has led to significant advances in a wide-variety of applications ranging from processors and optical displays to drug delivery vehicles and sensors.<sup>175-179</sup> The inclusion of nano features often provides an opportunity to add advanced properties such as high surface to volume ratio while retaining desirable bulk properties.

In recent years the fabrication of polymeric materials containing periodic order on the sub-micrometer scale has been of particular interest. Because the properties of polymers are largely dependent on monomer selection and processing techniques, their applications are far reaching, including tissue scaffolds, sensors, solar cells, electronics, and separation membranes, to name a few.<sup>175-179</sup> In each of these applications, nanometer sized structures have been shown to enhance the performance of the materials. For example, enhanced transport and mechanical properties, as facilitated by nanometer-sized features of polymer networks, can improve cell attachment and survival on synthetic materials<sup>180</sup> or increase the rate and degree of response to changes in external conditions for stimuli-sensitive polymers.<sup>181</sup> Furthermore, property changes can enhance the separation efficiency of polymeric membranes<sup>182</sup> or the rate of drug release<sup>183</sup> compared to polymer systems that do not contain ordered nanostructures. These sometimes dramatic improvements in functionality give nanostructured polymers a broader range of utility in advanced applications than their isotropic analogs. Thus, the ability to predict

and control micro- and nanostructure of a biomaterial is a crucial aspect of its development. Consideration of both the tissue type being replaced and the special needs of cells native to that tissue is critical. Many processing techniques have been developed to control the structure of polymers, some of which will be discussed here.

### Direct Fabrication

The most obvious way to incorporate structure into a polymer is to do so during the synthesis process without a physical template. Recent advances in 3D printing, for example, have made possible the facile construction of intricate materials. Though the variety of starting materials is still fairly limited for most common 3D printers, some offer printing of materials ranging from metals to hydrogels. One commercially available printer based on polymer fiber extrusion, for example, has been shown to print materials with easily tuned pore size to a resolution of  $1\ \mu\text{m}$ .<sup>184</sup> Furthermore, printed fibers can be made porous, hollow, or their surface made rough through combination with other techniques.<sup>185–188</sup> Fibrous materials fabricated using this technique have been shown to support the growth of many cell types and the regeneration of cartilage and vasculature.<sup>189–192</sup>

Many 3D printing technologies are based upon principles adopted from traditional photolithography techniques, which are still used today for the fabrication of structured polymers. In this method, monomers or prepolymers are either crosslinked or degraded by UV light. Thus, the use of a photomask with a pre-determined pattern allows for the selective polymerization or degradation of the material. If desired, the process can be repeated for multiple layers. Many researchers have used this technique to study the influence of surface topography on cell growth and directionality. Neurons, for example, have been demonstrated to prefer growing in the grooves of poly(hydroxyethyl methacrylate) materials fabricated in this manner.<sup>193,194</sup> PMMA with photolithographic

pores has also been demonstrated to retain RPCs better than non-porous materials during transplantation to the subretinal space.<sup>94</sup>

### Direct Templating

Another approach to the inclusion of architecture in fabricated polymeric materials is the use of a direct template. Porous polymers can be generated quite easily using porogens for example, which are merely particles or pockets that have the desired pore dimensions and geometry. Polymers are synthesized, crosslinked, or otherwise agglomerated around these domains, after which the porogen can be selectively removed from the final material. Porogens can be gases, as in the synthesis of poly(urethane) foams for cushions and other shock absorbent materials. In this process, gas generated during the polymerization reaction (typically carbon dioxide) coalesces and becomes trapped in the polymer network. Gas foamed polymers have been used as bone regeneration scaffolds and to study cell/material interactions.<sup>195–197</sup>

An emulsion can also be used as a template, or porogen, during polymerization. In this case, the polymerization reaction occurs around small pockets of discontinuous phase liquid, the size of which can be controlled by parameters such as mixing speed. The high surface area to volume ratio and consistent interconnected pores observed in several degradable and non-degradable emulsion templated polymers have led to their use in a number of tissue engineering and drug delivery applications.<sup>198</sup> Supercritical fluids, which behave like both liquids and gases, have also shown great promise recently as direct polymerization templates. These fluids have the ability to replace many organic solvents and thus are regarded favorably for improving biocompatibility, reducing processing time, and leaving a smaller ecological footprint.<sup>199</sup> Many successful biomaterials have been fabricated using supercritical fluids, including drug, protein, and DNA delivery devices, encapsulated cells and growth hormones, and bone and smooth muscle scaffolds.<sup>200,201</sup>



Many solid porogens are also employed as polymerization templates, including silica nanoparticles, nanotubular aluminum oxide, and salt crystals, among others. After polymerization, these porogens are typically removed by dissolution in solvent or degradation by heating, leaving behind a porous, often well-ordered architecture.<sup>202</sup> With new advances in the ability to fabricate nanomaterials comes also the opportunity to use increasingly small porogens for polymer templating. These templated materials are increasingly common in drug and gene delivery and tissue scaffolds.<sup>203,204</sup> Micro-contact printing, often called soft lithography, is a popular polymer templating technique wherein photolithography is used to create a rubbery PDMS “master” template that can be used to stamp a monomer or prepolymer onto a surface or can be filled directly with starting materials, then mechanically removed thereafter. Although the resolution of this technique is limited to macro and some micro architecture, its versatility and ease of use contribute to its continued popularity.<sup>205</sup> For retinal diseases specifically, PLGA/PHVB materials with grooves created by soft lithography were used to demonstrate that photoreceptors prefer to grow in material grooves,<sup>206</sup> while soft lithographic, porous PDMS has been used to demonstrate the negative impact of substrate topography on RPE growth.<sup>93</sup>

### Self-Assembled Templates

The organization of monomers into ordered geometries just prior to polymerization is one of the primary strategies utilized in the synthesis of polymers with controlled structures.<sup>207</sup> Two basic approaches are often used to produce or incorporate nanometer sized features in final polymer network architecture. The first approach takes advantage of the inherent differences in solubility, absorption, or binding affinity of a moiety in order to partition and segregate block copolymers, monomers, or pre-polymers into an organized matrix. After achieving the desired order, various polymerization methods may be utilized to generate the polymer network and lock-in the original order

of the matrix.<sup>208</sup> For example, molecular imprinting, in which a polymer is formed around a template or host molecule such as a protein or enzyme that interacts with functional groups on the monomer, has shown significant potential in many biosensing and separation applications.<sup>209</sup> As a result of polymerizing around a host or template molecule then removing it from the polymer matrix, molecular imprinted polymers (MIPs) contain specific sites with an induced geometry that favors strong binding affinity to the template molecule.

Another very effective method of polymer templating based on inherent solubility differences is the use of self-assembling molecules. For example, block copolymers consisting of two or more chemically immiscible homopolymers are very suitable for self-assembly, as chain length is relatively homogenous and can be readily controlled to tune the self-assembled geometry.<sup>202</sup> If the templating molecules serve as both the material framework and the template, one polymer can be selectively removed after the self-assembled phase is stabilized. The self-assembled system can also act only as the template and be removed entirely after polymerization or cross-linking occurs. This method is particularly attractive for generating nanostructure in organic polymers because the templating process may be applied to a wide variety of monomer and polymer precursors. Such versatility greatly expands the polymer chemistries in which nanostructure can be incorporated, leading to enhanced functionality of many polymer materials.

Another broad-scale approach to generating organized nanostructured polymer networks utilizes the promotion of self-assembly and aggregation of reactive species during the polymerization reaction. In this method, the induced, rather than inherent changes in solubility that occur as molecular weight increases during the reaction drive the self-assembly process.<sup>210-213</sup> One such process, known as polymerization induced phase separation (PIPS) is a particularly useful method for utilizing the changes in thermodynamics that accompany the polymerization reaction to generate nanostructured

materials. This technique takes advantage of thermodynamically driven phase separation events that occur during polymerization of two or more partially miscible monomers, or a monomer in an unreactive solvent or prepolymer. As polymerization proceeds and covalent crosslinks or linear chains are formed, the monomer species self-associates to a greater extent and demixes from the other formulation species. Although only limited control can be achieved using traditional thermal polymerization, growing evidence suggests that more precise control can be achieved through the use of photopolymerization.<sup>214,215</sup> This method has been used to fabricate numerous biomaterials, including PLGA with pores normal to its surface. Retinal progenitor cells demonstrated good attachment and differentiation on such porous degradable scaffolds.<sup>117</sup>

One promising method of controlling polymer nanostructure combines aspects of both broad-scale approaches by using self-assembling lyotropic liquid crystal (LLC) systems as polymerization templates to direct polymer morphology. The LLC templating process has been utilized to generate nanostructure in a wide-range of polymer systems, resulting in polymers that contain useful property relationships that are often not observed in traditional or isotropic polymer systems.<sup>181,216-221</sup> The utilization of such a method, however, changes the kinetics of polymerization significantly, a factor that should be considered carefully and is advantageous in some cases. LLCs are typically formed at high concentrations of surfactant molecules with distinct polar and non-polar domains. When introduced to a solvent such as water, these surfactants can self-assemble into geometries with nanometer size dimensions as they move to minimize thermodynamically unfavorable interactions with the solvent.<sup>222,223</sup>

Concentration and geometry largely dictate the ability of a surfactant to form LLC phases. Typically, spherical micelles are formed at low surfactant concentration and the hexagonal, bicontinuous cubic, and lamellar mesophases are formed with increasing surfactant concentration (Figure 4).<sup>224</sup> The structure of self-assembled LLC phases can be described by the attractive and repulsive interactions between surfactant and solvent.

Attractive forces include hydrogen bonding, hydrophobic, and Van der Waals interactions. These interactions are the drive for self-assembly, promoting the aggregates of surfactant that form LLC mesophases. On the other hand, repulsive interactions such as steric hindrance, electric double-layers, and hydration oppose the self-assembly process.

The balance of attractive and repulsive forces dictates the geometry of surfactant aggregates. For example, ethylene oxide repeat units or ionic head groups of surfactants can form hydrogen bonds with water and promote the self-assembly process.

Additionally, the aliphatic chains of these surfactants are insoluble in water and contribute to attractive hydrophobic forces that stabilize the mesophase. In other words, the formation of self-assembled surfactant aggregates is due to the favorable interaction of the polar head groups with water and the agglomeration of hydrophobic chains to shield themselves from and minimize their contact with water. Changes in surfactant concentration often alter the LLC mesophase due to shifts in attractive and repulsive forces, as summarized in Table 1. Modulating surfactant concentration provides a facile method of controlling the order of LLC mesophases.<sup>225</sup>

The packing parameter,  $\rho$ , is often used to relate molecular structure and surfactant concentration to the morphology of surfactant aggregates.<sup>227</sup> This dimensionless shape parameter, also known as the critical packing parameter (CPP), is directly proportional to the effective volume of the surfactant ( $V$ ) and inversely proportional to the length of the hydrocarbon chain ( $l_c$ ) and effective area of the surfactant head group ( $a_0$ ). Thus, the expression for CPP shown in Table 1 can be utilized as a first approximation to estimate which phase a particular surfactant may form. A packing parameter equal to unity typically corresponds to the formation of a lamellar phase while the bicontinuous cubic and hexagonal mesophases are formed at progressively smaller packing parameters. Conversely, inverse phases with similar geometries are formed at packing parameters greater than one.

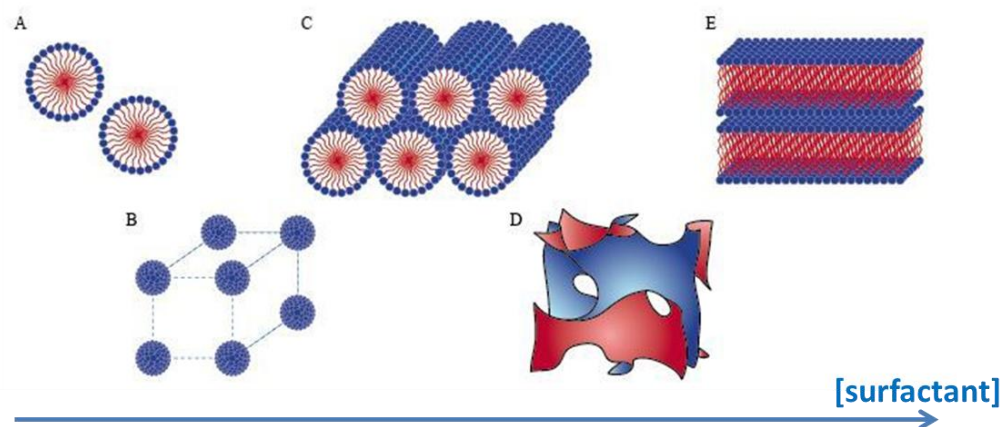


Figure 4. Representations of typical lyotropic liquid crystalline phases and geometries. Shown are A) micellar, B) cubic micellar, C) hexagonal, D) biocontinuous cubic, and E) lamellar.

Table 1. Relationships between amphiphile shape, water content, and preferred aggregate structure, based on the Israelachvili Model (adapted from Gin et al. 2001).<sup>226</sup>

Amphiphile "shape"	Amphiphile structure	$\rho = \frac{V}{a_0 l_c}$	Rel. H <sub>2</sub> O content	Aggregate Structure
 hydrophobic tail(s) $l_c$ hydrophilic headgroup $a_0$ (conical)		$< 1/3$	high	
(truncated cone)		$1/3 - 1/2$	medium	
(cylindrical)		$\sim 1$	medium	
(conical)		$> 1$	low	

Typically, an increase in surfactant concentration increases the packing parameter partly by reducing the effective area of the surfactant head group due to changes in the attractive forces and competitive "binding" for water molecules with the hydrophilic head

group.<sup>227</sup> In addition to changes in surfactant concentration, pH or ionic strength of the solvent can be modulated to change the effective areas and volumes of surfactant molecules. For example, an increase in ionic strength can screen the repulsive forces between two ionic heads of the quaternary ammonium surfactant dodecyl trimethylammonium bromide (DTAB), lowering the effective area of the surfactant head group, reducing the surfactant volume, and subsequently increasing the CPP. Thus, control of these nanostructures is readily available through a variety of methods. However, the ordered LLC assemblies, or phases, alone lack the mechanical strength required for most separation, biological, catalysis, drug delivery, and other applications. To take full advantage of nanostructured liquid crystalline order in material applications, polymers with the order of well-known self-organized liquid crystalline phases may be synthesized using nanostructured surfactant assemblies as templates to direct polymer structure.

Organized LLC phases can be used to control polymer nanostructure by serving as polymerization templates. In this method, the water- and oil-soluble domains that are inherent in the mesophase are used to segregate monomers. As in the schematic shown in Figure 5, if a photocurable polar monomer such as poly(ethylene glycol) diacrylate (PEGDA) is incorporated into the LLC phase, the monomer will preferentially segregate in the water soluble domains of the parent template and adopt a geometry that directly resembles that of the self-assembled phase.<sup>228</sup> Likewise, if a hydrophobic monomer such as hexanediol diacrylate (HDDA) is added to the phase, the monomer will preferentially segregate in the oil-soluble domains of the LLC phase.<sup>229</sup> Photopolymerization can then be utilized to cure the monomer/LLC formulation and potentially transfer the order of the parent template to the polymer system.

These changes in polymer structure typically result in useful property changes. For example, the molecular weight of linear poly(n-decyl acrylate) formed in LLC templates increases significantly compared to an isotropic control in otherwise identical polymerization conditions.<sup>230</sup> Many studies have shown interesting structure/property

relationships in crosslinked polymers templated with LLCs as well. Surface area can increase as much as 7-fold, and permeability as much as 5-fold when a LLC template is used during polymerization.<sup>218,231</sup> As expected based on these porosity changes, water uptake of the final polymer increases when a LLC template is used. Interestingly, accompanying increases in compressive modulus have been observed as well.<sup>219</sup> This behavior contradicts traditional hydrogel behavior wherein increases in water uptake result in decreases in modulus. Furthermore, when templated with LLCs, hydrolysable crosslinked networks degrade in only half the time of their non-templated counterparts.<sup>173</sup>

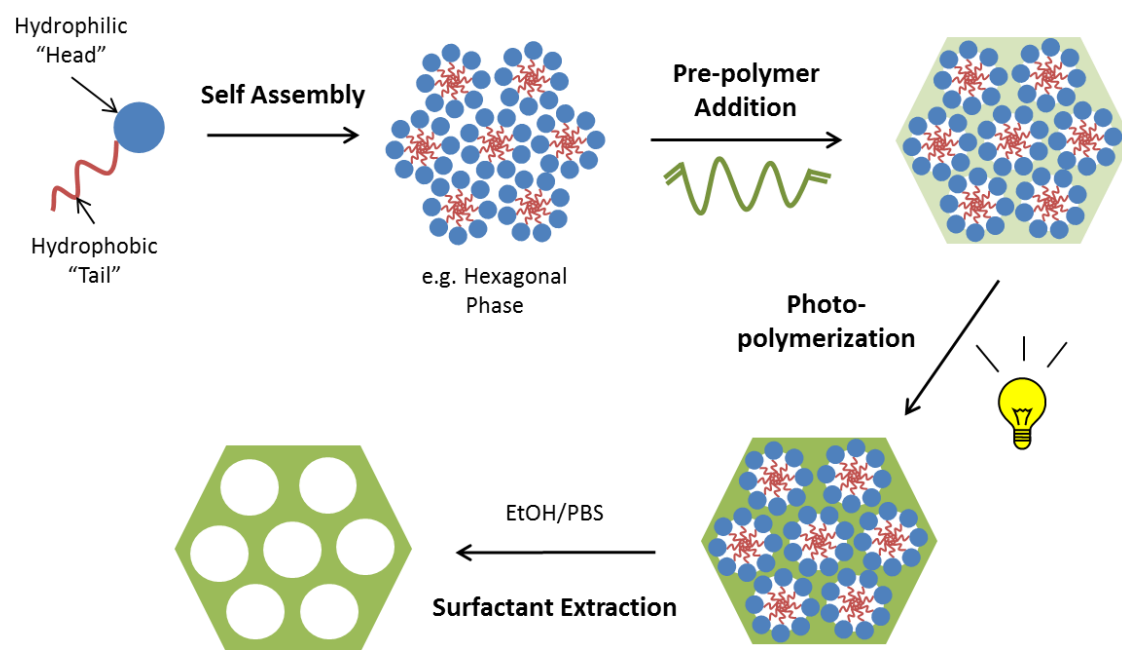


Figure 5. Schematic of the process of templating crosslinked PEG with surfactant in ordered LLC geometries.

Importantly, many studies have shown that the properties of LLC templated polymers can be controlled using the geometry of the mesophase.<sup>218,219,221,229</sup> Changes in the surfactant concentration alone dictate final structure, and thus final properties. Thus,

materials with identical chemical compositions but varying properties can readily be generated through the use of LLC templating and photopolymerization.

### Photopolymerization

Photopolymerization involves the use of photons from light to initiate the formation of polymer chains or cross-linked networks from monomers, oligomers, or functionalized pre-polymers. The primary motivation for using photopolymerization for surfactant templating over traditional thermal curing is the ability to control the reaction temporally. Even with a small amount of photoinitiator, photopolymerization reactions occur very rapidly,<sup>232–234</sup> allowing the structure imparted by the template discussed above to be kinetically “trapped.” Generally the faster the reaction rate, the more the final polymer structure will resemble the structure of its surfactant template.<sup>235,236</sup> The relatively slow reaction kinetics typical of thermal polymerization are not favorable for surfactant templating and lead to final properties similar to those observed for non-templated controls.<sup>218</sup>

The second advantage of using photopolymerization is the ability to control the reaction spatially. Because light is necessary to create reactive species, regions that are not exposed remain unreacted. Thus, a simple photomask can be used to create patterned polymers,<sup>193,194</sup> or to selectively incorporate molecules in certain regions of a material.<sup>237</sup> Lastly, and perhaps most importantly for biomaterials, photopolymerization reactions occur readily at ambient conditions and do not require the use of harsh or toxic chemicals such as solvents, acids, or bases. This advantage widens the use of photopolymerization in biomedical applications significantly to include, for example, *in situ* polymerization<sup>238,239</sup> and cell encapsulation.<sup>240–242</sup>

The mechanism of free radical photopolymerization is quite simple. First, a reactive radical species that will start the polymerization reaction is generated. When exposed to light of the appropriate wavelength, a photoinitiator cleaves to generate free



radicals that initiate polymerization by reacting with electron-rich double bonds. Since not all radicals are equally reactive, quantum yield of initiation, or efficiency,  $\phi$ , representing the number of propagating chains initiated per photon of light absorbed, is used to account for these differences. After radicals that are capable of initiating the polymerization reaction are generated, the second step in the initiation process is the addition of the free radical to reactive monomer ( $M$ ). As the second step is much faster than the first, the total photoinitiation rate,  $R_i$ , is given by:

$$R_i = 2\phi I_a \quad (1)$$

where  $I_a$  is the intensity of light absorbed by the photoinitiator.

Next, monomer is continually added to the growing polymer chain to form a high molecular weight polymer, which is referred to as the propagation step. The rate of propagation, or rate of polymerization, is then given by:

$$R_p = k_p [P_n \cdot] [M] = k_p [R \cdot] [M] \quad (2)$$

where  $k_p$  is the propagation rate constant and  $n$  represents the number of monomer units added to the growing polymer chain, otherwise known as the degree of polymerization. The propagation rate constant is generally assumed to be independent of polymer chain length.

The final stage of the polymerization reaction is the termination step, in which radicals on the growing polymer chains react to form a “dead” polymer. Although there are two basic mechanisms of termination for radical chain polymerization, the two mechanisms are often lumped together into one termination rate,

$$R_t = k_t [P_n \cdot] [P_m \cdot] = 2k_t [R \cdot]^2 \quad (3)$$

Assuming the radical concentration to be at quasi steady state ( $R_i = R_t$ ) and solving for the immeasurable radical concentration gives

$$[R \cdot] = \sqrt{\frac{\phi I_a}{k_t}} \quad (4)$$

Finally, this expression can be substituted into the rate expression (Equation 2) to yield

$$R_p = k_p[M] \sqrt{\frac{\phi I_a}{k_t}} \quad (5)$$

Additional relevant photopolymerization behaviors are not directly evident from the above polymerization rate equations. For example, as the reaction proceeds, growing polymer chains become less mobile as their molecular weight increases. Thus, the mobility of the radical, which is attached to the growing chains, decreases as polymerization proceeds while the mobility of un-reacted monomer is relatively unaffected. Therefore, changes in  $k_p$  that may occur before the gel point with increasing chain length can be neglected, while simultaneous changes in  $k_t$  cannot be overlooked. At low conversions, the viscosity of the reacting system is low and two reactive functional groups can diffuse relatively unhindered. In this stage, the polymerization rate is controlled by segmental diffusion of the polymer chains. As the polymerization progresses to higher conversions, the system viscosity increases and diffusion of polymer chains, which is rate-limiting for termination, slows. Furthermore, as the termination rate decreases, the rate of polymerization increases. This auto-acceleration, known as the Trommsdorff effect, has historically played an important role in understanding photopolymerization kinetics in LLC systems. At even higher conversions, the viscosity of the system may become so large that the translation of polymer chains throughout the matrix is much slower than propagation through double bonds in the network. In other words, at higher conversions the polymerization rate is said to be diffusion limited. As the ratio of monomer functionality to molecular weight is increased, the onset of autoacceleration is decreased to lower conversions due to the increase in viscosity and close proximity of polymer reactive groups. Furthermore, the ultimate conversion of double bonds tends to decrease with increasing crosslinking density due to diffusion limitations during the reaction.

Other types of photopolymerization, such as those that use step growth thiol-ene chemistry, are also growing in popularity. Thiol-ene polymerization involves the radical addition of thiols across carbon-carbon double bonds. In the past decade these reactions have gained favor because they produce materials that are inherently more regularly structured than their chain polymerization counterparts, incredibly versatile and modular, and can occur at relatively mild reaction conditions.<sup>243</sup> Changing the number of thiol or ene groups present can also control the mechanical properties of the resulting hydrogels.<sup>244</sup> Bowman and Anseth have successfully synthesized thiol-acrylate hydrogels for biomaterial applications,<sup>128,239</sup> and others have even functionalized chitosan for use in thiol-ene reactions,<sup>245</sup> but the use of thiol-ene chemistry and photopolymerization could be advantageous for making hydrogels of natural polymers.

#### Research Summary

As medical technology advances, the need for safe and effective biomaterials grows. Biosensors, drug and gene delivery systems, orthopedic implants, and tissue scaffold are increasingly important for the understanding and treatment of injury and disease. One of the main challenges facing the biomaterials field is to understand how all material properties work together to facilitate favorable interaction with cells and tissues and the optimized long-term effect of these interactions. Because their properties can be readily tuned, many are biocompatible, and they are widely available at a relatively low cost, polymers are a promising class of biomaterials. Even though a polymer may demonstrate biocompatibility in vitro, it may be too stiff to be implanted without causing tissue damage, or not porous enough to allow nutrients to diffuse to crucial local tissues. Elucidating the effect of biochemical properties, mechanical properties, and morphology independently and inter-dependently for individual applications and classes of applications can enhance the ability to optimize material synthesis and processing.

Furthermore, as these interactions are better understood for specific applications, results can be extrapolated to related applications and their broader implications realized.

Although several scaffolds have been developed for use in the sub-retinal space, none have been tested using cells that are in the process of differentiating. Since the manipulation of mature photoreceptor cells is very difficult *in vitro*, successful cell-based therapies will likely be based on progenitor or even stem cell cultures. Thus, demonstrating in general the ability to use scaffolds as a platform for differentiating immature stem cells to more mature neural progenitor cells, for example, is an important first step in achieving therapeutic success. The feasibility of using PLGA as a model platform for retinal regeneration is explored in Chapter 3 of this work. The subsequent three chapters each highlight one of the three key design parameters: biochemical properties, physical properties, and morphology. In Chapter 4, the power of polymer biocompatibility is demonstrated using *in vitro* and *in vivo* models. The effects of coating known toxic materials (copper nanoparticles) with a material known to be highly biocompatible (chitosan) are elucidated and discussed. The importance of physical properties, namely compressive modulus, and their appropriate measurement, are demonstrated in Chapter 5. Therein, the compressive moduli of ocular tissues are presented relative to those of common biomaterials. In Chapter 6, the influence of morphology, induced by surfactant templating, on the physical properties and cell/material interactions of a model PEG system is determined. Finally, Chapter 7 describes an approach that builds upon the results from the preceding chapters. Neural progenitor cells were successfully differentiated on surfactant-templated, photo-crosslinked chitosan with a compressive modulus near that of native retinal tissue. Together with the previous four chapters, this culminating chapter presents a promising approach to the design of retinal regenerative tissue scaffolds; one that incorporates control of biochemical properties, mechanical properties, and material morphology to further understand and tune cell/material interactions.

## CHAPTER 2

### OBJECTIVES

Even with more than 2 million people in the United States affected by retinal degenerative diseases, only a very limited number of cases can be effectively treated. One of the most promising approaches is the transplantation of replacement photoreceptor cells from pluripotent stem cells to the sub-retinal space. Despite their proven ability to integrate with host tissues, differentiate into mature cell types, and in some cases improve retinal function, cells injected as a bolus have an extremely low survival rate. In large part this poor cell survival can be attributed to a lack of physical support during injection. Without physical integration, many cells are either washed away from or fail to anchor in the often heavily damaged sub-retinal space. Many researchers have attempted to design materials to provide support to implanted cells for regrowth of the retina or its underlying layers. Despite the identification of several natural and synthetic polymers that can support cell proliferation and differentiation, none have been successful *in vivo*. The successful design of a cell transplantation system for the sub-retinal space requires careful consideration of important design parameters. In particular, the biochemical properties, physical properties, and morphology of the material should be evaluated. Furthermore, how these parameters affect the final effectiveness of the material *in vitro* and *in vivo* should be investigated in order to tune the properties and optimize material performance.

In this work, we aim to design a regenerative scaffold for the retina and determine the interplay among three key design parameters: biocompatibility, physical properties, and morphology. This overall goal will be accomplished as we

1. Demonstrate the feasibility of using a synthetic scaffold to grow and differentiate induced pluripotent stem cells to neural progenitor cells

2. Examine the biocompatibility of chitosan and how it contributes to otherwise toxic materials
3. Identify the target compressive modulus for retinal regenerative scaffolds by measuring the compressive modulus of ocular tissues
4. Determine the effect of morphology, as induced by surfactant templating, on material physical properties and biocompatibility
5. Study MiPSC growth and differentiation on chitosan scaffolds with varying degrees of porosity, biocompatibility, and compressive modulus.

The first objective (Chapter 3) introduces the concept of growing and differentiating MiPSCs on synthetic materials. Porous PLGA scaffolds were fabricated using a simple salt leaching technique and these degradable materials were seeded with MiPSCs. When cultured on porous PLGA scaffolds *in vitro*, cells were able to proliferate rapidly and mature into neural cell types in a short period of time. Evaluating the capacity of materials to not just sustain growth, but also to support differentiation is an important step towards the rational design of cell and tissue replacement strategies. After the feasibility of this concept is demonstrated, three key design parameters are evaluated in the subsequent three objectives.

The second objective (Chapter 4) explores the impact of biochemical properties on interactions between cells and materials. Copper nanoparticles, which are known to be highly toxic, especially in the lungs, were coated with chitosan, a naturally occurring polymer known to be biocompatible. Particle size, zeta potential, and morphology were characterized with and without coating. *In vitro* toxicity of chitosan coated particles was significantly lower than non-coated particles for two independent cell types, two time points, and a range of doses. Conversely, *in vivo* toxicity and inflammatory response upon nasal installation was higher for mice exposed to chitosan coated particles than their non-coated counterparts. These results suggest the powerful impact that polymer selection can have on cell/material interactions, as properties such as mucoadhesion may

play an important role *in vivo* and almost no role *in vitro*. Careful selection of materials and thorough investigation of their biochemical properties is crucial for each application.

The importance of physical properties, namely compressive modulus, is examined in the third objective (Chapter 5). Matching the mechanical properties of a material to the mechanical properties of its intended *in vivo* surroundings requires appropriate characterization of those tissues. The compressive moduli of various ocular tissues, including the retina, choroid, and RPE, were measured using dynamic mechanical analysis. The compressive modulus of the retina is an order of magnitude lower than previously reported tensile modulus values but similar to the compressive modulus of some polymers used in sub-retinal implants. These results demonstrate the importance of correctly characterizing mechanical properties and serve as a benchmark for the design of future materials for the sub-retinal space.

In the fourth objective (Chapter 6), the effect of morphology on cell/material interactions is examined. The morphology of cross-linked PEG was altered using a simple surfactant templating approach. These changes in morphology resulted in a two-fold increase in water uptake and a corresponding two-fold decrease in compressive modulus. The toxicity of cross-linked PEG was unaffected by the surfactant templating process, as was the adhesion of MiPSCs to the material surface. These results demonstrate the capability of surfactant templating to enact important changes in physical properties without sacrificing beneficial biochemical properties.

Finally, the fifth objective (Chapter 7) describes the design of a stem cell scaffold for the sub-retinal space by combination of the results from the previous four objectives. A chitosan derivative capable of undergoing cross-linking by exposure to light was synthesized. This functionalized chitosan was templated with various surfactants to create soft, biocompatible hydrogels and the resulting physical properties, namely compressive modulus and water uptake, were examined. The effect of templating with quaternary ammonium surfactant on water uptake was especially poignant, with the material

absorbing about three times as much as its isotropic counterpart. The incorporation of comonomers also affected physical properties by generally decreasing water uptake and increasing compressive modulus. Furthermore, neural progenitor cells were successfully differentiated on surfactant-templated, photo-crosslinked chitosan with a compressive modulus near that of native retinal tissue. Together with the previous four chapters, this culminating chapter presents a promising approach to the design of retinal regenerative tissue scaffolds; one that incorporates control of biochemical properties, physical properties, and material morphology to further understand and tune cell/material interactions.

The successful design of biomaterials for the sub-retinal space could have a significant impact on available treatments for blinding eye diseases. As we understand how to optimize material properties to meet the needs of the eye, we are better able to alleviate the symptoms of previously incurable diseases. These advances will likely also be applicable to diverse biomaterial applications as well. Since the retina is part of the central nervous system, successful materials for the sub-retinal space could also function well as scaffolds for nerve regeneration to treat spinal cord injuries, for example. Nerve regeneration in the peripheral nervous system is another likely possibility for these materials. In short, the results reported herein will add to the growing body of research aimed to understand and control cell/material interactions. The work presented here will also contribute to the development of a systematic design process for biomaterials using combined optimization of morphology, physical characteristics, and biochemistry.



## CHAPTER 3

### DIFFERENTIATION OF INDUCED PLURIPOTENT STEM CELLS TO NEURAL PROGENITOR CELLS ON A THIN, POROUS PLGA SCAFFOLD

#### Introduction

Age-related macular degeneration, one of the leading causes of blindness in the western world, is characterized by death of the light sensing photoreceptor cells of the outer neural retina and irreversible blindness. The restoration of vision to those suffering from neurodegenerative diseases, especially with extensive photoreceptor cell loss occurring prior to diagnosis, may require treatment beyond existing drug and/or gene therapies. Cellular or tissue replacements represent promising strategies for vision resoration. For example, many studies demonstrate the feasibility of using stem cells to achieve photoreceptor cell regeneration;<sup>10-22</sup> however, the development of an optimal stem cell transplantation approach is crucial to ultimate success. Currently, devastating cell loss and minimal cellular integration occur upon transplantation of cells to the sub-retinal space. A bolus injection of photoreceptor cells, for example, has been shown in several studies to result in less than 0.01% survival of transplanted cells and an even smaller amount of integration within host retinal tissue.<sup>13,18</sup> These less than ideal results are due, in large part, to the lack of physical support that donor cells experience following the bolus injection and are particularly acute when retinal degeneration has reached late stages at the time of injection.

Both degradable and non-degradable scaffolds have been studied extensively as a means to provide the needed support to donor cells. For example, parylene-C based films have been used as a vehicle for the delivery of stem cell derived RPE cells to the subretinal space.<sup>156,246,247</sup> In comparison to bolus RPE cell injections, delivery of RPE cells on parylene-C scaffolds drastically increased donor cell survival and viability

following transplantation.<sup>156</sup> Furthermore, PLGA based scaffolds have been shown to increase the survival and integrative capacity of retinal progenitor cells following transplantation.<sup>19,117</sup> Despite these and other successes, the range of viable cell types and appropriate scaffold materials that create a favorable environment *in vitro* and *in vivo* for cell growth and differentiation is still limited.

This study aims to extend the functionality of retinal regenerative scaffolds beyond basic cell survival and growth by elucidating the ability of PLGA to support differentiation of immature induced pluripotent stem cells (iPSCs) to more mature neural progenitor cells. In this work we examine the differentiation of murine iPSCs on a porous PLGA scaffold fabricated using a simple salt-leaching /solvent-casting technique. The results presented here serve to demonstrate the feasibility of differentiating cells directly on synthetic scaffolds intended for implantation. This research provides additional options for cell types appropriate for effective transplantation to the subretinal space and thus adds to the promising treatment options for blinding retinal degenerative diseases.

## Materials and Methods

### Scaffold Fabrication

Poly(D,L-lactide-co-glycolide) (PLGA) scaffolds were prepared using a standard solvent-casting and particle-leaching method (see Figure 6). Briefly, 200 mg of PLGA 50:50 (Resomer® RG 503; Boehringer Ingelheim KG, Ingelheim, Germany) was dissolved in 3 ml of dichloromethane (DCM). Sodium chloride (NaCl, 2 g) was added to the polymer solution and the suspension was poured into a glass mold. The material was dried at room temperature and pressure for 2 to 3 hours, and the resulting composite was immersed in excess of distilled water to extract NaCl. This leaching process was carried out for 48 hours at room temperature with constant stirring and regular distilled water exchange (every 12 hours). PLGA scaffolds were freeze dried and stored in a desiccator until use. Prior to the addition of cells, PLGA scaffolds were coated with collagen (BD

Bioscience, 25 $\mu$ g/ml), laminin (Gibco, 50 $\mu$ g/ml) and fibronectin (Sigma-Aldrich, 100  $\mu$ g/ml).

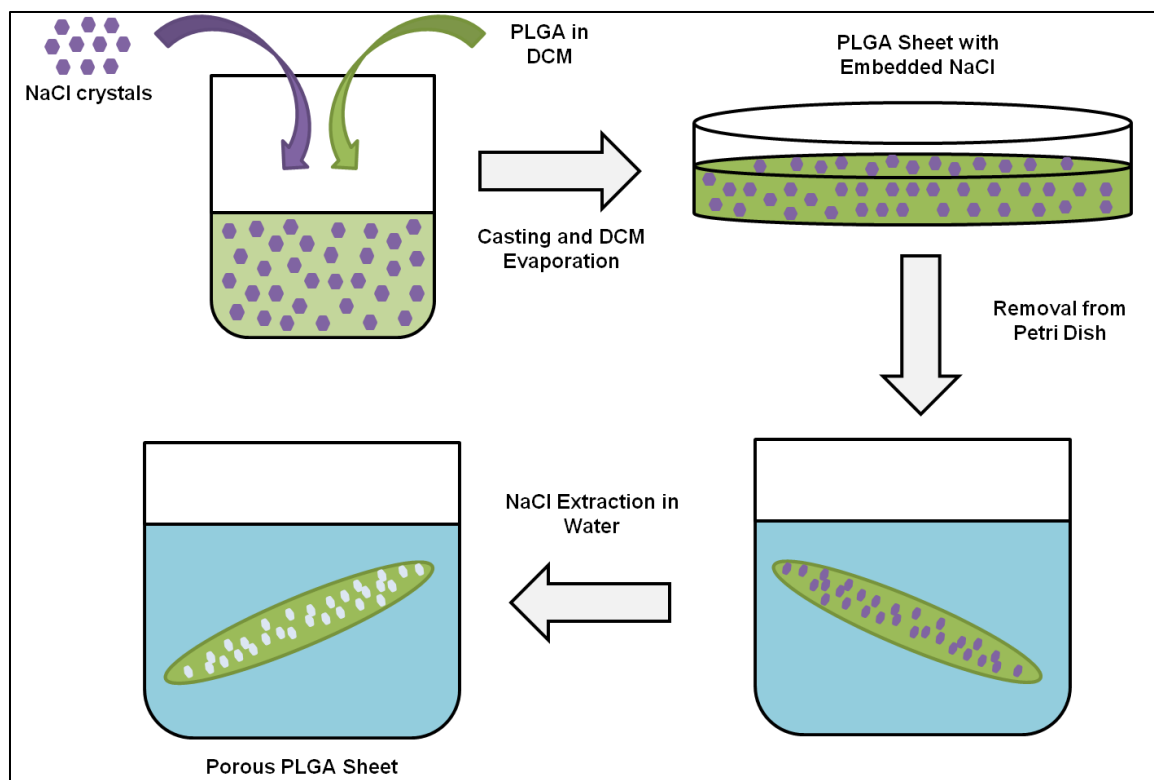


Figure 6. Schematic of porous PLGA scaffolds fabrication process

### Cell Culture

Fibroblasts were isolated from dsRed mouse umbilical cord and de-differentiated using a retroviral approach to yield murine induced pluripotent stem cells (MiPSCs), as described elsewhere.<sup>21,248</sup> To begin differentiation, MiPSCs were gently thawed from a frozen stock, centrifuged, and resuspended in embryoid body (EB) formation media (DMEM F-12 media (Gibco, Grand Island, NY) containing 10% knockout serum replacement (Gibco) 2% B27 supplement (Gibco) 1% N2 supplement (Gibco), 1% L-glutamine (Gibco), 1% 100x NEAA (Gibco), 1% Primocin (Invitrogen, Grand Island,

NY), 1ng/ml noggin (R&D Systems, Minneapolis, MN), 1ng/ml Dkk-1 (R&D Systems), 1ng/ml IGF-1 (R&D Systems) and 0.5ng/ml bFGF (R&D Systems)), and plated at a density of  $\sim 50$  cell clumps/cm<sup>2</sup> on an ultra-low cluster plate (Corning, Lowell, MA). Cell clumps were cultured for 5 days in this manner, after which the embryoid bodies were removed, washed and seeded on top of PLGA scaffolds at a concentration of 30-40 EBs/cm<sup>2</sup>. The embryoid bodies were then cultured in EB differentiation media 1 (EB formation media plus 10ng/ml IGF-1 (R&D Systems) and 1ng/ml bFGF (R&D Systems)) for 10 days and EB differentiation media 2 (EB differentiation media 1 with 10uM of the Notch signaling inhibitor, DAPT (Calbiochem, Gibbstown, NJ)) until day 16. Finally, the iPSCs were cultured in EB differentiation media 3 (EB differentiation media 2 with 2ng/ml of aFGF (R&D Systems)) for the final 2 days of the 18 day experiment. All cells were cultured in a humid 37 °C environment with 5% CO<sub>2</sub>.

#### Scanning Electron Microscopy

PLGA samples with cells were fixed with glutaraldehyde, then stained with osmium tetroxide. Samples were then washed with 0.1mM of cacodylate buffer solution before being completely dried using a critical point drying (CPD) apparatus. PLGA samples without cells were examined directly after lyophilization. In either case, after drying, samples were cut to approximately 5 mm x 5 mm, then taped to an aluminum SEM stub using double-sided tape. A gold-palladium coating was applied using an argon beam K550 sputter coater (Emitech Ltd., Kent, England). Images were captured using a Hitachi S-4800 SEM (Hitachi High-Technologies, Ontario, Canada) at an accelerating voltage of 4 kV.

#### Porosity Quantification

Three independent SEM images of porous PLGA without cells, all taken at the same magnification, were used to measure scaffold pore size in ImageJ. Briefly, after opening each image, the scale was set using the existing scale bar. The image threshold

was adjusted to the default black and white settings, and then the pores were measured using the “Analyze Particles” feature with a minimum area of 3 square pixels and no upper limit.

### Growth Quantification

Cell proliferation was quantified using a colorimetric assay. Briefly, differentiating cells were grown on 5 mm round punches of porous PLGA in a 96 well plate for 1, 3, 8, and 16 days. To serve as a negative control, scaffolds without cells were also allowed to incubate using the same conditions for the same amount of time. To serve as a positive control, several wells of a coated 96-well plate were seeded with a known numbers of cells ( $1.5 \times 10^5$  and  $1.5 \times 10^4$ ) on the day prior to analysis. The following day, each scaffold was transferred to a fresh 100  $\mu$ L of media in the same plate as the controls. MTT reagent (10  $\mu$ L, 3-(4,5-dimethylthiazol-2-yl)-2,5-diphenyltetrazolium bromide, Millipore, Billerica, MA) was added to each well and the plate was incubated at cell culture conditions for 4 hours. The solution was removed from each well and discarded, leaving behind insoluble MTT crystals. These crystals were dissolved by adding 100  $\mu$ L of developing solution (0.04 M HCl in isopropanol) to each well and mixing to homogeneity. Scaffolds were then removed from their wells and the absorbance was measured at 570 nm (Tecan Infinite M200 Pro, Tecan Group Ltd., Männedorf, Switzerland). Relative absorbance was obtained by subtracting the average absorbance for cell-free PLGA wells and dividing by the average absorbance of the  $1.5 \times 10^5$  control wells.

## Results

### Scaffold Characterization

The porosity of a tissue scaffold can be an extremely important aspect of its properties. In this work, the size and density of pores were characterized qualitatively and

quantitatively using scanning electron microscopy. As seen in Figure 7A, salt-leached PLGA scaffolds before being seeded with cells have a dense pore network with randomly distributed pore sizes of widely varying size with the majority being less than 10  $\mu\text{m}$  in diameter. In fact, quantitative analysis (Figure 7B) indicates that pores range in area from about 200  $\text{nm}^2$  to more than 10  $\mu\text{m}^2$  with the most commonly occurring pores (15%) being about 400  $\text{nm}^2$ . As pore size increases, the frequency of pores decreases non-linearly.

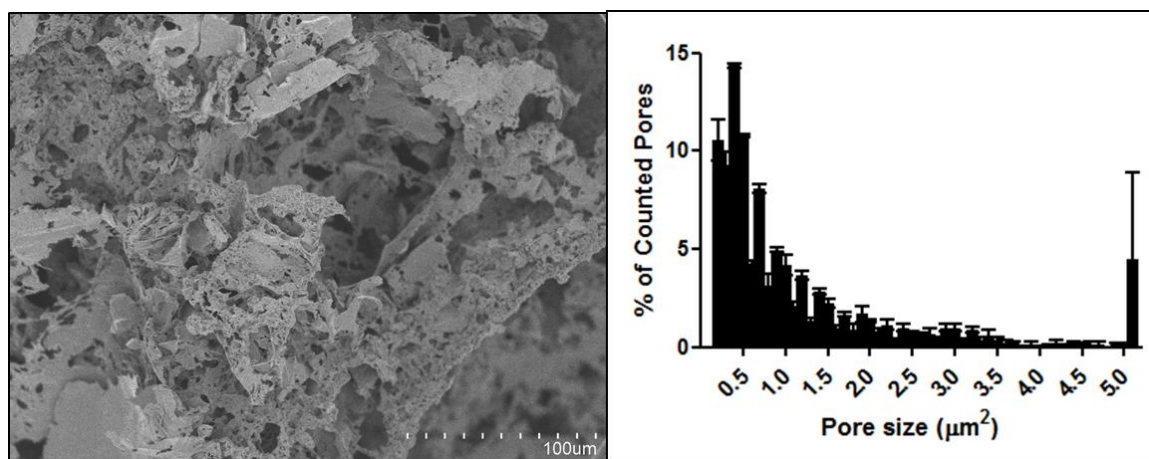


Figure 7. Characterization of PLGA scaffold porosity: A) scanning electron micrograph of a scaffold and B) histogram of pore sizes based on three independent scanning electron micrographs.

### Cell Proliferation

In addition to being a strong indicator of scaffold biocompatibility, cell proliferation on a scaffold is important to understand in order to maximize efficiency and appropriately manage time and resources prior to implantation. Figure 8A and B show PLGA scaffolds after one and two weeks in culture, respectively. After one week, cells appear to have covered most of the surface of the scaffold. After two weeks, however, cells begin proliferating in layers and are much more dense than at one week.

Furthermore, noticeable degradation of the scaffold is evident as cells rebuild using their own extracellular matrix molecules. Cell proliferation was also evaluated quantitatively using the MTT assay. Accordingly, the relative number of cells on the scaffold (Figure 8C) increased gradually from very few at day one to about  $5 \times 10^4$  at day eight. By day sixteen when the last measurement was collected, the average number of cells was rapidly approaching  $1.5 \times 10^5$ .

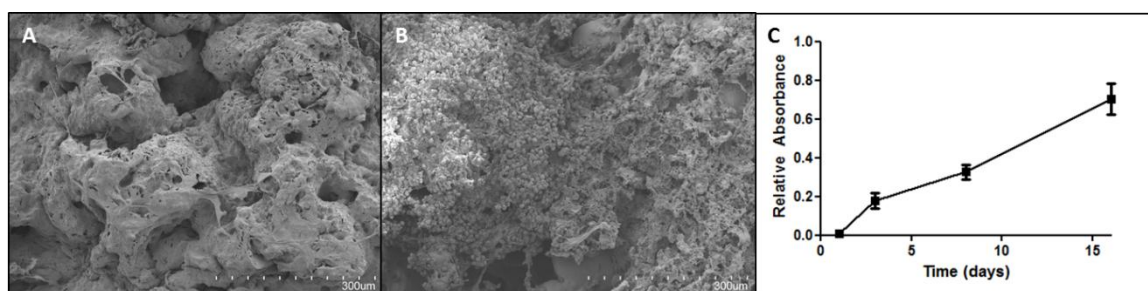


Figure 8. Cell proliferation on porous PLGA scaffolds was captured after 1 week (A) and 2 weeks (B) using scanning electron microscopy and quantified using an MTT assay (C).

### Cell Differentiation

When examined at high magnification (Figure 9), cells grown on porous PLGA scaffolds for only one week demonstrate morphology indicative of neuronal differentiation. For example, groups of neurites, which project from the main cell bodies, can be clearly seen at all magnifications. At low magnifications (Figure 9A), these neurites are difficult to detect through the cell layer but visible in less densely populated scaffold areas. When examined more closely (Figure 9B), the scaffolds demonstrate good cell adherence, and a portion have maintained their rounded stem cell morphology. Importantly, many cells can also be seen extending neurites to form connections with neighboring cells (Figure 9C). Certain areas have dense neurite networks with some visible branching (Figure 9D).



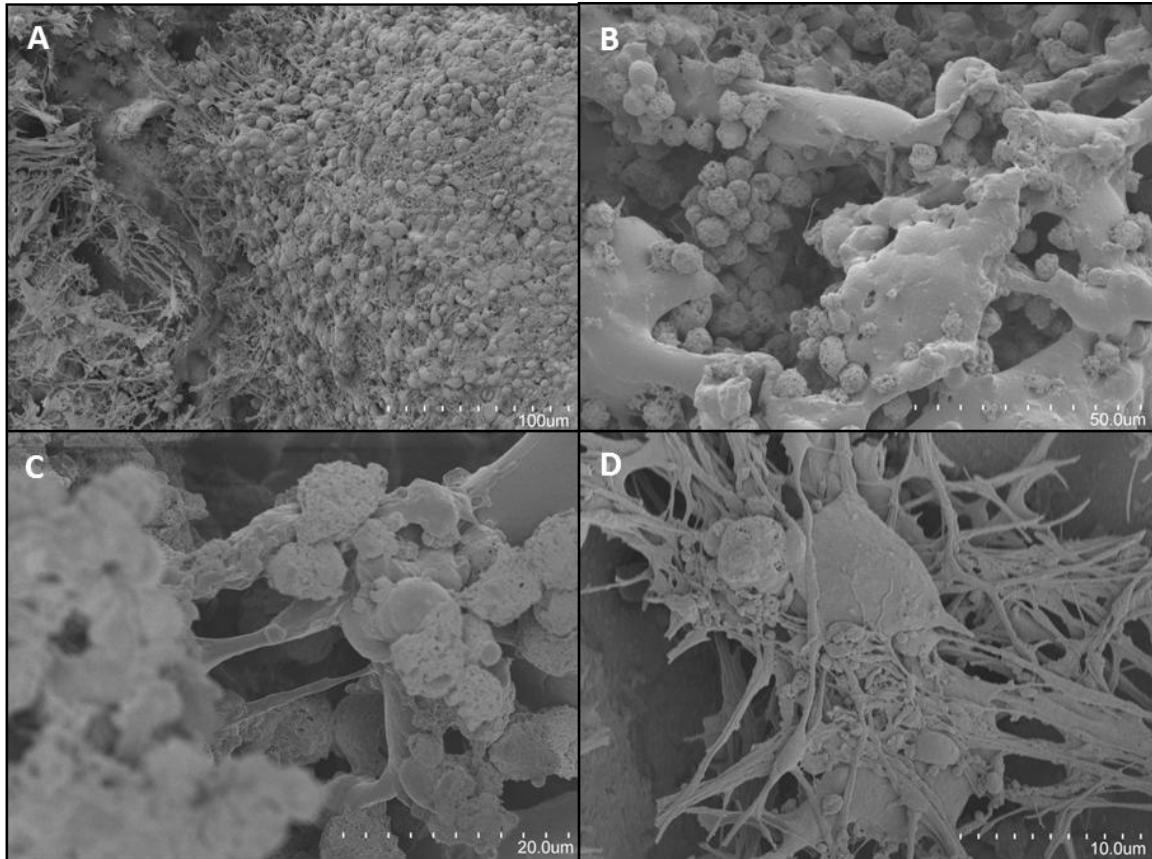


Figure 9. Cell differentiation on porous PLGA scaffolds captured at various magnifications after 1 week.

After two weeks, cells cover the majority of the scaffold surface (Figure 10A-B). Since neurons do not proliferate, cells that have maintained their stem cell morphology are primarily responsible for increases in cell density. At high magnifications, neurite networks are even more dense than at one week (Figure 10C-D). Furthermore, many of the neurites are highly branched, indicating a high degree of cell interconnectivity.



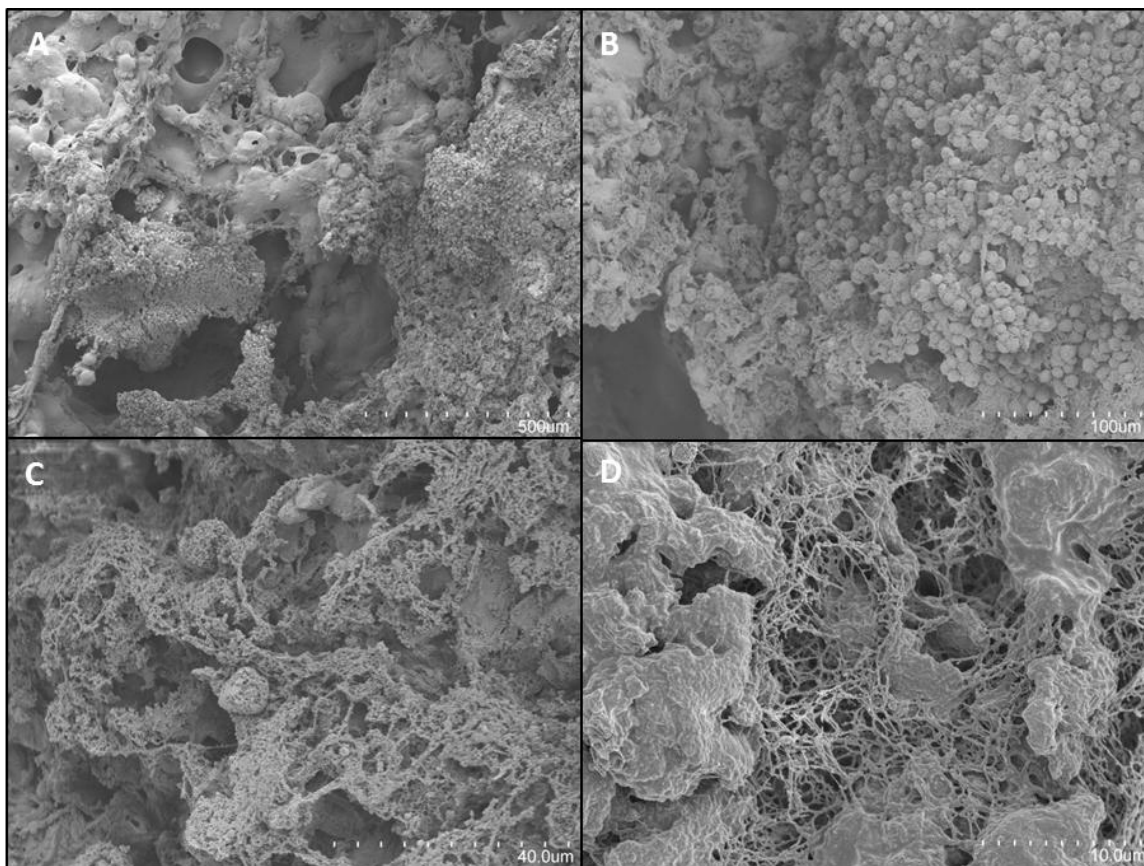


Figure 10. Cell differentiation on porous PLGA scaffolds captured at various magnifications after 2 weeks.

### Discussion

In theory, donor cell physical support issues can be addressed using natural or synthetic scaffolds on which cells attach prior to being implanted in the subretinal space. Although some have investigated the use of allogenic scaffolds from donor tissue such as the lens capsule<sup>24</sup>, Descemet's membrane<sup>25</sup>, Bruch's membrane<sup>26</sup>, amniotic membrane<sup>27,28</sup>, and the inner limiting membrane<sup>29</sup> for the transplantation of regenerative cells to the eye, these approaches have only seen real success with RPE cells and are limited by tissue availability. Similarly, collagen and its derivatives have been explored for decades, both as allogenic and xenogenic scaffold materials. For example, vibratomed

gelatin blocks were used as early as 1989 to stabilize photoreceptor and RPE sheets during transplantation<sup>33,34</sup>. Further use of this technique, however, has revealed issues with unwanted neural rosette formation<sup>35</sup>, rapid retraction of axons<sup>36</sup> and some folding in the subretinal space<sup>34</sup>. Thin collagen sheets have also shown some promise as ocular support materials for both donor tissue and *in vitro* RPE cells<sup>37-39</sup>. However, the use of collagen has also been shown to significantly up-regulate several angiogenic genes in RPE cells<sup>40</sup>, which cause very detrimental side effects.

Several synthetic materials have also been investigated for the purpose of supporting replacement cells during during transplantation. These include inorganic materials, poly(methyl methacrylate) (PMMA)<sup>94</sup>, poly(glycerol sebacate) (PGS)<sup>105</sup>, and poly(caprolactone) (PCL)<sup>107</sup>. However, by far the most commonly investigated synthetic material is poly(lactic-co-glycolic acid) (PLGA). Thin, degradable PLGA scaffolds were first shown to support the growth of RPE cells nearly 20 years ago,<sup>249</sup> and the biomaterial interactions with retinal phenotypes have been closely studied for many years. In addition to its ability to support both fetal and adult human RPE cells<sup>113-115</sup>, PLGA, when rendered porous, also supports the growth of retinal progenitor cells (RPCs)<sup>116,117</sup>. In fact, transplantation of these RPC-laden PLGA constructs resulted in 10-fold and 16-fold increases in cell survival and delivery, respectively, compared to a bolus injection.<sup>117</sup> Furthermore, micropatterned PLGA has been shown to support the growth of primary photoreceptors for a short period of time<sup>206</sup>, a strong indication of its promise as a retinal cell delivery scaffold.

As autologous cells are less likely to elicit an immune response than allogenic donor cells, the use of patient-specific iPSCs is critical to future treatment strategies. This approach will be especially important for those suffering from advanced blindness, which typically involves extensive membrane degeneration and thus, loss of retinal immune privilege. Furthermore, differentiating these iPSCs directly on their intended implantable substrate rather than dissociating them and seeding onto a scaffold after differentiation

could help retain desired morphologies and extracellular matrix. In turn, this cell line selection could make for a more efficient and effective pre-transplantation time period.

In this work, PLGA scaffolds with randomly distributed pores ranging in size from 200 nm<sup>2</sup> to 10 μm<sup>2</sup> were fabricated using a simple salt leaching technique. Most of the pores (>65%) were less than 1 μm<sup>2</sup>, with the greatest fraction (15%) being about 400 nm<sup>2</sup>. After one week, iPSCs seeded on these scaffolds had proliferated to coat the surface. Many of these cells also extended neurites to form connections with neighboring cells, indicating that they had differentiated into neuronal phenotypes. At two weeks, cells began growing in layers on the scaffold, and neurite networks were very dense and highly branched. These results demonstrate the feasibility of differentiating iPSCs directly on synthetic constructs. When cultured on porous PLGA scaffolds *in vitro*, cells were able to proliferate rapidly and mature into neuronal cell types in a short period of time. Evaluating the capacity of materials to not just sustain growth, but also to support differentiation is an important step towards the rational design of cell and tissue replacement strategies. In summary, the findings presented here expand the collection of appropriate cell types for replacement therapies that involve scaffolds to include iPSCs and also contribute to the greater understanding of how cells interact with their environment and growth substrate. In time, these realizations can be used to develop more effective therapies for blinding eye diseases.

CHAPTER 4  
CHITOSAN COATING OF COPPER NANOPARTICLES REDUCES IN  
VITRO TOXICITY AND INCREASES INFLAMMATION IN THE  
LUNG\*

Despite their potential for a variety of applications, copper nanoparticles induce very strong inflammatory responses and cellular toxicity following aerosolized delivery. Coating metallic nanoparticles with polysaccharides, such as biocompatible and antimicrobial chitosan, has the potential to reduce this toxicity. In this study, copper nanoparticles were coated with chitosan using a newly developed and facile method. The presence of coating was confirmed using x-ray photoelectron spectroscopy (XPS), rhodamine tagging of chitosan followed by confocal fluorescence imaging of coated particles, observed increases in particle size and zeta potential. Further physical and chemical characteristics were evaluated using dissolution and x-ray diffraction (XRD) studies. The chitosan coating was shown to significantly reduce the toxicity of copper nanoparticles after 24 and 52 hours and the generation of reactive oxygen species as assayed by DHE oxidation after 24 hours in vitro. Conversely, inflammatory response, measured using the number of white blood cells, total protein, and cytokines/chemokines in the bronchoalveolar fluid of mice exposed to chitosan coated versus uncoated copper nanoparticles, was shown to increase, as was the concentration of copper ions. These results suggest that coating metal nanoparticles with mucoadhesive polysaccharides (e.g. chitosan) could increase their potential for use in controlled release of copper ions to cells, but will result in a higher inflammatory response if administered via the lung.

---

\*Worthington, K.L.S. et al. (2013) Chitosan coating of copper nanoparticles reduces in vitro toxicity and increases inflammation in the lung. *Nanotechnology* 24, 395101.<sup>342</sup>

### Introduction

In order to develop successful treatments for those with severe retinal degeneration and vision loss, it is crucial to develop effective transplantation systems for the delivery of restorative cellular therapies. Several researchers have attempted to overcome donor cell physical support issues using natural or synthetic scaffolds on which cells attach prior to being implanted in the subretinal space. While many have seen success *ex vivo*, material successes *in vivo*, especially long term, are very limited. The increasing demand for biomaterials, including for the treatment of eye diseases, drives research toward the identification of key design parameters for optimizing material effectiveness and speeding the development of viable treatments for those suffering from chronic disease or injury. The first and most obvious design criterion to consider when developing a biomaterial is its biochemical properties. The implantation of a non-compatible material can lead to material failure and even more serious complications, as can a material with improper degradation products or time.

By definition, the most compatible and interactive polymers are those that occur naturally in the body. Mammalian derived whole tissues or molecules have been used for decades to build biomaterials, especially scaffolds, but their availability is limited. Naturally occurring polymers that are not found in mammals can also be used as biomaterials. Chitosan, an attractive polysaccharide for biomaterials, is a naturally occurring molecule that is directly obtained by deacetylation of chitin, the main component of crustacean shells and fungal cell walls. Additionally, chitosan is cationic in solutions of dilute acid and one of the most abundant biopolymers on earth. Many chitosan properties lend themselves well to wound-healing applications, including its biocompatibility in mammals<sup>59,60</sup> and antimicrobial<sup>61,62</sup> properties. These properties have led to a diverse number of medical applications, including haemostatic wound dressings,<sup>63-65</sup> direct wound filling,<sup>66</sup> drug<sup>269-272</sup> and gene<sup>273-276</sup> delivery, and tissue engineering.<sup>277-280</sup> Thus, the inclusion of chitosan in biomaterials is likely to have a

significant impact on overall material biocompatibility. To probe the extent of this impact, chitosan was used as a coating for a material known to be highly toxic, copper nanoparticles. Although some have investigated various chitosan coating methods for metal-oxide NPs<sup>281</sup> and even studied their biocompatibility,<sup>282</sup> no study to date has shown the impact of chitosan coating of Cu NPs on *in vitro* toxicity and *in vivo* inflammatory responses. Such information is critical to improving the understanding of chitosan and its relationship to overall material biocompatibility.

Furthermore, nanotechnology plays an increasingly central role in technological innovation in a broad range of fields ranging from cosmetics to sustainable energy. Nanoparticles (NPs) often combine useful properties of bulk materials such as magnetism, conductivity and stability with a very high surface to volume ratio, increasing reactivity. Thus, many important applications for metal NPs are receiving research attention – attention that could impact society in a variety of important ways. For example, the magnetic properties of iron oxide NPs lend themselves well to biomedical applications such as targeting, imaging, and hyperthermia treatments.<sup>250</sup> Due to their high conductivity, copper (Cu), Cu NPs are most traditionally used for applications such as nanofluids<sup>251,252</sup> to facilitate increased heat transfer and for high throughput catalysis applications<sup>253,254</sup> due to increased reactivity with higher surface area. More recently, however, studies have demonstrated the antimicrobial activity of Cu NPs against methicillin-resistant *Staphylococcus aureus* (MRSA) and *Escherichia coli* in suspension<sup>255</sup> and *Saccharomyces cerevisiae*, *Escherichia coli*, and several other microbes when released in a controlled manner from polymer films.<sup>256</sup> Other potential biomedical applications have been demonstrated with other types of metal nanoparticles, including photo-thermal ablation of tumor cells<sup>257</sup> and medical imaging.<sup>258,259</sup> Furthermore, the release of copper ions from NPs could prove useful in diseases associated with abnormally low accumulation of copper ions in certain regions of the body, such as Menke's disease.<sup>260,261</sup>

Despite their potential use, copper and other metal oxide NPs are limited by their widely demonstrated toxic properties. Indeed, metal oxide NPs have been shown to negatively affect the reproduction and embryonic development of white worms<sup>262</sup> and zebra fish embryos.<sup>263</sup> Likewise, the effects of metal oxide NPs on mammalian cells and on whole organisms can be severe, affecting the central nervous system,<sup>264</sup> and especially the lungs upon inhalation.<sup>265</sup> In a murine model, host defense against bacterial infections was shown to be significantly lowered by exposure to copper oxide NPs in a dose-dependent manner.<sup>266</sup> Another study conducted comparing the toxicity of iron (Fe) and copper nanoparticles (Cu NPs) using a murine model by Pettibone *et al.* clearly shows greater inflammatory responses triggered by Cu NPs than Fe NPs.<sup>265</sup> Furthermore, a study by Yang *et al.* has shown that Cu NPs with greater surface oxidation have higher ROS generating capacity.<sup>267</sup> These researchers also observed a correlation between the surface ligand chain length and the extent of oxidation, which consequently affects the ROS generation and toxicity of the Cu NPs. Therefore, research to understand how to overcome this inherent toxicity is critical, since addressing the issue is necessary for future applications of metal oxide NPs.

Coating metallic NPs with polysaccharides can potentially overcome the drawbacks mentioned above by increasing stability, improving size distributions, increasing biocompatibility and introducing chemical groups that allow for further functionalization of the NPs.<sup>268</sup> Furthermore, these long chain carbohydrate molecules can potentially inhibit surface oxidation of the nanoparticles that may lead to increased toxicity.<sup>267</sup>

In this study, the effect of chitosan coatings on Cu NP physical properties and toxicity were evaluated. The coated particles were optimized and thoroughly characterized using dynamic light scattering, fluorescent tagging, microscopy, and surface analysis. The impact of the chitosan coating on the level of toxicity induced *in vitro* was assessed using human adenocarcinomic alveolar (A549) cells, as well as the *in*



*in vivo* inflammatory response of mice following nasal instillation of coated particles, characterized by differential white blood cell counts and cytokine/chemokine concentration analysis. The information gained through this work provides a basis for understanding the effect of chitosan on NP toxicity and how polysaccharide coatings on NP surfaces alter their characteristics and behavior in biological settings.

### Materials and Methods

#### Reagents

Cu NPs (25 nm, partially passivated with 10% oxygen, Nanostructured and Amorphous Materials, Inc., Houston, TX), Tween<sup>®</sup> 80 (Fisher Scientific, Hampton, NH), sodium bicarbonate (Sigma-Aldrich, St. Louis, MO), ethylenediaminetetraacetic disodium salt (EDTA, Fischer Scientific), and sodium dodecyl sulfate (SDS, Research Products International Corporation, Mount Prospect, IL) were used as received.

Chitosan (2 g, low molecular weight, 96.1% deacetylation, 1% w/v in 1% v/v acetic acid 35 cps, Sigma Aldrich) was dissolved in dilute acetic acid (200 mL, 1% v/v), vacuum filtered, and precipitated using 1 N sodium hydroxide. The precipitate was then mixed with 500 mL of purification buffer (0.1 M sodium bicarbonate, 20 mM EDTA, 0.5% w/v SDS) for 30 minutes, filtered, rinsed, and dialyzed using a Snakeskin<sup>®</sup> dialysis tube (MWCO 10,000) against nanopure water for 2 days (water was replaced approximately every 12 hours). After dialysis, the chitosan was vacuum filtered again, resuspended in a small amount of nanopure water, frozen overnight at -20 °C, and lyophilized.

#### Cu NP Coating

Cu NPs (50 mg) were placed in a 20 mL glass vial and suspended in 10 mL of a dilute solution of Tween<sup>®</sup> 80 (5 mg/mL nanopure water) by mixing overnight with a magnetic stir bar. The resulting solution was then dialyzed (Snakeskin<sup>®</sup> dialysis tube,



MWCO 3500) against nanopure water for 6 hours (water was replaced approximately every 90 minutes). Meanwhile, a solution of chitosan was prepared by mixing chitosan (50 mg) with 1% v/v acetic acid (10 mL) to homogeneity, adjusting the pH to ~5.8 with 1 N sodium hydroxide, and then adding acetate buffer (50 mM, pH 5.5) to a final volume of 20 mL. To accomplish the final chitosan coating, 1 mL of dialyzed particles was mixed with 9 mL of the chitosan solution overnight. The finished particles were then centrifuged at 4000 rpm for 15 minutes, the supernatant was decanted, and the particles were resuspended to the desired concentration with nanopure water.

### Particle Size Analysis

The size of coated and uncoated Cu NPs was measured by JEOL JEM-1230 transmission electron microscope equipped with a Gatan UltraScan 1000 2kx2k CCD acquisition system. A small drop (10  $\mu$ L) of sample solution was left on a 400-mesh TEM copper grid that was pre-coated with a Formvar<sup>®</sup> 0.5% solution in ethylene dichloride film (Electron Microscopy Sciences, Hatfield, PA) for 2 minutes. Whatman<sup>®</sup> filter paper was then used to remove any excess liquid and the grid was air dried. The TEM images were processed using ImageJ (Image Processing and Analysis in Java, Version 1.46b). The hydrodynamic diameter and surface charge of particles in solution were measured in distilled water at 25 °C using dynamic light scattering (Zeta Sizer Nano ZS, Malvern Instruments, Southborough, MA).

### Composition Analysis

X-ray diffraction (XRD) patterns were collected using a Rigaku Miniflex II Diffractometer with a Co source. XRD analysis was conducted according to the following protocol. The solutions containing Cu NPs, Cu NPs + Tw and Cu NPs + Tw + Ch were centrifuged at 22,000 rpm for 1 hour in air tight centrifuge vials and the supernatant carefully removed, leaving ~200  $\mu$ L in the vial. Then using a micropipette, the solid was mixed well with the remaining solution and placed on the XRD slides, dried

overnight in a dessicator, and diffraction patterns were collected. The unprocessed sample of Cu NPs was also analyzed to investigate the effects of oxidation during the treatment process.

### Surface Analysis

The surface functionality of the coated Cu NPs was analyzed using x-ray photoelectron spectroscopy (XPS, Axis Ultra XPS, Kratos, Chestnut Ridge, NY) and confocal microscopy. For XPS analysis, sample preparation followed a standard procedure. Briefly, 20  $\mu$ L droplets of each solution were carefully pipette onto a small square of clean, heavy duty aluminum foil. The droplets were allowed to dry, and then the resulting spot was analyzed using XPS. The resulting data were calibrated and analyzed using XPS software (CasaXPS 2.3.15, Casa Software Ltd., Estepona, Spain). The area under the curve for each atomic signal was calculated using an “area under the curve” function of another data analysis software (GraphPad Prism version 5.02 for Windows, GraphPad Software, San Diego, CA) and used to estimate ratios of the number of atoms on the surface of the particles. The confocal microscopic analysis was conducted using rhodamine-conjugated chitosan prepared according to the following protocol. A 5 mg/mL chitosan solution was prepared as previously described. 100 mg 1-ethyl-3-(3-dimethylaminopropyl) carbodiimide HCl (EDC, Thermo Scientific, Rockford, IL), 50 mg N-hydroxysulfosuccinimide (sulfo-NHS, Thermo Scientific), and 5 mg Rhodamine B (Sigma-Aldrich) were dissolved in 0.1 M 2-(N-mopholino)ethanesulfonic (MES) buffer (1 mL) with the pH adjusted to 6. After mixing for two hours, this solution (1 mL) was added to a 5 mg/mL chitosan solution (9 mL), prepared as described previously, and allowed to react for six hours. The resulting product was dialyzed (Snakeskin<sup>®</sup> dialysis tube, MWCO 10,000) against nanopure water for 2 days and lyophilized. The rhodamine-conjugated chitosan was used to coat Cu NPs using the same method as described above. For imaging, two coverslips were placed on a glass slide

spaced about 3 cm apart to form a thin chamber. A drop of copper particles coated with fluorescent-labeled chitosan was added between coverslips. Another coverslip was placed on top of this chamber to facilitate uniform thickness and to spread the drop. The arrangement was sealed using clear fingernail polish. Images were acquired using a Bio-Rad Radiance 2100 multi-photon microscope (Bio-Rad Laboratories, Hercules, CA). The images were processed using ImageJ (Image Processing and Analysis in Java, Version 1.46b).

#### Dissolution of the Coated and Uncoated Particles

The dissolution studies were conducted using a Varian inductively coupled plasma optical emission spectrophotometer (ICP-OES). The experiments were conducted according to the following protocol. Cu NPs, Tween + NPs and Cu NPs + Tw + Ch containing solutions were sonicated for 5 minutes and 1.5 mL aliquot was filtered using 0.2  $\mu\text{m}$  filters (Xpertec) into centrifuge vials. The filtered samples were centrifuged at 22,000 rpm for 45 minutes to ensure complete removal of any remaining Cu NPs in the filtered solutions. From the supernatant 0.5 mL was carefully transferred into 4.5 mL of 2%  $\text{HNO}_3$  followed by the analysis by ICP-OES with a calibration curve of 5, 10, 25 and 50 ppm. A total of five replicates were conducted for each sample.

#### Cytotoxicity Analysis in vitro

The cytotoxicity of chitosan coated Cu NPs was determined using an MTS assay. A549 (adenocarcinomic human alveolar basal epithelial) cells were seeded at a density of  $1 \times 10^4$  cells/well in RPMI-1640 medium (Gibco<sup>®</sup>, Life Technologies Corporations, NY) at 37 °C and 5%  $\text{CO}_2$  in a 96-well plate. The media were supplemented with 10% fetal bovine serum (FBS, Atlanta Biologicals, GA), 10 mM HEPES (Gibco<sup>®</sup>), 50  $\mu\text{g}/\text{mL}$  gentamycin sulfate (Cellgro, VA), 1 mM sodium pyruvate (Gibco<sup>®</sup>), and 1 mM Glutamax<sup>™</sup> (Gibco<sup>®</sup>). After 24 hours, the medium was discarded and replaced with 100  $\mu\text{L}$  fresh media in each well. Various concentrations (0.01 – 0.09  $\mu\text{g}/\text{mL}$ ) of each

treatment in phosphate buffered saline (PBS, Invitrogen) were then added to each well at a volume of 100  $\mu$ L. The cells were incubated for either 24 or 52 hours, the treatment removed, and fresh media (100  $\mu$ L) added. 20  $\mu$ L of CellTiter 96<sup>®</sup> Aqueous One solution reagent (Promega Corporation, Madison, WI), which changes from MTS tetrazolium to formazan in proportion to the number of live cells present, was added to each well. The cells were incubated between one and four hours, then the formazan product was quantified by spectrophotometric analysis (SpectraMax Plus384, Molecular Devices, Sunnyvale, CA) using the absorbance at 490 nm, according to the company protocol.

Reactive oxygen species (ROS) production was estimated by measuring the oxidation of dihydroethidium (DHE, Molecular Probes, Eugene, Oregon), which becomes fluorescent upon oxidation with superoxide. A549 cells ( $2-4 \times 10^5$  cells per 60 mm Petri dish) were cultured 24 hours, exposed to one of the three NP treatments (2 mL at 50  $\mu$ g Cu NPs per mL) for 24 hours, and then tested for DHE oxidation as described previously.<sup>283</sup> Briefly, the cells were washed once with PBS and labeled at 37 °C for 40 minutes in PBS containing 5 mM pyruvate with DHE (10  $\mu$ M; in 1% DMSO). Culture plates were placed on ice to stop the labeling, trypsinized, and resuspended in ice-cold PBS. Samples were analyzed using a FACScan flow cytometer (Becton Dickinson Immunocytometry Systems, Inc., Mountain View, CA; excitation 488 nm, emission 585 nm band-pass filters). The mean fluorescence intensity (MFI) of 10,000 cells was analyzed in each sample and corrected for auto-fluorescence from unlabeled cells. The MFI data were normalized to levels from A549 cells treated with PBS only.

#### Animal Models

An inflammation mouse model was used in these studies. Mice (C57Bl/6, males, 6 weeks old) were purchased from The Jackson Laboratory (Bar Harbor, ME). The instillation protocol was approved by the Institutional Animal Care and Use Committee and complied with the NIH Guidelines. Animals were housed in a vivarium in

polypropylene, fiber-covered cages in HEPA-filtered Thoren caging units (Hazelton, PA, USA) in the Pulmonary Toxicology Facility at the University of Iowa. They were acclimatized for 10 days prior to the exposures. Food (sterile Teklad 5% stock diet, Harlan, Madison, WI, USA) and water (via an automated watering system) was provided *ad libitum* and a 12-hr light-dark cycle was maintained in the animal room.

#### Nasal Instillation Exposure

Animals in each experimental group (n = 6): Cu NPs, Cu NPs + Tw, and Cu NPs + Tw + Ch, were exposed to tested material by nasal instillation. Each mouse was exposed twice with 50  $\mu$ L (Cu NPs and Cu NPs + Tw groups) and with 100  $\mu$ L (Cu NPs + Tw + Ch) of exposure solution with a 1 hour interval between each dosing. The total dose of Cu NPs in each experimental group, as measured by inductively coupled plasma-mass spectrometry (ICP-MS, X Series, Thermo Scientific, Waltham, MA, USA) was approximately 30  $\mu$ g/mouse (33.5, 34.3, and 29.0  $\mu$ g/mouse in Cu NPs, Cu NPs + Tw, and Cu NPs + Tw + Ch group, respectively). Suspensions of tested materials were prepared, as described above and vortexed immediately before the instillation exposure. Nasal instillation was conducted under anesthesia by inhalation of isoflurane (3 %) using a precision Fortec vaporizer (Cyprane, Keighley, UK). Naïve mice (mice with no exposure) served as a control group. All mice were euthanized 24 hours post exposure by overdose inhalation of isoflurane, cervical dislocation and exsanguinations, after which bronchoalveolar lavage (BAL) fluid and lung tissues were collected.

#### Bronchoalveolar Lavage (BAL) Fluid

The lungs from 6 mice in each group were lavaged *in situ* three times with approximately 1 mL of sterile saline (0.9% sodium chloride solution, Baxter, Deerfield, IL, USA). The lavage fluid was centrifuged (800 x g for 5 min at 4 °C), the total white blood cells were counted using a hemocytometer and the supernatants were stored at -80°C for later analyses. For differential cell counts, resuspended cells in Hank's balanced

salt solution and fetal calf serum, were spun (800 x g, 3 min, Cytospin 4, Thermo Shandon, Thermo Scientific, Waltham, MA, USA) onto microscope slides and air-dried. The cells were then stained using HEMA 3<sup>®</sup> stain set (PROTOCOL<sup>®</sup>, Fisher Scientific Company LLC, Kalamazoo, MI) and the number of macrophages, neutrophils and lymphocytes (total of 400 total cells per each animal) were counted.

A Bradford protein assay (Bio-Rad Laboratories, Inc., Hercules, CA, USA) was used to measure total protein levels in BAL fluid supernatants and lactate dehydrogenase (LDH) activity was determined by a Cytotoxicity Detection Kit (Roche Diagnostics, Penzberg, Germany). Concentrations of selected inflammatory cytokines/chemokines (tumor necrosis factor [TNF]- $\alpha$ , interferon [IFN]- $\gamma$ , interleukin [IL]-6, IL-12(p40), keratinocyte-derived cytokine [KC], and macrophage inflammatory protein [MIP]-1 $\alpha$ ) were measured in the BAL fluid using a multiplexed fluorescent bead-based immunoassay (BioRad Laboratories, Inc., Hercules, CA). The lowest limit of detection (LLOD) for cytokine assays was calculated by dividing the lowest detected point on the standard curve by  $\sqrt{2}$ . (IL-6 = 0.52, IL-12(p40) = 0.72, IFN- $\gamma$  = 1.03, KC = 1.42, MIP-1 $\alpha$  = 1.47 and TNF- $\alpha$  = 2.02 pg/mL)

#### Copper Analysis in Exposure Solutions, Lung Tissue, and BAL Fluid

The lungs from mice in each group were harvested at the time of necropsy and stored at  $-80^{\circ}\text{C}$ . Tissues were dried using a freeze dryer for approximately 16 hrs at  $1.3 \times 10^{-1}$  mBar and  $-50^{\circ}\text{C}$  (Labconco Corp., Kansas City, MO, USA) and subsequently weighed. Dried lungs were placed in 50 mL digestion tubes and high purity nitric acid and hydrochloric acid were added (Optima grade, Fisher Scientific, Pittsburgh, PA, USA). Tissues were then digested in 36-well HotBlock<sup>™</sup> (Environmental Express, Mt. Pleasant, SC, USA) at  $95^{\circ}\text{C}$  for 6 hrs. The concentration of Cu ions was determined by

inductively coupled plasma-mass spectrometry (ICP-MS, X Series, Thermo Scientific, Waltham, MA, USA). Each sample was spiked with an internal standard at 20 µg/L.

### Statistical Analysis

The results were analyzed using the statistical analysis package included in the analytical software (GraphPad Prism 5.02). For the *in vitro* results, a two-way analysis of variance (ANOVA) was performed, followed by Bonferroni post-tests between each group. When the data could not be assumed to be normal in distribution (ROS and *in vivo* results), a Kruskal-Wallis one-way analysis of variance on ranks test was performed, followed by Dunn's multiple comparison tests. Data are expressed as a mean ± standard error. *P*-values less than 0.05 were considered significant.

### Results and Discussion

A chitosan coating was applied to Cu NPs to study the effect of the polysaccharide on NP physical properties, toxicity *in vitro*, and inflammatory response *in vivo* upon nasal instillation. The physical properties were first examined visually using transmission electron microscopy (TEM, Figure 11). The copper particles alone (Cu NPs, Figure 11A) appear to have a smooth, round morphology. The particles aggregate in water to some degree, making applications using copper particles in water difficult. A direct coating method was first attempted by mixing Cu NPs with a solution of chitosan in acetic acid and buffer. This method, however, caused even more significant aggregation and dissolution of copper ions from the particles. Additionally, the solution appeared to gel, trapping the Cu NPs in a semi-solid matrix. To stabilize the Cu NPs in the aqueous environment and protect them from dissolution, a pre-coating of surfactant (Tween<sup>®</sup> 80) was applied prior to coating the particles with chitosan. The hydrophobic chains of the Tween<sup>®</sup> 80 molecule adsorb via Van der Waals forces (physisorption) to the hydrophobic Cu NPs,<sup>284</sup> leaving a hydrophilic external layer to the coating. It has been proposed that the  $\pi$  orbital associated with the carbon-carbon double bond in the



surfactant's alkyl chain also contributes to its strong interaction with metal NP surfaces and increases its ability to stabilize them.<sup>285</sup> Thus, this initial coating process should help to solubilize Cu NPs, as has been shown for other NPs.<sup>286</sup> The copper particles coated only with Tween<sup>®</sup> 80 (Cu NPs + Tw, Figure 11B), however, exhibited a rough morphology and were heavily aggregated, potentially because the concentration of Tween<sup>®</sup> 80 used was above the critical micelle concentration of only 10  $\mu\text{M}$ .<sup>287</sup>

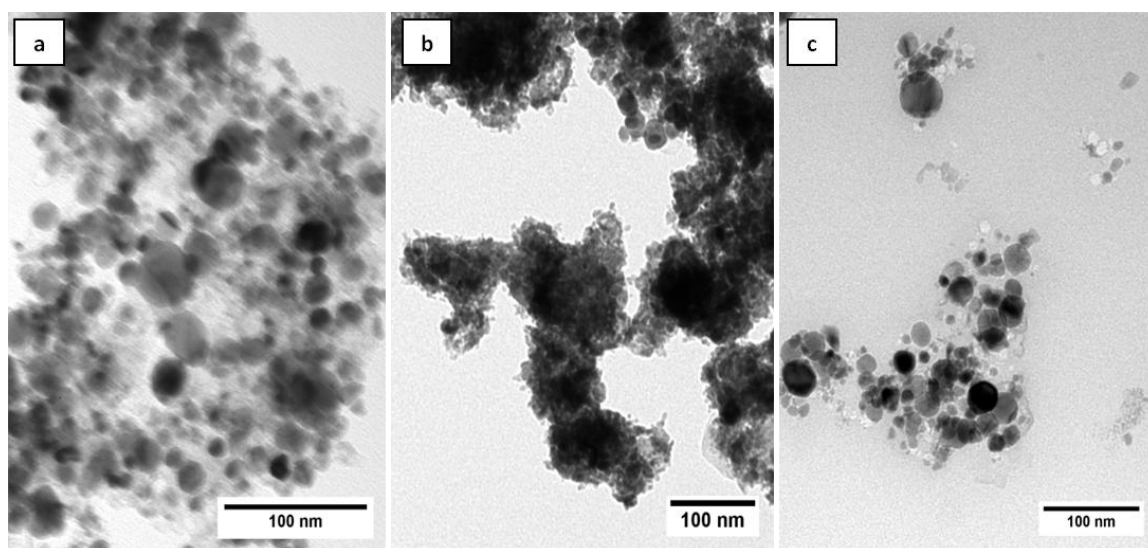


Figure 11. TEM images of Cu NPs with a) no coating (Cu NPs), b) a Tween<sup>®</sup> 80 coating (Cu NPs + Tw), and c) a Tween<sup>®</sup> 80 coating followed by chitosan coating (Cu NPs + Tw + Ch)

We hypothesize that charged, hydrophilic chitosan molecules can adsorb to the externally presented hydrophilic groups of the Tween<sup>®</sup> molecules by physisorption, or Van der Waals interactions. Once the chitosan coating was applied (Cu NPs + Tw + Ch, Figure 11C), these particles demonstrated a smooth, spherical morphology and aggregated to a lesser extent than the copper particles alone or the Tween<sup>®</sup>-coated particles, likely due to increased repulsive forces between the positively charged



nanoparticles. Further study of chitosan's interaction with polysorbate surfactants that are coated on NPs would certainly be beneficial for understanding the processes involved in the coating process described herein. To provide a visual confirmation of chitosan coated on the NP surface, Rhodamine B conjugated chitosan derivatives were prepared and used to coat Cu NPs in the same manner as regular chitosan. Because Rhodamine B is fluorescent and Cu NPs are not, the chitosan on the particles' surface could now be detected using fluorescent microscopy (Figure 12A).

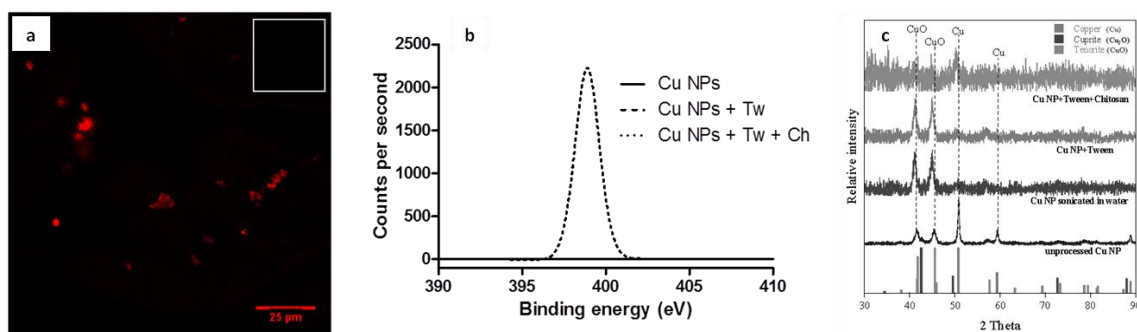


Figure 12. Physical characterization of coated and uncoated Cu NPs. Shown are a) confocal microscopy images of Cu NPs with no coating (inset), and coated with Tween<sup>®</sup> 80 and rhodamine-conjugated chitosan; b) XPS data in the Ni 1s binding energy region for Cu NPs, Cu NPs + Tw, and Cu NPs + Tw + Ch where only the Cu NPs + Tw + Ch show the presence of nitrogen on the surface of nanoparticles; and c) XRD characterization of Cu NPs, Cu NPs + Tw, Cu NPs + Tw + Ch, and unprocessed Cu NPs

To further characterize the coated particles, the hydrodynamic diameter, charge, and surface composition were determined using dynamic light scattering (DLS) and x-ray photoelectron spectroscopy (XPS). For ease of comparison, the size and charge information is summarized in Table 2. The measured hydrodynamic diameter of the Cu NPs before coating, after pre-coating with Tween<sup>®</sup> 80, and after chitosan coating were  $187 \pm 10$  nm,  $495 \pm 66$  nm, and  $260 \pm 25$  nm, respectively. Although these measured sizes are much larger than those observed using TEM, the overall size trends were consistent;

chitosan-coated particles were slightly larger than Cu NPs alone and the Tween<sup>®</sup> 80 coated NPs were highly aggregated and difficult to measure. The charge measurements showed a significant increase in positive charge (from  $15.4 \pm 3.2$  mV to  $43.4 \pm 1.7$  mV) when Cu NPs were coated with chitosan. Since chitosan is a cationic molecule, these results give further evidence that the Cu NPs were, in fact, coated with chitosan.

Table 2. Size, zeta potential, and dissolution of Cu NPs with and without coating

	Cu NPs	Cu NPs + Tw	Cu NPs + Tw + Ch
Radius (nm) <sup>†</sup>	$187 \pm 10$	$495 \pm 66^{\dagger\dagger}$	$260 \pm 25$
Zeta Potential (mV) <sup>†</sup>	$15.4 \pm 3.2$	$13.6 \pm 0.3^{\dagger\dagger}$	$43.4 \pm 1.7$
Dissolved Cu (ppm)	$15.7 \pm 0.1$	$12.4 \pm 0.6$	$27.2 \pm 0.4$

<sup>†</sup>n=3, <sup>††</sup>Data quality report indicated poor data quality and high likelihood of aggregation

As a final confirmation of the chitosan coating, the surface composition of the NPs was analyzed using XPS. All three NP formulations (Cu NPs, Cu NPs + Tw, Cu NPs + Tw + Ch) exhibited peaks at three corresponding bonding energies standard for copper, confirming the presence of Cu. A scanning trace specific to nitrogen (Figure 12B) showed no representative signals for the Cu NPs or Cu NPs + Tw samples. On the other hand, a very distinct peak at a binding energy of 390 mV was observed for the Cu NPs + Tw + Ch, indicating the presence of nitrogen, the source of which was from the chitosan free amine groups. The relative ratios of various atoms on the NP surface were also estimated by calculating the area under the XPS curves. The number of carbon and oxygen atoms relative to the number of copper atoms on the surface increased dramatically (~550% and ~680%, respectively) between the Cu NPs and Cu NPs + Tw + Ch groups, likely due to the addition of the high molecular weight polysaccharide with large quantities of both carbon and oxygen.

Coated and uncoated NPs were also characterized by XRD for their bulk composition to identify any changes taking place during the process of coating. The Cu NPs oxidize during the treatment process into CuO NPs (see Figure 12C). The diffraction patterns indicate that the unprocessed Cu NPs also contain CuO, likely due to surface oxidation of Cu NPs. As noted by the manufacturer, these NPs are in fact “partially” passivated with oxygen. This process can leave behind a surface coating that contains CuO and Cu<sub>2</sub>O phases as discussed previously.<sup>265</sup> Additionally, over time this oxide layer can become even thicker under ambient storage conditions.<sup>288</sup> However, here it is noted that upon treatment, a complete oxidation of the CuO is observed. It is possible that when the NPs are sonicated, the increase in temperature and breaking of the aggregates increases the exposed surface area, facilitating the oxidation process.

Dissolution studies indicated that uncoated and Tween<sup>®</sup> 80 coated NPs showed similar extents of copper dissolution (Table 2). Coating with chitosan, however, resulted in a two-fold increase in copper dissolution. Furthermore, solutions containing Cu NPs + Ch were darker blue in color than those containing Cu NPs, Cu NPs + Tw, or Cu NPs + Tw + Ch, which is due to dissolved Cu<sup>2+</sup> ions. These characteristics suggest that chitosan enhances dissolution when in direct contact with the Cu NP surface. Upon coating with the Tween<sup>®</sup> 80, chitosan assisted dissolution is inhibited. Therefore, Tween<sup>®</sup> acts as a protective coating that inhibits nearly complete dissolution of Cu NPs. It should be noted that because all of the particles examined have a significant oxide layer, as demonstrated in Figure 12C, the deliberate coatings applied (i.e. Tween<sup>®</sup> 80 and chitosan) can be considered independently with regard to the resulting toxicity and inflammatory response.

After fully characterizing the physical properties of the coated Cu NPs, the *in vitro* toxicity was analyzed in human alveolar epithelial (A549) cells using a standard MTS cell viability assay. To confirm that the differences in toxicity observed in A549 cells could be extrapolated to other cell lines, the treatments were also tested in HEK-293

(human embryonic kidney) cells. The cells were very sensitive to Cu NPs and Cu NPs + Tw and less-so to their chitosan-coated counterparts (Cu NPs + Tw + Ch) after 24 and 52 hours of exposure (Figure 13A). Cells treated with 5  $\mu\text{g}$  Cu NPs + Tw + Ch were four times more viable after 24 hours and five times more viable after 52 hours than those treated with 5  $\mu\text{g}$  Cu NPs. The median lethal dose ( $\text{LD}_{50}$ ) of Cu NPs + Tw + Ch was the highest of all treatments for both exposure times, while the chitosan-coated Cu NPs had the lowest  $\text{LD}_{50}$  values in each case. Similar results were observed in the HEK-293 cells (data not shown). This decrease in toxicity is also correlated with a two-fold decrease in the cells' generation of reactive oxygen species (Figure 13B) when treated with Cu NPs + Tw + Ch compared to Cu NPs. The presence of chitosan coating on Cu NPs apparently lowers the environmental stress for cells, increasing their viability relative to other Cu NP exposures. These dramatic differences in dose-related toxicity *in vitro* demonstrate that coating Cu NPs with chitosan protects exposed cells from Cu NPs and significantly reduces their toxicity, thus increasing their biocompatibility and perhaps suitability for various biomedical applications.

The effect of chitosan coating of Cu NPs on the inflammatory response upon nasal instillation was also investigated. Twenty-four hours after nasal instillation of Cu NPs, Cu NPs + Tw, or Cu NPs + Tw + Ch, exposed mice had lost an average of 12% of their starting body weight (average weight loss of  $2.81 \pm 0.41$ ,  $2.56 \pm 0.32$  and  $2.59 \pm 0.43$  g, respectively). After necropsy, analyses of cellularity and concentration of cytokines/chemokines in the bronchoalveolar lavage (BAL) fluid and copper in the excised lung tissue were performed.

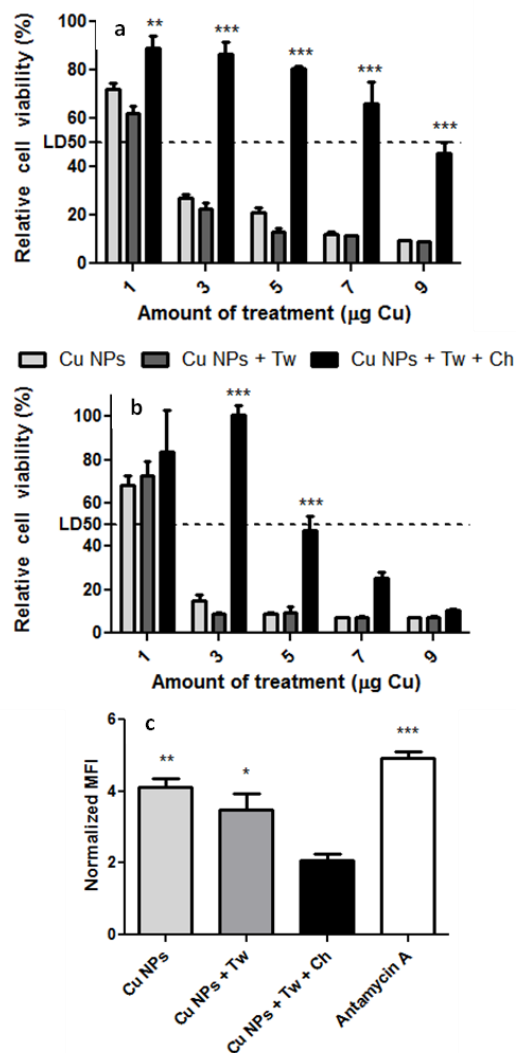


Figure 13. Toxicity of coated and uncoated Cu NPs to A549 cells. Toxicity was measured relative to untreated cells of coated and uncoated Cu NPs on A549 cells exposed for a) 24 and b) 52 hours. Statistical analysis was performed by a two-way analysis of variance followed by Bonferonni post tests. DHE oxidation levels (c) of A549 cells after 24 hours of exposure to coated and uncoated Cu NPs. Statistical analysis was performed by a Kruskal-Wallis test followed by Dunn's post tests. For all panels, the statistical significance shown is relative to Cu NPs. Error bars represent the standard error mean, \*\*  $p < 0.01$ , \*\*\*  $p < 0.001$

The concentration of Cu (NPs and ions) deposited in the lung tissue of all exposed animals (adjusted for the Cu in control mice) was about 30 µg/g lung dry weight (Table 3). The concentration of Cu ions in the BAL fluid supernatants was also measured. This

analysis revealed a higher copper ion concentration in the BAL fluid of lungs exposed to chitosan-coated Cu NPs than the other treatments (Table 3). This result corresponds well with the increased dissolution of copper from chitosan-coated Cu NPs *ex vivo* (Table 2).

Table 3. Characterization of lung tissue and fluid after nasal instillation of coated and uncoated Cu NPs. Except where noted, data was obtained from the post-necropsy BAL fluid. Data are expressed as mean  $\pm$  standard error.

	Cu in Lung Tissue <sup>†</sup>	Cu <sup>†</sup>	Total Cells/Mouse	Total Protein	LDH Activity
	( $\mu\text{g/g}$ dry weight)	( $\mu\text{g/L}$ )	( $\times 10^{-3}$ )	( $\mu\text{g/mL}$ )	(U/L)
Naïve	-	-	168 $\pm$ 15	63.6 $\pm$ 1.8	21 $\pm$ 4
Cu NPs	30.4 $\pm$ 5.3	36.4 $\pm$ 13.4	765 $\pm$ 102	142 $\pm$ 19	31 $\pm$ 5
Cu NPs + Tw	27.9 $\pm$ 5.8	46.2 $\pm$ 13.7	756 $\pm$ 89	172 $\pm$ 24	27 $\pm$ 7
Cu NPs + Tw + Ch	28.8 $\pm$ 6.6	88.5 $\pm$ 26.5	1,920 $\pm$ 777	378 $\pm$ 111 <sup>#</sup>	73 $\pm$ 14 <sup>*</sup>

\*  $p < 0.01$ , activity of LDH in BAL fluid was significantly higher in Cu NPs + Tw + Ch (one-way ANOVA followed by Tukey test) compared to Cu NPs, <sup>†</sup>Data were corrected for concentration of Cu in the naïve group, <sup>#</sup> $p = 0.063$

The total number of white blood cells recovered in the BAL fluid (Table 3) was the highest in the group of animals exposed to chitosan-coated copper NPs ( $1,920 \pm 777 \times 10^3$  cells/mouse), and while the number of cells from the animals exposed to uncoated Cu NPs was much lower ( $765 \pm 102 \times 10^3$  cells/mouse), this difference was not shown to be statistically significant. Similarly, the concentration of total protein and activity of LDH in the supernatants of BAL fluid were higher in the chitosan-coated Cu NP group compared to the Cu NPs group (Table 3,  $p < 0.01$  and  $p = 0.063$ , respectively). The number of neutrophils (key inflammatory cells in the lung) in the BAL fluid (Figure 14A) was 3.5 times higher in the chitosan-coated Cu NPs group ( $1,580 \pm 799 \times 10^3$  cells/mouse) than the Cu NPs alone group ( $456 \pm 108 \times 10^3$  cells/mouse).

Correspondingly, the percentage of neutrophils in the BAL fluid was highest in the chitosan coated Cu NPs group followed by Cu NPs alone and Cu NPs + Tw groups (71%, 56% and 51%, respectively).

Out of six selected inflammatory cytokines/chemokines that were analyzed in the supernatants of BAL fluid (Figure 14B), IL-6 and KC had higher levels in chitosan-coated Cu NPs than uncoated Cu NPs, corresponding well with the higher neutrophil counts in Figure 14A. The concentration of IFN- $\gamma$  and TNF- $\alpha$  were below the lower limit of detection (LLOD, 1.03 and 2.02 pg/mL, respectively) in all experimental groups. These *in vivo* results show that chitosan-coated Cu NPs elicit higher pulmonary inflammatory responses than their uncoated counterparts. The higher response is demonstrated by the increased total cell and neutrophil numbers in the BAL fluid as well as increased concentrations of inflammatory cytokine/chemokines (IL-6 and KC) in mice exposed to Cu NPs + Tw + Ch as opposed to Cu NPs and Cu NPs + Tw. Likewise, pulmonary cytotoxicity represented by increased activity of LDH in the BAL fluid was higher in groups exposed to chitosan-coated Cu NPs. Chitosan-coated Cu NPs are more likely to have a high residence time in the lungs due to the well-known mucoadhesive properties of chitosan.<sup>289,290</sup> Chitosan has been shown, in fact to enhance pulmonary delivery of calcitonin from PLGA nanospheres by this phenomenon coupled with the opening of tight junctions.<sup>290</sup> The inability to clear these coated NPs causes a higher concentration of copper (from NPs and ions) to remain stagnant during the first 24 hours after exposure, eliciting a higher inflammatory response than non-mucoadhesive Cu NPs that can be cleared relatively quickly from the lungs. Furthermore, chitosan has been shown to have a powerful effect on the tight junctions and permeability of mucus-rich epithelial cells;<sup>291</sup> an effect that is enhanced when the chitosan is in NP form.<sup>292,293</sup>

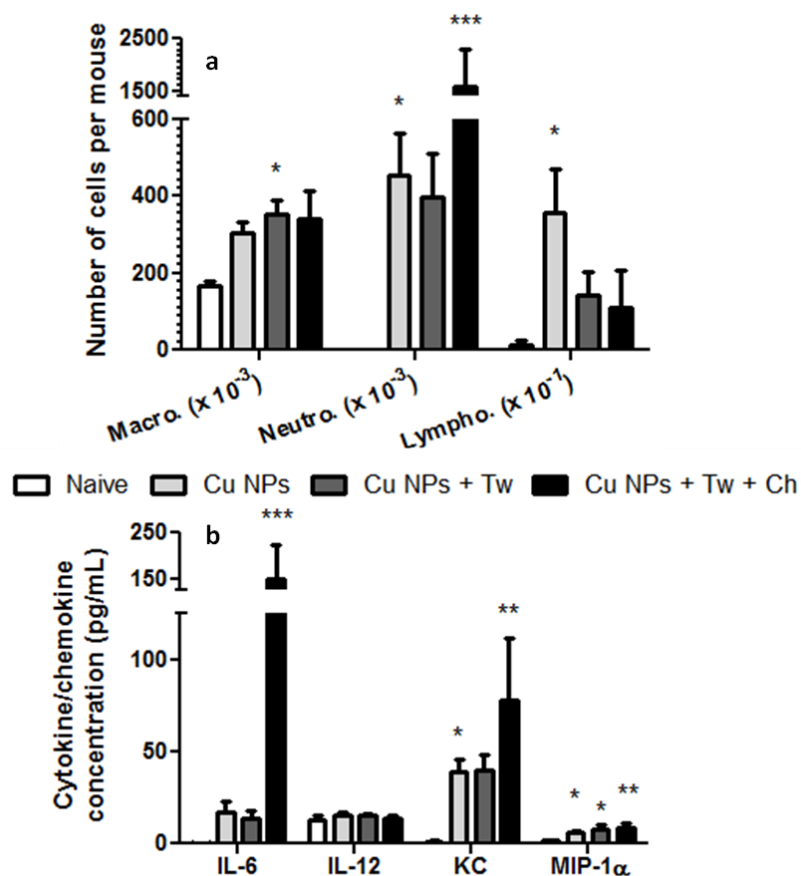


Figure 14. Inflammatory response in the post-necropsy lung BAL fluid 24 hrs after nasal instillation of coated and uncoated Cu NPs. Differential cell counts (a) show the number of macrophages, neutrophils and lymphocytes, while chemokine/cytokine analysis (b) shows the levels of selected inflammatory markers. Statistical analyses were performed by Kruskal-Wallis tests for each cell type or chemokine/cytokine followed by Dunn's post tests. Statistical comparisons shown are relative to the naive group for each cell type or inflammatory marker. The differences between all other groups are not statistically significant. Error bars represent the standard error mean,  $n = 5-7$ , \*  $p < 0.05$ , \*\*\*  $p < 0.001$ , \*\*\*  $p < 0.001$

### Conclusions

The addition of a chitosan coating to Cu NPs changed physical properties and toxicity *in vitro* and *in vivo*. The size of the NPs increased by roughly 50%, but the morphology of the chitosan coated particles was smooth and round, in contrast to aggregated and rough Tween® 80 coated Cu NPs. The presence of chitosan coating was



confirmed using fluorescent imaging of Cu NPs coated with Rhodamine B conjugated chitosan. The presence of cationic chitosan on the particle surface also caused the particle charge to increase significantly. XPS analysis demonstrated the presence of chitosan on the surface of the coated NPs via the clearly detectable presence of nitrogen. The *in vitro* toxicity of chitosan coated Cu NPs was significantly lower than uncoated Cu NPs for two different cell types, two time points, and a range of doses. LD50 values were highest for chitosan-coated NPs and lowest for Cu NPs + Tw, indicating that coating with chitosan protects cells in culture from the toxic effects of Cu NPs. Conversely, an increase in inflammatory response was observed for mice exposed to chitosan-coated Cu NPs versus uncoated Cu NPs. These results suggest that coating metal NPs with mucoadhesive polysaccharides (e.g. chitosan) decreases their ability to be cleared from the lungs, prolonging the exposure of cells and tissue to toxic metal oxides and producing a dramatic acute inflammatory response. Despite the differences in toxicity *in vitro* and *in vivo* in the lung, chitosan-coated Cu NPs for the controlled release of copper ions in the treatment of copper-deficiency diseases such as Menke's disease could still be beneficial, provided that a different route of administration is utilized (i.e. intravenous). Although chitosan coating was, in fact, shown to increase the inflammatory response of Cu NPs administered via nasal instillation, it was also shown to dramatically decrease toxicity *in vitro*. Thus, this study demonstrates the importance of not only a thorough analysis of NP physical properties, but also a careful analysis of toxicity, especially regarding making inferences about *in vivo* exposures and effects based on *in vitro* studies.

## CHAPTER 5

### MECHANICAL PROPERTIES OF MURINE AND PORCINE OCULAR TISSUES IN COMPRESSION<sup>†</sup>

Sub-retinal implantation of foreign materials is becoming an increasingly common feature of novel therapies for retinal dysfunction. The ultimate compatibility of implants depends not only on their *in vitro* chemical compatibility, but also on how well the mechanical properties of the material match those of the native tissue. In order to optimize the mechanical properties of retinal implants, the mechanical properties of the mammalian retina itself must be carefully characterized. In this study, the compressive moduli of eye tissues, especially the retina, were probed using a dynamic mechanical analysis instrument in static mode. The retinal compressive modulus was lower than that of the sclera or cornea, but higher than that of the RPE and choroid. Compressive modulus remained relatively stable with age. Conversely, apparent retinal softening occurred at an early age in mice with inherited retinal degeneration. Compressive modulus is an important consideration for the design of retinal implants. Polymer scaffolds with moduli that are substantially different than that of the native tissue in which they will ultimately reside will be less likely to aid in the differentiation and development of the appropriate cell types *in vitro* and will have reduced biocompatibility *in vivo*.

#### Introduction

Inherited retinal degenerative diseases such as retinitis pigmentosa, Leber congenital amaurosis, and Stargardt disease are characterized by death of the light sensing photoreceptor cells of the outer neural retina and irreversible blindness. For neurodegenerative diseases such as these, drug and/or gene therapy alone may not

---

<sup>†</sup> Worthington, K. S. *et al.* (2014) Mechanical Properties of Murine and Porcine Ocular Tissues in Compression. *Exp. Eye Res.* 121, 194–99.<sup>341</sup>

suffice, especially in patients who have suffered extensive photoreceptor cell loss prior to molecular diagnosis of their gene defect. Under these circumstances, strategies focused on cellular or tissue replacement will be beneficial. Many studies suggest that the use of stem cells to achieve such a goal is now feasible;<sup>10-22,294,295</sup> however, a major remaining hurdle is the development of an optimal cell transplantation system. Current delivery methods typically result in massive cell loss and limited cellular integration following transplantation. For instance, several studies have shown that following bolus photoreceptor cell injection, less than 0.01% of transplanted cells survive and even fewer actually integrate within the host retina.<sup>13,18</sup> In large part, poor integration can be attributed to the lack of donor cell support following the bolus injection. These results are particularly common when attempting to perform subretinal transplants in late stage retinal degenerative hosts that have lost the majority of their outer retina due to photoreceptor cell death.

In an attempt to increase cellular survival and subsequent integration following retinal progenitor/stem cell (RPC) transplantation, several researchers have designed polymer scaffolds as vehicles for delivery of drugs or cells to the subretinal space.<sup>19,156,296-300</sup> Most implanted materials are tested for material or chemical biocompatibility (which is clearly an essential property of an implanted polymer) prior to implantation using *in vitro* culture techniques. However, the mechanical properties of material also play an important role in the ultimate compatibility, efficacy and outcome of the implant *in vivo*. To overcome potential rejection issues and for stimulation of optimal cellular differentiation and transplant integration, it is generally believed that the mechanical properties of an implanted material should match those of the recipient tissue as closely as possible. Thus, directing stem cell differentiation and cellular proliferation with mechanical cues<sup>146,147</sup> has long been utilized for generating cartilage<sup>148</sup> and bone.<sup>149</sup> More recently this concept has also been applied to materials meant to regenerate softer tissues such as tendons,<sup>150</sup> cardiac valves,<sup>151</sup> cardiac muscles,<sup>152,153</sup> and neurons.<sup>154,155</sup> In

order to obtain an optimal match between implant and native tissue, therefore, the mechanical properties of the native tissue need to be thoroughly characterized in normal and diseased states.

Although some mechanical properties of the retina were described as early as 1987,<sup>301</sup> the extremely delicate nature of this neural tissue has limited the extent of its characterization. Attaching retinal samples to displacement probes, for example, is a commonly reported challenge, originally overcome by using synthetic adhesive to bind the retina to the probes. More recent work has addressed this challenge by using mechanical pressure to tightly clamp samples to analysis probes,<sup>159,301</sup> leading to examination of retinal mechanical properties of the retina using uniaxial tension. Some insight into the pathophysiology of retinal tearing was gained following these analyses. For instance, the retina was found to have a relatively short (compared to the choroid) reversible elastic phase followed by a large irreversible plastic deformation.<sup>302</sup> From these stress and strain studies, the tensile modulus of the retina was estimated to be about 100 kiloPascals (kPa).<sup>303,304</sup>

As described, the mechanical properties of the retina have been characterized thus far using tension applied parallel to the isotropic retinal plane (Figure 15B). Given the layered nature of the retina, however, mechanical properties are not likely to be the same if characterized using compression perpendicular to the isotropic plane of the retina (Figure 15C). For the purpose of developing cell delivery scaffolds, the transverse compressive mechanical properties are a better representation of actual mechanical pressures encountered by cells and tissues during chronic implantation. In this study, the compressive modulus of porcine and murine ocular tissues was examined. The effects of aging and disease on the murine retinal compressive modulus were also characterized. In an effort to begin to identify mechanically appropriate materials for retinal differentiation and transplantation, the transverse compressive modulus values for retinal tissue were compared to relevant synthetic materials.

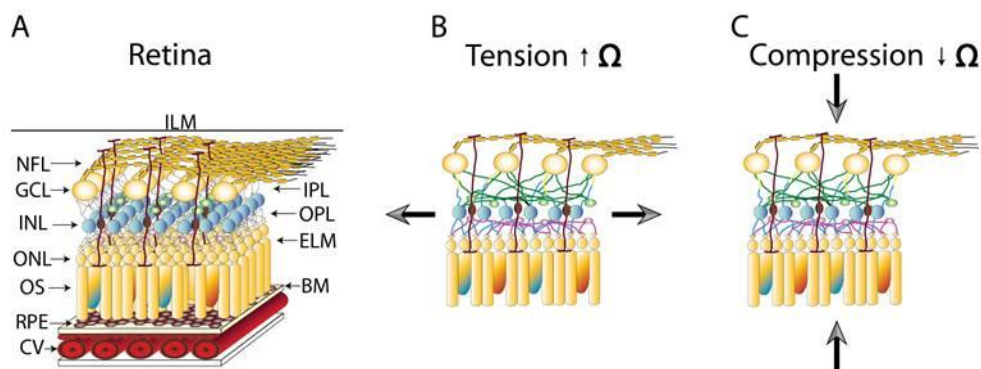


Figure 15. Schematic of the retina (A) under tension (B) and compression (C) showing directionality of forces.

## Materials and Methods

### Animals and Dissection

For testing of mouse retinal modulus, C57Bl/6J were used as a *wild type* control line (stock number 000664; Jackson Laboratories, Bar Harbor, ME). To test the effect of retinal degeneration on mouse retinal modulus we used the mutant line C3H/HeJ<sup>Pde6rd1</sup> (stock number 000659; Jackson Labs), which develops rapid retinal degeneration due to rod photoreceptor cell death. Mice were euthanized using CO<sub>2</sub> inhalation, followed by cervical dislocation. Eyes were enucleated and the anterior segment was removed by carefully cutting around the circumference of the eye along the limbus. Once exposed, the lens and vitreous were removed, leaving the posterior cup consisting of the retina, choroid and sclera. Retinas were then carefully separated and maintained in their natural cup-like form with the cupped portion open, facing up in the sample basin. The edges of the retinal cup were then teased out to their most extreme limit without damaging the sample. Each mouse retina measured was treated identically. During compression, the retina flattened, with a very small amount of, if any, tissue remaining folded over the edge around the retina. It should be noted that this small extra layer of tissue may have

artificially increased the observed modulus slightly. As cutting the retina in the traditional cloverleaf pattern introduced a high degree of inconsistency, this method was not chosen. Pig eyes (Iowa outbred swine, 5 months of age) were obtained from a local slaughterhouse, transported on ice and dissected within two hours of harvest. Whole pig globes were processed in the same manner as mouse eyes above, except the retina was not removed from the choroid. Instead, a 5mm biopsy punch was used to cut out retinal samples for modulus testing, which were then separated from the choroid and other layers. A biopsy punch was also used to isolate specimens of cornea, choroid and sclera for testing. Prior to modulus measurements, all tissues were maintained in 1X Hank's buffered salt solution (HBSS, 340 mOsm/L, Sigma-Aldrich, St. Louis, MO).

### Polymers

Polydimethylsiloxane (PDMS, SYLGARD® 184 silicone elastomer kit, Dow Corning, Midland, MI) samples were formed using a 10:1 ratio of base to cross-linker. The blend was mixed by vortexing, poured into a petri dish, and cured in an oven for two days at 50 °C. The soft cross-linked poly(ethylene glycol) (PEG) samples were formed using 22.5 weight percent (wt%) PEG dimethacrylate (PEGDMA, MW 875, Sigma-Aldrich, St. Louis, MO), 22.5 wt% PEG methacrylate (PEGMA, MW 500, Sigma-Aldrich) and 0.1 wt% photoinitiator (Irgacure-651, Ciba Specialty Chemicals, Tarrytown, NY), in HBSS. The stiff cross-linked PEG samples were formed using 55 wt% PEGDMA, 22.5 wt% PEGMA, and 0.1 wt% photoinitiator in HBSS. These mixtures were vortexed and then photopolymerized with 365 nm light for 10 minutes in a laminate glass mold. Many other crosslinked PEG formulations with varying composition were prepared in the same manner to further demonstrate the flexibility of using polymeric materials. To prepare the gelatin samples, 4 grams (g) of gelatin crystals (Knox original unflavored gelatin) were mixed with 29 mL of cold HBSS. Boiling HBSS (88 mL) was added to this mixture, and the resulting solution was stirred to homogeneity, poured into a

petri dish, and refrigerated for 24 hours. All polymers were stored in HBSS for two days at room temperature, after which disks from each polymer species were punched with a 5 mm biopsy punch.

### Stress and Strain Measurement

The mechanical properties of all samples were measured using a dynamic mechanical analysis instrument (DMA Q800 V7.0 Build 113, TA Instruments, New Castle, DE) equipped with a submersion compression clamp in static mode. Prior to each group of measurements, the drive shaft position, clamp mass, clamp offset, and clamp compliance were calibrated according to suggested protocols. Each sample was carefully transferred to the basin of the clamp either in HBSS using a wide-tipped Pasteur pipette (for soft tissue samples, Figure 16A and B) or carefully with forceps (for polymer, cornea, and sclera samples). Any excess water or buffer surrounding the sample was removed using a syringe. Once the sample was installed, the top portion of the clamp was gently lowered onto the sample surface, the furnace was closed to maintain constant temperature and prevent disturbances, and a pre-load force of 0.0001 N was applied to the sample. The force was then gradually increased to a final value of 0.2 N at a rate of 0.02 N/min and displacement data were collected every 2 seconds as the sample (which was not confined) was compressed. Crosslinked PEG samples were measured in a fully hydrated state as per the method used for other samples, and also in a semi-hydrated state after initial compression, at which time most liquid had escaped the crosslinked network. All samples were assumed to be cylindrical with a diameter of 5 mm, except the whole mouse retinas, which had a diameter of 3 mm. All retinal thicknesses (mouse and pig) were estimated based on histology (data not shown), while the thicknesses of polymer and more robust tissue samples were measured using the initial displacement of the clamp before testing began. Sample thicknesses are provided in Table 4-Table 6.

### Data Analysis

From the recorded displacement (reported in  $\mu\text{m}$ ) and static force (reported in N) values, the infinitesimal strain ( $\epsilon$ ) and stress ( $\sigma$ ) were calculated as follows:

$$\epsilon = \frac{D - D_0}{z} \quad (6)$$

$$\sigma = \frac{C * F}{A} \quad (7)$$

where D is displacement,  $D_0$  is initial displacement (which accounts for any changes brought about by the initial pre-load force), z is the sample thickness, F is static force, A is sample cross-sectional area, and C is a necessary correction factor provided by the instrument manufacturer based on sample geometry.

Modulus is defined as the ratio of stress increase to strain increase in the elastic deformation region. Values of stress at absolute strain values between 0 and 0.1 (0% and 10% deformation) were plotted and the slope estimated using a trend line function. Although most samples exhibited non-linear behavior overall, linear behavior was typically observed at low compressive strain, as expected. A few samples, however, exhibited non-linear behavior in the 0 to 0.1 strain range, likely due to unusually low ultimate yield strains (premature retinal tearing or breakage) in some cases, or measurement errors associated with the instrument in others. Because the stress/strain behavior in the specified range was not linear for these samples, they were not included in the final analysis. The total number of samples in each group and the number of samples used in the analysis are given in Table 4-Table 6.

### Statistics

Modulus data were analyzed for significance using one-way analysis of variance followed by Tukey's multiple comparison tests. Differences were considered significant at  $p\text{-value} < 0.05$ . Statistically significant outliers were rejected if identified using a Q test



with 95% confidence limits. Cross-linked PEG moduli were predicted for a range of formulations based on a three-component mixture design (DesignExpert 9.0.0.7, StatEase Inc., Minneapolis, MN) with design points at each vertex ( $n = 3$ ), at each axis third ( $n = 3$ ), the overall centroid ( $n = 3$ ), and at three internal check blends ( $n = 6$ ) for a total of 13 design points and 48 measurements.

### Results

Accurately determining the compressive modulus of the retina lays the groundwork for the future design of polymer based cell delivery scaffolds. We began by studying eye tissues isolated from swine, which are structurally similar to analogous human tissues. To test compressive moduli, 5mm biopsy punches of the retina, and (for comparison purposes) the retinal pigment epithelium (RPE)/choroid, sclera, and cornea were placed in a submersion compression clamp connected to a dynamic mechanical analysis instrument (which was employed here in static mode). As shown in Figure 16A and B, samples were positioned in the center of the clamp basin and excess fluid was carefully removed. Following proper positioning, an increasing amount of stress was applied and the resulting strain recorded; both of which were used to calculate the modulus. As shown in Figure 16C, of the tissues tested, the highest modulus recorded corresponded to the sclera at  $35.1 \pm 3.4$  kPa. This finding was not surprising considering the fact that this tissue is largely composed of irregularly layered collagen fibrils. The cornea, which is nearly uniform in thickness and largely constructed of perfectly parallel collagen fibrils, exhibited a modulus 25% lower than that of the sclera ( $25.0 \pm 0.9$  kPa). The retina, which is primarily composed of neurons and their axons, had a modulus 63% lower than that of the cornea ( $10.5 \pm 2.67$  kPa). Lastly, the choroid and RPE combined (a loose vascular connective tissue and neuroepithelial monolayer) had a modulus more than 40% lower than even that of the retina. ( $5.4 \pm 0.74$  kPa).

Table 4. Sample size, mean, standard error of the mean, and average or estimated thickness for each group of porcine tissue samples.

	Sclera	Cornea	Retina	Choroid/RPE
N	5	9 <sup>†</sup>	17	5
Mean (kPa)	35.1	25.0	10.5	5.4
S.E.M. (kPa)	3.38	0.91	2.67	0.74
z (mm)	1.78 <sup>§</sup>	2.56	0.30 <sup>‡</sup>	-

<sup>†</sup>One statistical outlier was removed prior to analysis

<sup>‡</sup>Based on histological measurements

<sup>§</sup>Sclera, choroid, and RPE were measured together

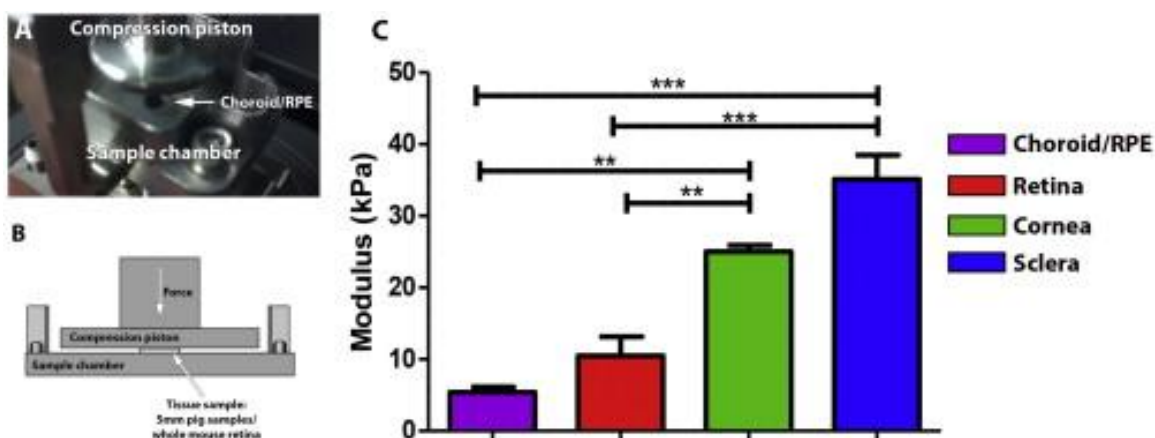


Figure 16. Mechanical analysis of eye tissues in compression. 5 mm circular punches of the RPE/Choroid (A) are shown in the DMA compression clamp. B: A schematic diagram depicting the compression paradigm/tissue instrument interaction. The mean compressive modulus (C) of porcine corneal and sclera tissue is greater than that of retinal tissue, while the modulus of choroid with retinal pigment epithelium (RPE) is slightly lower. Error bars represent standard error of the mean, \*\* $p < 0.01$ , \*\*\* $p < 0.001$ .

In addition to determining the compressive modulus of the retina of swine, we sought to determine the effects of both aging and retinal degenerative disease on retinal mechanical integrity. For these studies, wild type C57BL/6J and mutant C3H/HeJ<sup>Pde6rd1</sup> mouse retinas were used. As shown in Figure 17 (solid markers), the retinal compressive moduli of wild type C57BL/6J mice does not change significantly from initial values

obtained at 5 weeks. This relatively constant modulus is sustained for up to 36 weeks of age. Based on these results, the retinal modulus remains relatively stable under normal aging conditions.

Due to the aggressive nature of the retinal degeneration observed in the C3H/HeJ<sup>Pde6rdl</sup> mouse, i.e. significant degeneration observed by 3 weeks of age, these animals were studied immediately post-weaning and at 6 and 12 weeks of age. Unlike wild type mice, the retinal compressive moduli of the C3H/HeJ<sup>Pde6rdl</sup> mouse decreased from initial recordings taken at 3 weeks of age (Figure 17, open markers). By 12 weeks of age, a time in which the C3H/HeJ<sup>Pde6rdl</sup> mice have little to no outer nuclear layer remaining, the retinal modulus was much lower than the previous time point (Figure 17, open markers). Furthermore, the mean modulus of 12-week-old C3H/HeJ<sup>Pde6rdl</sup> retina was reduced by more than 90% compared to the *wild type* C57BL6 mouse at a similar age ( $p < 0.05$ ). These results demonstrate that retinal degenerative disease significantly affects the mechanical properties of the retina.

Table 5. Sample size before and after outlier and aberrant data rejection, mean, standard error of the mean, and estimated thickness for each group of murine retina samples

	Wild Type (BL6)				Degenerate (C3H)		
	5 wks	13 wks	24 wks	36 wks	3 wks	6 wks	11 wks
N	6	5	5	6	9 <sup>†</sup>	6	6
Mean (kPa)	17.3	27.6	17.3	18.3	8.8	9.9	1.8
S.E.M. (kPa)	4.29	9.38	7.47	1.67	2.29	4.16	0.33
z (μm)	225 <sup>‡</sup>	225 <sup>‡</sup>	225 <sup>‡</sup>	225 <sup>‡</sup>	180 <sup>‡</sup>	150 <sup>‡</sup>	100 <sup>‡</sup>

<sup>†</sup>One statistical outlier was removed prior to analysis

<sup>‡</sup>Based on histological measurements

As the ultimate goal of determining retinal modulus is to guide the future design of polymer based cell delivery scaffolds, we next attempted to determine the compressive modulus of a set of polymer materials generated in our lab. The materials chosen

(PDMS, crosslinked PEG, and gelatin) were selected based upon their biocompatibility and their previous use in the eye.<sup>34,36,90,93,249</sup> Furthermore, as a group these materials cover a wide spectrum of mechanical properties relevant to biomaterials. The compressive modulus of each polymer is shown in Figure 18. PDMS had the highest modulus ( $380 \pm 16$  kPa), followed by stiff crosslinked PEG ( $309 \pm 24$  kPa), soft crosslinked PEG ( $24.9 \pm 6.8$  kPa) and gelatin ( $2.99 \pm 0.68$  kPa). These measured values correspond well with previously reported compressive moduli for the same or similar formulations of each polymer.<sup>221,305,306</sup> Of these polymers, the soft cross-linked PEG and gelatin most closely matched the range of moduli identified for the neural retina. However, it is important to note that the mechanical properties of all three materials can be modified by changing molecular weight and crosslinking density, as demonstrated for cross-linked PEG (data not shown). Thus, each material has the potential to be used for future cell delivery applications.

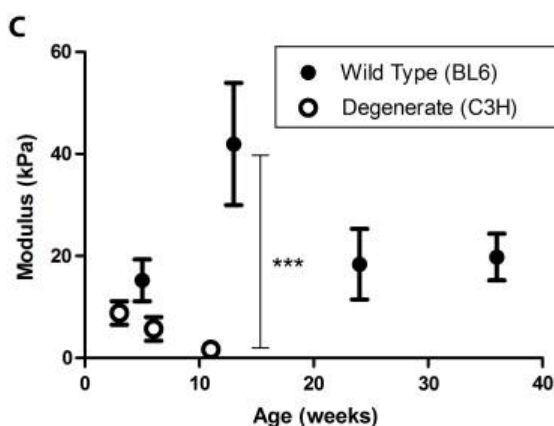
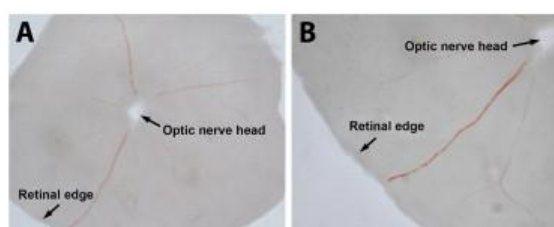


Figure 17. Moduli of whole mouse retinas at different ages and disease states. A–B: Exemplary whole mouse retina that has been dissected free of the optic cup, placed photoreceptor side down and prepared for compression analysis. As liquid is removed surface tension allows the dissected retina to lay flat (A), edges of the retinal cup are gently teased out to their most extreme limit taking care not to disrupt tissue integrity (B). C: Analysis of the development and degeneration of mouse retina mechanical properties demonstrate that the compressive modulus of mouse retina stays relatively constant in the range of ages examined (wild type C57BL/6J) but rapidly deteriorates with mutation-induced degeneration (C3H/HeJ<sup>Pde6rd1</sup>). Error bars represent standard error of the mean, \*\*\*p < 0.001.

Table 6. Sample size, mean, standard error of the mean, and average thickness for each group of polymer samples.

	Gelatin	Soft PEG	Stiff PEG	PDMS
N <sub>Analyzed</sub>	4 <sup>†</sup>	6	6	4 <sup>†</sup>
Mean (kPa)	2.99	24.9	308.5	379.6
S.E.M. (kPa)	0.68	6.84	23.86	15.74
z (mm)	0.39	1.18	1.22	1.61

<sup>†</sup>One statistical outlier was removed prior to analysis

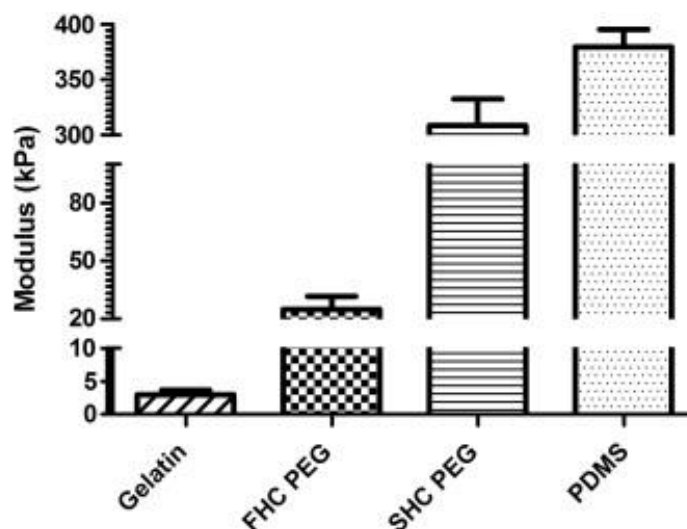


Figure 18. Compressive modulus of various polymers. The compressive modulus of gelatin and fully-hydrated crosslinked PEG (FHC PEG) most closely approximate the transverse compressive modulus observed for healthy retinas, where semi-hydrated crosslinked PEG (SHC PEG) and fully hydrated PDMS moduli are much higher. Error bars represent standard error of the mean.

### Discussion

Since the development of the first intraocular lens (See Moore et al. 2011<sup>307</sup> for a discussion of the first poly(methyl methacrylate)-based Ridley lens), the use of polymer based materials for the treatment of blinding eye diseases has been widely studied. To date a variety of different polymer materials, both biodegradable and non-biodegradable, have been used in the eye for applications ranging from retinal stimulation to drug/cell delivery. For example, biodegradable poly(lactic-co-glycolic acid) (PLGA) microspheres have been shown to be well tolerated and to maintain their ability to provide sustained release of incorporated drug following intravitreal injection.<sup>20,308,309</sup> When used for cell delivery, PLGA based scaffolds have been shown to increase the survival and integrative capacity of retinal stem cells following transplantation.<sup>19,117</sup> As a strategy to treat age related macular degeneration, non-degradable parylene-C based films have been used as a vehicle for the delivery of stem cell derived RPE cells.<sup>156,246,247</sup> In comparison to bolus

RPE cell injections, delivery of RPE cells on parylene-C scaffolds drastically increased donor cell survival and viability following transplantation.<sup>156</sup>

Despite these encouraging results, none of these polymers are well tolerated by the host retina.<sup>19,156</sup> In the case of the electrospun PLGA systems, the negative effects observed could in large part be explained by the inherent rigidity of the scaffold and its mechanical incongruity with the remaining host retinal tissue,<sup>19,117</sup> resulting in injury to the delicate retinal neurons. These findings point to the need for newly developed polymer systems to more closely mimic the physical properties of the native tissue in which they will eventually be placed. Achieving material biomimicry is not only important for permanent implantation, but also in situations where the role of the polymer is to enhance cellular differentiation and development *in vitro*.

To date, the majority of published studies have focused on determining the structural properties of the retina in the horizontal dimension, i.e., perpendicular to the path of light in the living tissue. In one such uniaxial tension study, Chen and coworkers found the modulus of the retina to be approximately 100 kPa, while that of the choroid and sclera were about 2.4 megaPascals (MPa) and 16.6 MPa, respectively.<sup>158</sup> They also found that the direction in which the sample was cut significantly affected the tensile modulus.<sup>158</sup> In a later study, these and similar differences were shown to be attributed to the presence and size of blood vessels in the tissue.<sup>159</sup> Although mechanical properties can be uniform with respect to direction for most synthetic materials, this isotropy does not translate to complex anisotropic biological tissues, especially those that are layered, such as the retina. Rather, a compressive force applied to the surface of the retina will deform the structures within and between the synaptic and nuclear layers in a much different way than a force applied along the length of the layers. For the purpose of developing cell delivery scaffolds, this transverse compressive stress and strain behavior would appear to be a better representation of the actual mechanical pressures encountered during chronic implantation, i.e. the pressure generated by placing a foreign material into

the subretinal space is of a compressive nature rather than a tensile or shear force. Likewise, the modulus of the polymer or tissue that a developing or transplanted cell will perceive is more similar to that obtained under a transverse compressive rather than a uniaxial tensile force. As suspected, in the current study, the modulus of the retina was found to be much lower than those obtained in a lateral direction. As indicated above, this difference is likely due to interconnectivity of the plexiform layers, the nerve fiber layer, the vascular system and the inner and outer limiting membranes.

In summary, this study helps lay the foundation for appropriate material selection and modulation for applications involving retinal cell differentiation and retinal transplantation.



## CHAPTER 6

### PHYSICAL AND BIOCHEMICAL PROPERTIES OF SURFACTANT TEMPLATED POLY(ETHYLENE GLYCOL) DIMETHACRYLATE

#### Introduction

In recent years the fabrication of polymeric materials containing order on the sub-micron scale has captured a great deal of research attention. Because a wide range of properties of polymers are enabled based on monomer selection and processing techniques, their applications are far reaching, including tissue scaffolds, sensors, solar cells, electronics, and separation membranes, to name a few.<sup>175-179</sup> In each of these applications, nanometer sized structures can enhance the performance of the materials. For example, enhanced transport and mechanical properties, as facilitated by nanometer-sized features of polymer networks, can increase the rate and degree of response to changes in external conditions for stimuli-sensitive polymers.<sup>181</sup> Furthermore, property changes can enhance the separation efficiency of polymeric membranes<sup>182</sup> or the rate of drug release<sup>183</sup> compared to polymer systems that do not contain ordered nanostructures. These dramatic improvements in functionality potentially give nanostructured polymers a broader range of utility in advanced applications than their isotropic analogs.

One promising method of controlling polymer nanostructure uses self-assembling surfactant systems as polymerization templates to direct polymer morphology. This templating process has been utilized to generate nanostructure in a number of polymer systems, resulting in polymers that contain useful property relationships that are often not observed in traditional or isotropic polymer systems.<sup>181,216-221</sup> Organized surfactant molecules can be used to control polymer nanostructure by serving as polymerization templates. In this method, the water- and oil-soluble domains that are inherent in the system are used to segregate monomers. Figure 19 shows a representative fabrication scheme that utilizes self- assembled surfactants as polymerization platforms to generate

nanostructured polymer networks. If a photocurable polar monomer such as poly(ethylene glycol) dimethacrylate (PEGDMA) is incorporated into the LLC phase, the monomer will preferentially segregate in the water soluble domains of the parent template and adopt a geometry that directly resembles that of the self-assembled phase.<sup>228</sup> Photopolymerization can then be utilized to cure the monomer/LLC formulation and transfer the order of the parent template to the polymer system.

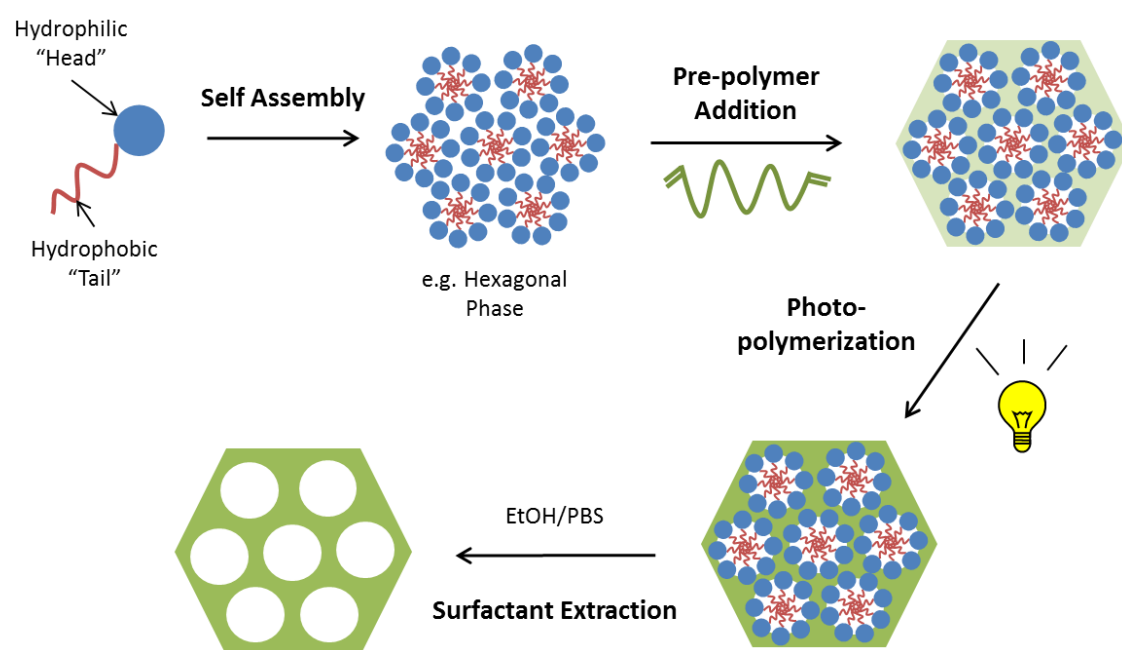


Figure 19. Schematic of the process of templating crosslinked PEG with surfactants

Despite the positive results in using this method to generate ordered polymers with improved physical properties, little is known about how the induced order affects material interactions with biological systems. Furthermore, the process used to obtain this order utilizes surfactants, most of which are toxic *in vitro* and *in vivo* at or below their critical micelle concentrations.<sup>310–321</sup> Although a few studies have demonstrated biocompatibility of surfactant templated copolymers of poly(lactic acid) (PLA) and PEG

without closely examining residual surfactant and its effects,<sup>174,180</sup> a more thorough understanding of how surfactant templating affects cell adhesion, proliferation, and differentiation, could provide opportunity for much needed improvements to biomaterials for a range of applications. For example, for the case of biosensor coatings or drug delivery devices, it may be desirable to use a material that is non-adherent (anti-fouling) and has high diffusivity. Typically, however, traditional polymers used for anti-fouling coatings, such as poly(dimethyl siloxane) (PDMS) and poly (ethylene sulfone) (PES) are relatively hydrophobic.<sup>322–325</sup> PEG, however, has a unique ability to repel protein and bacterial adhesion while maintaining some degree of hydrophilicity.<sup>326–328</sup> If the order and thus diffusional capabilities and mechanical properties, could be further enhanced or controlled, the application of anti-adhesion PEG materials could be increased. Understanding the relationship between physical and biochemical properties will help to improve these and other materials and is a necessary step for integrating surfactant templating into future biomaterial fabrication processes for other applications.

Using crosslinked PEG as a model system, we explore the effect of surfactant templating on final polymer properties in this work. Physical properties, including morphology, water uptake and compressive modulus can be tuned using this technique. Herein we aim to understand how physical properties change in relation to biochemical properties such as toxicity and bioadhesion. The equilibrium water uptake and compressive modulus, both of which play important roles in biomaterial performance, were measured for templated and non-templated crosslinked PEG. Furthermore, we explore how the templating process affects biochemical properties by measuring viability of cells exposed to material extracts and cell adhesion to material surfaces.

## Materials and Methods

### Sample Preparation

PEG dimethacrylate (PEGDMA,  $M_n$  875, Sigma-Aldrich, St. Louis, MO) was templated prior to polymerization using three surfactants: the non-ionic polyoxyethylene (23) lauryl ether (Brij 30, Sigma-Aldrich), cationic dodecyl trimethylammonium bromide (DTAB, Sigma-Aldrich), and anionic sodium dodecyl sulfate (SDS, Research Products International, Mount Prospect, IL), all with the same hydrocarbon chain length (structures shown in Figure 20). Briefly, 50 wt% PEGDMA was mixed in a glass vial with 30 wt% surfactant, 19.9 wt% distilled water and 0.1 wt% photoinitiator (Irgacure 651, BASF, Florham Park, NJ) to homogeneity by vortexing and gentle heating. In the case of non-templated (isotropic) samples, the 30 wt% surfactant was replaced with water. A small amount of each mixture was loaded into a laminate glass mold using a Pasteur pipette and capillary action. Each mixture was polymerized in the mold by exposure to UV light (365 nm, 4 mW/cm<sup>2</sup>) for 10 minutes. The glass mold was then deconstructed and the resulting 1 mm film carefully removed. Finally, 5 mm and 8 mm biopsy punches were used to cut multiple circular punches from each film.

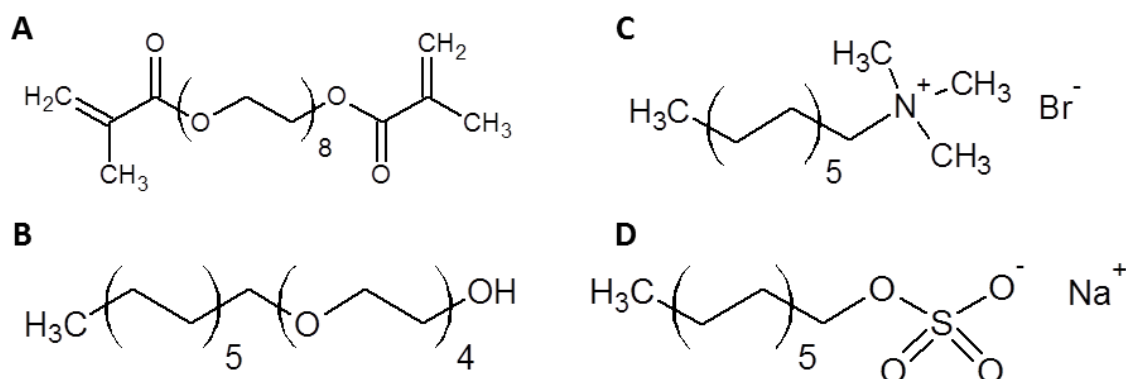


Figure 20. Chemical structures of A) PEGDMA 875, B) Brij 30, C) DTAB, and D) SDS

### Diffraction Studies

To examine the structure of templated PEG samples, small angle x-ray scattering (SAXS) and polarized light microscopy (PLM) were employed. For SAXS, a small amount of pre-polymerized mixture was placed in the instrument sample holder between two pieces of Mylar film. Samples were analyzed using a Nonius FR590 SAXS apparatus equipped with a standard Röntgen tube with a Ni-filtered Cu K $\alpha$  line of 1.54 Å as the radiation source at an intensity of 35 kV and 20 mA, a Kratky type collimation system, and a PSD 50M position-sensitive linear detector (Hecus M. Braun, Gras, Austria). Each sample was then polymerized, in the holder, as described above, and a second profile was collected using the same settings as before polymerization. To further examine structure, a small amount of pre-polymerized sample was placed between a glass slide and cover slip and examined using PLM (Eclipse E600 POL, Nikon Instruments Inc., Melville, NY).

### Morphology

After seven days of surfactant extraction in acetone, samples were frozen by submersion in liquid nitrogen and quickly fractured. The fractured samples were freeze-dried overnight, then prepared for SEM analysis. Briefly, samples were mounted to an aluminum stub using colloidal silver with the fractured edge facing up. Samples were coated with a gold-palladium mixture using an argon beam sputter coater (K550, Emitech Ltd., Kent, England). SEM images were collected using a Hitachi S-4800 (Hitachi High-Technologies, Ontario, Canada) at an accelerating voltage of 4 kV.

### Physical Properties

The effect of surfactant templating on physical properties was examined using both water uptake and compressive modulus. After surfactant extraction, 8mm disks were transferred to excess PBS for three days to reach equilibrium swelling. Samples were

then removed from the liquid, patted dry, and weighed. After drying overnight, the samples were weighed again. The water uptake was calculated as follows:

$$\text{WaterUptake}(\%) = 100 \times \left( \frac{W_w - W_D}{W_D} \right) \quad (8)$$

where  $W_w$  and  $W_D$  represent the weight of the sample when wet and dry, respectively.

The compressive modulus was measured using a dynamic mechanical analysis instrument (DMA Q800 V7.0 Build 113, TA Instruments, New Castle, DE) equipped with a submersion compression clamp in static mode. Prior to each group of measurements, the drive shaft position, clamp mass, clamp offset, and clamp compliance were calibrated according to suggested protocols. Fully hydrated 8 mm samples were carefully placed in the center of the basin. Once the sample was installed, the top portion of the clamp was gently lowered onto the sample surface, the furnace was closed to maintain constant temperature and prevent disturbances, and a pre-load force of 0.0001 N was applied to the sample. The force was then gradually increased to a final value of 0.2 N at a rate of 0.02 N/min and displacement data were collected every 2 seconds as the sample was compressed. All samples were assumed to be cylindrical with a diameter of 8 mm. Thickness was measured using the initial displacement of the clamp before testing began.

### Surfactant Extraction

Directly after being polymerized and punched, 5 mm samples were transferred to excess extraction solvent, later exchanged on Days 1 and 3 of the study. Three solvents were examined for their ability to extract surfactant: ethanol, acetone, and a 50/50 blend of ethanol and phosphate buffered saline (PBS). Extraction of surfactant over time was examined gravimetrically. Briefly, at the desired time point, samples were removed from the extraction solvent, dried overnight in a vacuum oven and weighed. This weight was

compared to the weight of samples dried directly after polymerization to obtain a measure of surfactant removal (% initial dry weight).

The effect of surfactant removal was also measured qualitatively using the cellular toxicity of leaching products. After seven days of surfactant extraction, the samples were washed three times (1 hr per wash) with excess PBS. Each 5 mm diameter sample was then incubated in 200  $\mu$ L cell culture media (see below) overnight at 37 °C. The following day, 150  $\mu$ L of this conditioned media was used to feed cells growing in a corresponding 96-well plate.

### Cell Culture and Toxicity

Fibroblasts were isolated from dsRed mouse umbilical cord and de-differentiated using a retroviral approach to yield murine induced pluripotent stem cells (MiPSCs), as described elsewhere.<sup>21,248</sup> For this study, MiPSCs were gently thawed from a frozen stock, centrifuged, and resuspended in MiPS media [Dulbecco's Modified Eagle Media with F12 (Gibco, Grand Island, NY) supplemented with 15% fetal bovine serum, 1% 100X non-essential amino acids (Gibco), 1% L-glutamine (Gibco), 1% Primocin (Gibco), and 8 nL/mL  $\beta$ -mercaptoethanol (Sigma-Aldrich)] then plated in a 6-well plate pre-coated with Matrigel (Growth factor reduced basement membrane matrix, Corning, Tewksbury, MA) and kept in a humidified, 37 °C incubator with 5% CO<sub>2</sub>. Media was replaced daily and cells were divided and re-plated every two days until needed.

One day prior to the desired toxicity time point, cells were removed from the 6-well plate using 0.25% trypsin with EDTA (Gibco), centrifuged, and resuspended in MiPS media. A Matrigel pre-coated 96-well plate was then seeded with MiPSCs at a concentration of 10,000 cells per well and incubated overnight before being fed conditioned media. The viability of cells was measured one day after the conditioned media feeding.

The effect of conditioned media on the viability of MiPSCs was measured using a colorimetric MTT assay. This assay correlates cell viability to the activity of NADPH-dependent cellular oxidoreductase enzyme, which reduces the tetrazolium dye MTT [3-(4,5-dimethylthiazol-2-yl)-2,5-diphenyltetrazolium bromide] to its purple, insoluble formazan. Conditioned media was replaced with 100  $\mu$ L fresh media and 10  $\mu$ L MTT reagent (Millipore, Billerica, MA), then the plate was incubated at cell culture conditions for four hours. All liquid was then removed from the wells, leaving behind insoluble purple crystals. To dissolve crystals, 100  $\mu$ L development solution (0.04 M HCl in isopropanol) was added to each well and mixed well until all crystals had dissolved. The color intensity was then measured using the absorbance at 570 nm (Tecan Infinite M200 Pro, Tecan Group Ltd., Männedorf, Switzerland). To calculate relative viability, each well was compared to a set of control wells wherein the cells were not exposed to conditioned media.

For attachment studies, 5 mm diameter samples (after surfactant removal and swelling in PBS) were transferred to a 96-well plate and coated with 200  $\mu$ L Matrigel solution for one hour. Meanwhile, cells were removed from their plate and re-suspended as described above. Each 5 mm sample was seeded with 15,000 MiPSCs and the 96-well plate was placed in the incubator. Media was carefully exchanged daily until seven days post-seeding.

## Results and Discussion

### Diffraction

Even though hydrophobic chain length is the same for all surfactant templates studied, SAXS suggests that only the ionic surfactants impart nanostructure on the final PEG material. As seen in Figure 21A, both the isotropic sample and the sample templated with Brij 30 have smooth SAXS profiles, indicating a lack of nanostructure. In both cases there no change after polymerization is observed. Conversely, the sample templated with



DTAB has SAXS scattering peaks at 2 and 3 nm<sup>-1</sup>, indicating the presence of nanostructure. Typically some structure is lost during polymerization, resulting in decreases in scattering intensity as mixture components move to more favorable, aggregated domains. The DTAB sample structure, however, appears to be stabilized to some degree by the polymerization reaction, as during polymerization the 3 nm<sup>-1</sup> peak diminishes significantly, but the primary 2 nm<sup>-1</sup> peak increases in intensity and shifts slightly to a lower scattering angle. Strong evidence of nanostructure is also observed in the SDS templated sample, as witnessed by the three peaks between 1 and 2 nm<sup>-1</sup> and one peak at 3.3 nm<sup>-1</sup>. As expected, these scattering peaks decrease in intensity during polymerization with some disappearing completely. Although well-ordered systems can be categorized by the ratio of scattering angles observed using SAXS, neither of these samples have the necessary well-ordered characteristics to index to a specific nanostructure. This inability to categorize the morphology is an indication that the structure is probably a mixture of different nanostructure geometries and may even contain some order on the micron scale.

The lack of nanostructure in the isotropic and Brij 30 templated samples is further corroborated by their lack of light birefringence when observed with PLM (data not shown). Samples templated with the two ionic surfactants, however, exhibit strong birefringence (Figure 21B-C). As with the SAXS evaluation, neither pattern exhibited by the two nanostructured samples provides enough information to adequately characterize the structure.

### Morphology and Physical Properties

The surfactant templating process described may also result in controlled changes in final polymer physical properties. This concept is demonstrated well by the noticeable changes in the morphology of crosslinked PEG after being templated with various surfactants. As seen in Figure 22, even templating with Brij 30, which does not impart

measurable nanostructure to the final polymer, results in subtle changes in morphology. Compared to the isotropic polymer, the non-ionic surfactant templated sample (Figure 22B) did not fracture in a smooth manner and appears to have some roughness. Changes in morphology are even more pronounced for the ionic surfactant templated samples. In both cases, the crosslinked PEG is quite porous after being templated, with measureable pores (using this method) ranging from less than 500 nanometers to a few microns. In the case of DTAB templated PEG (Figure 22D), this porosity is much more homogenous than for SDS templated PEG, both in terms of pore size and distribution, resulting in a more consistent sample.

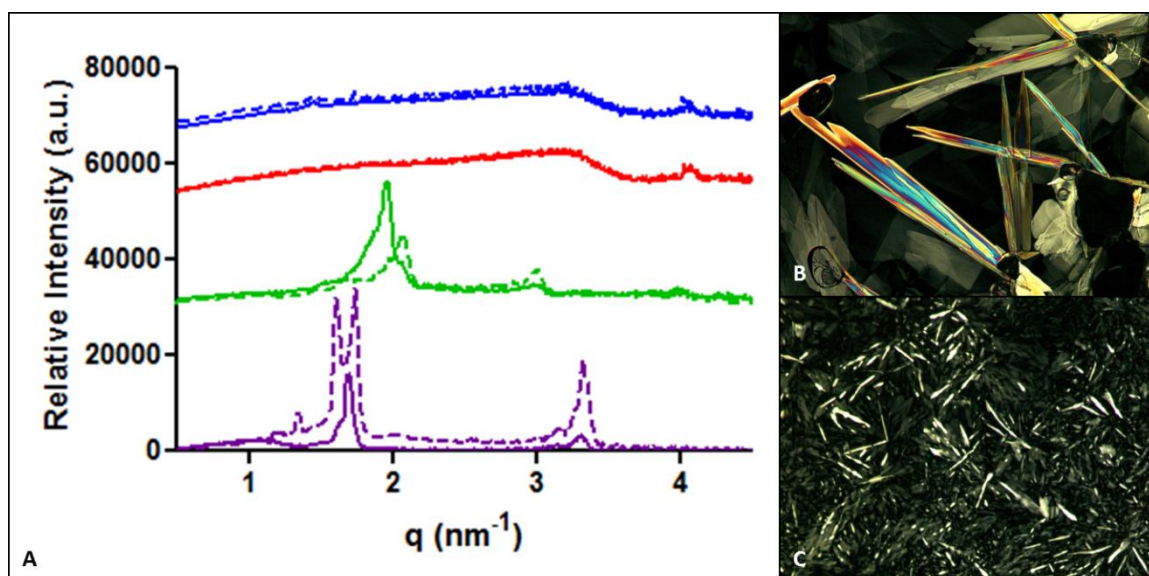


Figure 21. Small x-ray scattering (A) before (dotted lines) and after polymerization (solid lines) and polarized light microscopy (B-C) post-polymerization evaluation of nanostructure of PEG templated with no surfactant (blue), Brij 30 (red), DTAB (green), and SDS (purple).

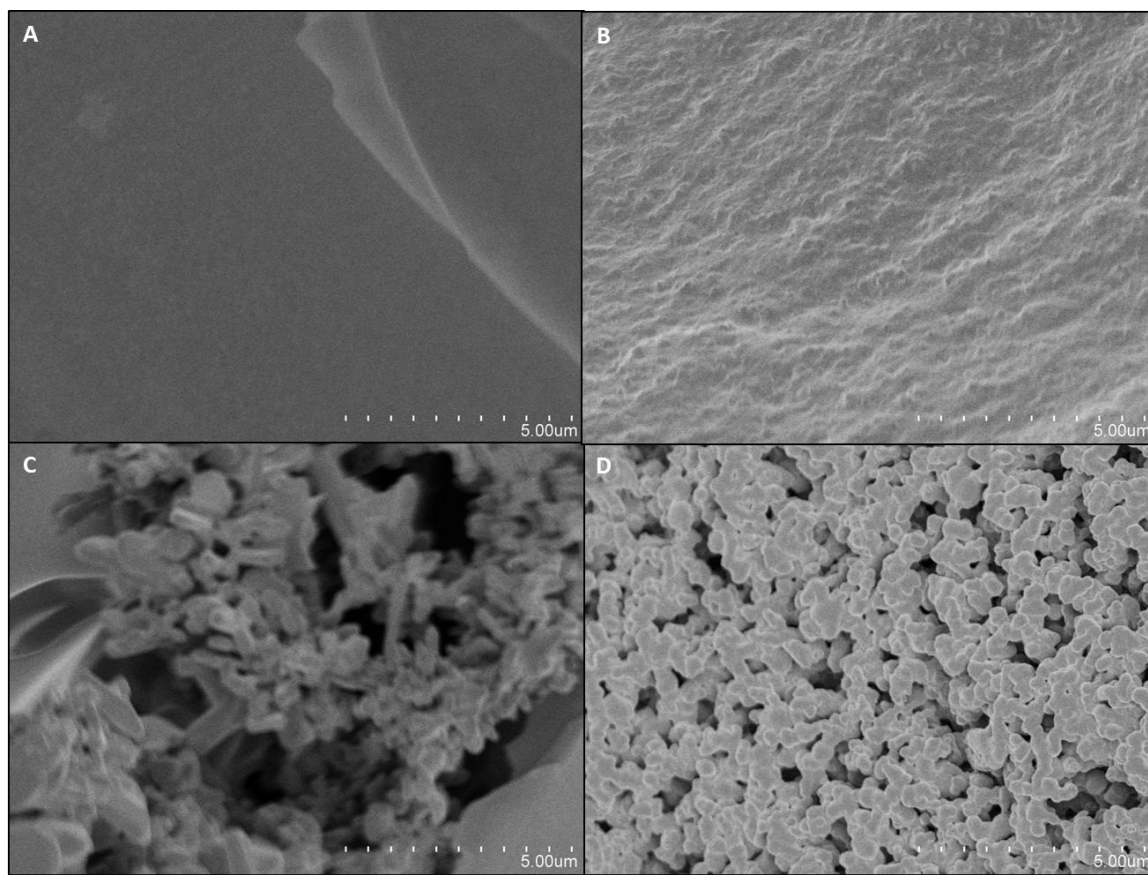


Figure 22. SEM images showing the morphology of PEG templated with no surfactant (A), Brij 30 (B), SDS (C), and DTAB (D).

The morphological differences described above are accompanied by changes in physical properties, including water uptake and compressive modulus. For biological applications, water uptake is an important consideration, as it directly relates to the diffusion of nutrients and cell signaling molecules, for example. The porosity imparted to crosslinked PEG via surfactant (i.e. DTAB) templating results in greater void spaces available for transport of water (or other molecules) into the polymer matrix. As seen in Figure 23A, this results in a significant ( $p < 0.01$ ) increase in water uptake compared to the isotropic PEG – the porous, DTAB templated PEG absorbs almost 50% more water than its non-templated counterpart. However, even though the Brij 30 templated sample

did not have any observable porosity or nanostructure, it absorbed significantly more water than both the isotropic ( $p < 0.001$ ) and the DTAB ( $p < 0.05$ ) templated samples. This is equivalent to a 70% increase in water uptake over the isotropic control. Because of its larger and more compatible hydrophilic head (compared with ionic surfactants), Brij 30, when present during the polymerization of PEG, decreases the ultimate crosslinking density by increasing the effective volume of the continuous phase. This results in larger spaces between PEG chains (although not as large as the pores seen for DTAB templated samples) and thus, greater opportunity for diffusion through the network.

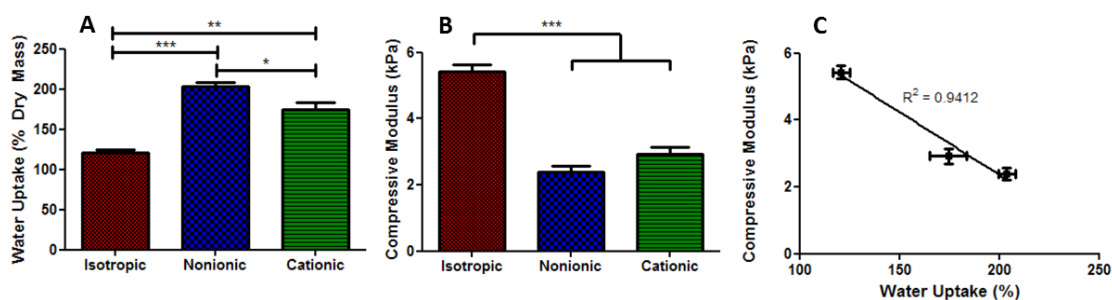


Figure 23. Water uptake (A) and compressive modulus (B) of PEG hydrogels templated with no surfactant (red), non-ionic surfactant (Brij 30, blue), and cationic surfactant (DTAB, green) are inversely correlated (C). Statistical significance was determined using two-way analysis of variance (ANOVA). \* $p < 0.05$ , \*\* $p < 0.01$ , \*\*\* $p < 0.001$

Generally, increases in water uptake are paired with decreases in compressive modulus. Figure 23B shows that, as expected, templating with either non-ionic (Brij 30) or cationic (DTAB) surfactant caused a significant decrease in compressive modulus ( $p < 0.001$ ). Although swollen PEG hydrogels are already quite soft (~5 kPa), this modulus, along with the water uptake, can be tuned by adding surfactant during polymerization. In fact the relationship between these two properties is fairly quantifiable (Figure 23C) with compressive modulus and water uptake inversely proportional with an  $R^2$  value of

0.9412. Because the templating process does not significantly change the final chemical composition of the material, it is an attractive option for tuning polymer properties without risking a change in biochemical behavior.

### Surfactant Extraction and Biocompatibility

Given potential toxicity of surfactant in biological systems, the degree of surfactant removal after the templating process is important to ascertain. As such, removal of surfactant was studied in order to identify best practices and better understand the removal process. In acetone, surfactant seems to be removed from crosslinked PEG samples relatively quickly when measured gravimetrically (e.g. Figure 24A). However, this method of tracking surfactant content is not very sensitive to very small amounts of surfactant, which can have a significant impact on biocompatibility. A better indication of surfactant removal is the toxicity of remaining components as they leach out of the sample. When using this measure, smaller differences between groups can be observed while gaining knowledge about how remaining components may affect cells, as seen in Figure 24B. For example, acetone appears to be a relatively poor extraction solvent compared to ethanol and its blend with PBS, although the differences are small for most surfactants. Furthermore, the cells exhibited an unexpectedly low viability on the isotropic sample in the acetone group, indicating that perhaps the PBS wash following surfactant extraction was not adequate for removing the solvent from the sample. It is also possible that this data point is simply an outlier, in which case little difference between extraction solvents can be surmised from the data. What is certain, however, is that regardless of extraction solvent, the leaching products of Brij 30 templated samples are more toxic than either isotropic or ionic surfactant templated samples. This behavior indicates that despite the apparent near quantitative removal of Brij 30 from the PEG network as measured gravimetrically, the removal of this non-ionic surfactant is less efficient than its ionic counterparts.

This difference can be attributed to several factors. First, covalent incorporation of surfactant via hydrogen abstraction (type II photopolymerization) probably occurs to a small degree for all three surfactants. It should be noted, however, that the hydrophilic domain of Brij 30 is not only much larger than the ionic surfactants', but is also more compatible, as it is essentially a short PEG chain itself. Furthermore, ether groups, as found in the hydrophilic head of Brij 30, have been shown to be especially susceptible to hydrogen abstraction and thus, in this case, covalent incorporation.<sup>329</sup> This increases the probability that a surfactant molecule will become covalently incorporated, which perhaps leads to more entanglement and physical entrapment of free surfactant molecules. Furthermore, owing to their charged groups and lower molecular weight, the ionic surfactants are also more soluble in all of the polar extraction solvents than Brij 30, making their extraction more efficient than that of the nonionic surfactant. On the other hand, the molecules leaching from other isotropic and templated PEG samples do not appear to be toxic under the conditions used for this study.

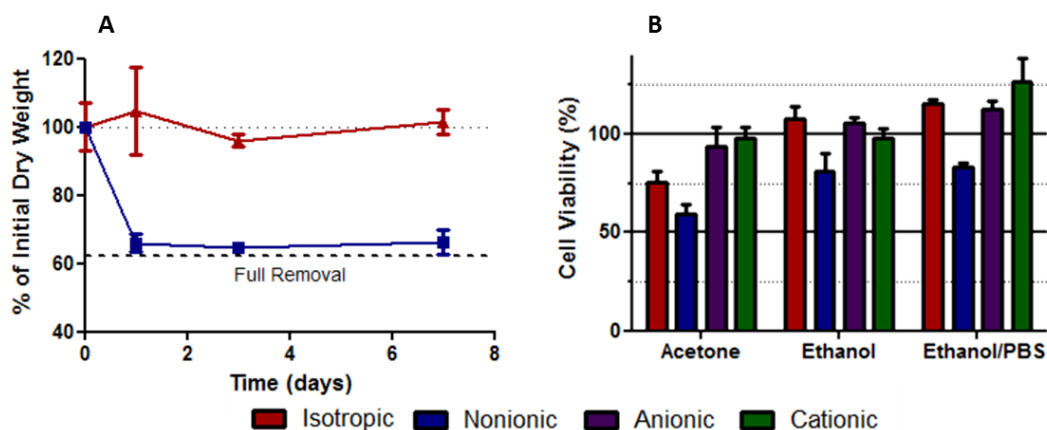


Figure 24. Removal of nonionic surfactant (Brij 30) using acetone as solvent with time, as measured gravimetrically (A) and the relative efficiency of various extraction solvents (B) after one week, measured using cell viability.



Changes in physical properties brought about by surfactant templating have been readily demonstrated herein, but these changes do not result in changes in biochemical properties. Although its extracts were not toxic (Figure 24B), crosslinked PEG, regardless of whether it was templated with surfactant or not, is non-adherent. Although the surface is coated in the same manner as a standard cell culture plate (typically polystyrene), MiPSCs, when given up to one week to attach and grow on the surface, cells demonstrate a rounded morphology and formed clumps with other cells (Figure 25). Even when grown on non-coated polystyrene, cells eventually attach to the surface (data not shown), so simple differences in molecular adsorption of coating molecules (i.e. Matrigel) cannot explain this anti-adhesion effect completely. Importantly, the cell binding properties of PEG appear to be unchanged by the surfactant templating process.

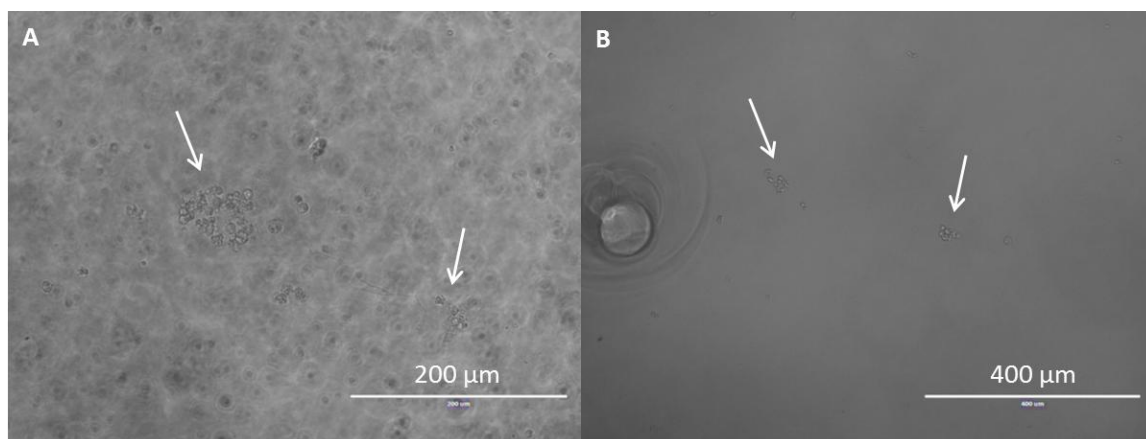


Figure 25. MiPSC cells grown on isotropic (A) and Brij 30 templated (B) crosslinked PEG after one week. White arrows mark groups of non-adherent cells.

### Conclusions

We have demonstrated here that the properties of PEG hydrogels, including morphology, water uptake, and compressive modulus, can be altered using surfactant templating. Templating with both Brij 30 and DTAB resulted in a significant increase in

water uptake and a significant decrease in compressive modulus. Brij 30 templated samples absorbed 200% of their dry weight, which is almost twice as much as non-templated samples. Water uptake and compressive modulus were shown to be inversely correlated. Thus, the templating process reduced compressive modulus by nearly half. These alterations are achieved without unfavorably affecting biocompatibility or anti-fouling properties. That is, the viability of cells exposed to polymer extracts was not significantly different between templated and non-templated groups. Furthermore, both templated and non-templated polymer surfaces were non-adherent and did not support the attachment of cells. In order to validate these results, cell attachment should be studied using a more appropriate cell line, preferably fibroblasts. These findings can be used to improve and tune diffusional properties of coatings for biosensors or drug delivery and orthopedic devices for example, while maintaining biocompatibility and anti-fouling properties.



## CHAPTER 7

### PROPERTY CONTROL OF CHITOSAN HYDROGELS FOR NEURONAL DIFFERENTIATION

Retinal degenerative diseases such as age-related macular degeneration (AMD) and retinitis pigmentosa (RP) make up just one class of many neural degenerative disorders that impair millions of people in the developing world.<sup>3,4</sup> As is typical for neurodegenerative disorders, very few clinical treatments for blinding eye diseases like RP and AMD offer long-term maintenance of decreased visual function, and none offer restoration of lost vision.<sup>5-7</sup> Evidence does suggest, however, that the sensitive layers of the retina can be restored by injection of functional autologous donor cells, offering hope for the development of successful treatments for these life-altering diseases.<sup>10-22</sup> The delivery efficiency of injected cells, however, is still very poor. Less than 0.1% of injected cells survive longer than a few days in the sub-retinal space, and even fewer integrate with the native tissue, which is necessary for function restoration.<sup>13,18</sup> This poor delivery can be attributed to high shear forces during injection and a lack of physical support post-injection.

The primary approach for overcoming poor replacement cell delivery efficiency is the implantation of a cell-laden biomaterial.<sup>111,330,331</sup> A scaffold can help shield cells from fluid flow shear forces and also act as a physical support to hold cells in the appropriate location at the back of the eye post-implantation. Although many have suggested various materials for this purpose that demonstrate good biocompatibility *in vitro*, none of these materials are both derived from sustainable sources and support long-term cell viability and integration *in vivo*. Herein we explore new methods for tuning the final properties of retinal regenerative scaffolds, including the consideration of biochemical compatibility, mechanical properties, and structure.

Many synthetic materials have been fabricated for the purpose of retinal regeneration, including poly(methyl methacrylate) (PMMA),<sup>94</sup> poly(glycerol sebacate) (PGS),<sup>105</sup> and poly(caprolactone) (PCL).<sup>107</sup> Poly(lactic-co-glycolic acid) (PLGA), however, is the most commonly investigated anterior ocular material. Thin, degradable PLGA scaffolds were first shown to support the growth of RPE cells nearly twenty years ago, and have the focus of many studies.<sup>249</sup> When rendered porous, PLGA also supports the growth of retinal progenitor cells (RPCs).<sup>116,117</sup> In fact, in one study transplantation of these RPC-laden PLGA constructs resulted in 10-fold and 16-fold increases in cell survival and delivery, respectively.<sup>117</sup> Furthermore, micropatterned PLGA has been shown to even support the growth of primary photoreceptors for a short period of time.<sup>206</sup> Despite these successes, the stiffness of PLGA scaffolds complicates their transplantation and causes damage to surrounding tissues.<sup>17,19</sup> Furthermore, acidic degradation products can accumulate in the sub-retinal space and cause inflammation and cell death.<sup>332,333</sup>

Many naturally occurring materials offer similar or better biocompatibility than PLGA without the undesirable mechanical properties and toxic degradation products. Donor tissues such as the lens capsule<sup>24</sup>, Descemet's membrane<sup>25</sup>, Bruch's membrane<sup>26</sup>, amniotic membrane<sup>27,28</sup>, and the inner limiting membrane<sup>29</sup> have been used for the transplantation of regenerative cells to the eye, but their use is limited by tissue availability and they pose some risk of rejection complications. Similarly, collagen and its derivatives have been explored for decades, both as allogenic and xenogenic scaffold materials. For example, vibratomed gelatin blocks were first used more than 25 years ago to stabilize photoreceptor and RPE sheets during transplantation.<sup>33,34</sup> Further use of this technique, however, has revealed issues with unwanted neural rosette formation,<sup>35</sup> rapid retraction of axons<sup>36</sup> and some folding in the subretinal space.<sup>34</sup> Thin collagen sheets have also shown some promise as ocular support materials for both donor tissue and *in vitro* RPE cells.<sup>37-39</sup> However, the use of collagen has also been shown to significantly

up-regulate several angiogenic genes in RPE cells,<sup>40</sup> a detrimental side effect, especially for retinal degenerative diseases.

Chitosan, a derivative of one of the most abundant biopolymers on earth (chitin), is an attractive option for biomaterial fabrication and could provide significant advantages for retinal progenitor cell scaffolds. This biopolymer has repeatedly demonstrated biocompatibility<sup>59,60</sup> and is widely considered to be antimicrobial.<sup>61,62</sup> Thus, it is often incorporated into medical materials, including drug and gene delivery systems, wound dressings, and tissue engineering scaffolds.<sup>63–66,269–280</sup> The effectiveness and mechanical properties of chitosan materials can be improved by introducing physical associations or chemical cross-links. Reversible physical interactions can readily be formed between chitosan and small anions like sulfates, polyelectrolytes such as poly(acrylic acid), and even some metal ions like  $\text{Cu}^{2+}$  to form hydrogels.<sup>334–337</sup> These physically associated networks typically have very weak mechanical properties, rendering them difficult to manipulate post-fabrication. Furthermore, since the associations are reversible, their dissolution is difficult to control in varying environmental conditions.<sup>334</sup> Chemical cross-linking of chitosan chains produces more robust hydrogels with no dissolution. This covalent bonding can be accomplished with a variety of crosslinkers, including glutaraldehyde, formaldehyde, diisocyanates, and more recently genipin, a molecule isolated from the gardenia fruit.<sup>334,335,338</sup>

Cross-linking using photopolymerization provides the opportunity to control the extent of reaction in both time and space. In this manner, material cross-linking density can be altered simply by adjusting light intensity or exposure time. The material structure can also be controlled by selectively exposing only certain areas of the prepolymerization mixture. In addition, since crosslinkers are covalently incorporated, there is no need to closely monitor their removal after the reaction completion. Though this approach has been used several times for drug delivery and tissue engineering applications, control of

the resulting hydrogel structure, mechanical properties, and application to neuronal differentiation has yet to be fully explored.<sup>135–137</sup>

Though hydrogels in general, including those composed primarily of chitosan, have inherent porosity, their properties may benefit by the incorporation of controlled, intentional structure. One promising method of controlling polymer structure uses self-assembling surfactant systems as polymerization templates to direct polymer morphology. This templating process has been utilized to generate structure in a number of polymer systems, resulting in polymers that possess useful property relationships that are often not observed in traditional or isotropic polymer systems.<sup>181,216–221</sup>

Organized surfactant molecules can be used to control polymer nanostructure by serving as polymerization templates. In this method, the water- and oil-soluble domains that are inherent in the system are used to segregate monomers. Thus, if a photo-crosslinkable polar monomer such as a methacrylate-functionalized chitosan (MFCTS) is incorporated into the LLC phase, the monomer will preferentially segregate in the water soluble domains of the parent template and may adopt a geometry that resembles that of the self-assembled phase.<sup>228</sup> Photopolymerization can then be utilized to cure the formulation potentially allowing for transfer of the order from the parent template to the polymer system.

The critical packing parameter,  $\rho$ , is often used to relate molecular structure and surfactant concentration to the morphology of surfactant aggregates:<sup>227</sup>

$$\rho = \frac{V}{a_0 l_c} \quad (9)$$

where  $V$  is the effective volume of the surfactant,  $l_c$  is the length of the hydrocarbon chain, and  $a_0$  is the effective area of the surfactant hydrophilic head group. An increase in surfactant concentration increases the packing parameter partly by reducing the effective area of the surfactant head group due to changes in the attractive forces and competitive “binding” for water molecules.<sup>227</sup> In addition to changes in surfactant concentration, the

length of the hydrocarbon can be modulated to inversely influence the critical packing parameter. A packing parameter equal to unity typically corresponds to the formation of a lamellar phase while the bicontinuous cubic, hexagonal, and micellar mesophases are formed at progressively smaller packing parameters. Thus, control of these nanostructures is readily available through changing surfactant concentration or hydrophobic chain length.

A growing body of evidence suggests that in addition to chemical compatibility and structure, mechanical properties of a biomaterial play a very important role in cell phenotype determination.<sup>146,147</sup> Furthermore, matching the mechanical properties of the tissue that will ultimately surround an implant helps to prevent inflammation and damage. Facile tuning of hydrogel mechanical properties using crosslinker size and density has been demonstrated in many photo-curable systems. The incorporation of templating molecules offers another point with which to tune ultimate material stiffness, as the incorporation of structure has been shown to significantly influence water uptake and compressive modulus.<sup>181,216–221</sup>

Here we control the properties of material and biological properties of crosslinked MFCTS hydrogels for use as retinal regenerative scaffolds. The effect of templating with four different families of surfactant is elucidated and is significant for water uptake, morphology, and compressive modulus. Furthermore, copolymerization with three different difunctional monomers exhibits a concentration-dependent effect on water uptake and compressive modulus. Added control is demonstrated by combining surfactant templating and copolymerization techniques. Furthermore, several surfactant-templated chitosan hydrogels were evaluated for bioactivity. In this work, functionalized chitosan hydrogels demonstrated suitability as scaffolds for neuronal differentiation of mouse induced pluripotent stem cells (MiPSCs) showing great potential for use in retinal regeneration.

## Materials and Methods

### Chitosan Functionalization

Chitosan was functionalized with methacrylate groups by a Michael addition reaction based on a previously reported method.<sup>136</sup> First, 1 g of low molecular weight chitosan (96.1% deacetylation, 1% w/v in 1% v/v acetic acid 35 cps, Sigma Aldrich, St. Louis, MO) was dissolved in 50 mL 1% acetic acid with 40 mL ethanol until homogenous. Thereafter, 5 mL 3-(acryloyloxy)-2-hydroxypropyl methacrylate (AOHPMA, Sigma-Aldrich) was added dropwise while stirring. This mixture was allowed to react for 48 hours at room temperature. For reaction confirmation by <sup>1</sup>H nuclear magnetic resonance (NMR), the raw reaction products were dialyzed against distilled water for two days. The resulting suspension of chitosan was then frozen and lyophilized. Purified, naïve chitosan and functionalized chitosan were each dissolved in D<sub>2</sub>O with a small amount of acetic acid. The solutions were analyzed using a Bruker Avance-300 probe.

### Sample Preparation

MFCTS hydrogels were prepared using photopolymerization. To determine the effect of surfactant molecular weight and chemistry on hydrogel properties, four families of surfactant were investigated: polyethylene glycol / polypropylene glycol block copolymers (<sup>®</sup>Pluronic), polyoxyethylene cetyl ethers (<sup>®</sup>Brij), non-ionic polysorbates (<sup>®</sup>Tween), and cationic quaternary ammonium salts (all purchased from Sigma-Aldrich). The general chemical structures of each surfactant family can be found in Figure 26, while detailed information about each surfactant's chain lengths can be found in Table 7. For this study, one inverse triblock copolymer, Pluronic 31R1, which has poly(propylene glycol) ends and a poly(ethylene glycol) core was examined in addition to three traditional Pluronic. Additionally, the effect of quaternary surfactant counter ion was studied by including one chloride salt (DTAC) in contrast to the other bromide salts. As a control, non-templated FCTS hydrogels were also prepared by replacing the 30 wt%

surfactant with an additional 30 wt% acetic acid. The final material properties were tuned by incorporating additional cross-linking moieties. Three co-monomers were investigated: poly(ethylene glycol) diacrylate (MW 575, Sigma-Aldrich), acrylic acid (Sigma-Aldrich), and glycerol diacrylate (glycerol 1,3-diglycerolate diacrylate, Sigma-Aldrich). Finally, the effect of incorporating both surfactant templating and co-polymerization was examined using PEGDA and the quaternary ammonium surfactant DTAB. The water-soluble photoinitiator Irgacure 2959 (BASF, Ludwigshafen, Germany) was used for all samples at 0.1 wt%. Sample formulations are tabulated in Table 8.

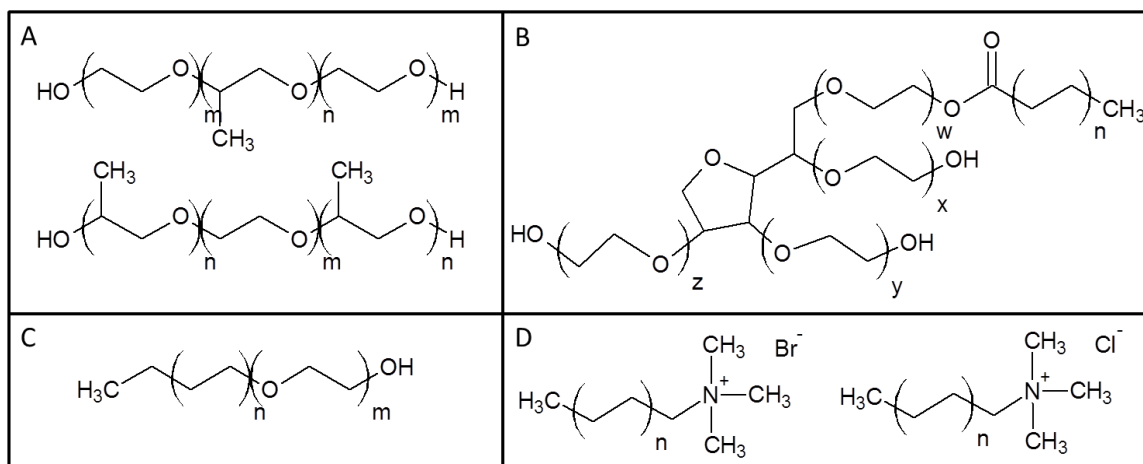


Figure 26. Chemical structures of the four surfactant families: A) Pluronic block copolymers, B) Tween, C) polyoxyethylene cetyl ether (Brij), and D) quaternary ammonium surfactants

An appropriate amount of each sample component (see Table 8) was mixed to homogeneity in a glass vial using vortex mixing and gentle heating, if necessary. About 1 g of each mixture was then transferred by pipette and capillary action to a laminate mold constructed from whole glass slides and glass slide fragment spacers (1 mm thick) that were pre-treated with <sup>®</sup>Rain-X, a hydrophobic silicone release treatment. Samples were then exposed to broad spectrum UV light (100 W mercury spot lamp, UVP LLC, Upland,

CA) with no filter for 10 minutes. After polymerization, the mold was deconstructed and disks were cut from the thin sheet using 5 mm and 8 mm biopsy punches. Samples were transferred immediately to an excess of 50/50 1 M phosphate buffered saline (PBS) and 95% ethanol with continuous mixing by shaking to remove residual surfactant and unreacted species. Non-templated samples were transferred to PBS after two days, while templated samples were transferred to PBS after extraction in solvent (PBS/ethanol) for one week with the solvent being exchanged on days two and four.

Table 7. Chain length information for surfactants used to template functionalized chitosan hydrogels.

	Hydrophilic Length (m or w + x + y + z)	Hydrophobic Length (n)
<b>Pluronic</b>		
L35	11	16
L92	8	50
P123	20	69
P121	5	68
31R1	7	25
<b>Brij</b>		
30	23	5
56	10	7
52	2	7
<b>Tween</b>		
20	20	5
60	20	8
<b>Quat. Amm. Salts</b>		
DTAC	-	12
DTAB	-	12
TTAB	-	14
CTAB	-	16



Table 8. Formulations for samples prepared in this study with. Values are given in wt% of total sample.

	MFCTS	Surfactant	Co-Monomer	Acetic Acid	I-2959
Surfactant Templating	50	30	0	19.9	0.1
Copolymerization	10 – 80	0	10 – 80	9.9	0.1
Combined Approach	50	0 – 30	15	4.9 – 34.9	0.1

### Physical Properties

Changes in hydrogel absorption due to surfactant templating and copolymerization were examined by quantifying sample swelling. 8 mm disk samples were removed from the PBS solution, patted dry, and weighed. After drying overnight, the samples were weighed again. The water uptake was calculated as follows:

$$WaterUptake(\%) = 100 \times \left( \frac{W_w - W_D}{W_D} \right) \quad (10)$$

where  $W_w$  and  $W_D$  represent the weight of the sample when wet and dry, respectively.

The compressive modulus was measured using a dynamic mechanical analysis instrument (DMA Q800 V7.0 Build 113, TA Instruments, New Castle, DE) equipped with a submersion compression clamp in static mode. Prior to each group of measurements, the drive shaft position, clamp mass, clamp offset, and clamp compliance were calibrated according to suggested protocols. Fully hydrated 8 mm samples were carefully placed in the center of the basin. Once the sample was installed, the top portion of the clamp was gently lowered onto the sample surface, the furnace was closed to maintain constant temperature and prevent disturbances, and a pre-load force of 0.0001 N was applied to the sample. The force was then gradually increased to a final value of 0.2 N at a rate of 0.02 N/min and displacement data were collected every 2 seconds as the sample was compressed. All samples were assumed to be cylindrical with a diameter

measured using digital calipers just prior to mechanical testing. Sample thickness was measured using the initial displacement of the clamp before testing began.

The properties of select functionalized chitosan hydrogels were studied at low and high pH. Acetate buffer was prepared at pH 3 and pH 5 using sodium acetate and acetic acid. Basic buffer was prepared at pH 9 and pH 11 using sodium hydroxide and sodium tetraborate or sodium bicarbonate, respectively. These solutions were used in place of PBS after surfactant removal. Water uptake and compressive modulus were measured in the same manner as at neutral pH.

For morphology characterization, 8 mm disks of selected samples were frozen by submersion in liquid nitrogen and freeze-dried overnight, then prepared for SEM analysis. Briefly, samples were mounted to an aluminum stub using colloidal silver and coated with a gold-palladium mixture using an argon beam sputter coater (K550, Emitech Ltd., Kent, England). SEM images were collected using a Hitachi S-4800 (Hitachi High-Technologies, Ontario, Canada) at an accelerating voltage of 5 kV.

### Bioactivity

Fibroblasts were isolated from dsRed mouse umbilical cord and de-differentiated using a retroviral approach to yield murine induced pluripotent stem cells (MiPSCs), as described elsewhere.<sup>21,248</sup> For this study, MiPSCs were gently thawed from a frozen stock, centrifuged, and resuspended in MiPS media [Dulbecco's Modified Eagle Media with F12 (Gibco, Grand Island, NY) supplemented with 15% fetal bovine serum, 1% 100X non-essential amino acids (Gibco), 1% L-glutamine (Gibco), 1% Primocin (Gibco), and 8 nL/mL  $\beta$ -mercaptoethanol (Sigma-Aldrich)] then plated in a 6-well plate pre-coated with Matrigel (Growth factor reduced basement membrane matrix, Corning, Tewksbury, MA) and kept in a humidified, 37 °C incubator with 5% CO<sub>2</sub>. Media was replaced daily and cells were divided and re-plated every two days until needed.

Due to variations in shrinkage among the selected groups, 5 mm diameter punches of functionalized chitosan hydrogel fabricated with 30 wt% DTAB or DTAB + PEG were used for bioactivity studies, while 8 mm punches of the non-templated and 30 wt% Brij 56 hydrogels were needed to achieve similar ultimate dimensions. After surfactant extraction and a PBS wash, these MFCTS hydrogel disks were transferred to a 96-well plate and coated with Matrigel at room temperature for one hour. MiPSCs were removed from the 6-well plate described above using trypsin, centrifuged, and resuspended in fresh media to a concentration of  $1 \times 10^6$  cells/mL. After removing the remaining liquid from the Matrigel coating, 20  $\mu$ L of cell suspension was added directly onto each hydrogel sample and the plate was incubated for twenty minutes. Once the cells had attached to the surface, an additional 100  $\mu$ L differentiation media [DMEM F-12 media (Gibco, Grand Island, NY) containing 10% knockout serum replacement (Gibco) 2% B27 supplement (Gibco) 1% N2 supplement (Gibco), 1% L-glutamine (Gibco), 1% 100x NEAA (Gibco), 1% Primocin (Invitrogen, Grand Island, NY), 1ng/ml noggin (R&D Systems, Minneapolis, MN), 1ng/ml Dkk-1 (R&D Systems), 1ng/ml IGF-1 (R&D Systems) and 0.5ng/ml bFGF (R&D Systems)], was added to each well. The plate was then incubated in a humid 37 °C environment with 5% CO<sub>2</sub>. Media was replaced once per day. Attachment, growth, and differentiation were monitored using phase contrast microscopy.

### Results and Discussion

In order to develop iPSC scaffolds for retinal regeneration, we fabricated hydrogels with controlled biochemistry, morphology, and mechanical properties. Photocross-linking and surfactant templating were used as tools to control these properties for methacrylate functionalized chitosan materials. To confirm functionalization of chitosan with methacrylate moieties, reaction products were confirmed using nuclear magnetic resonance, shown in Figure 27. Two of the largest peaks, at 1 and 2 ppm, can

be attributed to the presence of water and acetic acid, respectively, in the spectra of chitosan before and after reaction. Chitosan has several characteristic peaks, which are relatively unchanged by the reaction, including those representing protons on the four tertiary carbons in the molecule's backbone (at 3.0, 3.5, 3.7, and 4.8 ppm) and the secondary carbon pendant to the chitosan backbone (3.4 ppm). Compared to naïve chitosan, the spectrum collected for the functionalized chitosan contains two additional peaks at 5.5 and 6 ppm. These match well with tabulated values for methacrylate protons,<sup>339</sup> indicating that indeed the chitosan chains are functionalized with pendant methacrylate groups after the Michael addition reaction. Relative to the peaks attributed to backbone protons, these methacrylate peaks are very small, implying a low degree of substitution. The polymerization of this moderately scarcely functionalized chitosan derivative should result in loosely cross-linked hydrogels with high water uptake and low compressive modulus.

### Surfactant Templating

Surfactant templating can be used to control the physical properties of MFCTS hydrogels. As seen in Figure 28A, block copolymers are powerful tools for adjusting these materials' water uptake. In fact, the incorporation of 30 wt% Pluronic L35 during the polymerization process decreased water uptake by 50% while Pluronic P121 increased it by nearly 100%, with other molecular weights and chemical compositions having effects in between those two extremes. Furthermore, other families of surfactant, such as Tween (Figure 28B), can also be used to control the water uptake of functionalized chitosan hydrogels. Although this family had a less dramatic effect than Pluronic, Tween 20 decreased water uptake by 40% while Tween 60 increased it by 50%. On the other hand, although polyoxyethylene cetyl ethers have been shown in other studies to impart structure on polymers and thereby alter their properties, at the concentrations used in this study they had only a small influence on the water uptake of

functionalized chitosan hydrogels. Hydrogels templated with Brij 52 absorbed more water than those templated with Brij 56, Brij 30, or no surfactant, while Brij 30 templated samples were not different than non-templated controls. The most dramatic change in water uptake was observed for samples templated with quaternary ammonium surfactants. All of the quaternary ammonium surfactants studied spurred a three-fold increase in water uptake when used as polymerization templates for MFCTS hydrogels (Figure 28C). As described here, this library of surfactants can be used to adjust the final water uptake of chitosan hydrogels from as low as 150 wt% up to more than 1500 wt%, offering control across an entire order of magnitude without changing the chemical composition of the final material.

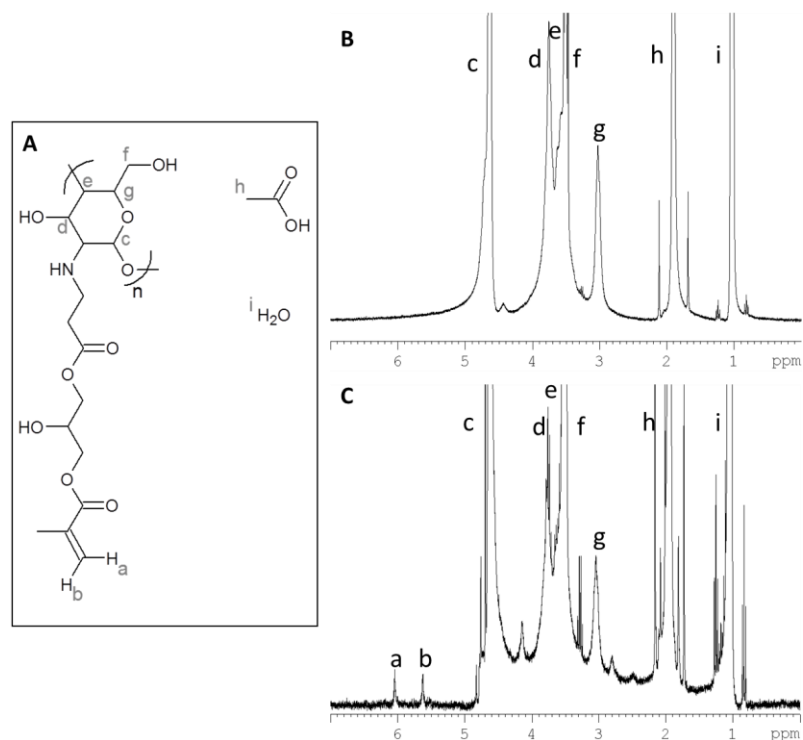


Figure 27. Nuclear magnetic resonance profile of naïve (B) and methacrylate functionalized (C) chitosan. Each peak corresponds to a distinct proton, as labeled in panel A.

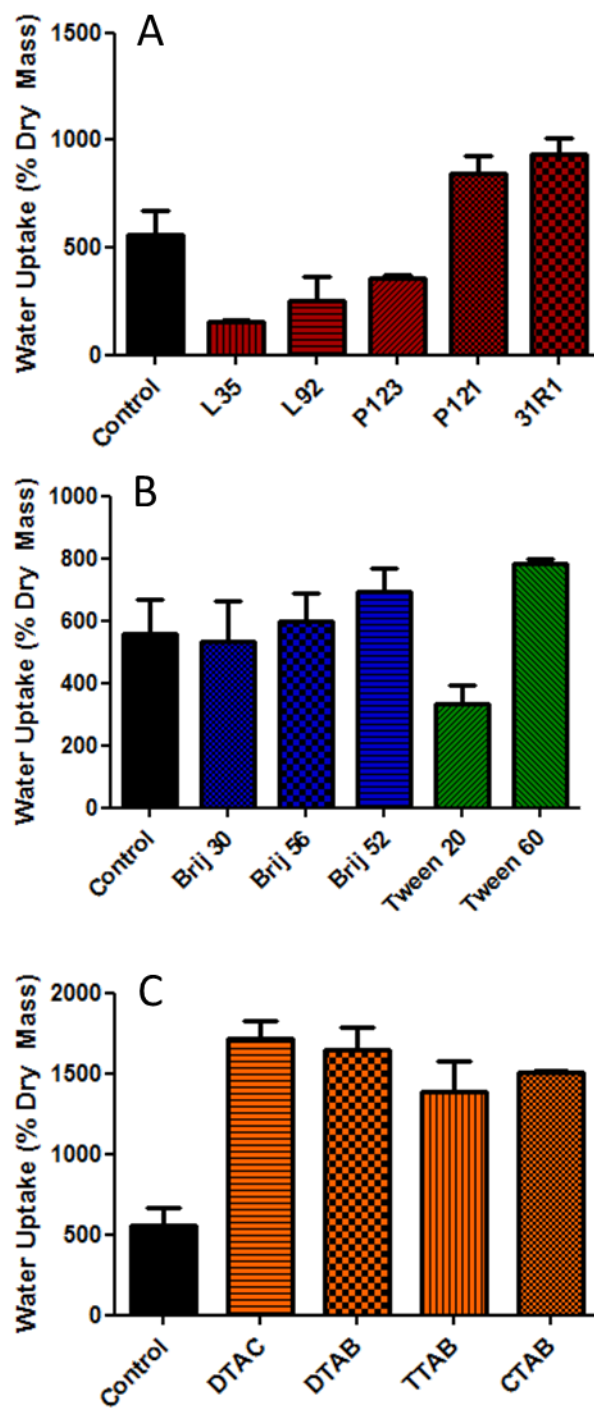


Figure 28. Water uptake of 50 wt% MFCTS hydrogels templated with A) Pluronic block copolymers, B) Brij and Tween, and C) quaternary ammonium surfactants.  $N = 3$  and error bars represent the standard error of the mean.

Previous research suggests that surfactant geometry largely dictates self-assembled feature size. In the case of surfactant templating of hydrophilic monomers, agglomerates of discontinuous phase, or hydrophobic segments, form what later become pores within the network. Thus, the volume occupied by a surfactant's hydrophobic segment, which can be relatively approximated using molecular weight, is expected to correlate with water uptake. The trends observed in Figure 29 suggest that this is indeed true for MFCTS hydrogels. As the molecular weight of the polyester segment on Tween and Brij surfactants increases, so does the hydrogel water content ( $R^2 = 0.4570$ ). Likewise, water uptake increases in proportion to the poly(propylene glycol) segment length of Pluronic used to template chitosan hydrogels ( $R^2 = 0.6233$ ). This correlation does not hold for quaternary ammonium surfactants, possibly due to the very small size of their hydrophilic head groups relative to the other surfactants studied.

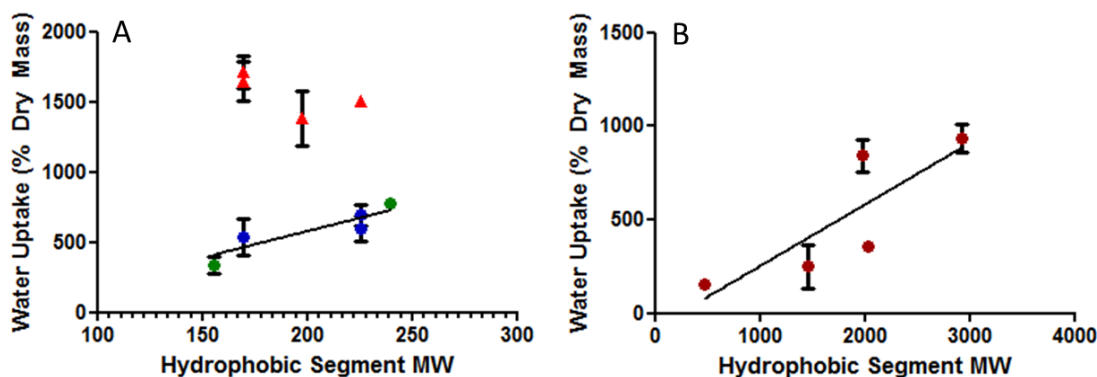


Figure 29. Water uptake of 50 wt% MFCTS hydrogels as a function of A) poly(ether) segment length in three families of surfactants: Tween (green), polyoxyethylene cetyl ether (blue) and quaternary ammonium (orange) and B) block copolymer hydrophobic segment length (red).  $N = 3$  and error bars represent the standard error of the mean.

The final properties of functionalized chitosan hydrogels are also dependent on pH. As shown in Figure 30A, chitosan hydrogels with and without surfactant-templated

structure undergo maximum swelling at pH 3 and minimum water uptake at pH 7. At pH 9, few changes from pH 7 are observed, while at pH 11 a large increase in water uptake is observed for non-templated and Brij 56 templated samples. This behavior is most likely due to degradation of chitosan chains and the resulting decrease in cross-linking density. Chitosan hydrogels templated with DTAB seem to undergo less dramatic changes in swelling across the pH spectrum, indicating greater stability and resilience than non-templated or Brij 56 templated samples. Like water uptake, the compressive modulus of chitosan hydrogels templated with DTAB is relatively constant at varying pH. Conversely, the compressive modulus of non-templated and Brij 56 templated samples at pH 9 is at a maximum and more than 15 times greater than the minimum compressive modulus observed at pH 11. Although pH does affect compressive modulus, especially in basic conditions, compressive moduli at neutral pH are in the same range as reported values for retinal and other neuronal tissue.<sup>340,341</sup> This low modulus can be attributed to the low cross-linking density resulting from a low degree of substitution.

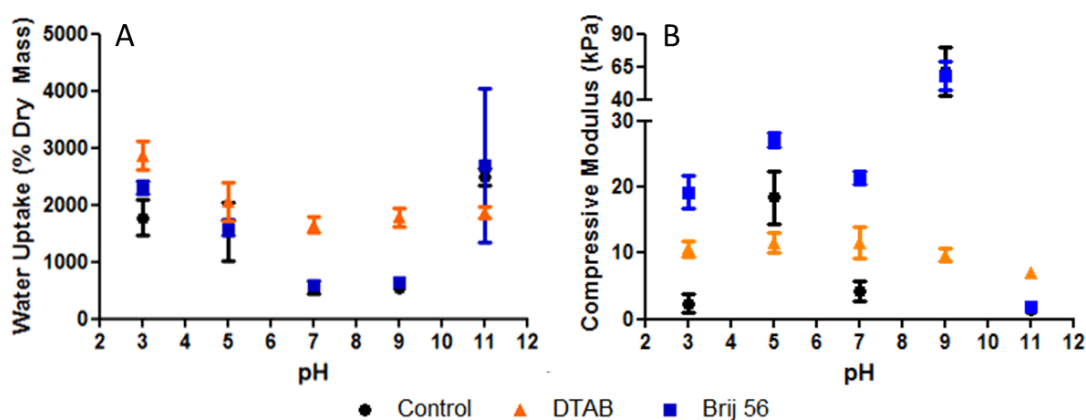


Figure 30. pH-dependent water uptake (A) and compressive modulus (B) of 50 wt% MFCTS hydrogels templated with 30 wt% Brij 56 or DTAB compared to non-templated controls.  $N = 3$  and error bars represent the standard error of the mean.



## Copolymerization

In addition to surfactant templating and pH, copolymerization with various crosslinkers can also be used to tune the physical properties of MFCTS hydrogels. Relatively low and high water uptake resulted from the copolymerization of functionalized chitosan with glycerol diacrylate and acrylic acid, respectively, at various concentrations (see Figure 31A). Copolymerization with PEGDA at various concentrations resulted in a fairly smooth inverse correlation between the amount of PEGDA and water uptake. Furthermore, the compressive modulus of copolymerized MFCTS hydrogels was 50 kPa or less for all three comonomers (Figure 31B) at low concentrations. However, for glycerol diacrylate, compressive modulus increased with increasing comonomer concentration. On the other hand, compressive modulus was relatively constant as the concentration of acrylic acid and PEGDA comonomer increased, with the exception of a very high measurement (~175 kPa) at 25% PEGDA. These results suggest the utility of copolymerization for controlling water uptake and compressive modulus of MFCTS hydrogels. Water uptake can be adjusted a full order of magnitude (50% - 500%) using PEGDA as a comonomer without significant changes to the compressive modulus. Likewise, compressive modulus can be adjusted more than an order of magnitude (5 kPa – 75 kPa) using glycerol diacrylate as a comonomer without significant changes to the water uptake.

The combination of copolymerization and surfactant templating can add even more power to the ability to control chitosan hydrogel properties. For example, at a fixed concentration of chitosan and PEGDA, low concentrations of surfactant template (DTAB) resulted in water uptake similar to a non-templated control, while concentrations greater than 10% result in water uptake that is slightly higher than the control samples (Figure 32A). Furthermore, the compressive modulus gradually decreased from 65 kPa to 5 kPa with the incorporation of more surfactant (Figure 32B). Thus, adjusting the surfactant concentration for a given comonomer concentration can provide control of the

properties within a more narrow range than adjusting the comonomer concentration alone.

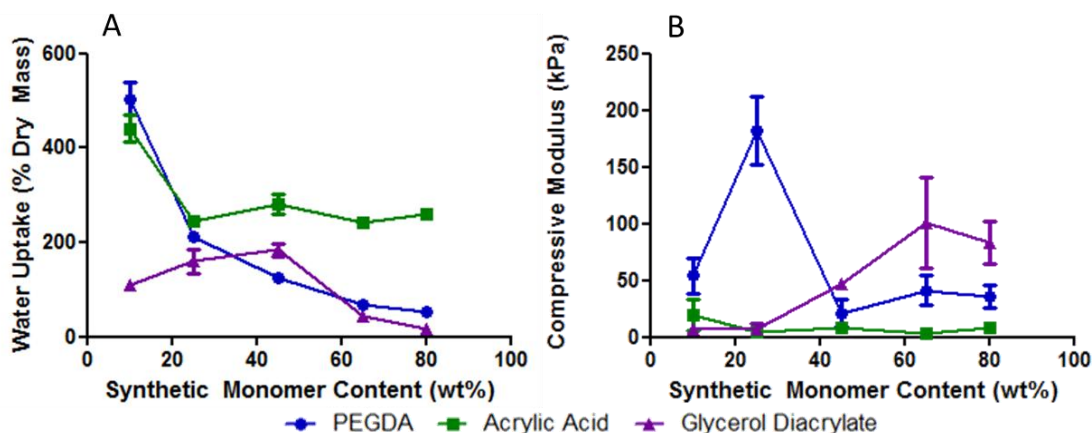


Figure 31. Water uptake (A) and compressive modulus (B) of MFCTS hydrogels copolymerized with PEGDA (blue), acrylic acid (green), and glycerol diacrylate (purple).  $N = 3$  and error bars represent the standard error of the mean.

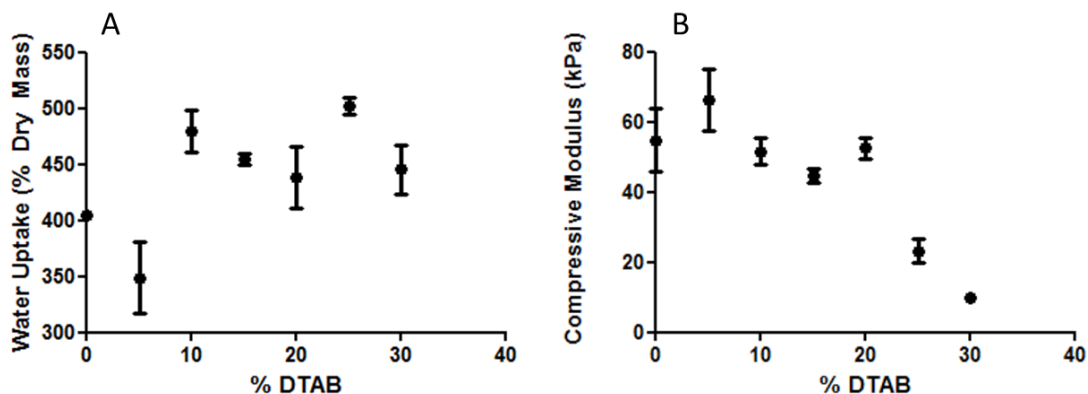


Figure 32. Water uptake (A) and compressive modulus (B) of 50 wt% FCTS hydrogels cross-linked with PEGDA and templated with varying concentrations of DTAB.  $N = 3$  and error bars represent the standard error of the mean.

### Bioactivity

To elucidate the effects of biochemical properties, water uptake, compressive modulus, and morphology on the ability of chitosan hydrogels to support the differentiation of stem cells towards neuronal cell types, several samples were selected for bioactivity evaluation: a non-templated control, a templated hydrogel with no change in water uptake over the control (Brij 56), a high water uptake sample (DTAB), and a templated, copolymerized sample (DTAB/PEG). The water uptake and compressive moduli of these selected samples are presented in Figure 33. As previously noted, DTAB samples had the highest water absorption of the samples, while no significant differences between the other groups were observed (Figure 33A). Compressive modulus was highest for the Brij 56 templated sample, while both DTAB templated samples were slightly more stiff than the non-templated control (Figure 33B). All four samples selected have a compressive modulus in the appropriate range for neural tissue.<sup>341</sup>

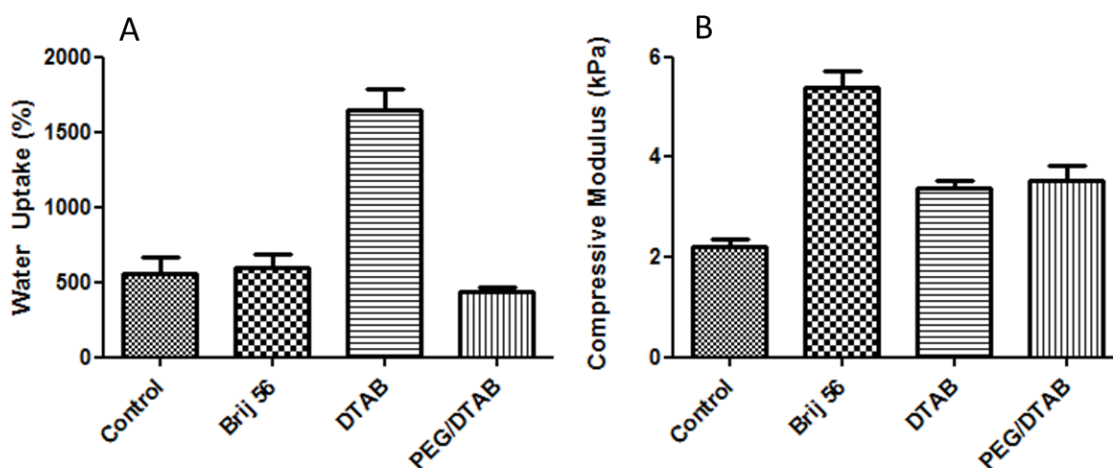


Figure 33. Water uptake (A) and compressive modulus (B) of MFCTS hydrogels templated with 30 wt% surfactant (Brij 56 or DTAB) or cross-linked with 15% PEGDA and templated with 15% DTAB. N = 3 and error bars represent the standard error of the mean.

Polymer morphology, or structure, can have a large impact on physical properties such as water uptake and compressive modulus, but also plays an important role in material bioactivity. The morphology of selected MFCTS hydrogels is impacted by surfactant templating. As seen in Figure 34A, chitosan hydrogels polymerized without a surfactant template have a very smooth, non-porous morphology as observed by SEM. The incorporation of Brij 56 induces some porosity, while the inclusion of DTAB has a dramatic effect on the material porosity. As seen in Figure 34C, DTAB templated chitosan contain randomly distributed pores around 100  $\mu\text{m}$  in size. These changes in morphology, induced by monomer segregation during polymerization, are likely the cause of such notable impacts on polymer properties.

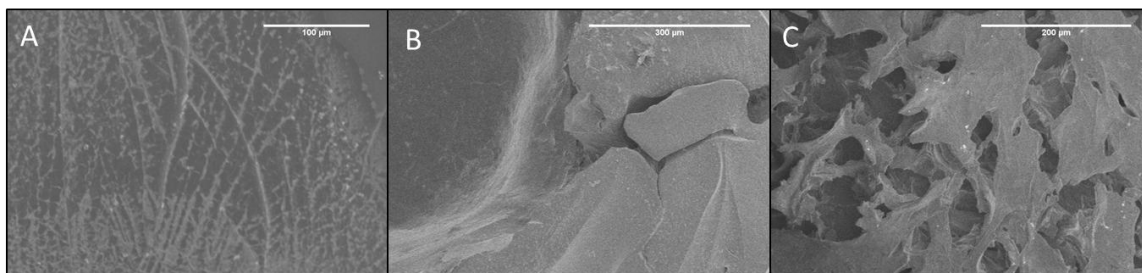


Figure 34. Scanning electron micrographs of MFCTS templated with no surfactant (A), 30 wt% Brij 56 (B), and 30 wt% DTAB (C). Scale bars represent 200  $\mu\text{m}$ .

Since differentiating cells are sensitive to biochemical, mechanical, and structural cues they receive from a material, directing their phenotypic fate can be challenging. To this end, we have demonstrated several methods available for tuning these properties in functionalized chitosan hydrogels. Next, we evaluated the ability to use these MFCTS hydrogels as differentiation platforms for MiPSCs. We found that indeed these biocompatible, soft, porous materials are able to support differentiating stem cells. In fact, after only one day, cells not only attached to the material, but also began forming

dendrites and axons on all but one sample (Figure 35). Due to sample opacity, DTAB templated FCTS/PEG copolymers were not evaluated by phase contrast microscopy. Cells on the underlying tissue culture plastic, however, appeared to be negatively affected by the presence of PEG, as their morphology was rounded and very few dendrites and axons were observed. Fewer cells were differentiating and attached to Brij templated chitosan hydrogels than on non-templated and DTAB templated samples. However, after three days in culture, cells were still differentiating and attached to all three surfaces, but in all cases many cells began to lose their morphology and detach from the surface. Because cells were growing both on the material and on the plate beneath the material, nutrients were being consumed too quickly for sustainable, long-term evaluation of growth and differentiation.

### Conclusions

Biocompatibility, stiffness, and morphology are all important characteristics of biomaterials that should be carefully tuned for optimal performance *in vitro* and *in vivo*. Here, we demonstrated property tuning using a biocompatible, naturally occurring polymer, chitosan. This polysaccharide was functionalized using Michael addition of the commercially available, difunctional molecule AOHPMA, leaving pendant methacrylate groups. Using a library of surfactants as templates during the photo-crosslinking of methacrylate-functionalized chitosan, we demonstrated that water uptake is generally correlated with surfactant hydrophobic segment length, except in the case of quaternary ammonium surfactants, which induce very large increases (more than three-fold) in MFCTS hydrogel water uptake relative to non-templated controls. In addition, though the properties of MFCTS hydrogels are dependent on pH, these effects are dampened for quaternary ammonium templated samples, resulting in more robust, resilient materials. Furthermore, incorporation of comonomers offers yet another tool for tuning water uptake and compressive modulus of chitosan hydrogels.

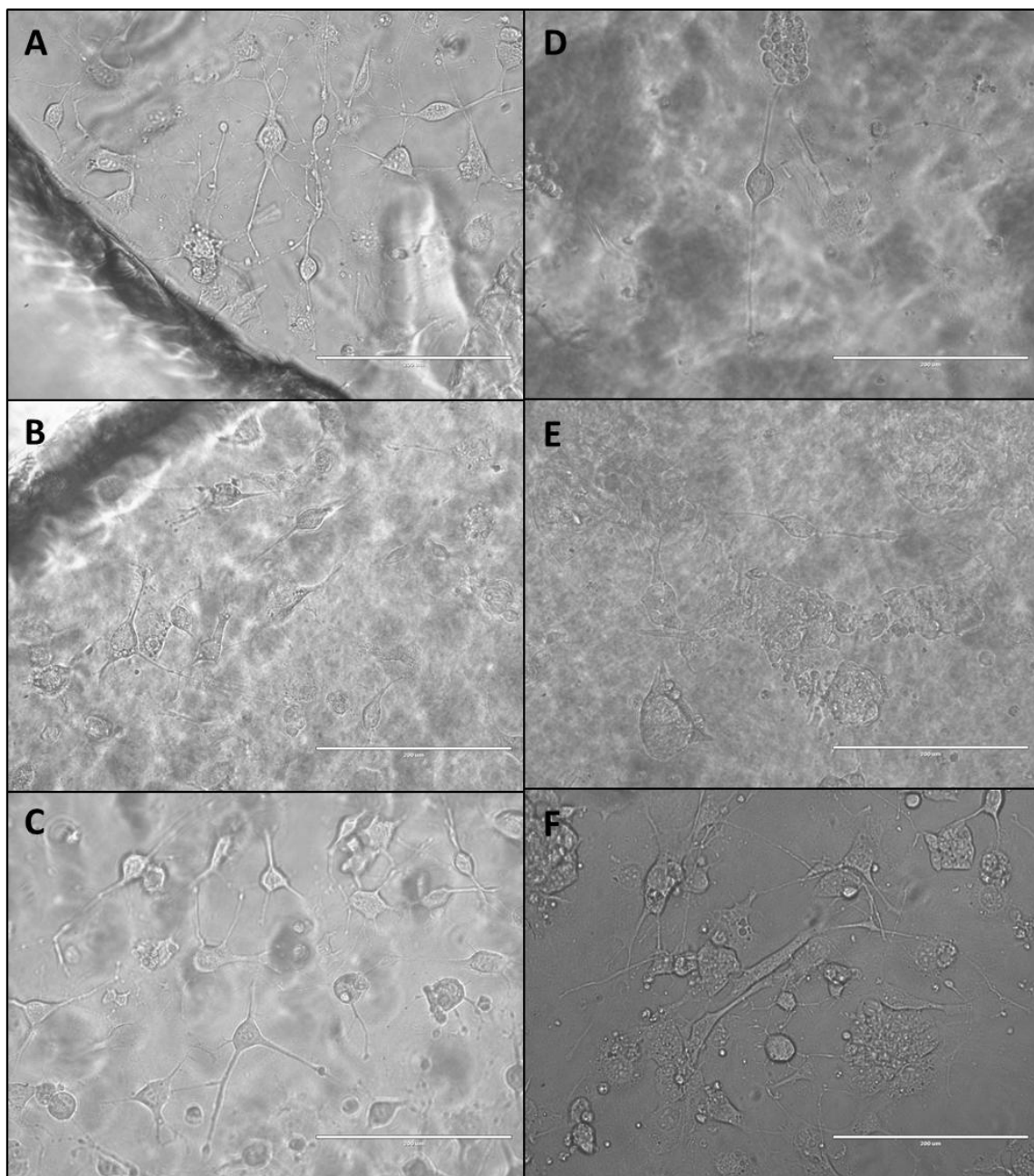


Figure 35. Phase contrast micrographs of neuronal cells differentiating on 50 wt% MFCTS hydrogels with no surfactant template (A, D), 30 wt% Brij 56 (B, E), and 30 wt% DTAB (C, F) after one day (A-C) and three days (D-F) in culture. Scale bar represents 200  $\mu\text{m}$ .

Combining copolymerization and surfactant templating provides a means to further optimize properties. These property changes brought about by surfactant



templating can be attributed in large part to morphology changes that occur on the micron scale. For example, chitosan hydrogels templated with quaternary ammonium surfactant are very porous compared to the relatively smooth non-templated samples, which is a likely explanation for their dramatic differences in water uptake. The incorporation of PEGDA crosslinker negatively impacted chitosan hydrogel bioactivity, but all of the homopolymer samples demonstrated MiPSC cell attachment and differentiation towards neuronal phenotypes. These results show the effect of surfactant templating on the properties of chitosan hydrogels. Herein several approaches were successfully used to tune chitosan hydrogel properties to tissue appropriate ranges. MFCTS are biocompatible, have mechanical properties close to those of the native retina, and can be made with structure that enhances diffusion and could potentially facilitate physical and chemical cell signaling. These bioactive, controllable materials are a promising option for the transplantation of iPSCs for the mitigation of retinal degeneration.

## CHAPTER 8

### CONCLUSIONS AND RECOMMENDATIONS

The treatment of blinding eye diseases caused by retinal degeneration could be greatly enhanced by the successful design of biomaterials for the sub-retinal space. By carefully controlling the biochemical properties, mechanical properties, and morphology of polymeric materials, the interactions between cells and materials can be better understood and predicted for potential use as induced pluripotent stem cell scaffolds for the amelioration of retinal degeneration.

#### Biochemical Properties

The transplantation of materials laden with induced pluripotent stem cells, which can be formed from adult skin cells, is a promising treatment option for retinal degenerative diseases. Because this cell type can be developed from each patient's own cells, its use in cell replacement therapies results in a greater likelihood of integration with host tissue and a reduced risk of rejection compared to donor tissues or cells. To this end, the feasibility of growing and differentiating induced pluripotent stem cells (iPSCs) on synthetic scaffolds was demonstrated here. In this work, PLGA scaffolds with randomly distributed pores ranging in size from 200 nm<sup>2</sup> to 10 μm<sup>2</sup> were fabricated using a simple salt leaching technique. Most of the pores (>65%) were less than 1 μm<sup>2</sup>, with the greatest fraction (15%) being about 400 nm<sup>2</sup>. After one week, iPSCs seeded on these scaffolds had proliferated to coat the surface. Many of these cells also extended neurites to form connections with neighboring cells, indicating that they had differentiated into neuronal phenotypes. At two weeks, cells began growing in layers on the scaffold, and neurite networks were very dense and highly branched. Differentiation of iPSCs directly on their intended implantable substrate rather than dissociating them and seeding onto a scaffold after differentiation could help retain desired morphologies and extracellular matrix, making for a more efficient and effective pre-transplantation time period. When



cultured on porous PLGA scaffolds *in vitro*, cells were able to proliferate rapidly and mature into neuronal cell types within one week. Evaluating the capacity of materials to not just sustain growth, but also to support differentiation is an important step towards the rational design of cell and tissue replacement strategies. These findings expand the collection of appropriate cell types for replacement therapies that involve scaffolds to include iPSCs and also contribute to the greater understanding of how cells interact with their environment and growth substrate. In time, these realizations can be used to develop more effective therapies for blinding eye diseases.

The biocompatibility of chitosan and how it contributes to overall toxicity when combined with otherwise toxic materials was also examined. The addition of a chitosan coating to copper nanoparticles changed their physical properties and toxicity *in vitro* and *in vivo*. The size of the chitosan coated copper nanoparticles was roughly 50% greater than non-coated copper nanoparticles, but the morphology of the chitosan coated particles was smooth and round, in contrast to aggregated and rough surfactant coated copper nanoparticles. The presence of chitosan coating on the copper nanoparticles was confirmed by fluorescence of rhodamine-B conjugated chitosan, an increase of particle charge due to the presence of cationic chitosan, and the presence of surface nitrogen clearly detectable by XPS. Interestingly, the *in vitro* toxicity of chitosan coated copper nanoparticles was significantly lower than their uncoated counterparts for two different cell types, two time points, and a range of doses. These results strongly suggest that coating with chitosan protects cells in culture from the toxic effects of copper nanoparticles. Conversely, an increase in inflammatory response was observed for mice exposed to chitosan-coated copper nanoparticles versus the uncoated controls. These results suggest that coating toxic metal nanoparticles with mucoadhesive polysaccharides (e.g. chitosan) decreases their ability to be cleared from the lungs, prolonging the exposure of cells and tissue to toxic metal oxides and producing a dramatic acute inflammatory response. This study demonstrates the power of naturally occurring

molecules to overcome bioactivity challenges. Furthermore, it highlights the importance of not only a thorough analysis of physical properties, but also a careful analysis of how biocompatibility is affected by specific *in vivo* environments.

### Mechanical Properties

The interaction between cells and their environment is closely related to mechanical cues. As material stiffness can affect tissue inflammation upon implantation and also help dictate cell fate, it should be closely examined during the design process. For the purpose of developing cell delivery scaffolds for retinal regeneration, the transverse compressive stress and strain behavior of the retina is an important starting point. This behavior serves as a representation of the mechanical pressures encountered during chronic implantation and the modulus that a developing cell will perceive. The compressive modulus of various porcine ocular tissues was measured in this work. Of the tissues tested, the sclera had the highest modulus (35 kPa), while the choroid and RPE combined had the lowest (5 kPa). The compressive modulus of the retina (10 kPa) is 10 fold lower than its previously reported tensile modulus. This finding demonstrates the importance of correctly characterizing mechanical properties in order to identify material property targets. Furthermore, the compressive modulus of mouse retina was relatively constant with age for a wild type mouse. However, the retinal compressive modulus of retinal degenerative mice decreased quite rapidly. By 12 weeks of age, the retinal modulus was much lower than at three weeks of age. Furthermore, the mean modulus at 12 weeks was 90% lower than the wild type mouse at a similar age ( $p < 0.05$ ). These results demonstrate that retinal degenerative disease significantly affects the mechanical properties of the retina. Several polymers have compressive moduli that match those of ocular tissues. The compressive modulus of crosslinked PEG, for example, was tuned to achieve a value very close to that of the retina. These findings help lay the foundation for

appropriate material selection and modulation for retinal cell differentiation applications and for transplantation to the retina.

### Morphology

Mimicking the extracellular matrix environment is a powerful way to optimize interactions between cells and biomaterials. Appropriate material morphology can facilitate the diffusion of nutrients and signaling molecules, as well as provide cues related to differentiation and directionality. Thus, the control of material morphology is a key aspect of biomaterial development for retinal regeneration applications. Surfactant templating is a useful tool for inducing structure-property relationships not available in non-structured materials. The effects of surfactant templating on material physical properties and biocompatibility were further elucidated herein. The properties of PEG hydrogels, including morphology, water uptake, and compressive modulus, can be altered using surfactant templating. Templating with both Brij 30 and DTAB resulted in a significant increase in water uptake and a significant decrease in compressive modulus. In fact, Brij 30 templated samples absorbed 200% of their dry weight, which is almost twice as much as non-templated samples. Furthermore, water uptake and compressive modulus were inversely correlated. Thus, for the systems studied, the templating process reduced compressive modulus by nearly half. These alterations were achieved without unfavorably affecting biocompatibility or anti-fouling properties. That is, the viability of cells exposed to polymer extracts was not significantly different between templated and non-templated groups. Both templated and non-templated polymer surfaces were non-adherent and did not support the attachment of cells. These findings can be used to improve and tune diffusional properties of coatings for biosensors or drug delivery and orthopedic devices for example, while maintaining biocompatibility and anti-fouling properties. These results also suggest that morphology alone may not be powerful enough to overcome bioactivity limitations.

Biocompatibility, stiffness, and morphology are all important characteristics of biomaterials that should be carefully tuned for optimal performance *in vitro* and *in vivo*. In the last chapter, the properties of methacrylate functionalized chitosan (MFCTS) hydrogels were tuned using various techniques. Selected surfactants were used as polymerization templates and shown to significantly affect water uptake, which was generally correlated with surfactant hydrophobic segment length, except in the case of quaternary ammonium surfactants. These cationic surfactants, however, induce very large increases (more than three-fold) in MFCTS hydrogel water uptake relative to non-templated controls. In addition, though the properties of MFCTS hydrogels are dependent on pH, these effects are dampened for quaternary ammonium templated samples, resulting in more robust, resilient materials. Incorporation of comonomers offers yet another tool for tuning water uptake and compressive modulus of chitosan hydrogels. In addition, combining copolymerization and surfactant templating provides a means to fine-tune properties. These property changes brought about by surfactant templating can be attributed in large part to morphology changes that occur on the micron scale, as witnessed by SEM imaging. Furthermore, although the incorporation of PEGDA crosslinker negatively impacted chitosan hydrogel bioactivity, all of the homopolymer samples demonstrated MiPSC cell attachment and differentiation towards neuronal phenotypes. These results offer a first look at the effect of surfactant templating and scaffold morphology on the properties of chitosan hydrogels. In addition, several approaches were successfully used to tune chitosan hydrogel properties to within tissue-appropriate ranges. This tuning provides a mechanism for altering performance of chitosan hydrogels, which are very promising materials for retinal and other neural regeneration. MFCTS hydrogels are biocompatible, have mechanical properties close to those of the native retina, and can be made to contain structure that enhances diffusion and could potentially facilitate physical and chemical cell signaling. These results provide

yet another step towards the optimization of biomaterials: an endeavor that may increase the quality of life or even extend the mortality of millions of individuals worldwide.

### Recommendations

While this work has contributed to the overall understanding of biomaterial property tuning for optimal performance, much work remains in order to achieve optimal design of retinal regenerative scaffolds and many techniques could improve cell/material interactions and overall material performance. Furthermore, applications to other ocular tissues or even other organs altogether could benefit from the results presented here.

If the degeneration of tissue is a direct result of inherited disease rather than injury, then cellular therapy approaches used for regeneration must include appropriate cell types. In many cases, the transplantation of patient-specific cells may result in short-term tissue regeneration but long-term recapitulation of disease. Even in the case of degeneration due to injury, donor cells only closely mimic patient cells, and there is always a chance of rejection. The ideal cell type for replacement therapy is one that is patient-derived but lacks the disease-causing genetic defect. Genome editing is an increasingly popular technique for “fixing” these genetic defects, and is thus a powerful tool for creating corrected, patient-specific cells. An important next step for the development of retinal regenerative biomaterials is to demonstrate the ability of these corrected, patient-specific cells to attach to and integrate with materials *in vitro*.

### Biochemical Properties

Since many surfactants are cytotoxic at very low concentrations, the complete extraction of surfactant after its use as a polymerization template is a major concern when using this technique for biomaterials. Although some methods were used herein to understand the extent of surfactant retention within materials, a quantitative approach would provide additional detail and perhaps provide the ability to predict and control the extent of surfactant retention. Spectroscopic techniques such as infrared spectroscopy,

Raman spectroscopy, and/or nuclear magnetic resonance, all of which are readily accessible, should be used to quantify surfactant retention in templated polymers, provided that surfactants are carefully selected or modified with identifiable functional groups. As sample thickness and geometry affect diffusion of unreacted species during the extraction process, these factors should be investigated, along with reaction rate, polymer crosslinking density, surfactant molecular weight, and photoinitiator species. The tracking of residual surfactant should also be used to understand the relationship between surfactant concentration and cell viability and differentiation.

While the use of functionalized chitosan for the formation of biocompatible hydrogels was successful in these studies, other functionalized biomolecules are also likely to interact favorably with iPSCs. Though the functionalization of extracellular matrix molecules such as elastin, collagen, and fibrinogen has been demonstrated to some extent, none have attempted to use these as scaffolds for iPSCs or for retinal regeneration. Once functionalized, these molecules should be blended together or with other functional molecules to closely mimic the chemical composition and mechanical integrity of naturally occurring extracellular matrices in various organs and tissues. Furthermore, the covalent incorporation of signaling peptides or proteins should be used to enhance the ability of materials to bind cells and guide their differentiation. Attachment peptides such as RGD and YIGSR should be investigated as a starting point for peptide inclusion. Then, the inclusion of differentiation factors that are typically added to cell culture media (e.g. Noggin, dKK1, IGF-1, and bfgf) should be investigated as a means to promote cell differentiation to desired phenotypes. Eventually, chemical gradients of these molecules should be created within a material in order to study cell migration and development spatially.

During the cell seeding process, many cells do not attach to the material surface simply because they get washed away with excess fluid. For very valuable cells, such as patient-specific iPSCs, this is an undesirable scenario. One approach to mitigate the loss

of cells is to encapsulate them directly into a material. This method also serves to force cells into a 3D environment instead of waiting for them to migrate on their own. Encapsulation can readily be accomplished using high molecular weight crosslinked PEG, as has been shown in other studies. Water soluble chitosan, which is commercially available, should also be functionalized using the described Michael-addition reaction. Thus, cells will be encapsulated in these biocompatible chitosan hydrogels without having to expose them to damaging acidic environments. Encapsulation of cells in other functionalized biomolecules should also be investigated. The encapsulation of retinal progenitor cells or photoreceptor precursor cells by photopolymerization, however, should be handled with care. Since these cells are meant to sense light, they are especially sensitive to exposure to high energy photons. For this purpose, the use of water-soluble visible-light photoinitiators should be explored more deeply.

### Mechanical Properties

The relationship between iPSC or RPC development and compressive modulus is an important step towards designing effective ocular biomaterials. Using a sliding photomask to create a light gradient and thus a cross-linking density gradient, a single material with a gradient of stiffness could easily be fabricated. This approach should be applied to many different materials, adding a second factor to study the property-function relationship. Fine-tuning the compressive modulus of a material in order to selectively differentiate photoreceptors versus glial cells, for example, will facilitate very specific cellular replacement strategies relevant to a myriad of eye diseases.

Mechanical properties are suspected to play a major role in the pathology of glaucoma, a blinding eye disease associated with degeneration of axons inside of and leading to the optic nerve. As cells gather at the optic nerve to exit the eye and enter the brain, they pass through a porous structure called the lamina crebosa. Some researchers claim that axon degeneration is due to a weakening of the lamina crebosa, while others

disagree. To help understand the role of lamina crebosa stiffness in glaucoma, porous materials with varying mechanical properties should be fabricated and used as scaffolds for retinal glia. By using these materials as a model for the lamina crebosa, we will gain a greater understanding about how glaucoma works, leading to the development better treatments.

Fuch's dystrophy, a corneal disease involving degeneration of the endothelium, is another ophthalmic disease with few long-term treatments. Total corneal transplant, though effective, is a difficult procedure, is dependent on donor tissue availability, and, like any donor transplant, poses a risk of rejection. The transplantation of a thin, optically clear scaffold with attached, patient-specific endothelium could serve the same purpose at a lower cost and reduced risk. Mechanical property tuning should be used to produce a material that is more robust than a donor cornea, simplifying the procedure and increasing the chance of success. Several thin, clear polymer sheets of crosslinked chitosan or elastin should be fabricated and their tensile moduli and optical clarity measured over a range of crosslinking densities. Thereafter, adhesion of patient-specific endothelial cells should be evaluated using existing cell culture protocols and the techniques described in this work. Finally, these endothelial sheets should be transplanted and tracked long term *in vivo*.

### Morphology

A more thorough investigation of microstructure and its effects on cell/material interactions will serve to identify target porosities for future materials. Microfabrication techniques, for example, should be used to create porous materials with controlled sizes and spacing. Particle leaching with extractable microparticles of various sizes should also be used to impart controlled porosity to a material. This could be accomplished very simply using the salt leaching approach described in Chapter 3 if a series of sieves are used to isolate groups of salt crystals with similar sizes. Thereafter, various cell types



should be seeded onto these materials and an optimal structure identified. One application that would benefit greatly from the pursuit of controlled porosity materials is an artificial trabecular meshwork for the treatment of glaucoma. The trabecular meshwork is a porous structure that regulates fluid flow out of the eye. When its structure is altered, pressure can build up in the eye, sometimes leading to optic nerve damage, and thus glaucoma. An artificial structure that mimics the porosity of the trabecular meshwork should be developed and implanted in its place. This approach may help alleviate ocular pressure, which is currently the only treatment that has been shown to ameliorate the symptoms of glaucoma.

Substrate surface geography and its relation to cell guidance and differentiation should also be examined in future studies. The alignment of regenerated photoreceptors, for example, is important for their proper function. Materials with transverse channels should be fabricated using 3D printing or more traditional microfabrication techniques. Channel width, spacing, and chemistry should be investigated in order to identify optimum conditions for photoreceptor cell guidance. 3D printing is a promising approach for controlling polymer microstructure. Using this method, intricately structured materials made of functionalized biomolecules or synthetic degradable and non-degradable polymers can be fabricated directly in a single step. Furthermore, combinations of materials and structures can be employed in order to build multi-layered materials. An artificial retina should be created using this multi-layered approach. For example, a porous choroidal layer should be printed with encapsulated endothelial cells, followed by a thin, acellular transport membrane (artificial Bruch's membrane). Thereafter, RPE cells should be seeded, followed by a soft hydrogel layer with encapsulated photoreceptor precursor cells. In essence, a total artificial retina with patient-specific cells should be constructed *in vitro*. These artificial retinal materials should be used to study disease development *in vitro*, offering an accessible, disposable platform for studying pathophysiology. Furthermore, corrected cells should be seeded in

this artificial retina and thereby used to demonstrate correct retinal function, allowing *in vitro* trouble shooting before commitment to *in vivo* transplantation. After demonstration of appropriate function, this entire construct should be transplanted to the diseased sub-retinal space, replacing all layers of degenerated tissue. Alternatively, selected layers, grown in close proximity to anatomically correct surrounding cells, could be detached from the construct and transplanted in isolation.

## APPENDIX A

### MATERIALS AND METHODS

This chapter describes the fabrication and characterization of biomaterials, including degradable scaffolds, coated nanoparticles, and hydrogels. The first section describes the polymers, photoinitiators, surfactants and approaches used to create property-controlled biomaterials. In the second section, characterization techniques are described including methods for analyzing structure, morphology, surface chemistry, water uptake, and compressive modulus. Lastly, methods used to determine the impact of polymer properties on bioactivity are delineated. Descriptions of cell culture lines, media, and methods are provided.

#### Materials and Sample Preparation

##### Monomers and Polymers

Several commercially available polymers were used in this study to elucidate the effect and control of biochemical properties, mechanical properties, and morphology. Degradable polymers used include poly(D,L-lactide-co-glycolide) (PLGA, Resomer<sup>®</sup> RG 503; Boehringer Ingelheim KG, Ingelheim, Germany), chitosan (96.1% deacetylation, 1% w/v in 1% v/v acetic acid 35 cps, Sigma Aldrich, St. Louis, MO), and gelatin (Knox original unflavored gelatin). Non-degradable monomers and pre-polymers used include poly(ethylene glycol) diacrylate (PEGDA, MW 575, Sigma-Aldrich), PEG dimethacrylate (PEGDMA, MW 875, Sigma-Aldrich), PEG methacrylate (PEGMA, MW 500, Sigma-Aldrich), glycerol diacrylate (glycerol 1,3-diglycerolate diacrylate, Sigma-Aldrich), 3-(acryloyloxy)-2-hydroxypropyl methacrylate (AOHPMA, Sigma-Aldrich), poly(dimethyl siloxane) (PDMS, SYLGARD<sup>®</sup> 184 silicone elastomer kit, Dow Corning, Midland, MI), and acrylic acid (Sigma-Aldrich). The chemical structures of these molecules are shown in Figure 36.

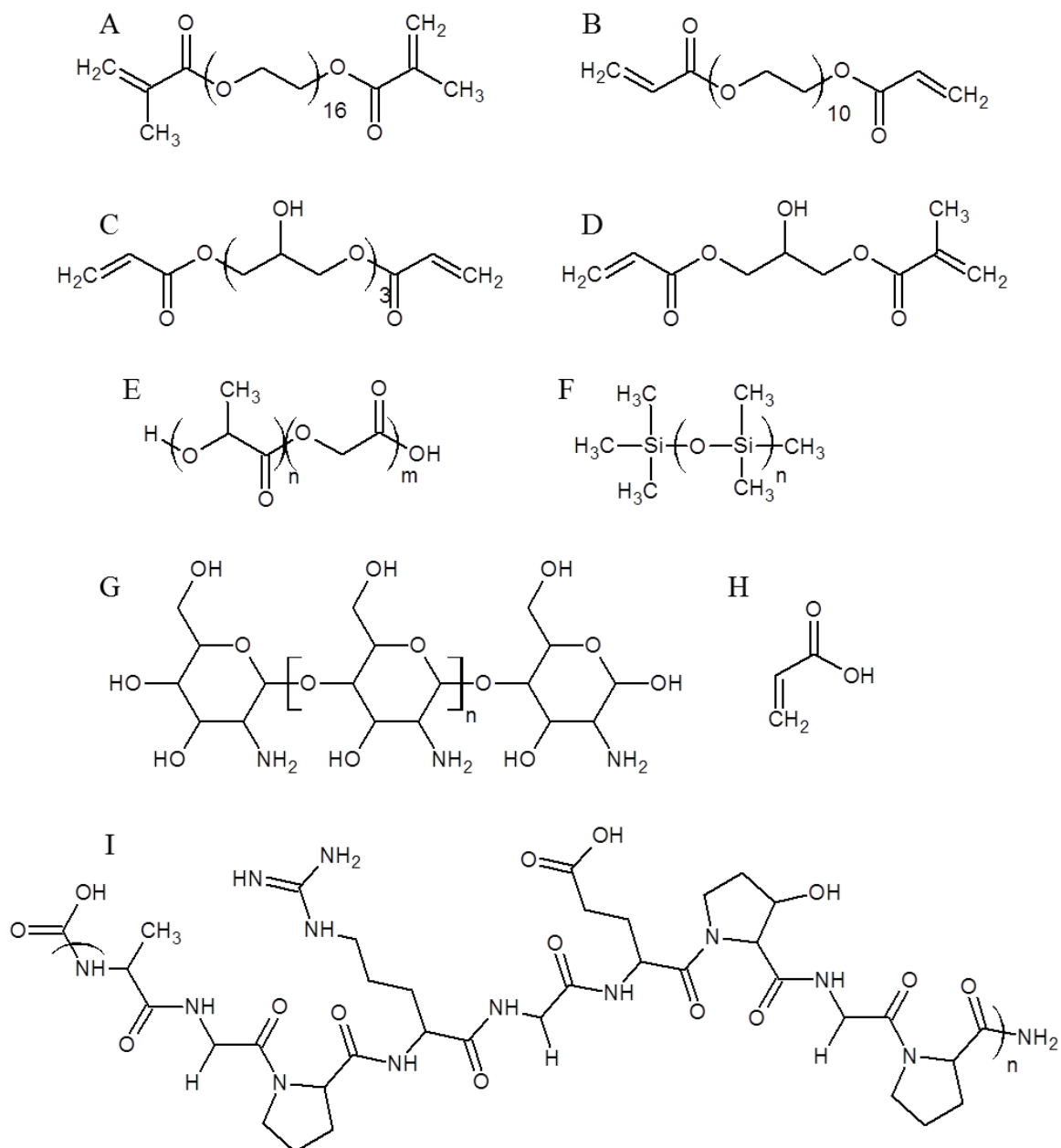


Figure 36. Monomers and prepolymers used to create property-controlled biomaterials, including A) PEGDMA, B) PEGDA, C) glycerol diacrylate, D) AOHPMA, E) PLGA, F) PDMS, G) chitosan, H) acrylic acid and I) gelatin

Degradable PLGA scaffolds were prepared using solvent casting and particle leaching. PLGA (200 mg) was dissolved in dichloromethane (3 mL), mixed with sodium chloride (2 g), then poured into a glass petri dish. This slurry was dried at room

temperature and pressure for 2 to 3 hours, and then the scaffolds were immersed in excess distilled water for 48 hours. Finally, PLGA scaffolds were freeze dried and stored in a desiccator until use.

To demonstrate the importance of biocompatibility, copper nanoparticles were coated with chitosan by first coating with surfactant. Copper nanoparticles (50 mg) were placed in a 20 mL glass vial and suspended in 10 mL of a dilute solution of Tween<sup>®</sup> 80 (5 mg/mL in nanopure water) by mixing overnight with a magnetic stir bar. The resulting solution was then dialyzed (MWCO 3500) against nanopure water for 6 hours. Meanwhile, a solution of chitosan was prepared by mixing chitosan (50 mg) with 1% v/v acetic acid (10 mL) to homogeneity, adjusting the pH to ~5.8 with 1 M sodium hydroxide, and then adding acetate buffer (50 mM, pH 5.5) to a final volume of 20 mL. To accomplish the final chitosan coating, 1 mL of dialyzed particles was mixed with 9 mL of the chitosan solution overnight. The finished particles were then centrifuged at 4000 rpm for 15 minutes, the supernatant was decanted, and the particles were resuspended to the desired concentration with nanopure water. To adequately characterize these coated particles, a small batch was prepared using rhodamine-conjugated chitosan. To conjugate the fluorescent molecule to chitosan, 100 mg 1-ethyl-3-(3-dimethylaminopropyl) carbodiimide HCl (EDC, Thermo Scientific, Rockford, IL), 50 mg N-hydroxysulfosuccinimide (sulfo-NHS, Thermo Scientific), and 5 mg Rhodamine B (Sigma-Aldrich) were dissolved in 0.1 M 2-(N-mopholino)ethanesulfonic (MES) buffer (1 mL) with the pH adjusted to 6. After mixing for two hours, this solution (1 mL) was added to a 5 mg/mL chitosan solution (9 mL) and allowed to react for six hours. The resulting product was dialyzed (MWCO 10,000) against nanopure water for 2 days and lyophilized. The rhodamine-conjugated chitosan was used to coat Cu NPs using the same method as described above.

To make chitosan hydrogels, chitosan was functionalized with methacrylate groups by a Michael addition reaction based on a previously reported method.<sup>136</sup> First, 1

g of chitosan was dissolved in 50 mL 1% acetic acid with 40 mL ethanol and mixed until homogenous. Thereafter, 5 mL AOHPMA was added dropwise while stirring. This mixture was allowed to react for 48 hours at room temperature.

The compressive moduli of gelatin, PDMS, and cross-linked PEG were measured to compare to ocular tissues. Gelatin samples were prepared by mixing 4 g of gelatin crystals with 29 mL of cold saline solution. Boiling saline solution (88 mL) was added to this mixture, and the resulting solution was stirred to homogeneity, poured into a petri dish, and refrigerated for 24 hours. PDMS samples were formed using a 10:1 ratio of base to cross-linker. The blend was mixed by vortexing, poured into a petri dish, and cured in an oven for two days at 50 °C. Soft cross-linked PEG samples were formed using 22.5 weight percent (wt%) PEGDMA, 22.5 wt% PEGMA and 0.1 wt% photoinitiator (Irgacure-651, Ciba Specialty Chemicals, Tarrytown, NY), in saline solution. Stiff cross-linked PEG samples were formed using 55 wt% PEGDMA, 22.5 wt% PEGMA, and 0.1 wt% photoinitiator in saline solution. These mixtures were vortexed and then photopolymerized with 365 nm light for 10 minutes in a laminate glass mold.

### Surfactants

Various surfactants were used as polymerization templates, including polyoxyethylene cetyl ethers (Brij<sup>®</sup>), PEG/PPG [poly(propylene glycol)] block copolymers (Pluronic<sup>®</sup>), polysorbate detergents (Tween<sup>®</sup>), and quaternary ammonium salts. General chemical structures of these surfactants are shown in Figure 37. Within each surfactant family, varying hydrophobic and/or hydrophilic chain lengths were used (see Table 9) to vary the geometry of self-assembled mesophases. It should be noted that Pluronic<sup>®</sup> 31R1 has inverse copolymer blocks: PPG ends with a PEG core. Furthermore, unlike surfactants listed from the same family, Tween<sup>®</sup> 80 is mono-unsaturated. Lastly,

DTAC is a chloride salt, while the other quaternary ammonium salts investigated are bromide salts. All surfactants were purchased from Sigma-Aldrich and used as received.

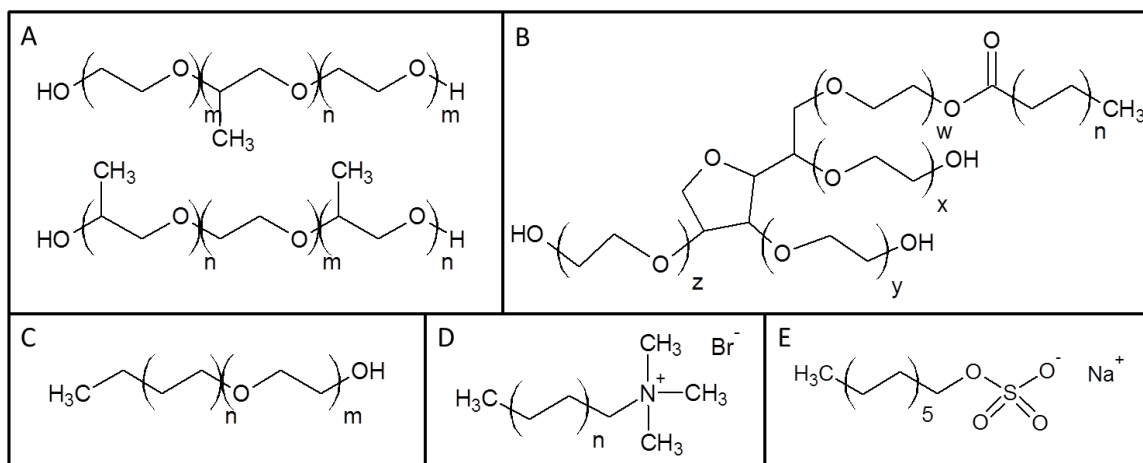


Figure 37. Chemical structures of surfactants used for templating, including A) Pluronic block copolymers, B) Tween, C) Brij, D) quaternary ammonium salts, and E) sodium dodecyl sulfate.

### Polymerization and Processing

Surfactant templated hydrogels were prepared by mixing pre-polymer, surfactant, solvent, (water or dilute acetic acid), and photoinitiator at the desired concentrations in a small glass vial by vortexing and gentle heating, when necessary. The chemical structures of the two photoinitiators (Irgacure<sup>®</sup> 651 and 2959, BASF, Florham Park, NJ) used in these studies, along with their radical species, are shown in Figure 38. In order to prevent oxygen quenching of free radicals during polymerization, laminate molds were constructed using glass slides and small binder clips (see Figure 39). A small amount of each mixture was transferred to the glass mold using a pipette and capillary action and polymerized by exposing the mold to UV light (100 W mercury spot lamp, UVP LLC, Upland, CA) for ten minutes. After polymerization, molds were deconstructed and the thin polymers were cut with 5 mm or 8 mm biopsy punches.

Table 9. Chain lengths of surfactants used for templating

	Hydrophilic Length (m or w + x + y + z)	Hydrophobic Length (n)
<b>Pluronic</b>		
L35	11	16
L92	8	50
P123	20	69
P121	5	68
31R1	7	25
<b>Brij</b>		
30	23	5
56	10	7
52	2	7
<b>Tween</b>		
20	20	5
60	20	8
80	20	8
<b>Quat. Amm. Salts</b>		
DTAC	-	12
DTAB	-	12
TTAB	-	14
CTAB	-	16

Directly after being polymerized and punched, 5 mm samples were transferred to excess extraction solvent (acetone, ethanol, or ethanol/saline blend) for seven days, with solvent exchanged on day one and day three. For surfactant extraction studies, samples were removed from the extraction solvent at the desired time point, dried overnight in a vacuum oven and weighed. This weight was compared to the weight of samples dried directly after polymerization to obtain a measure of surfactant removal (% initial dry weight).



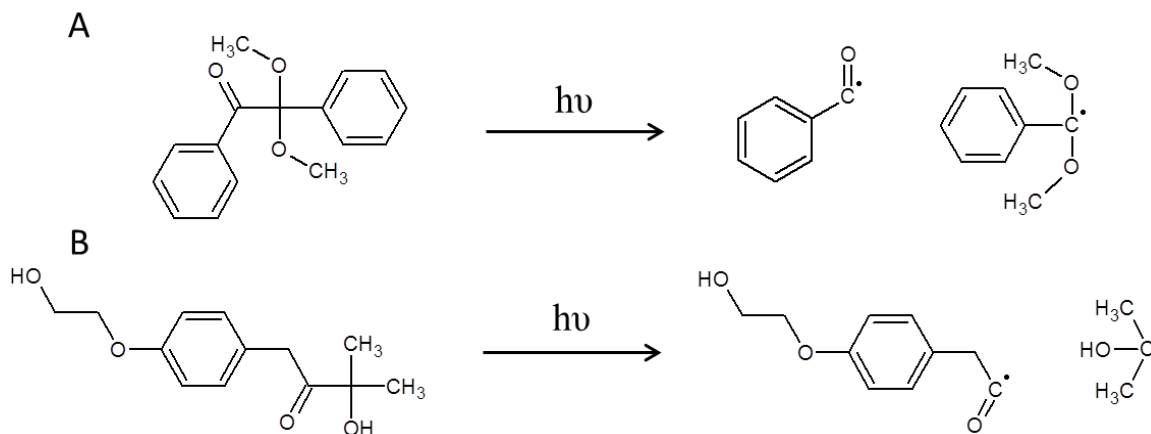


Figure 38. Schematic of the cleavage of A) Irgacure<sup>®</sup> 651 and B) Irgacure<sup>®</sup> 2959 upon exposure to UV light to yield two free radicals.

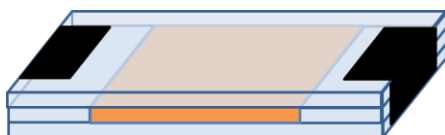


Figure 39. Drawing of glass mold used for polymerization of surfactant templated pre-polymer (orange) constructed using whole and fragmented glass slides (blue), and small binder clips (black)

## Characterization

### Chemical Composition

The surface functionality of coated copper nanoparticles was analyzed using x-ray photoelectron spectroscopy (XPS, Axis Ultra XPS, Kratos, Chestnut Ridge, NY) and confocal microscopy. For XPS analysis, 20  $\mu\text{L}$  droplets of each solution were carefully pipetted onto a small square of clean, heavy duty aluminum foil. The droplets were allowed to dry, and then the resulting spot was analyzed. Data were calibrated and analyzed using XPS software (CasaXPS 2.3.15, Casa Software Ltd., Estepona, Spain).

The area under the curve for each atomic signal was calculated using an “area under the

curve” function of GraphPad Prism (version 5.02 for Windows, GraphPad Software, San Diego, CA) and used to estimate ratios of the number of atoms on the surface of the particles. The confocal microscopic analysis was conducted using rhodamine-conjugated chitosan. For imaging, two coverslips were placed on a glass slide spaced about 3 cm apart to form a thin chamber. A drop of copper particles coated with fluorescent-labeled chitosan was added between coverslips. Another coverslip was placed on top of this chamber to facilitate uniform thickness and to spread the drop. The arrangement was sealed using clear fingernail polish. Images were acquired using a Bio-Rad Radiance 2100 multi-photon microscope (Bio-Rad Laboratories, Hercules, CA). The images were processed using Image J (Image Processing and Analysis in Java, Version 1.46b).

### Structure

The morphology of many samples was examined using scanning electron microscopy (SEM). Samples with attached cells were fixed with 4% paraformaldehyde and stained with osmium tetroxide. Samples were then washed with .1mM of cacodylate buffer solution before being completely dried via critical point drying (CPD). Samples without cells were examined directly after being lyophilized. After drying, samples were affixed to an aluminum SEM stub using double-sided tape or a silver colloid adhesive. A gold-palladium coating was applied using an argon beam K550 sputter coater (Emitech Ltd., Kent, England). Images were captured using a Hitachi S-4800 SEM (Hitachi High-Technologies, Ontario, Canada) at an accelerating voltage of 4-5 kV.

The size of coated and uncoated copper nanoparticles was measured by JEOL JEM-1230 transmission electron microscope equipped with a Gatan UltraScan 1000 2kx2k CCD acquisition system. A small drop (10  $\mu$ L) of sample solution was left on a 400-mesh TEM copper grid that was pre-coated with a Formvar<sup>®</sup> 0.5% solution in ethylene dichloride film (Electron Microscopy Sciences, Hatfield, PA) for 2 minutes. Whatman<sup>®</sup> filter paper was then used to remove any excess liquid and the grid was air

dried. The TEM images were processed using Image J. The hydrodynamic diameter and surface charge of particles in solution were measured in distilled water at 25 °C using dynamic light scattering (Zeta Sizer Nano ZS, Malvern Instruments, Southborough, MA).

To examine the structure of templated hydrogels, small angle x-ray scattering (SAXS) and polarized light microscopy (PLM) were employed. For SAXS, a small amount of pre-polymerized mixture was placed in the instrument sample holder between two pieces of Mylar film. Samples were analyzed using a Nonius FR590 SAXS apparatus equipped with a standard Röntgen tube with a Ni-filtered Cu K $\alpha$  line of 1.54 Å as the radiation source at an intensity of 35 kV and 20 mA, a Kratky type collimation system, and a PSD 50M position-sensitive linear detector (Hecus M. Braun, Gras, Austria). Each sample was then polymerized, in the holder, as described above, and a second profile was collected using the same settings as before polymerization. To further examine structure, a small amount of pre-polymerized sample was placed between a glass slide and cover slip and examined using PLM (Eclipse E600 POL, Nikon Instruments Inc., Melville, NY).

### Physical Properties

To examine water uptake of various samples, 8mm disks were transferred to excess PBS for three days to reach equilibrium swelling. Samples were then removed from the liquid, patted dry, and weighed. After drying overnight, the samples were weighed again. The water uptake was calculated as follows:

$$WaterUptake(\%) = 100 \times \left( \frac{W_w - W_D}{W_D} \right) \quad (11)$$

where  $W_w$  and  $W_D$  represent the weight of the sample when wet and dry, respectively.

Polymer mechanical properties were measured using a dynamic mechanical analysis instrument (DMA Q800 V7.0 Build 113, TA Instruments, New Castle, DE) equipped with a submersion compression clamp in static mode. Prior to each group of

measurements, the drive shaft position, clamp mass, clamp offset, and clamp compliance were calibrated according to suggested protocols. Each sample was carefully transferred to the basin of the clamp and any excess water or buffer surrounding the sample was removed using a syringe. Once the sample was installed, the top portion of the clamp was gently lowered onto the sample surface, the furnace was closed to maintain constant temperature and prevent disturbances, and a pre-load force of 0.0001 N was applied to the sample. The force was then gradually increased and displacement data were collected every 2 seconds as the sample was compressed. All samples were assumed to be cylindrical.

From the recorded displacement (reported in  $\mu\text{m}$ ) and static force (reported in N) values, the infinitesimal strain ( $\epsilon$ ) and stress ( $\sigma$ ) were calculated as follows:

$$\epsilon = \frac{D - D_0}{z} \quad (12)$$

$$\sigma = \frac{C * F}{A} \quad (13)$$

where D is displacement,  $D_0$  is initial displacement (which accounts for any changes brought about by the initial pre-load force), z is the sample thickness, F is static force, A is sample cross-sectional area, and C is a necessary correction factor provided by the instrument manufacturer based on sample geometry. Modulus is defined as the ratio of stress increase to strain increase in the elastic deformation region. Values of stress at absolute strain values between 0 and 0.1 (0% and 10% deformation) were plotted and the slope estimated using a trend line function.

### Bioactivity

#### Cell Culture and Seeding

A549 (adenocarcinomic human alveolar basal epithelial) cells were used to evaluate the toxicity of chitosan coated copper nanoparticles. These cells were grown in

RPMI-1640 medium (Gibco<sup>®</sup>, Life Technologies Corporations, NY) at 37 °C and 5% CO<sub>2</sub>. The media were supplemented with 10% fetal bovine serum (FBS, Atlanta Biologicals, GA), 10 mM HEPES (Gibco<sup>®</sup>), 50 µg/mL gentamycin sulfate (Cellgro, VA), 1 mM sodium pyruvate (Gibco<sup>®</sup>), and 1 mM Glutamax<sup>™</sup> (Gibco<sup>®</sup>).

For all other *in vitro* studies, fibroblasts were isolated from dsRed mouse umbilical cord and de-differentiated using a retroviral approach to yield murine induced pluripotent stem cells (MiPSCs), as described elsewhere.<sup>21,248</sup> For this study, MiPSCs were gently thawed from a frozen stock, centrifuged, and resuspended in MiPS media [Dulbecco's Modified Eagle Media with F12 (Gibco, Grand Island, NY) supplemented with 15% fetal bovine serum, 1% 100X non-essential amino acids (Gibco), 1% L-glutamine (Gibco), 1% Primocin (Gibco), and 8 nL/mL β-mercaptoethanol (Sigma-Aldrich)] then plated in a 6-well plate pre-coated with Matrigel (Growth factor reduced basement membrane matrix, Corning, Tewksbury, MA) and kept in a humidified, 37 °C incubator with 5% CO<sub>2</sub>. Media was replaced daily and cells were divided and re-plated every two days.

Prior to being seeded with MiPSCs, polymer scaffolds were coated with Matrigel, which was allowed to adsorb and gel on the surface at room temperature for one hour. Meanwhile, cells were removed from their plate and re-suspended as described above. Each 5 mm sample was seeded with  $1.5 \times 10^4$  -  $2 \times 10^4$  MiPSCs. Once the cells attached to the surface, an additional 100 µL differentiation media [DMEM F-12 media (Gibco, Grand Island, NY) containing 2% B27 supplement (Gibco) 1% N2 supplement (Gibco), 1% L-glutamine (Gibco), 1% 100x NEAA (Gibco), 1% Primocin (Invitrogen, Grand Island, NY), 1ng/ml noggin (R&D Systems, Minneapolis, MN), 1ng/ml Dkk-1 (R&D Systems), 1ng/ml IGF-1 (R&D Systems) and 0.5ng/ml bFGF (R&D Systems)], was added to each well. The plate was then incubated in a humid 37 °C environment with 5% CO<sub>2</sub>. Media was replaced once per day. Attachment, growth, and differentiation were monitored using phase contrast microscopy.

### Proliferation and Viability

Cell proliferation assays were used to measure cell density on PLGA scaffolds, toxicity of coated nanoparticles and surfactant templated crosslinked PEG, and attachment to templated crosslinked PEG. The selected MTS/MTT assay correlates cell viability to the activity of NADPH-dependent cellular oxidoreductase enzyme, which reduces the tetrazolium dye MTT [3-(4,5-dimethylthiazol-2-yl)-2,5-diphenyltetrazolium bromide)] to its purple, insoluble formazan.

For cell proliferation and attachment studies, differentiating MiPSCs were grown on 5 mm round punches of polymer in a 96 well plate for 1, 3, 8, and 16 days. To serve as a negative control, scaffolds without cells were also allowed to incubate in the same conditions for the same amount of time. To serve as a positive control, several wells of a coated 96-well plate were seeded with a known number of cells ( $1.5 \times 10^5$ ) on the day prior to analysis. The following day, each scaffold was transferred to a fresh 100  $\mu$ L of media. MTT reagent (10  $\mu$ L, Millipore, Billerica, MA) was added to each well and the plate was incubated at cell culture conditions for 4 hours. The solution was removed from each well and discarded, leaving behind insoluble MTT crystals. These crystals were dissolved by adding 100  $\mu$ L of developing solution (0.04 M HCl in isopropanol) to each well and mixing to homogeneity. Scaffolds were then removed from their wells and the absorbance was measured at 570 nm (Tecan Infinite M200 Pro, Tecan Group Ltd., Männedorf, Switzerland). Relative absorbance was obtained by subtracting the average absorbance for cell-free sample wells and dividing by the average absorbance of positive control wells.

For surfactant extraction studies, crosslinked PEG samples were washed three times (1 hr per wash) with excess PBS after seven days of surfactant extraction in solvent (see above). Each 5 mm diameter sample was then incubated in 200  $\mu$ L MiPS media overnight at 37 °C. The following day, 150  $\mu$ L of this conditioned media was used to feed cells growing in a corresponding 96-well plate. One day prior to analysis, MiPSCs were

removed from the 6-well plate using 0.25% trypsin with EDTA (Gibco), centrifuged, and resuspended in MiPS media. A Matrigel pre-coated 96-well plate was then seeded with MiPSCs at a concentration of 10,000 cells per well and incubated overnight before being fed conditioned media. From this point, the MTT assay was performed in the same manner described above for proliferation studies.

In the case of copper nanoparticles, the viability of A549 cells ( $10^4$  cells/well) was used to measure toxicity. After 24 hours, the medium was discarded and replaced with 100  $\mu$ L fresh media. Various concentrations (0.01 – 0.09  $\mu$ g/mL) of each treatment in phosphate buffered saline (PBS, Invitrogen) were then added to each well at a volume of 100  $\mu$ L. The cells were incubated for either 24 or 52 hours, the treatment removed, and fresh media (100  $\mu$ L) added. 20  $\mu$ L of CellTiter 96<sup>®</sup> Aqueous One solution reagent (Promega Corporation, Madison, WI) was added to each well. The cells were incubated between one and four hours, then the formazan product was quantified by spectrophotometric analysis (SpectraMax Plus384, Molecular Devices, Sunnyvale, CA) using the absorbance at 490 nm.

Toxicity was also evaluated using reactive oxygen species (ROS) production, which was estimated by measuring the oxidation of dihydroethidium (DHE, Molecular Probes, Eugene, Oregon), which becomes fluorescent upon oxidation with superoxide. A549 cells ( $2-4 \times 10^5$  cells per 60 mm Petri dish) were cultured 24 hours, exposed to one of the three copper nanoparticle treatments (2 mL at 50  $\mu$ g Cu NPs per mL) for 24 hours, and then tested for DHE oxidation as described previously.<sup>283</sup> Briefly, the cells were washed once with PBS and labeled at 37 °C for 40 minutes in PBS containing 5 mM pyruvate with DHE (10  $\mu$ M; in 1% DMSO). Culture plates were placed on ice to stop the labeling, trypsinized, and resuspended in ice-cold PBS. Samples were analyzed using a FACScan flow cytometer (Becton Dickinson Immunocytometry Systems, Inc., Mountain View, CA; excitation 488 nm, emission 585 nm band-pass filters). The mean fluorescence intensity (MFI) of 10,000 cells was analyzed in each sample and corrected

for auto-fluorescence from unlabeled cells. The MFI data were normalized to levels from A549 cells treated with PBS only.

### Animals

An inflammation mouse model was used to study the *in vivo* effect of chitosan on the toxicity of copper nanoparticles. Mice (C57Bl/6, males, 6 weeks old, Jackson Laboratory, Bar Harbor, ME) were acclimatized for 10 days prior to exposure. Each mouse was exposed twice with 50-100  $\mu\text{L}$  of exposure solution by nasal instillation with a 1 hour interval between each dosing. The total dose of copper nanoparticles in each experimental group, as measured by inductively coupled plasma-mass spectrometry (ICP-MS, X Series, Thermo Scientific, Waltham, MA, USA) was approximately 30  $\mu\text{g}/\text{mouse}$ . Nasal instillation was conducted under anesthesia by inhalation of isoflurane (3 %) using a precision Fortec vaporizer (Cyprane, Keighley, UK). Naïve mice (mice with no exposure) served as a control group. All mice were euthanized 24 hours post exposure by overdose inhalation of isoflurane, cervical dislocation and exsanguination, after which bronchoalveolar lavage (BAL) fluid and lung tissues were collected.

The lungs from 6 mice in each group were lavaged *in situ* three times with approximately 1 mL of sterile saline. The lavage fluid was centrifuged, the total white blood cells were counted using a hemocytometer and the supernatants were stored at  $-80^{\circ}\text{C}$ . For differential cell counts, resuspended cells in Hank's balanced salt solution and fetal calf serum, were spun (800 x g, 3 min, Cytospin 4, Thermo Shandon, Thermo Scientific, Waltham, MA, USA) onto microscope slides and air-dried. The cells were then stained using HEMA 3<sup>®</sup> stain set (PROTOCOL<sup>®</sup>, Fisher Scientific Company LLC, Kalamazoo, MI) and the number of macrophages, neutrophils and lymphocytes (total of 400 total cells per each animal) were counted.

A Bradford protein assay (Bio-Rad Laboratories, Inc., Hercules, CA, USA) was used to measure total protein levels in BAL fluid supernatants and lactate dehydrogenase



(LDH) activity was determined by a Cytotoxicity Detection Kit (Roche Diagnostics, Penzberg, Germany). Concentrations of selected inflammatory cytokines/chemokines were measured in the BAL fluid using a multiplexed fluorescent bead-based immunoassay (BioRad Laboratories, Inc., Hercules, CA). The lowest limit of detection (LLOD) for cytokine assays was calculated by dividing the lowest detected point on the standard curve by  $\sqrt{2}$ .

The lungs from mice in each group were harvested at the time of necropsy and stored at  $-80^{\circ}\text{C}$ . Tissues were freeze-dried and subsequently weighed. Dried lungs were placed in 50 mL digestion tubes and high purity nitric acid and hydrochloric acid were added (Optima grade, Fisher Scientific, Pittsburgh, PA, USA). Tissues were then digested in a 36-well HotBlock™ (Environmental Express, Mt. Pleasant, SC, USA) at  $95^{\circ}\text{C}$  for 6 hour. The concentration of copper ions was determined by inductively coupled plasma-mass spectrometry (ICP-MS, X Series, Thermo Scientific, Waltham, MA, USA). Each sample was spiked with an internal standard at  $20\ \mu\text{g/L}$ .

For mechanical testing of mouse retinal modulus, C57Bl/6J were used as a *wild type* control line (stock number 000664; Jackson Laboratories, Bar Harbor, ME). To test the effect of retinal degeneration on mouse retinal modulus we used the mutant line C3H/HeJ<sup>Pde6rd1</sup> (stock number 000659; Jackson Labs), which develops rapid retinal degeneration due to rod photoreceptor cell death. Mice were euthanized using CO<sub>2</sub> inhalation, followed by cervical dislocation. Eyes were enucleated and the anterior segment was removed by carefully cutting around the circumference of the eye along the limbus. Once exposed, the lens and vitreous were removed, leaving the posterior cup consisting of the retina, choroid and sclera. Retinas were then carefully separated and maintained in their natural cup-like form with the cupped portion open, facing up in the sample basin. The edges of the retinal cup were then teased out to their most extreme limit without damaging the sample.

Pig eyes (Iowa outbred swine, 5 months of age) were obtained from a local slaughterhouse, transported on ice and dissected within two hours of harvest. Whole pig globes were processed in the same manner as mouse eyes above, except the retina was not removed from the choroid. Instead, a 5mm biopsy punch was used to cut out retinal samples for modulus testing, which were then separated from the choroid and other layers. A biopsy punch was also used to isolate specimens of cornea, choroid and sclera for testing. Prior to modulus measurements, all tissues were maintained in 1X Hank's buffered salt solution (HBSS, 340 mOsm/L, Sigma-Aldrich, St. Louis, MO). All retinal thicknesses (mouse and pig) were estimated based on histology.

## REFERENCES

- (1) Fernald, R. D. (1997) The Evolution of Eyes. *Brain. Behav. Evol.* 50, 253–259.
- (2) Willoughby, C. E., Ponzin, D., Ferrari, S., Lobo, A., Landau, K., and Omid, Y. (2010) Anatomy and physiology of the human eye: effects of mucopolysaccharidoses disease on structure and function - a review. *Clin. Experiment. Ophthalmol.* 38, 2–11.
- (3) Coleman, H. R., Chan, C.-C., Ferris, F. L., and Chew, E. Y. (2008) Age-related macular degeneration. *Lancet* 372, 1835–45.
- (4) Hartong, D. T., Berson, E. L., and Dryja, T. P. (2006) Retinitis pigmentosa. *Lancet* 368, 1795–809.
- (5) Ferrara, N., Damico, L., Shams, N., Lowman, H., and Kim, R. (2006) Development of ranibizumab, an anti-vascular endothelial growth factor antigen binding fragment, as therapy for neovascular age-related macular degeneration. *Retina* 26, 859–70.
- (6) Gehrs, K. M., Anderson, D. H., Johnson, L. V, and Hageman, G. S. (2006) Age-related macular degeneration--emerging pathogenetic and therapeutic concepts. *Ann. Med.* 38, 450–71.
- (7) Den Hollander, A. I., Roepman, R., Koenekoop, R. K., and Cremers, F. P. M. (2008) Leber congenital amaurosis: genes, proteins and disease mechanisms. *Prog. Retin. Eye Res.* 27, 391–419.
- (8) Dagnelie, G. (2012) Retinal implants: emergence of a multidisciplinary field. *Curr. Opin. Neurol.* 25, 67–75.
- (9) Dowling, J. (2005) Artificial human vision. *Expert Rev. Med. Devices* 2, 73–85.
- (10) Barber, A. C., Hippert, C., Duran, Y., West, E. L., Bainbridge, J. W. B., Warren-Cornish, K., Luhmann, U. F. O., Lakowski, J., Sowden, J. C., Ali, R. R., and Pearson, R. A. (2013) Repair of the degenerate retina by photoreceptor transplantation. *Proc. Natl. Acad. Sci. U. S. A.* 110, 354–359.
- (11) Gonzalez-Cordero, A., West, E. L., Pearson, R. A., Duran, Y., Carvalho, L. S., Chu, C. J., Naeem, A., Blackford, S. J. I., Georgiadis, A., Lakowski, J., Hubank, M., Smith, A. J., Bainbridge, J. W. B., Sowden, J. C., and Ali, R. R. (2013) Photoreceptor precursors derived from three-dimensional embryonic stem cell cultures integrate and mature within adult degenerate retina. *Nat. Biotechnol.* 31, 741–+.
- (12) Gust, J., and Reh, T. A. (2011) Adult Donor Rod Photoreceptors Integrate into the Mature Mouse Retina. *Invest. Ophthalmol. Vis. Sci.* 52, 5266–5272.

- (13) Klassen, H., Sakaguchi, D. S., and Young, M. J. (2004) Stem cells and retinal repair. *Prog. Retin. Eye Res.* 23, 149–181.
- (14) La Torre, A., Lamba, D. A., Jayabalu, A., and Reh, T. A. (2012) Production and transplantation of retinal cells from human and mouse embryonic stem cells. *Methods Mol. Biol.* 884, 229–246.
- (15) Lakowski, J., Han, Y.-T., Pearson, R. A., Gonzalez-Cordero, A., West, E. L., Gualdoni, S., Barber, A. C., Hubank, M., Ali, R. R., and Sowden, J. C. (2011) Effective Transplantation of Photoreceptor Precursor Cells Selected Via Cell Surface Antigen Expression. *Stem Cells* 29, 1391–1404.
- (16) Lamba, D. A., Gust, J., and Reh, T. A. (2009) Transplantation of Human Embryonic Stem Cell-Derived Photoreceptors Restores Some Visual Function in Crx-Deficient Mice. *Cell Stem Cell* 4, 73–79.
- (17) Ma, J., Kabiell, M., Tucker, B. A., Ge, J., and Young, M. J. (2011) Combining chondroitinase ABC and growth factors promotes the integration of murine retinal progenitor cells transplanted into Rho(-/-) mice. *Mol. Vis.* 17, 1759–1770.
- (18) MacLaren, R. E., Pearson, R. A., MacNeil, A., Douglas, R. H., Salt, T. E., Akimoto, M., Swaroop, A., Sowden, J. C., and Ali, R. R. (2006) Retinal repair by transplantation of photoreceptor precursors. *Nature* 444, 203–207.
- (19) Tucker, B. A., Redenti, S. M., Jiang, C., Swift, J. S., Klassen, H. J., Smith, M. E., Wnek, G. E., and Young, M. J. (2010) The use of progenitor cell/biodegradable MMP2–PLGA polymer constructs to enhance cellular integration and retinal repopulation. *Biomaterials* 31, 9–19.
- (20) Yao, J., Tucker, B. A., Zhang, X., Checa-Casalengua, P., Herrero-Vanrell, R., and Young, M. J. (2011) Robust cell integration from co-transplantation of biodegradable MMP2-PLGA microspheres with retinal progenitor cells. *Biomaterials* 32, 1041–1050.
- (21) Tucker, B. A., Mullins, R. F., Streb, L. M., Anfinson, K., Eyestone, M. E., Kaalberg, E., Riker, M. J., Drack, A. V., Braun, T. A., and Stone, E. M. (2013) Patient-specific iPSC-derived photoreceptor precursor cells as a means to investigate retinitis pigmentosa. *Elife* 2, e00824.
- (22) West, E. L., Gonzalez-Cordero, A., Hippert, C., Osakada, F., Martinez-Barbera, J. P., Pearson, R. A., Sowden, J. C., Takahashi, M., and Ali, R. R. (2012) Defining the Integration Capacity of Embryonic Stem Cell-Derived Photoreceptor Precursors. *Stem Cells* 30, 1424–1435.
- (23) Biomaterials Market - 2017 | Polymer Biomaterials | MarketsandMarkets.

- (24) Hartmann, U., Sistani, F., and Steinhorst, U. H. (1999) Human and porcine anterior lens capsule as support for growing and grafting retinal pigment epithelium and iris pigment epithelium. *Graefe's Arch. Clin. Exp. Ophthalmol.* 237, 940–945.
- (25) Thumann, G., Schraermeyer, U., Bartz-Schmidt, K. U., and Heimann, K. (1997) Descemet's membrane as membranous support in RPE/IPE transplantation. *Curr. Eye Res.* 16, 1236–1238.
- (26) Tezel, T. H., Del Priore, L. V., and Kaplan, H. J. (2004) Reengineering of aged Bruch's membrane to enhance retinal pigment epithelium repopulation. *Invest. Ophthalmol. Vis. Sci.* 45, 3337–48.
- (27) Capeáns, C., Piñeiro, A., Pardo, M., Sueiro-López, C., Blanco, M. J., Domínguez, F., and Sánchez-Salorio, M. (2003) Amniotic membrane as support for human retinal pigment epithelium (RPE) cell growth. *Acta Ophthalmol. Scand.* 81, 271–7.
- (28) Stanzel, B. V., Espana, E. M., Grueterich, M., Kawakita, T., Parel, J.-M., Tseng, S. C. G., and Binder, S. (2005) Amniotic membrane maintains the phenotype of rabbit retinal pigment epithelial cells in culture. *Exp. Eye Res.* 80, 103–12.
- (29) Beutel, J., Greulich, L., Lüke, M., Ziemssen, F., Szurman, P., Bartz-Schmidt, K.-U., and Grisanti, S. (2007) Inner limiting membrane as membranous support in RPE sheet-transplantation. *Graefes Arch. Clin. Exp. Ophthalmol.* 245, 1469–73.
- (30) Olsen, D. (2003) Recombinant collagen and gelatin for drug delivery. *Adv. Drug Deliv. Rev.* 55, 1547–1567.
- (31) Collagen engineering for biomaterial use. *Clin. Mater.*
- (32) Li, Y., and Yu, S. M. (2013) Targeting and mimicking collagens via triple helical peptide assembly. *Curr. Opin. Chem. Biol.* 17, 968–75.
- (33) Silverman, M. S., and Hughes, S. E. (1989) Transplantation of photoreceptors to light-damaged retina. *Invest. Ophthalmol. Vis. Sci.* 30, 1684–90.
- (34) Del Priore, L. V., Tezel, T. H., and Kaplan, H. J. (2004) Survival of allogeneic porcine retinal pigment epithelial sheets after subretinal transplantation. *Invest. Ophthalmol. Vis. Sci.* 45, 985–92.
- (35) Silverman, M. S., Hughes, S. E., Valentino, T. L., and Liu, Y. (1992) Photoreceptor transplantation: Anatomic, electrophysiologic, and behavioral evidence for the functional reconstruction of retinas lacking photoreceptors. *Exp. Neurol.* 115, 87–94.
- (36) Khodair, M. A., Zarbin, M. A., and Townes-Anderson, E. (2003) Synaptic plasticity in mammalian photoreceptors prepared as sheets for retinal transplantation. *Invest. Ophthalmol. Vis. Sci.* 44, 4976–4988.

- (37) Bhatt, N. S., Newsome, D. A., Fenech, T., Hessburg, T. P., Diamond, J. G., Miceli, M. V, Kratz, K. E., and Oliver, P. D. (1994) Experimental transplantation of human retinal pigment epithelial cells on collagen substrates. *Am. J. Ophthalmol.* 117, 214–21.
- (38) Thumann, G., Hueber, A., Dinslage, S., Schaefer, F., Yasukawa, T., Kirchhof, B., Yafai, Y., Eichler, W., Bringmann, A., and Wiedemann, P. (2006) Characteristics of iris and retinal pigment epithelial cells cultured on collagen type I membranes. *Curr. Eye Res.* 31, 241–9.
- (39) Lu, J. T., Lee, C. J., Bent, S. F., Fishman, H. A., and Sabelman, E. E. (2007) Thin collagen film scaffolds for retinal epithelial cell culture. *Biomaterials* 28, 1486–94.
- (40) Imai, H., Honda, S., Kondo, N., Ishibashi, K., Tsukahara, Y., and Negi, A. (2007) The upregulation of angiogenic gene expression in cultured retinal pigment epithelial cells grown on type I collagen. *Curr. Eye Res.* 32, 903–10.
- (41) Daamen, W. F., Veerkamp, J. H., van Hest, J. C. M., and van Kuppevelt, T. H. (2007) Elastin as a biomaterial for tissue engineering. *Biomaterials* 28, 4378–98.
- (42) Waterhouse, A., Wise, S. G., Ng, M. K. C., and Weiss, A. S. (2011) Elastin as a nonthrombogenic biomaterial. *Tissue Eng. Part B. Rev.* 17, 93–9.
- (43) Annabi, N., Tsang, K., Mithieux, S. M., Nikkhah, M., Ameri, A., Khademhosseini, A., and Weiss, A. S. (2013) Highly Elastic Micropatterned Hydrogel for Engineering Functional Cardiac Tissue. *Adv. Funct. Mater.* 23.
- (44) Cao, J., Sun, C., Zhao, H., Xiao, Z., Chen, B., Gao, J., Zheng, T., Wu, W., Wu, S., Wang, J., and Dai, J. (2011) The use of laminin modified linear ordered collagen scaffolds loaded with laminin-binding ciliary neurotrophic factor for sciatic nerve regeneration in rats. *Biomaterials* 32, 3939–48.
- (45) Francisco, A. T., Mancino, R. J., Bowles, R. D., Brunger, J. M., Tainter, D. M., Chen, Y.-T., Richardson, W. J., Guilak, F., and Setton, L. A. (2013) Injectable laminin-functionalized hydrogel for nucleus pulposus regeneration. *Biomaterials* 34, 7381–8.
- (46) Swindle-Reilly, K. E., Papke, J. B., Kutosky, H. P., Throm, A., Hammer, J. A., Harkins, A. B., and Willits, R. K. (2012) The impact of laminin on 3D neurite extension in collagen gels. *J. Neural Eng.* 9, 046007.
- (47) Shapira-Schweitzer, K., and Seliktar, D. (2007) Matrix stiffness affects spontaneous contraction of cardiomyocytes cultured within a PEGylated fibrinogen biomaterial. *Acta Biomater.* 3, 33–41.
- (48) Iwasaki, N., Kasahara, Y., Yamane, S., Igarashi, T., Minami, A., and Nisimura, S. (2010) Chitosan-Based Hyaluronic Acid Hybrid Polymer Fibers as a Scaffold Biomaterial for Cartilage Tissue Engineering. *Polymers (Basel).* 3, 100–113.

- (49) Lai, J.-Y. (2012) Solvent Composition is Critical for Carbodiimide Cross-Linking of Hyaluronic Acid as an Ophthalmic Biomaterial. *Materials (Basel)*. 5, 1986–2002.
- (50) Yamane, S., Iwasaki, N., Majima, T., Funakoshi, T., Masuko, T., Harada, K., Minami, A., Monde, K., and Nishimura, S.-I. (2005) Feasibility of chitosan-based hyaluronic acid hybrid biomaterial for a novel scaffold in cartilage tissue engineering. *Biomaterials* 26, 611–9.
- (51) Vepari, C., and Kaplan, D. L. (2007) Silk as a Biomaterial. *Prog. Polym. Sci.* 32, 991–1007.
- (52) Wang, Y., Kim, H.-J., Vunjak-Novakovic, G., and Kaplan, D. L. (2006) Stem cell-based tissue engineering with silk biomaterials. *Biomaterials* 27, 6064–82.
- (53) Widhe, M., Johansson, J., Hedhammar, M., and Rising, A. (2012) Invited review current progress and limitations of spider silk for biomedical applications. *Biopolymers* 97, 468–78.
- (54) Czaja, W. K., Young, D. J., Kawecki, M., and Brown, R. M. (2007) The future prospects of microbial cellulose in biomedical applications. *Biomacromolecules* 8, 1–12.
- (55) Sun, J., and Tan, H. (2013) Alginate-Based Biomaterials for Regenerative Medicine Applications. *Materials (Basel)*. 6, 1285–1309.
- (56) Torres, F. G., Commeaux, S., and Troncoso, O. P. (2013) Starch- based biomaterials for wound- dressing applications. *Starch - Stärke* 65, 543–551.
- (57) Kim, I.-Y., Seo, S.-J., Moon, H.-S., Yoo, M.-K., Park, I.-Y., Kim, B.-C., and Cho, C.-S. (2008) Chitosan and its derivatives for tissue engineering applications. *Biotechnol. Adv.* 26, 1–21.
- (58) Shi, C. M., Zhu, Y., Ran, X. Z., Wang, M., Su, Y. P., and Cheng, T. M. (2006) Therapeutic potential of chitosan and its derivatives in regenerative medicine. *J. Surg. Res.* 133, 185–192.
- (59) De Souza, R., Zahedi, P., Allen, C. J., and Piquette-Miller, M. (2009) Biocompatibility of injectable chitosan–phospholipid implant systems. *Biomaterials* 30, 3818–3824.
- (60) Mi, F.-L., Tan, Y.-C., Liang, H.-F., and Sung, H.-W. (2002) In vivo biocompatibility and degradability of a novel injectable-chitosan-based implant. *Biomaterials* 23, 181–191.
- (61) No, H. K., Young Park, N., Ho Lee, S., and Meyers, S. P. (2002) Antibacterial activity of chitosans and chitosan oligomers with different molecular weights. *Int. J. Food Microbiol.* 74, 65–72.



- (62) Du, Y., Zhao, Y., Dai, S., and Yang, B. (2009) Preparation of water-soluble chitosan from shrimp shell and its antibacterial activity. *Innov. Food Sci. Emerg. Technol.* 10, 103–107.
- (63) Pusateri, A. E., McCarthy, S. J., Gregory, K. W., Harris, R. A., Cardenas, L., McManus, A. T., and Goodwin, C. W. (2003) Effect of a chitosan-based hemostatic dressing on blood loss and survival in a model of severe venous hemorrhage and hepatic injury in swine. *J. Trauma-Injury Infect. Crit. Care* 54, 177–182.
- (64) Wedmore, I., McManus, J. G., Pusateri, A. E., and Holcomb, J. B. (2006) A special report on the chitosan-based hemostatic dressing: Experience in current combat operations. *J. Trauma-Injury Infect. Crit. Care* 60, 655–658.
- (65) Brown, M. A., Daya, M. R., and Worley, J. A. (2009) Experience with Chitosan Dressings in a Civilian Ems System. *J. Emerg. Med.* 37, 1–7.
- (66) Paul, W., and Sharma, C. P. (2004) Chitosan and alginate wound dressings: a short review. *Trends Biomater. Artif. Organs* 18, 18–23.
- (67) Gustafson, S. B., Fulkerson, P., Bildfell, R., Aguilera, L., and Hazzard, T. M. (2007) Chitosan dressing provides hemostasis in swine femoral arterial injury model. *Prehospital Emerg. Care* 11, 172–178.
- (68) Valentine, R., Athanasiadis, T., Moratti, S., Robinson, S., and Wormald, P.-J. (2009) The efficacy of a novel chitosan gel on hemostasis after endoscopic sinus surgery in a sheep model of chronic rhinosinusitis RID B-4422-2009. *Am. J. Rhinol. Allergy* 23, 71–75.
- (69) Gorzelanny, C., Poepelmann, B., Pappelbaum, K., Moerschbacher, B. M., and Schneider, S. W. (2010) Human macrophage activation triggered by chitotriosidase-mediated chitin and chitosan degradation. *Biomaterials* 31, 8556–8563.
- (70) Guzman-Morales, J., Ariganello, M. B., Hammami, I., Thibault, M., Jolicoeur, M., and Hoemann, C. D. (2011) Biodegradable chitosan particles induce chemokine release and negligible arginase-1 activity compared to IL-4 in murine bone marrow-derived macrophages. *Biochem. Biophys. Res. Commun.* 405, 538–544.
- (71) Liu, X. F., Guan, Y. L., Yang, D. Z., Li, Z., and De Yao, K. (2001) Antibacterial action of chitosan and carboxymethylated chitosan. *J. Appl. Polym. Sci.* 79, 1324–1335.
- (72) Chung, Y. C., Wang, H. L., Chen, Y. M., and Li, S. L. (2003) Effect of abiotic factors on the antibacterial activity of chitosan against waterborne pathogens. *Bioresour. Technol.* 88, 179–184.



- (73) Hamilton, V., Yuan, Y., Rigney, D. A., Puckett, A. D., Ong, J. L., Yang, Y., Elder, S. H., and Bumgardner, J. D. (2006) Characterization of chitosan films and effects on fibroblast cell attachment and proliferation. *J. Mater. Sci. Med.* 17, 1373–1381.
- (74) Howling, G. I., Dettmar, P. W., Goddard, P. A., Hampson, F. C., Dornish, M., and Wood, E. J. (2001) The effect of chitin and chitosan on the proliferation of human skin fibroblasts and keratinocytes in vitro. *Biomaterials* 22, 2959–2966.
- (75) Scanga, V. I., Goraltchouk, A., Nussaiba, N., Shoichet, M. S., and Morshead, C. M. (2010) Biomaterials for neural-tissue engineering - Chitosan supports the survival, migration, and differentiation of adult-derived neural stem and progenitor cells. *Can. J. Chem. Can. Chim.* 88, 277–287.
- (76) Leipzig, N. D., Wylie, R. G., Kim, H., and Shoichet, M. S. (2011) Differentiation of neural stem cells in three-dimensional growth factor-immobilized chitosan hydrogel scaffolds. *Biomaterials* 32, 57–64.
- (77) Lewis, G. (2008) Alternative acrylic bone cement formulations for cemented arthroplasties: present status, key issues, and future prospects. *J. Biomed. Mater. Res. B. Appl. Biomater.* 84, 301–19.
- (78) Bettencourt, A., and Almeida, A. J. (2012) Poly(methyl methacrylate) particulate carriers in drug delivery. *J. Microencapsul.* 29, 353–67.
- (79) Amzallag, T., and Pynson, J. (2007) Biomatériaux dans la chirurgie du cristallin. *J. Fr. Ophtalmol.* 30, 757–767.
- (80) Righetti, P. G., and Gelfi, C. (1997) Electrophoresis gel media: the state of the art. *J. Chromatogr. B Biomed. Sci. Appl.* 699, 63–75.
- (81) Roll, S., Müller-Nordhorn, J., Keil, T., Scholz, H., Eidt, D., Greiner, W., and Willich, S. N. (2008) Dacron vs. PTFE as bypass materials in peripheral vascular surgery--systematic review and meta-analysis. *BMC Surg.* 8, 22.
- (82) Lawrence, E. L., and Turner, I. G. (2005) Materials for urinary catheters: a review of their history and development in the UK. *Med. Eng. Phys.* 27, 443–53.
- (83) Jacobs, C. A., Christensen, C. P., Greenwald, A. S., and McKellop, H. (2007) Clinical performance of highly cross-linked polyethylenes in total hip arthroplasty. *J. Bone Joint Surg. Am.* 89, 2779–86.
- (84) Sharkey, P. F., Hozack, W. J., Dorr, L. D., Maloney, W. J., and Berry, D. (2000) The bearing surface in total hip arthroplasty: evolution or revolution. *Instr. Course Lect.* 49, 41–56.

- (85) Lambert, J. M. (2006) The nature of platinum in silicones for biomedical and healthcare use. *J. Biomed. Mater. Res. B. Appl. Biomater.* 78, 167–80.
- (86) Kheir, J., Leslie, L., Fulmer, N., Edlich, R., and Gampper, T. (1998) Polydimethylsiloxane for augmentation of the chin, malar, and nasal bones. *J. Long. Term. Eff. Med. Implants* 8, 55–67.
- (87) Shoichet, M. S. (2010) Polymer Scaffolds for Biomaterials Applications. *Macromolecules* 43, 581–591.
- (88) Stolnik, S., Illum, L., and Davis, S. S. (1995) Long circulating microparticulate drug carriers. *Adv. Drug Deliv. Rev.* 16, 195–214.
- (89) Ratner, B. D., Hoffman, A. S., Schoen, F. J., and Lemons, J. E. (2004) Biomaterials Science: An Introduction to Materials in Medicine 2nd ed. Elsevier Inc.
- (90) Singh, S., Woerly, S., and Mclaughlin, B. J. (2001) Natural and artificial substrates for retinal pigment epithelial monolayer transplantation. *Biomaterials* 22, 3337–3343.
- (91) Von Recum, H., Kikuchi, A., Okuhara, M., Sakurai, Y., Okano, T., and Kim, S. W. (1998) Retinal pigmented epithelium cultures on thermally responsive polymer porous substrates. *J. Biomater. Sci. Polym. Ed.* 9, 1241–53.
- (92) Williams, R. L., Krishna, Y., Dixon, S., Haridas, A., Grierson, I., and Sheridan, C. (2005) Polyurethanes as potential substrates for sub-retinal retinal pigment epithelial cell transplantation. *J. Mater. Sci. Mater. Med.* 16, 1087–92.
- (93) Lim, J.-M. M., Byun, S., Chung, S., Park, T. H., Seo, J.-M. M., Joo, C.-K. K., Chung, H., and Cho, D.-I. I. (2004) Retinal pigment epithelial cell behavior is modulated by alterations in focal cell-substrate contacts. *Invest. Ophthalmol. Vis. Sci.* 45, 4210–4216.
- (94) Tao, S., Young, C., Redenti, S., Zhang, Y., Klassen, H., Desai, T., and Young, M. J. (2007) Survival, migration and differentiation of retinal progenitor cells transplanted on micro-machined poly(methyl methacrylate) scaffolds to the subretinal space. *Lab Chip* 7, 695–701.
- (95) Laurencin, C. T., Norman, M. E., Elgendy, H. M., el-Amin, S. F., Allcock, H. R., Pucher, S. R., and Ambrosio, A. A. (1993) Use of polyphosphazenes for skeletal tissue regeneration. *J. Biomed. Mater. Res.* 27, 963–73.
- (96) Andrianov, A., Sargent, J., Sule, S., Le Golvan, M., Woods, A., Jenkins, S., and Payne, L. (1998) Synthesis, physico-chemical properties and immunoadjuvant activity of water-soluble phosphazene polyacids. *J. Bioact. Compat. Polym.* 13, 243–256.

- (97) Gombotz, W. R., and Pettit, D. K. (1995) Biodegradable Polymers for Protein and Peptide Drug Delivery. *Bioconjug. Chem.* 6, 332–351.
- (98) Deshpande, A. A., Heller, J., and Gurny, R. (1998) Bioerodible polymers for ocular drug delivery. *Crit. Rev. Ther. Drug Carrier Syst.* 15, 381–420.
- (99) Heller, J., Barr, J., Ng, S. Y., Abdellauoi, K. S., and Gurny, R. (2002) Poly(ortho esters): synthesis, characterization, properties and uses. *Adv. Drug Deliv. Rev.* 54, 1015–1039.
- (100) Senior, P., Beech, G., Ritchie, G., and Dawes, E. (1972) Role of Oxygen Limitation in Formation of Poly-Beta-Hydroxybutyrate During Batch and Continuous Culture of *Azobacter-Beijerinckii*. *Biochem. J.* 128, 1193–&.
- (101) Miller, N. D., and Williams, D. F. (1987) On the biodegradation of poly- $\beta$ -hydroxybutyrate (PHB) homopolymer and poly- $\beta$ -hydroxybutyrate-hydroxyvalerate copolymers. *Biomaterials* 8, 129–137.
- (102) Barham, P. J., Keller, A., Otun, E. L., and Holmes, P. A. (1984) Crystallization and morphology of a bacterial thermoplastic: poly-3-hydroxybutyrate. *J. Mater. Sci.* 19, 2781–2794.
- (103) Knowles, J. C. (1993) Development of a Natural Degradable Polymer for Orthopaedic Use. *J. Med. Eng. Technol.* 17, 129–137.
- (104) Tezcaner, A., Bugra, K., and Hasırcı, V. (2003) Retinal pigment epithelium cell culture on surface modified poly(hydroxybutyrate-co-hydroxyvalerate) thin films. *Biomaterials* 24, 4573–4583.
- (105) Neeley, W. L., Redenti, S., Klassen, H., Tao, S., Desai, T., Young, M. J., and Langer, R. (2008) A microfabricated scaffold for retinal progenitor cell grafting. *Biomaterials* 29, 418–26.
- (106) Pitt, C. G., Gratzl, M. M., Jeffcoat, A. R., Zweidinger, R., and Schindler, A. (1979) Sustained drug delivery systems II: Factors affecting release rates from poly( $\epsilon$ -caprolactone) and related biodegradable polyesters. *J. Pharm. Sci.* 68, 1534–1538.
- (107) McHugh, K. J., Tao, S. L., and Saint-Geniez, M. (2014) Porous poly( $\epsilon$ -caprolactone) scaffolds for retinal pigment epithelium transplantation. *Invest. Ophthalmol. Vis. Sci.* 55, 1754–62.
- (108) TOrmalá, P., Pohjonen, T., and Rokkanen, P. (1998) Bioabsorbable polymers: Materials technology and surgical applications. *Proc. Inst. Mech. Eng. Part H J. Eng. Med.* 212, 101–111.

- (109) Athanasiou, K., Agrawal, C., Barber, F., and Burkhart, S. (1998) Orthopaedic applications for PLA-PGA biodegradable polymers. *Arthrosc. J. Arthrosc. Relat. Surg.* 14, 726–737.
- (110) Bergsma, J. (1995) Late degradation tissue response to poly( $\alpha$ -lactide) bone plates and screws. *Biomaterials* 16, 25–31.
- (111) Hynes, S. R., and Lavik, E. B. (2010) A tissue-engineered approach towards retinal repair: Scaffolds for cell transplantation to the subretinal space. *Graefe's Arch. Clin. Exp. Ophthalmol.* 248, 763–78.
- (112) Thomson, R. C., Giordano, G. G., Collier, J. H., Ishaug, S. L., Mikos, A. G., Lahiri-Munir, D., and Garcia, C. A. (1996) Manufacture and characterization of poly( $\alpha$ -hydroxy ester) thin films as temporary substrates for retinal pigment epithelium cells. *Biomaterials* 17, 321–327.
- (113) Giordano, G. G., Thomson, R. C., Ishaug, S. L., Mikos, A. G., Cumber, S., Garcia, C. A., and Lahiri-Munir, D. (1997) Retinal pigment epithelium cells cultured on synthetic biodegradable polymers. *J. Biomed. Mater. Res.* 34, 87–93.
- (114) Lu, L., Garcia, C. A., and Mikos, A. G. (1998) Retinal pigment epithelium cell culture on thin biodegradable poly(DL-lactic-co-glycolic acid) films. *J. Biomater. Sci. Polym. Ed.* 9, 1187–205.
- (115) Hadlock, T., Singh, S., Vacanti, J. P., and McLaughlin, B. J. (1999) Ocular cell monolayers cultured on biodegradable substrates. *Tissue Eng.* 5, 187–96.
- (116) Lavik, E. B., Klassen, H., Warfvinge, K., Langer, R., and Young, M. J. (2005) Fabrication of degradable polymer scaffolds to direct the integration and differentiation of retinal progenitors. *Biomaterials* 26, 3187–96.
- (117) Tomita, M., Lavik, E., Klassen, H., Zahir, T., Langer, R., and Young, M. J. (2005) Biodegradable polymer composite grafts promote the survival and differentiation of retinal progenitor cells. *Stem Cells* 23, 1579–1588.
- (118) Zheng, Q., and Zhao, X. (2010) Research of mechanical strength enhanced fibrin-PLGA hybrid scaffold with its effect on proliferation of rMSC. *E-POLYMERS*.
- (119) Massia, S. P., and Hubbell, J. A. (1990) Covalent surface immobilization of Arg-Gly-Asp- and Tyr-Ile-Gly-Ser-Arg-containing peptides to obtain well-defined cell-adhesive substrates. *Anal. Biochem.* 187, 292–301.
- (120) Stile, R. A., and Healy, K. E. (2001) Thermo-Responsive Peptide-Modified Hydrogels for Tissue Regeneration. *Biomacromolecules* 2, 185–194.

- (121) Dee, K. C., Andersen, T. T., and Bizios, R. (1999) Osteoblast population migration characteristics on substrates modified with immobilized adhesive peptides. *Biomaterials* 20, 221–227.
- (122) Burdick, J. A., and Anseth, K. S. (2002) Photoencapsulation of osteoblasts in injectable RGD-modified PEG hydrogels for bone tissue engineering. *Biomaterials* 23, 4315–4323.
- (123) Hersel, U., Dahmen, C., and Kessler, H. (2003) RGD modified polymers: biomaterials for stimulated cell adhesion and beyond. *Biomaterials* 24, 4385–4415.
- (124) Vandermeulen, G. W. M., and Klok, H.-A. (2004) Peptide/protein hybrid materials: enhanced control of structure and improved performance through conjugation of biological and synthetic polymers. *Macromol. Biosci.* 4, 383–98.
- (125) Rezaia, A., and Healy, K. E. Biomimetic peptide surfaces that regulate adhesion, spreading, cytoskeletal organization, and mineralization of the matrix deposited by osteoblast-like cells. *Biotechnol. Prog.* 15, 19–32.
- (126) Cai, L., Dinh, C. B., and Heilshorn, S. C. (2014) One-pot Synthesis of Elastin-like Polypeptide Hydrogels with Grafted VEGF-Mimetic Peptides. *Biomater. Sci.* 2, 757–765.
- (127) Jabbari, E. (2011) Bioconjugation of hydrogels for tissue engineering. *Curr. Opin. Biotechnol.* 22, 655–60.
- (128) DeForest, C. A., Sims, E. A., and Anseth, K. S. (2010) Peptide-Functionalized Click Hydrogels with Independently Tunable Mechanics and Chemical Functionality for 3D Cell Culture. *Chem. Mater.* 22, 4783–4790.
- (129) Cleophas, R. T. C., Riool, M., Quarles van Ufford, H. (Linda) C., Zaat, S. A. J., Kruijtzter, J. A. W., and Liskamp, R. M. J. (2014) Convenient Preparation of Bactericidal Hydrogels by Covalent Attachment of Stabilized Antimicrobial Peptides Using Thiol–ene Click Chemistry. *ACS Macro Lett.* 3, 477–480.
- (130) Ma, F.-H., Chen, J.-L., Li, Q.-F., Zuo, H.-H., Huang, F., and Su, X.-C. (2014) Kinetic assay of the Michael addition-like thiol-ene reaction and insight into protein bioconjugation. *Chem. Asian J.* 9, 1808–16.
- (131) Chang, J.-Y., Lin, J.-H., Yao, C.-H., Chen, J.-H., Lai, T.-Y., and Chen, Y.-S. (2007) In vivo evaluation of a biodegradable EDC/NHS-cross-linked gelatin peripheral nerve guide conduit material. *Macromol. Biosci.* 7, 500–7.
- (132) Liu, R., Ming, J., Zhang, H., and Zuo, B. (2012) EDC/NHS crosslinked electrospun regenerated tussah silk fibroin nanofiber mats. *Fibers Polym.* 13, 613–617.

- (133) Peng, J., Su, Y., Chen, W., Zhao, X., Jiang, Z., Dong, Y., Zhang, Y., Liu, J., and Xingzhong, C. (2013) Polyamide nanofiltration membrane with high separation performance prepared by EDC/NHS mediated interfacial polymerization. *J. Memb. Sci.* 427, 92–100.
- (134) Elahi, M., Guan, G., Wang, L., and King, M. (2014) Influence of Layer-by-Layer Polyelectrolyte Deposition and EDC/NHS Activated Heparin Immobilization onto Silk Fibroin Fabric. *Materials (Basel)*. 7, 2956–2977.
- (135) Tiwari, A., Grailer, J. J., Pilla, S., Steeber, D. A., and Gong, S. (2009) Biodegradable hydrogels based on novel photopolymerizable guar gum-methacrylate macromonomers for in situ fabrication of tissue engineering scaffolds RID F-4622-2011. *Acta Biomater.* 5, 3441–3452.
- (136) Gao, X., Zhou, Y., Ma, G., Shi, S., Yang, D., Lu, F., and Nie, J. (2010) A water-soluble photocrosslinkable chitosan derivative prepared by Michael-addition reaction as a precursor for injectable hydrogel. *Carbohydr. Polym.* 79, 507–512.
- (137) Amsden, B. G., Sukarto, A., Knight, D. K., and Shapka, S. N. (2007) Methacrylated glycol chitosan as a photopolymerizable biomaterial. *Biomacromolecules* 8, 3758–66.
- (138) Ono, K., Saito, Y., Yura, H., Ishikawa, K., Kurita, A., Akaike, T., and Ishihara, M. (2000) Photocrosslinkable chitosan as a biological adhesive. *J. Biomed. Mater. Res.* 49, 289–295.
- (139) Lu, G., Ling, K., Zhao, P., Xu, Z., Deng, C., Zheng, H., Huang, J., and Chen, J. (2010) A novel in situ-formed hydrogel wound dressing by the photocross-linking of a chitosan derivative. *Wound Repair Regen.* 18, 70–79.
- (140) Rickett, T. A., Amoozgar, Z., Tucheck, C. A., Park, J., Yeo, Y., and Shi, R. (2011) Rapidly Photo-Cross-Linkable Chitosan Hydrogel for Peripheral Neurosurgeries. *Biomacromolecules* 12, 57–65.
- (141) Farrokh-Siar, L., Rezai, K. A., Patel, S. C., and Ernest, T. T. (2009) Cryoprecipitate: An autologous substrate for human fetal retinal pigment epithelium.
- (142) Oganessian, A. (1999) A New Model of Retinal Pigment Epithelium Transplantation With Microspheres. *Arch. Ophthalmol.* 117, 1192.
- (143) Frangos, J., Eskin, S., McIntire, L., and Ives, C. (1985) Flow effects on prostacyclin production by cultured human endothelial cells. *Science (80-. )*. 227, 1477–1479.



- (144) Stoltz, J., Dumas, D., Wang, X., Payan, E., Mainard, D., Paulus, F., Maurice, G., Netter, P., and Muller, S. Influence of mechanical forces on cells and tissues. *Biorheology* 37, 3–14.
- (145) Li, D., Zhou, J., Chowdhury, F., Cheng, J., Wang, N., and Wang, F. (2011) Role of mechanical factors in fate decisions of stem cells. *Regen. Med.* 6, 229–40.
- (146) Zoldan, J., Karagiannis, E. D., Lee, C. Y., Anderson, D. G., Langer, R., and Levenberg, S. (2011) The influence of scaffold elasticity on germ layer specification of human embryonic stem cells. *Biomaterials* 32, 9612–9621.
- (147) Lee, J., Abdeen, A. A., Zhang, D., and Kilian, K. A. (2013) Directing stem cell fate on hydrogel substrates by controlling cell geometry, matrix mechanics and adhesion ligand composition. *Biomaterials* 34, 8140–8148.
- (148) Little, C. J., Bawolin, N. K., and Chen, X. (2011) Mechanical Properties of Natural Cartilage and Tissue-Engineered Constructs. *Tissue Eng. Part B-Reviews* 17, 213–227.
- (149) Parekh, S. H., Chatterjee, K., Lin-Gibson, S., Moore, N. M., Cicerone, M. T., Young, M. F., and Simon Jr., C. G. (2011) Modulus-driven differentiation of marrow stromal cells in 3D scaffolds that is independent of myosin-based cytoskeletal tension. *Biomaterials* 32, 2256–2264.
- (150) Kinneberg, K. R. C., Galloway, M. T., Butler, D. L., and Shearn, J. T. (2011) Effect of Implanting a Soft Tissue Autograft in a Central-Third Patellar Tendon Defect: Biomechanical and Histological Comparisons. *J. Biomech. Eng. Asme* 133, 91002.
- (151) Wang, H., Tibbitt, M. W., Langer, S. J., Leinwand, L. A., and Anseth, K. S. (2013) Hydrogels preserve native phenotypes of valvular fibroblasts through an elasticity-regulated PI3K/AKT pathway. *Proc. Natl. Acad. Sci.* 110, 19336–19341.
- (152) Guillemette, M. D., Park, H., Hsiao, J. C., Jain, S. R., Larson, B. L., Langer, R., and Freed, L. E. (2010) Combined Technologies for Microfabricating Elastomeric Cardiac Tissue Engineering Scaffolds. *Macromol. Biosci.* 10, 1330–1337.
- (153) Chen, Q.-Z., Bismarck, A., Hansen, U., Junaid, S., Tran, M. Q., Harding, S. E., Ali, N. N., and Boccaccini, A. R. (2008) Characterisation of a soft elastomer poly(glycerol sebacate) designed to match the mechanical properties of myocardial tissue. *Biomaterials* 29, 47–57.
- (154) Banerjee, A., Arha, M., Choudhary, S., Ashton, R. S., Bhatia, S. R., Schaffer, D. V., and Kane, R. S. (2009) The influence of hydrogel modulus on the proliferation and differentiation of encapsulated neural stem cells. *Biomaterials* 30, 4695–4699.

- (155) Yao, S., Liu, X., Wang, X., Merolli, A., Chen, X., and Cui, F. (2013) Directing neural stem cell fate with biomaterial parameters for injured brain regeneration. *Prog. Nat. Sci. Mater. Int.* 23, 103–112.
- (156) Diniz, B., Thomas, P., Thomas, B., Ribeiro, R., Hu, Y., Brant, R., Ahuja, A., Zhu, D., Liu, L., Koss, M., Maia, M., Chader, G., Hinton, D. R., and Humayun, M. S. (2013) Subretinal Implantation of Retinal Pigment Epithelial Cells Derived From Human Embryonic Stem Cells: Improved Survival When Implanted as a Monolayer. *Invest. Ophthalmol. Vis. Sci.* 54, 5087–5096.
- (157) Rosen, S. L. (1993) Fundamental principles of polymeric materials, pp 103 – 109. Wiley.
- (158) Chen, K., Rowley, A. P., and Weiland, J. D. (2010) Elastic properties of porcine ocular posterior soft tissues. *J. Biomed. Mater. Res. Part a* 93A, 634–645.
- (159) Chen, K., and Weiland, J. D. (2010) Anisotropic and inhomogeneous mechanical characteristics of the retina. *J. Biomech.* 43, 1417–1421.
- (160) Wheeler, J., Woods, J., Cox, M., Cantrell, R., Watkins, F., and Edlich, R. (1996) Evolution of hydrogel polymers as contact lenses, surface coatings, dressings, and drug delivery systems. *J. Long. Term. Eff. Med. Implants* 6, 207–217.
- (161) Bosman, F. T., and Stamenkovic, I. (2003) Functional structure and composition of the extracellular matrix. *J. Pathol.* 200, 423–428.
- (162) Golombick, T., Dajee, D., and Bezwoda, W. R. (1995) Extracellular-Matrix Interactions .2. Extracellular-Matrix Structure is Important for Growth-Factor Localization and Function. *Vitr. Cell. Dev. Biol.* 31, 396–403.
- (163) Schuppan, D. (1990) Structure of the Extracellular-Matrix in Normal and Fibrotic Liver - Collagens and Glycoproteins. *Semin. Liver Dis.* 10, 1–10.
- (164) Werle, M. J. (2008) Cell-to-cell signaling at the neuromuscular junction - The dynamic role of the extracellular matrix. *Ann. N. Y. Acad. Sci.* (Kaminski, H. J., and Barohn, R. J., Eds.) 1132, 13–18.
- (165) Dubruel, P., Schacht, E., Van Vlierberghe, S., Kirkpatrick, J., Unger, R., Fassina, L., and Visai, L. (2011) Gelatin as promising cell-interactive ECM mimicking biomaterial. *Tissue Eng. Part a* 17, 545.
- (166) Pham, Q. P., Kasper, F. K., Baggett, L. S., Raphael, R. M., Jansen, J. A., and Mikos, A. G. (2008) The influence of an in vitro generated bone-like extracellular matrix on osteoblastic gene expression of marrow stromal cells. *Biomaterials* 29, 2729–2739.



- (167) Elema, H., Groot, J. H., Nijenhuis, A. J., Pennings, A. J., Veth, R. P. H., Klompmaker, J., and Jansen, H. W. B. (1990) Use of porous biodegradable polymer implants in meniscus reconstruction. 2) Biological evaluation of porous biodegradable polymer implants in menisci. *Colloid Polym. Sci.* 268, 1082–1088.
- (168) Pilliar, R. (1987) Porous-Surfaced Metallic Implants for Orthopedic Applications. *J. Biomed. Mater. Res. Biomater.* 21, 1–33.
- (169) Groot, J. H., Nijenhuis, A. J., Bruin, P., Pennings, A. J., Veth, R. P. H., Klompmaker, J., and Jansen, H. W. B. (1990) Use of porous biodegradable polymer implants in meniscus reconstruction. 1) Preparation of porous biodegradable polyurethanes for the reconstruction of meniscus lesions. *Colloid Polym. Sci.* 268, 1073–1081.
- (170) Goldberg, M., Langer, R., and Jia, X. (2007) Nanostructured materials for applications in drug delivery and tissue engineering. *J. Biomater. Sci. Ed.* 18, 241–268.
- (171) Da Silva, E. E., Della Colleta, H. H. M., Ferlauto, A. S., Moreira, R. L., Resende, R. R., Oliveira, S., Kitten, G. T., Lacerda, R. G., and Ladeira, L. O. (2009) Nanostructured 3-D Collagen/Nanotube Biocomposites for Future Bone Regeneration Scaffolds. *Nano Res.* 2, 462–473.
- (172) Seidlits, S. K., Lee, J. Y., and Schmidt, C. E. (2008) Nanostructured scaffolds for neural applications. *Nanomedicine* 3, 183–199.
- (173) Clapper, J. D., Iverson, S. L., and Guymon, C. A. (2007) Nanostructured biodegradable polymer networks using lyotropic liquid crystalline templates. *Biomacromolecules* 8, 2104–2111.
- (174) Clapper, J. D., Pearce, M. E., Guymon, C. A., and Salem, A. K. (2008) Biotinylated biodegradable nanotemplated hydrogel networks for cell interactive applications. *Biomacromolecules* 9, 1188–1194.
- (175) Laslau, C., Williams, D. E., and Travas-Sejdic, J. (2012) The application of nanopipettes to conducting polymer fabrication, imaging and electrochemical characterization. *Prog. Polym. Sci.* 37, 1177–1191.
- (176) Muñoz, A., McConney, M. E., Kosa, T., Luchette, P., Sukhomlinova, L., White, T. J., Bunning, T. J., and Taheri, B. (2012) Continuous wave mirrorless lasing in cholesteric liquid crystals with a pitch gradient across the cell gap. *Opt. Lett.* 37, 2904–6.
- (177) Schricker, S. R., Palacio, M. L. B., and Bhushan, B. (2012) Designing nanostructured block copolymer surfaces to control protein adhesion. *Philos. Trans. A. Math. Phys. Eng. Sci.* 370, 2348–80.

- (178) Singh, N. K., Singh, S. K., Dash, D., Das Purkayastha, B. P., Roy, J. K., and Maiti, P. (2012) Nanostructure controlled anti-cancer drug delivery using poly( $\epsilon$ -caprolactone) based nanohybrids. *J. Mater. Chem.* 22, 17853.
- (179) Wang, Y., Tran, H. D., and Kaner, R. B. (2011) Applications of oligomers for nanostructured conducting polymers. *Macromol. Rapid Commun.* 32, 35–49.
- (180) Clapper, J. D., Skeie, J. M., Mullins, R. F., and Guymon, C. A. (2007) Development and characterization of photopolymerizable biodegradable materials from PEG-PLA-PEG block macromonomers. *Polymer (Guildf)*. 48, 6554–6564.
- (181) Forney, B. S., and Guymon, C. A. (2011) Fast Deswelling Kinetics of Nanostructured Poly(N-isopropylacrylamide) Photopolymerized in a Lyotropic Liquid Crystal Template. *Macromol. Rapid Commun.* 32, 765–769.
- (182) Bara, J. E., Kaminski, A. K., Noble, R. D., and Gin, D. L. (2007) Influence of nanostructure on light gas separations in cross-linked lyotropic liquid crystal membranes. *J. Memb. Sci.* 288, 13–19.
- (183) Guo, C., Wang, J., Cao, F., Lee, R. J., and Zhai, G. (2010) Lyotropic liquid crystal systems in drug delivery. *Drug Discov. Today* 15, 1032–40.
- (184) Moroni, L., de Wijn, J. R., and van Blitterswijk, C. A. (2006) 3D fiber-deposited scaffolds for tissue engineering: influence of pores geometry and architecture on dynamic mechanical properties. *Biomaterials* 27, 974–85.
- (185) El-Ayoubi, R., Eliopoulos, N., Diraddo, R., Galipeau, J., and Yousefi, A.-M. (2008) Design and Fabrication of 3D Porous Scaffolds to Facilitate Cell-Based Gene Therapy. *Tissue Eng. Part A* 14, 1037–1048.
- (186) Yun, H., Kim, S., and Park, E. K. (2011) Bioactive glass–poly ( $\epsilon$ -caprolactone) composite scaffolds with 3 dimensionally hierarchical pore networks. *Mater. Sci. Eng. C* 31, 198–205.
- (187) Moroni, L., Schotel, R., Sohier, J., de Wijn, J. R., and van Blitterswijk, C. A. (2006) Polymer hollow fiber three-dimensional matrices with controllable cavity and shell thickness. *Biomaterials* 27, 5918–26.
- (188) Bettahalli, N. M. S., Arkesteijn, I. T. M., Wessling, M., Poot, A. A., and Stamatialis, D. (2013) Corrugated round fibers to improve cell adhesion and proliferation in tissue engineering scaffolds. *Acta Biomater.* 9, 6928–35.
- (189) Woodfield, T. B. F., Malda, J., de Wijn, J., Péters, F., Riesle, J., and van Blitterswijk, C. A. (2004) Design of porous scaffolds for cartilage tissue engineering using a three-dimensional fiber-deposition technique. *Biomaterials* 25, 4149–61.

- (190) Rücker, M., Laschke, M. W., Junker, D., Carvalho, C., Schramm, A., Mülhaupt, R., Gellrich, N.-C., and Menger, M. D. (2006) Angiogenic and inflammatory response to biodegradable scaffolds in dorsal skinfold chambers of mice. *Biomaterials* 27, 5027–38.
- (191) Laschke, M. W., Rücker, M., Jensen, G., Carvalho, C., Mülhaupt, R., Gellrich, N.-C., and Menger, M. D. (2008) Incorporation of growth factor containing Matrigel promotes vascularization of porous PLGA scaffolds. *J. Biomed. Mater. Res. A* 85, 397–407.
- (192) Gloria, A., Causa, F., Russo, T., Battista, E., Moglie, R. Della, Zeppetelli, S., Santis, R. De, Netti, P. A., and Ambrosio, L. (2012) Three-Dimensional Poly( $\epsilon$ -caprolactone) Bioactive Scaffolds with Controlled Structural and Surface Properties.
- (193) Clarke, J. C., Tuft, B. W., Clinger, J. D., Levine, R., Figueroa, L. S., Guymon, C. A., and Hansen, M. R. (2011) Micropatterned methacrylate polymers direct spiral ganglion neurite and Schwann cell growth. *Hear. Res.* 278, 96–105.
- (194) Tuft, B. W., Li, S., Xu, L., Clarke, J. C., White, S. P., Guymon, B. A., Perez, K. X., Hansen, M. R., and Guymon, C. A. (2013) Photopolymerized microfeatures for directed spiral ganglion neurite and Schwann cell growth. *Biomaterials* 34, 42–54.
- (195) Thomson, R. C., Yaszemski, M. J., Powers, J. M., and Mikos, A. G. (1998) Hydroxyapatite fiber reinforced poly( $\alpha$ -hydroxy ester) foams for bone regeneration. *Biomaterials* 19, 1935–1943.
- (196) Sanzana, E. S., Navarro, M., Ginebra, M.-P., Planell, J. A., Ojeda, A. C., and Montecinos, H. A. (2014) Role of porosity and pore architecture in the in vivo bone regeneration capacity of biodegradable glass scaffolds. *J. Biomed. Mater. Res. A* 102, 1767–73.
- (197) Chatterjee, K., Kraigsley, A. M., Bolikal, D., Kohn, J., and Simon, C. G. (2012) Gas-Foamed Scaffold Gradients for Combinatorial Screening in 3D. *J. Funct. Biomater.* 3, 173–82.
- (198) Silverstein, M. S. (2014) PolyHIPEs: Recent advances in emulsion-templated porous polymers. *Prog. Polym. Sci.* 39, 199–234.
- (199) Cansell, F., Aymonier, C., and Loppinet-Serani, A. (2003) Review on materials science and supercritical fluids. *Curr. Opin. Solid State Mater. Sci.* 7, 331–340.
- (200) Davies, O. R., Lewis, A. L., Whitaker, M. J., Tai, H., Shakesheff, K. M., and Howdle, S. M. (2008) Applications of supercritical CO<sub>2</sub> in the fabrication of polymer systems for drug delivery and tissue engineering. *Adv. Drug Deliv. Rev.* 60, 373–87.

- (201) Quirk, R. A., France, R. M., Shakesheff, K. M., and Howdle, S. M. (2004) Supercritical fluid technologies and tissue engineering scaffolds. *Curr. Opin. Solid State Mater. Sci.* 8, 313–321.
- (202) Wu, D., Xu, F., Sun, B., Fu, R., He, H., and Matyjaszewski, K. (2012) Design and preparation of porous polymers. *Chem. Rev.* 112, 3959–4015.
- (203) Yao, D., Dong, S., Lu, Q., Hu, X., Kaplan, D. L., Zhang, B., and Zhu, H. (2012) Salt-leached silk scaffolds with tunable mechanical properties. *Biomacromolecules* 13, 3723–9.
- (204) Réthoré, G., and Pandit, A. (2010) Use of templates to fabricate nanoscale spherical structures for defined architectural control. *Small* 6, 488–98.
- (205) Shin, H. (2007) Fabrication methods of an engineered microenvironment for analysis of cell-biomaterial interactions. *Biomaterials* 28, 126–33.
- (206) Tezcaner, A., and Hicks, D. (2008) In vitro characterization of micropatterned PLGA-PHBV8 blend films as temporary scaffolds for photoreceptor cells. *J. Biomed. Mater. Res. A* 86, 170–81.
- (207) Hamley, I. W. (2003) Nanostructure fabrication using block copolymers. *Nanotechnology* 14, R39–R54.
- (208) Clapper, J. D., Sievens-Figueroa, L., and Guymon, C. A. (2008) Photopolymerization in polymer templating. *Chem. Mater.* 20, 768–781.
- (209) Verheyen, E., Schillemans, J. P., van Wijk, M., Demeniex, M.-A., Hennink, W. E., and van Nostrum, C. F. (2011) Challenges for the effective molecular imprinting of proteins. *Biomaterials* 32, 3008–20.
- (210) Liu, Y. (2013) Polymerization-induced phase separation and resulting thermomechanical properties of thermosetting/reactive nonlinear polymer blends: A review. *J. Appl. Polym. Sci.* 127, 3279–3292.
- (211) Schulze, M. W., McIntosh, L. D., Hillmyer, M. A., and Lodge, T. P. (2014) High-modulus, high-conductivity nanostructured polymer electrolyte membranes via polymerization-induced phase separation. *Nano Lett.* 14, 122–6.
- (212) Chan, P. K., and Rey, A. D. (1996) Polymerization-Induced Phase Separation. 1. Droplet Size Selection Mechanism. *Macromolecules* 29, 8934–8941.
- (213) Serbutoviez, C., Kloosterboer, J. G., Boots, H. M. J., and Touwslager, F. J. (1996) Polymerization-Induced Phase Separation. 2. Morphology of Polymer-Dispersed Liquid Crystal Thin Films. *Macromolecules* 29, 7690–7698.

- (214) Forney, B. S. B., Baguenard, C., and Guymon, C. A. (2013) Effects of Controlling Polymer Nanostructure Using Photopolymerization within Lyotropic Liquid Crystalline Templates. *Chem. Mater.* 25, 2950–2960.
- (215) Szczepanski, C. R., Pfeifer, C. S., and Stansbury, J. W. (2012) A new approach to network heterogeneity: Polymerization Induced Phase Separation in photo-initiated, free-radical methacrylic systems. *Polymer (Guildf)*. 53, 4694–4701.
- (216) Clapper, J. D., and Guymon, C. A. (2007) Nanostructured Biodegradable Polymer Composites Generated Using Lyotropic Liquid Crystalline Media. *Macromolecules* 40, 7951–7959.
- (217) Clapper, J. D., and Guymon, C. A. (2006) Compatibilization of immiscible polymer networks through photopolymerization in a lyotropic liquid crystal. *Adv. Mater.* 18, 1575–1580.
- (218) DePierro, M. A., Carpenter, K. G., and Guymon, C. A. (2006) Influence of polymerization conditions on nanostructure and properties of polyacrylamide hydrogels templated from lyotropic liquid crystals. *Chem. Mater.* 18, 5609–5617.
- (219) Lester, C. L., Smith, S. M., Colson, C. D., and Guymon, C. A. (2003) Physical properties of hydrogels synthesized from lyotropic liquid crystalline templates. *Chem. Mater.* 15, 3376–3384.
- (220) Sievens-Figueroa, L., and Guymon, C. A. (2009) Polymerization Kinetics and Nanostructure Evolution of Reactive Lyotropic Liquid Crystals with Different Reactive Group Position. *Macromolecules* 42, 9243–9250.
- (221) Clapper, J. D., and Guymon, C. A. (2007) Physical behavior of cross-linked PEG hydrogels photopolymerized within nanostructured lyotropic liquid crystalline templates. *Macromolecules* 40, 1101–1107.
- (222) Avestro, A.-J., Belowich, M. E., and Stoddart, J. F. (2012) Cooperative self-assembly: producing synthetic polymers with precise and concise primary structures. *Chem. Soc. Rev.* 41, 5881–95.
- (223) Bai, G., Wang, J., Yan, H., Li, Z., and Thomas, R. K. (2001) Thermodynamics of Molecular Self-Assembly of Two Series of Double-Chain Singly Charged Cationic Surfactants. *J. Phys. Chem. B* 105, 9576–9580.
- (224) Fong, C., Le, T., and Drummond, C. J. (2012) Lyotropic liquid crystal engineering-ordered nanostructured small molecule amphiphile self-assembly materials by design. *Chem. Soc. Rev.* 41, 1297–322.
- (225) Collings, P. J., and Hird, M. (1997) Introduction to Liquid Crystals: Chemistry and Physics, p 324. CRC Press.

- (226) Gin, D. L., Gu, W. Q., Pindzola, B. A., and Zhou, W. J. (2001) Polymerized lyotropic liquid crystal assemblies for materials applications. *Acc. Chem. Res.* *34*, 973–980.
- (227) Lee, Y. S. (2008) *Self-Assembly and Nanotechnology: A Force Balance Approach*, p 344. Wiley-Interscience; 1 edition.
- (228) Clapper, J. D., and Guymon, C. A. (2009) Nanostructured Hydrogels via Photopolymerization in Lyotropic Liquid Crystalline Systems. *Mol. Cryst. Liq. Cryst.* *509*, 772–780.
- (229) McCormick, D. T., Stovall, K. D., and Guymon, C. A. (2003) Photopolymerization in pluronic lyotropic liquid crystals: Induced mesophase thermal stability. *Macromolecules* *36*, 6549–6558.
- (230) DePierro, M. A., and Guymon, C. A. (2006) Photoinitiation and Monomer Segregation Behavior in Polymerization of Lyotropic Liquid Crystalline Systems. *Macromolecules* *39*, 617–626.
- (231) Lester, C. L., Colson, C. D., and Guymon, C. A. (2001) Photopolymerization kinetics and structure development of templated lyotropic liquid crystalline systems. *Macromolecules* *34*, 4430–4438.
- (232) Chatani, S., Kloxin, C. J., and Bowman, C. N. (2014) The power of light in polymer science: photochemical processes to manipulate polymer formation, structure, and properties. *Polym. Chem.* *5*, 2187.
- (233) Bowman, C. N., and Kloxin, C. J. (2008) Toward an Enhanced Understanding and Implementation of Photopolymerization Reactions. *AIChE J.* *54*, 2775–2795.
- (234) Decker, C. (2002) Kinetic Study and New Applications of UV Radiation Curing. *Macromol. Rapid Commun.* *23*, 1067–1093.
- (235) Forney, B. S., and Guymon, C. A. (2010) Nanostructure Evolution during Photopolymerization in Lyotropic Liquid Crystal Templates. *Macromolecules* *43*, 8502–8510.
- (236) Sievens-Figueroa, L., and Guymon, C. A. (2009) Cross-Linking of Reactive Lyotropic Liquid Crystals for Nanostructure Retention. *Chem. Mater.* *21*, 1060–1068.
- (237) Gandavarapu, N. R., Azagarsamy, M. A., and Anseth, K. S. (2014) Photo-click living strategy for controlled, reversible exchange of biochemical ligands. *Adv. Mater.* *26*, 2521–6.
- (238) Poshusta, A. K., Burdick, J. A., Mortisen, D. J., Padera, R. F., Ruhlman, D., Yaszemski, M. J., and Anseth, K. S. (2003) Histocompatibility of photocrosslinked



polyanhydrides: a novel in situ forming orthopaedic biomaterial. *J. Biomed. Mater. Res. A* 64, 62–9.

(239) Rydholm, A. E., Bowman, C. N., and Anseth, K. S. (2005) Degradable thiol-acrylate photopolymers: polymerization and degradation behavior of an in situ forming biomaterial. *Biomaterials* 26, 4495–4506.

(240) Jen, A. C., Wake, M. C., and Mikos, A. G. (1996) Review: Hydrogels for cell immobilization. *Biotechnol. Bioeng.* 50, 357–64.

(241) Fedorovich, N. E., Oudshoorn, M. H., van Geemen, D., Hennink, W. E., Alblas, J., and Dhert, W. J. A. (2009) The effect of photopolymerization on stem cells embedded in hydrogels. *Biomaterials* 30, 344–53.

(242) Baroli, B. (2006) Photopolymerization of biomaterials: issues and potentialities in drug delivery, tissue engineering, and cell encapsulation applications. *J. Chem. Technol. Biotechnol.* 81, 491–499.

(243) Kade, M. J., Burke, D. J., and Hawker, C. J. (2010) The Power of Thiol-ene Chemistry. *J. Polym. Sci. Part A-Polymer Chem.* 48, 743–750.

(244) Khire, V. S., Benoit, D. S. W., Anseth, K. S., and Bowman, C. N. (2006) Ultrathin gradient films using thiol-ene polymerizations RID B-1490-2008. *J. Polym. Sci. Part A-Polymer Chem.* 44, 7027–7039.

(245) Saboktakin, M. R., Tabatabaie, R. M., Maharramov, A., and Ramazanov, M. A. (2011) Synthesis and in vitro studies of biodegradable thiolated chitosan hydrogels for breast cancer therapy. *Int. J. Biol. Macromol.* 48, 747–752.

(246) Lu, B., Zhu, D., Hinton, D., Humayun, M. S., and Tai, Y.-C. (2012) Mesh-supported submicron parylene-C membranes for culturing retinal pigment epithelial cells. *Biomed. Microdevices* 14, 659–667.

(247) Ribeiro, R. M., Oregon, A., Diniz, B., Fernandes, R. B., Koss, M. J., Charafeddin, W., Hu, Y., Thomas, P., Thomas, B. B., Maia, M., Chader, G. J., Hinton, D. R., and Humayun, M. S. (2013) In Vivo Detection of hESC-RPE Cells via Confocal Near-Infrared Fundus Reflectance. *Ophthalmic Surg. Lasers Imaging* 44, 380–384.

(248) Tucker, B. A., Anfinson, K. R., Mullins, R. F., Stone, E. M., and Young, M. J. (2013) Use of a synthetic xeno-free culture substrate for induced pluripotent stem cell induction and retinal differentiation. *Stem Cells Transl. Med.* 2, 16–24.

(249) Lu, L. C., Yaszemski, M. J., and Mikos, A. G. (2001) Retinal pigment epithelium engineering using synthetic biodegradable polymers. *Biomaterials* 22, 3345–3355.

- (250) Pankhurst, Q. A., Thanh, N. T. K., Jones, S. K., and Dobson, J. (2009) Progress in applications of magnetic nanoparticles in biomedicine. *J. Phys. D-Applied Phys.* 42, 224001.
- (251) Chang, M.-H., Liu, H.-S., and Tai, C. Y. (2011) Preparation of copper oxide nanoparticles and its application in nanofluid. *Powder Technol.* 207, 378–386.
- (252) Yu, W., and Xie, H. (2012) A Review on Nanofluids: Preparation, Stability Mechanisms, and Applications. *J. Nanomater.* 435873.
- (253) Ramu, V. G., Bordoloi, A., Nagaiah, T. C., Schuhmann, W., Muhler, M., and Cabrele, C. (2012) Copper nanoparticles stabilized on nitrogen-doped carbon nanotubes as efficient and recyclable catalysts for alkyne/aldehyde/cyclic amine A(3)-type coupling reactions. *Appl. Catal. A-General* 431, 88–94.
- (254) Ranu, B. C., Chattopadhyay, K., Adak, L., Saha, A., Bhadra, S., Dey, R., and Saha, D. (2009) Metal nanoparticles as efficient catalysts for organic reactions. *Pure Appl. Chem.* 81, 2337–2354.
- (255) Ren, G., Hu, D., Cheng, E. W. C., Vargas-Reus, M. a, Reip, P., and Allaker, R. P. (2009) Characterisation of copper oxide nanoparticles for antimicrobial applications. *Int. J. Antimicrob. Agents* 33, 587–590.
- (256) Cioffi, N., Torsi, L., Ditaranto, N., Tantillo, G., Ghibelli, L., Sabbatini, L., Blevè-Zacheo, T., D'Alessio, M., Zambonin, P. G., and Traversa, E. (2005) Copper nanoparticle/polymer composites with antifungal and bacteriostatic properties. *Chem. Mater.* 17, 5255–5262.
- (257) Li, Y., Lu, W., Huang, Q., Huang, M., Li, C., and Chen, W. (2010) Copper sulfide nanoparticles for photothermal ablation of tumor cells. *Nanomedicine* 5, 1161–1171.
- (258) Na, H. Bin, Song, I. C., and Hyeon, T. (2009) Inorganic Nanoparticles for MRI Contrast Agents. *Adv. Mater.* 21, 2133–2148.
- (259) Tu, C., and Louie, A. Y. (2012) Nanoformulations for molecular MRI. *Wiley Interdiscip. Rev. Nanobiotechnology* 4, 448–457.
- (260) Brewer, G. J. (2003) Copper in medicine. *Curr. Opin. Chem. Biol.* 7, 207–212.
- (261) Sivasubramanian, K. N., and Henkin, R. I. (1978) Behavioral and dermatologic changes and low serum zinc and copper concentrations in two premature infants after parenteral alimentation. *J. Pediatr.* 93, 847–851.
- (262) Barros Amorim, M. J., and Scott-Fordsmand, J. J. (2012) Toxicity of copper nanoparticles and CuCl<sub>2</sub> salt to *Enchytraeus albidus* worms: Survival, reproduction and avoidance responses. *Environ. Pollut.* 164, 164–168.



- (263) Bai, W., Tian, W., Zhang, Z., He, X., Ma, Y., Liu, N., and Chai, Z. (2010) Effects of Copper Nanoparticles on the Development of Zebrafish Embryos. *J. Nanosci. Nanotechnol.* 10, 8670–8676.
- (264) Yang, Z., Liu, Z. W., Allaker, R. P., Reip, P., Oxford, J., Ahmad, Z., and Ren, G. (2010) A review of nanoparticle functionality and toxicity on the central nervous system. *J. R. Soc. Interface* 7, S411–S422.
- (265) Pettibone, J. M., Adamcakova-Dodd, A., Thorne, P. S., O’Shaughnessy, P. T., Weydert, J. a., and Grassian, V. H. (2008) Inflammatory response of mice following inhalation exposure to iron and copper nanoparticles. *Nanotoxicology* 2, 189–204.
- (266) Kim, J. S., Adamcakova-Dodd, A., O’Shaughnessy, P. T., Grassian, V. H., and Thorne, P. S. (2011) Effects of copper nanoparticle exposure on host defense in a murine pulmonary infection model. *Part. Fibre Toxicol.* 8, 29.
- (267) Shi, M., Kwon, H. S., Peng, Z., Elder, A., and Yang, H. (2012) Effects of Surface Chemistry on the Generation of Reactive Oxygen Species by Copper Nanoparticles. *ACS Nano* 6, 2157–2164.
- (268) Dias, A. M. G. C., Hussain, A., Marcos, A. S., and Roque, A. C. A. (2011) A biotechnological perspective on the application of iron oxide magnetic colloids modified with polysaccharides. *Biotechnol. Adv.* 29, 142–155.
- (269) Hombach, J., Hoyer, H., and Bernkop-Schnuerch, A. (2008) Thiolated chitosans: Development and in vitro evaluation of an oral tobramycin sulphate delivery system. *Eur. J. Pharm. Sci.* 33, 1–8.
- (270) Rekha, M. R., and Sharma, C. P. (2009) Synthesis and evaluation of lauryl succinyl chitosan particles towards oral insulin delivery and absorption. *J. Control. Release* 135, 144–151.
- (271) Saravanakumar, G., Min, K. H., Min, D. S., Kim, A. Y., Lee, C.-M., Cho, Y. W., Lee, S. C., Kim, K., Jeong, S. Y., Park, K., Park, J. H., and Kwon, I. C. (2009) Hydrotropic oligomer-conjugated glycol chitosan as a carrier of paclitaxel: Synthesis, characterization, and in vivo biodistribution. *J. Control. Release* 140, 210–217.
- (272) Ye, Y.-Q., Yang, F.-L., Hu, F.-Q., Du, Y.-Z., Yuan, H., and Yu, H.-Y. (2008) Core-modified chitosan-based polymeric micelles for controlled release of doxorubicin. *Int. J. Pharm.* 352, 294–301.
- (273) Fernandes, J. C., Tiera, M. J., and M., W. F. (2006) Chitosan Nanoparticles for Non-Viral Gene Therapy, in *Polysaccharides for Drug Delivery and Pharmaceutical Applications*, pp 177–200. American Chemical Society.

- (274) Lavertu, M., Methot, S., Tran-Khanh, N., and Buschmann, M. D. (2006) High efficiency gene transfer using chitosan/DNA nanoparticles with specific combinations of molecular weight and degree of deacetylation. *Biomaterials* 27, 4815–4824.
- (275) Kiang, T., Wen, H., Lim, H. W., and Leong, K. W. (2004) The effect of the degree of chitosan deacetylation on the efficiency of gene transfection. *Biomaterials* 25, 5293–5301.
- (276) Park, I. K., Kim, T. H., Kim, S. I., Akaike, T., and Cho, C. S. (2003) Chemical modification of chitosan for gene delivery. *J. Dispers. Sci. Technol.* 24, 489–498.
- (277) Crompton, K. E., Prankerd, R. J., Paganin, D. M., Scott, T. F., Horne, M. K., Finkelstein, D. I., Gross, K. A., and Forsythe, J. S. (2005) Morphology and gelation of thermosensitive chitosan hydrogels. *Biophys. Chem.* 117, 47–53.
- (278) Kim, S., Nishimoto, S. K., Bumgardner, J. D., Haggard, W. O., Gaber, M. W., and Yang, Y. (2010) A chitosan/beta-glycerophosphate thermo-sensitive gel for the delivery of ellagic acid for the treatment of brain cancer. *Biomaterials* 31, 4157–4166.
- (279) Ruel-Gariepy, E., Chenite, A., Chaput, C., Guirguis, S., and Leroux, J. C. (2000) Characterization of thermosensitive chitosan gels for the sustained delivery of drugs. *Int. J. Pharm.* 203, 89–98.
- (280) Ruel-Gariepy, E., Shive, M., Bichara, A., Berrada, M., Le Garrec, D., Chenite, A., and Leroux, J. C. (2004) A thermosensitive chitosan-based hydrogel for the local delivery of paclitaxel. *Eur. J. Pharm. Biopharm.* 57, 53–63.
- (281) Osuna, Y., Gregorio-Jauregui, K. M., Gerardo Gaona-Lozano, J., de la Garza-Rodriguez, I. M., Ilyna, A., Diaz Barriga-Castro, E., Saade, H., and Lopez, R. G. (2012) Chitosan-Coated Magnetic Nanoparticles with Low Chitosan Content Prepared in One-Step. *J. Nanomater.* 327562.
- (282) Shi, S.-F., Jia, J.-F., Guo, X.-K., Zhao, Y.-P., Chen, D.-S., Guo, Y.-Y., Cheng, T., and Zhang, X.-L. (2012) Biocompatibility of chitosan-coated iron oxide nanoparticles with osteoblast cells. *Int. J. Nanomedicine* 7, 5593–5602.
- (283) Zhu, Y., Kalen, A. L., Li, L., Lehmler, H.-J., Robertson, L. W., Goswami, P. C., Spitz, D. R., and Aykin-Burns, N. (2009) Polychlorinated-biphenyl-induced oxidative stress and cytotoxicity can be mitigated by antioxidants after exposure. *Free Radic. Biol. Med.* 47, 1762–1771.
- (284) Aslan, K., and Perez-Luna, V. H. (2002) Surface modification of colloidal gold by chemisorption of alkanethiols in the presence of a nonionic surfactant. *Langmuir* 18, 6059–6065.

- (285) Zhao, Y., Wang, Z., Zhang, W., and Jiang, X. (2010) Adsorbed Tween 80 is unique in its ability to improve the stability of gold nanoparticles in solutions of biomolecules. *Nanoscale* 2, 2114–2119.
- (286) Sun, W. Q., Xie, C. S., Wang, H. F., and Hu, Y. (2004) Specific role of polysorbate 80 coating on the targeting of nanoparticles to the brain. *Biomaterials* 25, 3065–3071.
- (287) Sivars, U., and Tjerneld, F. (2000) Mechanisms of phase behaviour and protein partitioning in detergent/polymer aqueous two-phase systems for purification of integral membrane proteins. *Biochim. Biophys. Acta - Gen. Subj.* 1474, 133–146.
- (288) Mudunkotuwa, I. A., Pettibone, J. M., and Grassian, V. H. (2012) Environmental Implications of Nanoparticle Aging in the Processing and Fate of Copper-Based Nanomaterials. *Environ. Sci. Technol.* 46, 7001–7010.
- (289) Zaru, M., Manca, M.-L., Fadda, A. M., and Antimisiaris, S. G. (2009) Chitosan-coated liposomes for delivery to lungs by nebulisation. *Colloids Surfaces B Biointerfaces* 71, 88–95.
- (290) Yamamoto, H., Kuno, Y., Sugimoto, S., Takeuchi, H., and Kawashima, Y. (2005) Surface-modified PLGA nanosphere with chitosan improved pulmonary delivery of calcitonin by mucoadhesion and opening of the intercellular tight junctions. *J. Control. Release* 102, 373–381.
- (291) Vllasaliu, D., Casettari, L., Fowler, R., Exposito-Harris, R., Garnett, M., Illum, L., and Stolnik, S. (2012) Absorption-promoting effects of chitosan in airway and intestinal cell lines: A comparative study. *Int. J. Pharm.* 430, 151–160.
- (292) Vllasaliu, D., Exposito-Harris, R., Heras, A., Casettari, L., Garnett, M., Illum, L., and Stolnik, S. (2010) Tight junction modulation by chitosan nanoparticles: Comparison with chitosan solution. *Int. J. Pharm.* 400, 183–193.
- (293) Hombach, J., and Bernkop-Schnürch, A. (2009) Chitosan solutions and particles: Evaluation of their permeation enhancing potential on MDCK cells used as blood brain barrier model. *Int. J. Pharm.* 376, 104–109.
- (294) Lamba, D. A., McUsic, A., Hirata, R. K., Wang, P.-R., Russell, D., and Reh, T. A. (2010) Generation, Purification and Transplantation of Photoreceptors Derived from Human Induced Pluripotent Stem Cells. *PLoS One* 5, e8763–e8763.
- (295) Tucker, B. A., Park, I.-H., Qi, S. D., Klassen, H. J., Jiang, C., Yao, J., Redenti, S., Daley, G. Q., and Young, M. J. (2011) Transplantation of Adult Mouse iPS Cell-Derived Photoreceptor Precursors Restores Retinal Structure and Function in Degenerative Mice. *PLoS One* 6, e18992–e18992.

- (296) Da Silva, G. R., Fialho, S. L., Siqueira, R. C., Jorge, R., and Cunha Junior, A. da S. (2010) Implants as drug delivery devices for the treatment of eye diseases. *Brazilian J. Pharm. Sci.* 46, 585–595.
- (297) Hu, Y., Liu, L., Lu, B., Zhu, D., Ribeiro, R., Diniz, B., Thomas, P. B., Ahuja, A. K., Hinton, D. R., Tai, Y.-C., Hikita, S. T., Johnson, L. V, Clegg, D. O., Thomas, B. B., and Humayun, M. S. (2012) A Novel Approach for Subretinal Implantation of Ultrathin Substrates Containing Stem Cell-Derived Retinal Pigment Epithelium Monolayer. *Ophthalmic Res.* 48, 186–191.
- (298) Janoria, K. G., Gunda, S., Boddu, S. H., and Mitra, A. K. (2007) Novel approaches to retinal drug delivery. *Expert Opin. Drug Deliv.* 4, 371–388.
- (299) Pritchard, C. D., Arner, K. M., Langer, R. S., and Ghosh, F. K. (2010) Retinal transplantation using surface modified poly(glycerol-co-sebacic acid) membranes. *Biomaterials* 31, 7978–7984.
- (300) Winter, J. O., Gokhale, M., Jensen, R. J., Cogan, S. F., and Rizzo, III, J. F. (2008) Tissue engineering applied to the retinal prosthesis: Neurotrophin-eluting polymeric hydrogel coatings. *Mater. Sci. Eng. C-Biomimetic Supramol. Syst.* 28, 448–453.
- (301) Wu, W., Peters, W. H., and Hammer, M. E. (1987) Basic Mechanical-Properties of Retina in Simple Elongation. *J. Biomech. Eng. Asme* 109, 65–67.
- (302) Wollensak, G., and Spoerl, E. (2004) Biomechanical characteristics of retina. *Retin. J. Retin. Vit. Dis.* 24, 967–970.
- (303) Basinger, B. C., Rowley, A. P., Chen, K., Humayun, M. S., and Weiland, J. D. (2009) Finite element modeling of retinal prosthesis mechanics. *J. Neural Eng.* 6, 55006.
- (304) Chen, K., and Weiland, J. D. (2012) Mechanical Characteristics of the Porcine Retina in Low Temperatures. *Retin. J. Retin. Vit. Dis.* 32, 844–847.
- (305) Armani, D., Liu, C., and Aluru, N. (1999) Re-configurable fluid circuits by PDMS elastomer micromachining, in *Micro Electro Mechanical Systems, 1999. MEMS '99. Twelfth IEEE International Conference on*, pp 222–227.
- (306) Wiwatwongwana, F., Klunathon, Y., Rangsi, W., Promma, N., and Pattana, S. (2012) Identification of Shear Modulus of Gelatin Blended with Carboxymethylcellulose Scaffolds Using Curve Fitting Method from Compressive Test. *J. Mater. Sci. Res. J Mater Sci Res* 1, 106–113.
- (307) Moore, D. B., Harris, A., and Siesky, B. (2011) Republished review: The world through a lens: the vision of Sir Harold Ridley. *Postgrad. Med. J.* 87, 307–310.

- (308) Checa-Casalengua, P., Jiang, C., Bravo-Osuna, I., Tucker, B. A., Molina-Martinez, I. T., Young, M. J., and Herrero-Vanrell, R. (2011) Retinal ganglion cells survival in a glaucoma model by GDNF/Vit E PLGA microspheres prepared according to a novel microencapsulation procedure. *J. Control. Release* 156, 92–100.
- (309) Jiang, C., Moore, M. J., Zhang, X., Klassen, H., Langer, R., and Young, M. (2007) Intravitreal injections of GDNF-loaded biodegradable microspheres are neuroprotective in a rat model of glaucoma. *Mol. Vis.* 13, 1783–1792.
- (310) Aránzazu Partearroyo, M., Ostolaza, H., Goñi, F. M., and Barberá-Guillem, E. (1990) Surfactant-induced cell toxicity and cell lysis. A study using B16 melanoma cells. *Biochem. Pharmacol.* 40, 1323–8.
- (311) Catalone, B. J., Kish-Catalone, T. M., Neely, E. B., Budgeon, L. R., Ferguson, M. L., Stiller, C., Miller, S. R., Malamud, D., Krebs, F. C., Howett, M. K., and Wigdahl, B. (2005) Comparative safety evaluation of the candidate vaginal microbicide C31G. *Antimicrob. Agents Chemother.* 49, 1509–20.
- (312) Dias, R. S., Innerlohinger, J., Glatter, O., Miguel, M. G., and Lindman, B. (2005) Coil-globule transition of DNA molecules induced by cationic surfactants: a dynamic light scattering study. *J. Phys. Chem. B* 109, 10458–63.
- (313) Dymond, M. K., and Attard, G. S. (2008) Cationic type I amphiphiles as modulators of membrane curvature elastic stress in vivo. *Langmuir* 24, 11743–51.
- (314) Fichorova, R. N., Tucker, L. D., and Anderson, D. J. (2001) The molecular basis of nonoxynol-9-induced vaginal inflammation and its possible relevance to human immunodeficiency virus type 1 transmission. *J. Infect. Dis.* 184, 418–28.
- (315) Inácio, Â. S., Mesquita, K. A., Baptista, M., Ramalho-Santos, J., Vaz, W. L. C., and Vieira, O. V. (2011) In vitro surfactant structure-toxicity relationships: implications for surfactant use in sexually transmitted infection prophylaxis and contraception. *PLoS One* (Covas, D. T., Ed.) 6, e19850.
- (316) Krebs, F. C., Miller, S. R., Catalone, B. J., Welsh, P. A., Malamud, D., Howett, M. K., and Wigdahl, B. (2000) Sodium dodecyl sulfate and C31G as microbicidal alternatives to nonoxynol 9: comparative sensitivity of primary human vaginal keratinocytes. *Antimicrob. Agents Chemother.* 44, 1954–60.
- (317) Matulis, D., Rouzina, I., and Bloomfield, V. A. (2002) Thermodynamics of cationic lipid binding to DNA and DNA condensation: roles of electrostatics and hydrophobicity. *J. Am. Chem. Soc.* 124, 7331–42.
- (318) Mesquita, P. M. M., Cheshenko, N., Wilson, S. S., Mhatre, M., Guzman, E., Fakioglu, E., Keller, M. J., and Herold, B. C. (2009) Disruption of tight junctions by

cellulose sulfate facilitates HIV infection: model of microbicide safety. *J. Infect. Dis.* 200, 599–608.

(319) Vieira, D. B., and Carmona-Ribeiro, A. M. (2006) Cationic lipids and surfactants as antifungal agents: mode of action. *J. Antimicrob. Chemother.* 58, 760–7.

(320) Vieira, O. V., Hartmann, D. O., Cardoso, C. M. P., Oberdoerfer, D., Baptista, M., Santos, M. A. S., Almeida, L., Ramalho-Santos, J., and Vaz, W. L. C. (2008) Surfactants as microbicides and contraceptive agents: a systematic in vitro study. *PLoS One* 3, e2913.

(321) Zhu, D.-M., and Evans, R. K. (2006) Molecular mechanism and thermodynamics study of plasmid DNA and cationic surfactants interactions. *Langmuir* 22, 3735–43.

(322) Wu, Z., Tong, W., Jiang, W., Liu, X., Wang, Y., and Chen, H. (2012) Poly(N-vinylpyrrolidone)-modified poly(dimethylsiloxane) elastomers as anti-biofouling materials. *Colloids Surf. B. Biointerfaces* 96, 37–43.

(323) Wu, G., Gan, S., Cui, L., and Xu, Y. (2008) Preparation and characterization of PES/TiO<sub>2</sub> composite membranes. *Appl. Surf. Sci.* 254, 7080–7086.

(324) Akar, N., Asar, B., Dizge, N., and Koyuncu, I. (2013) Investigation of characterization and biofouling properties of PES membrane containing selenium and copper nanoparticles. *J. Memb. Sci.* 437, 216–226.

(325) Choi, Y. H., Kim, J. C., Ahn, J. K., Ko, S. Y., Kim, D. H., and Lee, T. (2008) Anti-biofouling behavior of natural unsaturated hydrocarbon phenols impregnated in PDMS matrix. *J. Ind. Eng. Chem.* 14, 292–296.

(326) Ju, H., McCloskey, B. D., Sagle, A. C., Kusuma, V. A., and Freeman, B. D. (2009) Preparation and characterization of crosslinked poly(ethylene glycol) diacrylate hydrogels as fouling-resistant membrane coating materials. *J. Memb. Sci.* 330, 180–188.

(327) Ostuni, E., Chapman, R. G., Liang, M. N., Meluleni, G., Pier, G., Ingber, D. E., and Whitesides, G. M. (2001) Self-Assembled Monolayers That Resist the Adsorption of Proteins and the Adhesion of Bacterial and Mammalian Cells. *Langmuir* 17, 6336–6343.

(328) Senaratne, W., Andruzzi, L., and Ober, C. K. (2005) Self-assembled monolayers and polymer brushes in biotechnology: current applications and future perspectives. *Biomacromolecules* 6, 2427–48.

(329) Lee, T. Y., Guymon, C. A., Jönsson, E. S., and Hoyle, C. E. (2004) The effect of monomer structure on oxygen inhibition of (meth)acrylates photopolymerization. *Polymer (Guildf)*. 45, 6155–6162.

(330) Yao, J., Tao, S. L., and Young, M. J. (2011) Synthetic Polymer Scaffolds for Stem Cell Transplantation in Retinal Tissue Engineering. *Polymers (Basel)*. 3, 899–914.



- (331) Treharne, A. J., Gossel, M. C., Lotery, A. J., and Thomson, H. a. (2011) The chemistry of retinal transplantation: the influence of polymer scaffold properties on retinal cell adhesion and control. *Br. J. Ophthalmol.* 95, 768–73.
- (332) Koocheki, S., Madaeni, S. S., and Niroomandi, P. (2011) Application of hydroxyapatite nanoparticles in development of an enhanced formulation for delivering sustained release of triamcinolone acetonide. *Int. J. Nanomedicine* 6, 825–33.
- (333) Sung, H.-J., Meredith, C., Johnson, C., and Galis, Z. S. (2004) The effect of scaffold degradation rate on three-dimensional cell growth and angiogenesis. *Biomaterials* 25, 5735–42.
- (334) Bhattarai, N., Gunn, J., and Zhang, M. (2010) Chitosan-based hydrogels for controlled, localized drug delivery. *Adv. Drug Deliv. Rev.* 62, 83–99.
- (335) Sinha, V. R., Singla, A. K., Wadhawan, S., Kaushik, R., Kumria, R., Bansal, K., and Dhawan, S. (2004) Chitosan microspheres as a potential carrier for drugs. *Int. J. Pharm.* 274, 1–33.
- (336) Kofuji, K., Murata, Y., and Kawashima, S. (2005) Sustained insulin release with biodegradation of chitosan gel beads prepared by copper ions. *Int. J. Pharm.* 303, 95–103.
- (337) Qi, L., Xu, Z., Jiang, X., Li, Y., and Wang, M. (2005) Cytotoxic activities of chitosan nanoparticles and copper-loaded nanoparticles. *Bioorg. Med. Chem. Lett.* 15, 1397–9.
- (338) Thein-Han, W. W., Kitiyanant, Y., and Misra, R. D. K. (2008) Chitosan as scaffold matrix for tissue engineering. *Mater. Sci. Technol.* 24, 1062–1075.
- (339) National Institute of Advanced Industrial Science and Technology (AIST). Spectral Database for Organic Compounds.
- (340) Saha, K., Keung, A. J., Irwin, E. F., Li, Y., Little, L., Schaffer, D. V., and Healy, K. E. (2008) Substrate modulus directs neural stem cell behavior. *Biophys. J.* 95, 4426–38.
- (341) Worthington, K. S., Wiley, L. A., Bartlett, A. M., Stone, E. M., Mullins, R. F., Salem, A. K., Guymon, C. A., and Tucker, B. A. (2014) Mechanical Properties of Murine and Porcine Ocular Tissues in Compression. *Exp. Eye Res.* 121, 194–99.
- (342) Worthington, K. L. S., Adamcakova-Dodd, A., Wongrakpanich, A., Mudunkotuwa, I. A., Mapuskar, K. A., Joshi, V. B., Allan Guymon, C., Spitz, D. R., Grassian, V. H., Thorne, P. S., and Salem, A. K. (2013) Chitosan coating of copper nanoparticles reduces in vitro toxicity and increases inflammation in the lung. *Nanotechnology* 24, 395101.